Charge-Carrier Dynamics in Hybrid Metal Halide Perovskites for Next-Generation Solar Cells



Kimberley Jade Savill

Brasenose College

University of Oxford

A thesis submitted for the degree of

Doctor of Philosophy

Trinity 2020

Acknowledgements

This thesis, and the work presented within it, have been made possible by the support, encouragement, collaboration and company of a great many people and institutions, both during my time at Oxford and on the journey that brought me here. I am very grateful to all of them, and want to acknowledge some of the most significant below:

First of all, enormous thanks to my supervisor, Professor Laura Herz, who assured me when I first considered applying for a DPhil that I could make the switch from chemistry into physics, and whose guidance, support and good advice have ensured the truth of that ever since and taught me a great deal along the way.

Thanks also to the whole of the Semiconductors Group and Terahertz Photonics Group, who have collectively made the work environment in which my DPhil took shape such a positive, welcoming and interesting one. Specifically, thanks again to Professor Laura Herz, together with honorary second supervisor Professor Michael Johnston, for leading such a good group culture by example. Thanks to the postdocs and students preceding me who introduced me to the labs, to the unshakeable importance of tea breaks, and to the group in general with enthusiasm and patience for questions: Adam Wright, Chris Davies, Djamshid Damry, Elizabeth Parrott, Jay Patel, Jessica Boland, Juliane Borchert, Juliane Gong, Laura Martínez-Maestro, Rebecca Milot, Sabrina Sterzl, Timothy Crothers, and Waqaas Rehman. And to them as well as to those who started when I did or joined since, thanks for the collaborations both formal and informal, and all the scientific discussions, cryptic crosswords, park (or pub) lunches, croquet competitions and tea chats (both in person and via Teams) along the way: Aleksander Ulatowski, Alex Knight, Chelsea Xia, Elizabeth Duijnstee, Hannah Eggimann, James Ball, Kilian Lohmann, Kun Peng, Lavina Snoek, Leonardo Buizza, Mathias Rothmann, Michael Trimpl, Qianqian Lin, Robbie Oliver, and Silvia Motti.

While the people around me have shaped my DPhil experience in hugely significant ways, I wouldn't have been able to fund it in the first place without generous support from several sources. First and most significantly, I would like to thank the Rhodes Trust for bringing me to Oxford on a Rhodes Scholarship, funding me through three years of the DPhil, and supporting me throughout. Thanks also to Universities New Zealand for the LB Wood Travelling Scholarship, and Brasenose College for a Hulme Completion Grant, both of which have helped sustain me into a fourth year of study.

Beyond the realm of funding, I also owe many thanks to the Rhodes community as a whole, which has played a huge part in making my experience of Oxford both enjoyable and formative, and brought me across the path of so many good people and truly wonderful friends. To all of the Rhodes House staff, and in particular Mary Eaton, Nadiya Figueroa, Elizabeth Kiss, and Doyin Atewologun, thanks for all the work both visible and unseen that goes into making the space and time for this community in Oxford and beyond. I am enormously thankful for all the fellow scholars, and friends I have met through them, who have enriched and brightened my Oxford experience on even the darker days. Special mention to a few groups: to my fellow ANZers, and particularly Andrés, Emilie, Harj, Ilona, Jade, Jimmy, Matt, and Oscar, for making the Oxford years an adventure even before we arrived here, and more of a home once we did; to all the 4th$^+$ years who've stuck around at least as long as I have and been a joy to share that journey with; and to the Zoom regulars, especially Tonny, Oscar, Mayanka, Matthew, Martin, Majd, and Dylan, for making writing up during a pandemic so much less lonely than it might have been.

Looking back, I might never have considered pursuing a research degree without the encouragement and direction of excellent teachers and mentors. At Nayland College, whose many great teachers, huge variety of opportunities, and flexibility to treat students as individuals made my final years of school genuinely transformative, I owe particular thanks to Dr Treena Blythe, who gave me an ideal space to grow by inviting me into her class, encouraged me to be braver, and assured me that I could do a PhD if I wanted to; to Gaye Bloomfield, who helped me learn that there is such a thing as good enough work; and to John Walker, who gave up an astonishing number of hours to enable early morning and weekend maths sessions. And at Victoria University of Wellington, in whose chemistry department I found a striking sense of scientific community, I am especially grateful to both Dr Matthias Lein, my Honours supervisor, and Prof. Justin Hodgkiss for their support and generosity with advice and recommendations as I started on the path of postgraduate study.

Through every step in life so far, and no less so for this DPhil, I have been fortunate to have a wonderful family around and behind me. To Melanie and Tim Savill, my parents, thanks for really just about everything, but in particular for encouraging me onwards even when that means moving (back) to the other side of the world. And to Patrick Savill, my bigger younger brother, thanks for the letters, chats, actually making it over to visit, and most of all for being an all-round excellent sibling.

Finally, to Nicholas Bai Berg, who understood before I did what an amazing opportunity was in front of me, encouraged me to go after it, and has believed I would be up to the task no matter how many doubts I had, thank you for taking the leap in moving to Oxford, and for being on my team through every up and down along this journey.

Abstract

Hybrid metal halide perovskites have emerged over the last decade as highly promising materials for use in solar cells. Their advantages include low production costs, and rapidly increasing efficiencies to compete with those of commercially dominant silicon cells. Recently, increasing attention has been devoted to the use of perovskites in next-generation photovoltaic devices in order to overcome the efficiency limit for conventional single-junction cells. Work is still needed to identify the most promising perovskite materials for these applications, and to fully understand their relevant properties. This thesis contributes to both goals.

The challenge of identifying the true timescale of charge-carrier cooling in metal halide perovskites, and whether certain compositions in fact show exceptionally slow cooling, is addressed. This is central to assessing the viability of hot-carrier extraction in perovskite solar cells. Key sources of error in previous approaches to determine charge-carrier temperature, which have produced an orders-of-magnitude range of reported cooling times, are identified. An improved model, which accounts for the full photoluminescence lineshape and enables a consistent approach that can be applied to studies across different perovskite compositions, is then described.

Applying this improved model, charge-carrier cooling in $FASnI_3$ is studied, revealing that observations of a secondary regime of slow charge-carrier cooling are in fact attributable to electronic relaxation, state-filling and recombination in this energetically disordered material. This result highlights that careful analysis of charge-carrier cooling dynamics is vital to assessing the realistic prospects for hot-carrier solar cells. Photoluminescence polarisation memory in $FASnI_3$ is also examined, finding no persistent polarisation anisotropy within 270 fs. This points to a need for further study to identify the factors that lead such memory to arise from structural changes in certain perovskite compositions.

Finally, the effects of the SnF_2 additive commonly used to improve material quality of tin-containing perovskites are explored for $FA_{0.83}Cs_{0.17}Sn_xPb_{1-x}I_3$ across the lead-tin range. Significant beneficial effects from the suppression of tin oxidation and associated background hole doping, including reduced energetic disorder and increased charge-carrier mobilities and lifetimes, are found with as little as 1 mol% SnF_2 added. The larger amounts of additive that have commonly been used are found to contribute to detrimental non-radiative recombination. These results, unravelling the impacts of SnF_2 on both structural and optoelectronic properties, provide a foundation for control over the properties of mixed tin-lead perovskites for use as low-bandgap absorbers in all-perovskite tandem cells.

Contents

List of Publications viii

1 Introduction 1

2 Optoelectronic Properties of Tin-Lead Perovskites for Photovoltaics 5
- 2.1 Big picture: The need for solar energy . . . 6
- 2.2 Background: The rise of perovskites for photovoltaic applications . . . 7
  - 2.2.1 Hybrid metal halide perovskites . . . 8
  - 2.2.2 Development of perovskite solar cells over time . . . 9
- 2.3 Fundamentals: Optoelectronic properties of hybrid metal halide perovskites 11
  - 2.3.1 Excitation of charge carriers . . . 11
  - 2.3.2 Thermalisation and charge-carrier cooling . . . 12
  - 2.3.3 Recombination of charge carriers . . . 13
  - 2.3.4 Charge transport . . . 16
  - 2.3.5 Defects and trapping . . . 17
- 2.4 Focus: Tin-containing perovskites for next generation solar cell concepts 18
  - 2.4.1 Benefits of tin and tin-lead perovskites . . . 18
  - 2.4.2 Hot-carrier solar cells . . . 20
  - 2.4.3 All-perovskite tandem cells . . . 21
  - 2.4.4 Instability of tin-containing perovskites . . . 23
- 2.5 Key research questions addressed in this thesis . . . 24

3 Experimental Methods 26
- 3.1 Time-integrated photoluminescence spectroscopy . . . 27
  - 3.1.1 Experimental setup . . . 28
  - 3.1.2 Spectral response calibration . . . 30
- 3.2 Time-resolved photoluminescence spectroscopy . . . 33
  - 3.2.1 Upconversion spectroscopy . . . 34
  - 3.2.2 Time-correlated single photon counting . . . 44
- 3.3 Absorption spectroscopy . . . 49
  - 3.3.1 Determining absorbance . . . 49
  - 3.3.2 Fourier transform infrared spectroscopy . . . 51
  - 3.3.3 Experimental setup . . . 52

3.4 X-ray diffraction . . . 53
3.4.1 Theory . . . 53
3.4.2 Experimental setup . . . 55

4 Determining Charge-Carrier Temperature from Measured Spectra 56
4.1 Motivation . . . 57
4.2 Previous approaches to determining charge-carrier temperature . . . 58
4.2.1 Perovskite literature . . . 58
4.2.2 Historical context . . . 59
4.3 An improved, full lineshape model . . . 61
4.3.1 Choice of model . . . 61
4.4 Impact of adopting the full lineshape model . . . 65
4.4.1 Accounting for energy-dependent density of states . . . 70
4.4.2 Accounting for spectral broadening . . . 72
4.4.3 Fitting the full spectrum . . . 74
4.5 Conclusions . . . 77
4.6 Future outlook . . . 78

5 Charge-Carrier Cooling Dynamics and Photoluminescence Polarisation Memory Loss in $FASnI_3$ 79
5.1 Experimental details . . . 80
5.1.1 Samples . . . 80
5.1.2 Spectroscopy . . . 82
5.1.3 Analysis . . . 83
5.2 Charge-carrier cooling dynamics in $FASnI_3$ . . . 89
5.2.1 Motivation . . . 89
5.2.2 Results and discussion . . . 89
5.2.3 Conclusions . . . 93
5.3 Photoluminescence polarisation memory . . . 96
5.3.1 Motivation . . . 96
5.3.2 Results and discussion . . . 97
5.3.3 Conclusions . . . 101
5.4 Summary . . . 101
5.5 Future outlook . . . 102

6 Impact of Tin Fluoride Additive on the Properties of $FA_{0.83}Cs_{0.17}Sn_xPb_{1-x}I_3$ Perovskite Semiconductors 104
6.1 Motivation . . . 105
6.2 Experimental details . . . 106
6.2.1 Samples . . . 106
6.2.2 X-ray diffraction measurement . . . 108

6.2.3 Absorption and photoluminescence spectroscopy 108
6.2.4 Time-resolved photoluminescence measurement 109
6.2.5 Terahertz spectroscopy 110
6.2.6 Analysis 111
6.3 Results and discussion 114
6.3.1 Crystal structure 114
6.3.2 Background doping density 124
6.3.3 Photoluminescence lifetimes 126
6.3.4 Absorption and emission properties 128
6.3.5 Charge-carrier mobility 136
6.4 Conclusions 138
6.5 Future outlook 139

7 Conclusions and Outlook **141**

List of Abbreviations **145**

Appendices

A Supplementary figures, calculations, and sample characterisation for Chapter 5 **149**
A.1 $FASnI_3$ sample characterisation 149
A.2 Excitation density calculation 153
A.3 Power-dependent photoluminescence peak shift in $FASnI_3$ 154

B Supplementary figures and tables, and details of terahertz spectroscopy analysis, for Chapter 6 **158**
B.1 Structural characterisation by X-ray diffraction 158
B.2 Analysis of terahertz spectroscopy results 160
B.3 Supplementary absorption and photoluminescence figures 169

C Permissions for reuse of material previously published **173**
C.1 Reuse of content from self-authored articles 173
C.2 Reuse of content from articles authored by others 174

References **175**

List of Publications

Savill, K. J.; Klug, M. T.; Milot, R. L.; Snaith, H. J. and Herz, L. M. 'Charge-Carrier Cooling and Polarization Memory Loss in Formamidinium Tin Triiodide'. *J. Phys. Chem. Lett.*, 2019, **10**, 6038-6047

Ulatowski, A. M.; Wright, A. D.; Wenger, B.; Buizza, L. R. V.; Motti, S. G.; Eggimann, H. J.; **Savill, K. J.**; Borchert, J.; Snaith, H. J.; Johnston, M. B. and Herz, L. M. 'Charge-Carrier Trapping Dynamics in Bismuth-Doped Thin Films of $MAPbBr_3$ Perovskite'. *J. Phys. Chem. Lett.*, 2020, **11**, 3681-3688

Savill, K. J.; Ulatowski, A. M.; Farrar, M. D.; Johnston, M. B.; Snaith, H. J. and Herz, L. M. 'Impact of Tin Fluoride Additive on the Properties of Mixed Tin-Lead Iodide Perovskite Semiconductors'. *Adv. Funct. Mater.*, 2020, **30**, 2005594

1 Introduction

Since the Paris Agreement came into force in November 2016, the goal of limiting global temperature increase above pre-industrial levels to well below 2 °C has provided a focus to international efforts to combat climate change, now shared by 188 ratifying States and the European Union. [1, 2] Meeting this target in the context of increasing global demand for energy [3] urgently requires a transition away from fossil fuels in favour of renewable energy sources. Solar energy, installed capacity for which has been growing more rapidly than any other renewable over the last ten years, [4] is set to play a major role in the future energy landscape. Improving the performance of photovoltaic technologies could therefore be globally impactful.

Efficiency improvements in the crystalline silicon solar cells that currently dominate the market have been slow in recent years, whereas several competitor materials have shown promise. [5] Hybrid metal halide perovskites stand out from the field by combining cheap, low temperature, and scalable production from abundant precursor materials with impressive efficiency gains over the last decade. [5–7] To achieve still higher efficiencies, next-generation solar cell concepts beyond the conventional single-junction design are increasingly attractive. Perovskite materials are particularly promising for use in tandem

cells, [8, 9] and more speculatively in hot-carrier devices which offer even higher theoretical maximum efficiencies. [10, 11]

Understanding and control over the properties of tin-containing perovskites, which have to date been less well-studied than lead-based compositions, is needed for both of these applications. The work presented in this thesis addresses that need, as outlined below.

Thesis Overview

Chapter 2 contextualises the work in this thesis, providing an introduction to hybrid metal halide perovskites and their rapid ascent in the field of photovoltaics before reviewing the key optoelectronic properties of these materials. The existing understanding of processes affecting photoexcited charge carriers in perovskite materials, described in this chapter, introduces the importance of charge-carrier cooling and provides a framework for assessing the materials studied in this thesis. Chapter 2 then introduces the hot-carrier and tandem device concepts that aim to surpass the efficiency limits on conventional single-junction solar cells, motivating the work in this thesis, and reviews key properties of the tin-containing perovskites studied here for use in such next-generation devices.

Chapter 3 introduces the experimental techniques employed in this thesis, describing the theory underlying each technique and the specific setups used. The photoluminescence spectroscopy techniques which are particularly significant in this work, including time-resolved measurement by both upconversion and time-correlated single photon counting methods, are discussed in detail. The complementary technique of absorption spectroscopy is described, and a brief introduction to X-ray diffraction as a tool for structural characterisation is provided.

Chapter 4 addresses the phenomenon of charge-carrier cooling, a significant energy loss pathway in solar cells which hot-carrier devices seek to overcome. [12] Assessing the realistic prospects for success of perovskite hot-carrier solar cells has so far been made

difficult by the wide range of cooling times, and variety of suggested mechanisms, emerging from studies on hybrid metal halide perovskites. [11] In Chapter 4, the methods used previously to determine charge-carrier temperature from photoluminescence spectra are examined. Several significant sources of error, likely to contribute to the lack of consensus on cooling times, are identified. An improved model for determining charge-carrier temperature from the full photoluminescence lineshape is then presented. This enables more accurate results and greater consistency in approach between studies so that in future the process of charge-carrier cooling in perovskite materials may be more fully understood.

Chapter 5 continues on the theme of charge-carrier cooling, exploring ultrafast charge-carrier dynamics following photoexcitation in $FASnI_3$. This tin perovskite has been put forward as a particularly promising material for use in hot-carrier solar cells. [13] Using a combination of upconversion and time-correlated single-photon counting measurements, the evolution over time of $FASnI_3$ photoluminescence spectra including emission from hot carriers is examined. Charge-carrier temperatures are then determined using the model described in Chapter 4. By comparing charge-carrier cooling dynamics with overall photoluminescence decay, the appearance of unusually slow carrier cooling is found to arise from energetic disorder in this tin-based perovskite composition. This illustrates the importance of careful analysis to reveal the true timescale of charge-carrier cooling in perovskites. Polarisation-dependent photoluminescence measurements also reveal that polarisation memory in $FASnI_3$ is lost within a few hundred femtoseconds, while charge carriers are still hot. This finding contrasts with previous reports of persistent polarisation memory in several lead-based perovskites and suggests further research is needed to understand the role of polarisation memory in perovskite materials.

Chapter 6 unravels the effects of tin fluoride additive on $FA_{0.83}Cs_{0.17}Sn_xPb_{1-x}I_3$ perovskites across the tin-lead compositional range. While the role of tin-based perovskites in hot-carrier solar cells remains speculative, mixed tin-lead perovskites are already

important in tandem cells, [14] which also offer increased efficiency by reducing losses due to charge-carrier cooling. Suppressing the ready oxidation of tin to improve material quality is a pressing challenge for these applications. A large array of additives are therefore employed in the preparation of tin-lead perovskites, [15, 16] the most common being tin fluoride. In Chapter 6, the effects of this additive on $FA_{0.83}Cs_{0.17}Sn_xPb_{1-x}I_3$ are explored using a combination of photoluminescence, absorption, and X-ray diffraction measurements. Terahertz spectroscopy measurements performed by a collaborator provide additional insight. Beneficial effects identified to result from reduced formation of tin vacancies and lower background hole density with addition of tin fluoride include lower structural distortion and energetic disorder, and higher photoluminescence lifetimes and charge-carrier mobilities. The use of excess tin fluoride is found to have unwanted effects, enhancing loss pathways via non-radiative recombination. Addition of 1 % tin fluoride is found to optimise the desirable effects of the additive without detrimental side effects. These findings give direct insight into how the tin fluoride additive can be used to best effect, and provide a foundation for future investigations of additives in tin-lead perovskites by identifying the compositional range over which additive effects are most significant.

Finally, Chapter 7 brings together the conclusions from research presented in this thesis, and provides an outlook for future developments that could build upon this work.

2

Optoelectronic Properties of Tin-Lead Perovskites for Photovoltaics

Contents

2.1 Big picture: The need for solar energy 6
2.2 Background: The rise of perovskites for photovoltaic applications 7
2.2.1 Hybrid metal halide perovskites 8
2.2.2 Development of perovskite solar cells over time 9
2.3 Fundamentals: Optoelectronic properties of hybrid metal halide perovskites 11
2.3.1 Excitation of charge carriers 11
2.3.2 Thermalisation and charge-carrier cooling 12
2.3.3 Recombination of charge carriers 13
2.3.4 Charge transport 16
2.3.5 Defects and trapping 17
2.4 Focus: Tin-containing perovskites for next generation solar cell concepts 18
2.4.1 Benefits of tin and tin-lead perovskites 18
2.4.2 Hot-carrier solar cells 20
2.4.3 All-perovskite tandem cells 21
2.4.4 Instability of tin-containing perovskites 23
2.5 Key research questions addressed in this thesis 24

This chapter outlines the background to, and motivation for, the work presented in this thesis in the context of previous research. First, the importance of photovoltaic

technologies in transitioning to a sustainable energy system capable of meeting global demand is outlined. Hybrid metal halide perovskites are then introduced, and their rapid rise in the field of photovoltaic devices is described. The existing understanding of key optoelectronic properties of this material class, which underpin their successful application in devices, is then reviewed. Finally, the appeal of tin-containing perovskites for reduced toxicity and next-generation photovoltaic devices to break the single-junction efficiency limit is introduced. The specific device concepts of hot-carrier extraction and all-perovskite tandem cells, to which the results in this thesis are most relevant, are reviewed along with the challenges to realising the potential of tin-containing perovskites in such applications.

2.1 Big picture: The need for solar energy

Global demand for energy is growing, with a predicted rise of at least 1 % per year until 2040 based on existing and intended policies around the world, and demand for electricity increasing at a higher rate than overall demand. [3] Meanwhile, limiting global warming to 1.5 °C requires dramatic reductions in CO_2 emissions within this timescale, [17] making a shift away from burning fossil fuels an essential component in efforts to meet future energy demand. Alternative, renewable, energy sources are therefore needed, harnessing solar, tidal and wave, geothermal, wind, biomass or hydro power. Of these renewable technologies, solar energy represented the third largest share of installed capacity worldwide in 2019 and has shown the greatest growth in capacity over the preceding decade. [4] In addition to decreasing installation costs over time, photovoltaic technology has the advantages of low ecosystem impact when installed and usability on scales from local to industrial, [18] and abundant solar radiation at high intensities across many regions of the world. [19] Significant further growth in solar energy generation by 2040, to become the dominant contributor to total installed capacity worldwide, is predicted based on policies and targets stated to date. [3] The energy

efficiency, and financial and environmental costs, of photovoltaic devices are therefore significant considerations in the trajectory towards a sustainable energy future, and provide the underlying motivation for the work included in this thesis.

Currently, the large majority of commercial solar cells use a crystalline silicon absorber layer in a single junction cell architecture, with this technology having approximately 95 % market share. [20] Crystalline silicon cells offer good power conversion efficiencies exceeding 26 % in research cells, [21] which is close to the theoretical limit. The scope for further improvements to crystalline silicon cells is therefore small, and efficiency increases over the past two decades have been slow. [5] Additionally, production of solar grade silicon is an energy-intensive process that raises the energy consumption and greenhouse gas emissions involved in module production. [22, 23] Alternative light-absorbing materials that can be processed more cheaply and at lower temperatures, requiring less energy input, than crystalline silicon are therefore desirable for future improvements in performance relative to cost. Additionally, significantly higher efficiencies may be achieved by moving beyond conventional single junction cells to new device concepts such as tandem cells. Hybrid metal halide perovskites are particularly promising for both of these pathways to achieve better performing, lower cost photovoltaic devices.

2.2 Background: The rise of perovskites for photovoltaic applications

Among the range of alternative solar cell technologies that have been explored in recent decades, [5] hybrid metal halide perovskites stand out for their superior efficiency [21] and rapid increases in performance over time compared to competitors, as illustrated in Figure 2.1.

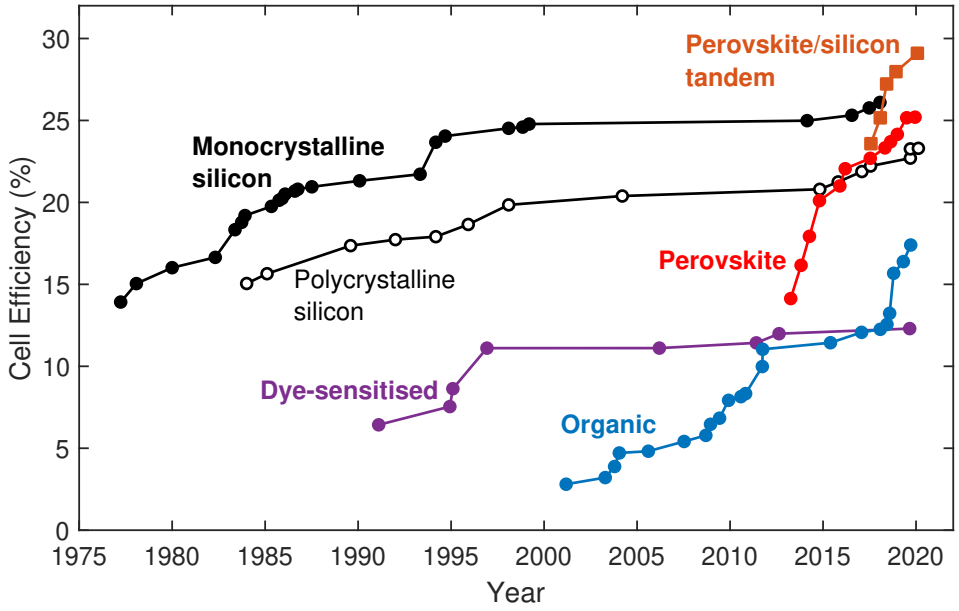


Figure 2.1: Development in best research cell efficiencies over time for silicon and emerging technologies including metal halide perovskites. Data obtained from reference [5].

2.2.1 Hybrid metal halide perovskites

Perovskites are a large family of materials, with chemical formulae of the form ABX_3 and the characteristic crystal structure as illustrated (for the ideal cubic phase) in Figure 2.2. The A and B sites are occupied by cations, the C sites by anions. Many oxide perovskites, with O^{2-} at the C site, are known and have been studied over the last 70 years for their properties including magnetism, magnetoresistance, superconductivity, and catalytic activity. [24] Hybrid metal halide perovskites (MHPs) with halide anions at the C site can also be synthesised, and first received investigation into their structural and optoelectronic properties in the 1970s and '80s. [25–27] The A cation in MHPs is monovalent, often either a small organic cation such as methylammonium (MA) or formamidinium (FA) which have the structures illustrated in Figure 2.2, or a metal cation such as Cs^+. A wide range of compositions are possible, with the ideal perovskite structure forming only for certain sizes of ion at each site in the lattice, as expressed by the Goldschmidt tolerance factor. [28] When larger A cations such as organic molecules

with longer carbon chains are introduced, layered or 2-dimensional perovskites can form with the large cations separating layers of inorganic octahedra. [29, 30]

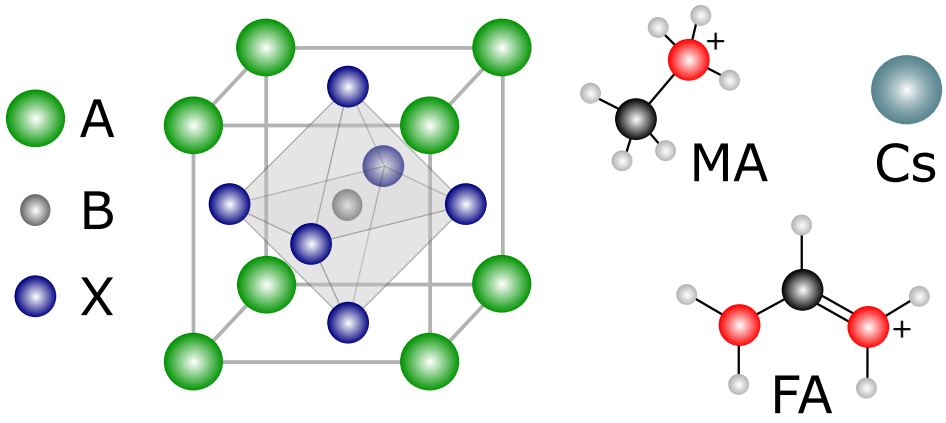


Figure 2.2: Characteristic cubic crystal structure of ABX_3 perovskite materials (left), and commonly used A cations in hybrid metal halide perovskites (right) showing chemical structure of the organic cations. MA = methylammonium, FA = formamidinium, with carbon atoms represented in black, nitrogen in red, hydrogen in light grey.

Along with their wide compositional variety, MHPs exhibit desirable properties for optoelectronic applications. Their semiconducting properties have been recognised for some time [31, 32] and applications in LEDs [33] and field-effect transistors [34] were explored before the massive growth in research on MHPs precipitated by their first uses in photovoltaic devices. [24] This thesis focusses on photovoltaic applications, for perovskite compositions with FA or mixed FACs cations at the A site, tin or mixed tin-lead cations at the B site, and iodide anions at the C site.

2.2.2 Development of perovskite solar cells over time

The first uses of MHPs in solar cells were based on the dye-sensitised solar cell (DSSC) architecture that had previously been demonstrated with molecular dyes used for light absorption and electron injection into a conductive layer. [35] The semiconducting MHPs were used in the role of sensitiser for conductive TiO_2 [36] in these DSSCs, absorbing incident light and then injecting photoexcited electrons into the mesoporous TiO_2 scaffold. While power conversion efficiency (PCE) reached around 7 % for such

devices, [37] degradation of the MHP in the presence of electrolyte materials was a persistent problem. [38] The subsequent development of all solid-state MHP solar cells, avoiding degradation due to the electrolyte, gave higher performance [39, 40] and was followed by meso-superstructured solar cells (MSSCs) in which the perovskite layer served as both absorber and electron conductor. [41, 42] The MSSC concept is illustrated in Figure 2.3A as the non injecting case, in contrast to DSSCs which would have a transport material surrounding the mesoporous scaffold and perovskite only on the surface of the mesoporous metal oxide as a sensitiser.

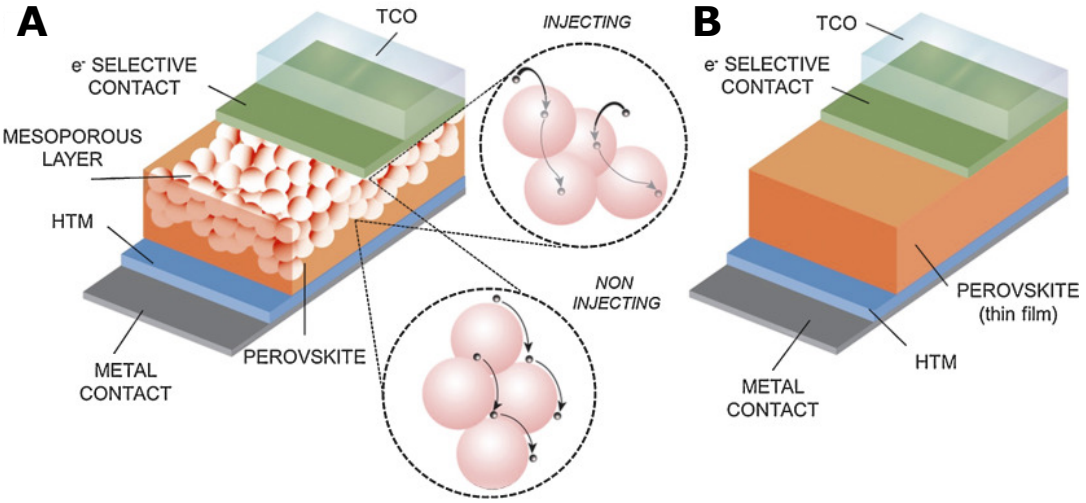


Figure 2.3: Development of perovskite solar cell device structures. **A)** Meso-superstructured solar cell structure in which there is no transport material interpenetrating with the mesoporous scaffold, and the perovskite material can act as both absorber and charge transport layer. The insets illustrate electron transport processes in the case of charge injection (as in dye-sensitised solar cells which share some features of this device structure) and in the non injecting MSSC case. **B)** Thin film planar heterojunction solar cell structure. In both (A) and (B), TCO = transparent conducting oxide, HTM = hole transport material. [Reproduced from reference [43] with permission from Elsevier.]

The mesoporous metal oxide scaffold used in MSSCs was soon found to be unnecessary, however, with MHP absorbers successfully incorporated in thin film planar heterojunction devices [42] as illustrated in Figure 2.3B, and rapid increases in PCE followed to exceed 20 % within a few years. [44–46] Low cost preparation techniques were also developed, with solution processing [6, 40] and vapour deposition [7, 44] both producing suitable

thin films, and offering routes to scale up for eventual commercialisation. [47] The planar heterojunction device architecture has since become well-established for MHP photovoltaics, and efficiencies have continued to increase to a current record for a single-junction perovskite cell of 25.2 %. [21] Still higher efficiencies have been achieved for multi-junction cells incorporating both perovskite and crystalline silicon absorber layers, [21] which have developed rapidly over a five year period. [48–50]

These advances have followed in large part from extensive exploration of different perovskite compositions, [51, 52] and optimisation of processing techniques and device stacks, [53–55] in pursuit of higher performance. Knowledge of the material properties that contribute to good photovoltaic performance in the various MHPs used has also developed over time. The remainder of this chapter covers key aspects of the present understanding, as well as open questions still remaining that are addressed in this thesis.

2.3 Fundamentals: Optoelectronic properties of hybrid metal halide perovskites

The suitability of MHPs for use in solar cells, evidenced by high device performances, arises from a combination of beneficial optoelectronic properties. Understanding these properties and the factors that affect them is an ongoing focus of research, including in this thesis, which builds on the foundation of previous work reviewed in this section.

2.3.1 Excitation of charge carriers

The absorption characteristics of MHPs are a significant contributor to their suitability for photovoltaic applications. These materials are typically direct bandgap semiconductors in which the maximum of the valence band and minimum of the conduction band are found at the same point in reciprocal space, [56] and have large absorption coefficients. [57] In addition to being strongly absorbing, MHPs typically have broad absorption spectra with a clear onset, [57, 58] and bandgap energy E_g can be tuned across the visible spectrum

by varying the perovskite composition. [59–62] This allows material selection to achieve an optimal bandgap for single- or multi-junction solar cell applications.

Following absorption of light with excitation of an electron into the conduction band, leaving behind a hole in the valence band, this pair of photoexcited charge carriers can remain associated with one another in a Coulombically bound state, forming an exciton. Dissociation into free charge carriers is limited by the exciton binding energy E_b, and in MHPs the value of E_b is often low such that excitons are only weakly bound, [58, 63, 64] and can dissociate at room temperature. Consequently, free charge carriers are dominant in the photoexcited population for many MHPs [65–69] which allows more ready extraction into charge transport layers in a photovoltaic device.

2.3.2 Thermalisation and charge-carrier cooling

Following absorption of light, charge carriers excited by photons with energy greater than E_g have excess kinetic energy. There are two processes by which this non-equilibrium population of excited charge carriers returns to equilibrium and dissipates the excess energy. Through carrier-carrier scattering, the population of charge carriers with excess energy becomes thermalised, and can be described by a temperature. [70–72] The term 'hot carriers' is then used to refer to this population retaining excess energy, which has a temperature higher than that of the lattice. The thermalisation process is rapid, typically occurring on the order of 100 fs, [73] and was found to take place over tens of femtoseconds in $MAPbI_3$. [72] For the measurements in this thesis, and over the sub-nanosecond to microsecond timescales relevant for carrier transport and subsequent extraction in solar cells, [74, 75] it can therefore be assumed that any photoexcited charge carriers with excess energy are already thermalised.

The second process, of greater relevance to photovoltaic devices, is the cooling of hot carriers to reach lattice temperature. Carrier cooling occurs by interaction between the

hot carriers and the lattice, transferring energy to phonons, [73, 76] and constitutes an intrinsic energy loss process that limits solar cell efficiency. This is often referred to as thermalisation loss, although charge-carrier cooling following the initial thermalisation process plays a significant role. [12] In MHPs, a wide range of cooling times have been reported from hundreds of femtoseconds [77, 78] to nanoseconds. [13] Some of the variation in experimentally determined cooling times has been attributed to excitation-density dependent effects such as a hot-phonon bottleneck, wherein a non-equilibrium population of hot phonons builds up and limits further cooling of hot carriers. [79, 80] Other explanations for apparent slow cooling of hot carriers have also been suggested, including Auger heating of carriers, [81–84] up-conversion of acoustic phonons, [85] and screening of the hot carriers by polaron formation. [86] As the range of suggested cooling mechanisms and observed timescales of carrier cooling indicates, understanding of this process in MHPs has not yet reached a consensus. This is addressed further in Chapters 4 and 5 of this thesis.

2.3.3 Recombination of charge carriers

Photoexcited charge carriers may relax back down in energy by a process of recombination, in which a photoexcited electron combines with a hole and returns to the valence band. In a solar cell, this is a current loss pathway that reduces the number of excited charge carriers available to be extracted as photocurrent. There are several types of recombination, classified based on how the rate of recombination depends upon the charge-carrier density n, which are captured in the following rate equation describing the overall decay in the charge-carrier population over time: [87]

$$\frac{dn}{dt} = -k_1 n - k_2 n^2 - k_3 n^3 \tag{2.1}$$

where k_i are the rate constants for first-, second-, and third-order recombination processes.

First-order recombination, with rate constant k_1, is typically referred to as monomolecular since the rate depends on one particle only. This scenario can arise for recombination of an exciton, but more commonly in MHPs where free charge carriers are dominant monomolecular recombination is a trap-mediated process. [88] In this case, as illustrated in Figure 2.4A, an electron (or hole) becomes trapped and can then recombine with a free hole (or electron) that encounters the trapped charge carrier, typically in a non-radiative process. [89] The trap states involved in this pathway typically arise due to defects, which are discussed further in Section 2.3.5 below, but trapping of either charge carrier at an interface following charge transfer can also give rise to first-order recombination kinetics. [90] Finally, pseudo-monomolecular recombination can occur when there is a high background density of either electrons or holes resulting from doping, with which photoexcited charge carriers can recombine radiatively. [91] Minimising k_1, by reducing the trap density or similarly the doping density, is beneficial for performance in photovoltaic devices as this can be a limiting factor for charge-carrier lifetime and diffusion length. [92]

Second-order recombination, referred to as bimolecular and having rate constant k_2, involves a free electron and free hole. This is a radiative process and is often the primary recombination pathway seen. [65, 67, 93] As illustrated in Figure 2.4B, the energy of photons emitted during bimolecular recombination reflects the energy of the photoexcited carriers involved, which may be higher up the band. Bimolecular recombination rates in MHPs are below the limit predicted by the Langevin model, which assumes free charge carriers recombine whenever they are closer together than their joint Coulomb capture radius, [66, 94, 95] a desirable feature in materials for photovoltaic applications. [87] It is now understood that the bimolecular recombination in MHPs is well-described as the inverse process to absorption, as is also the case for silicon and GaAs, rather than by the Langevin model. [96] Significant recombination is therefore to be expected for strongly

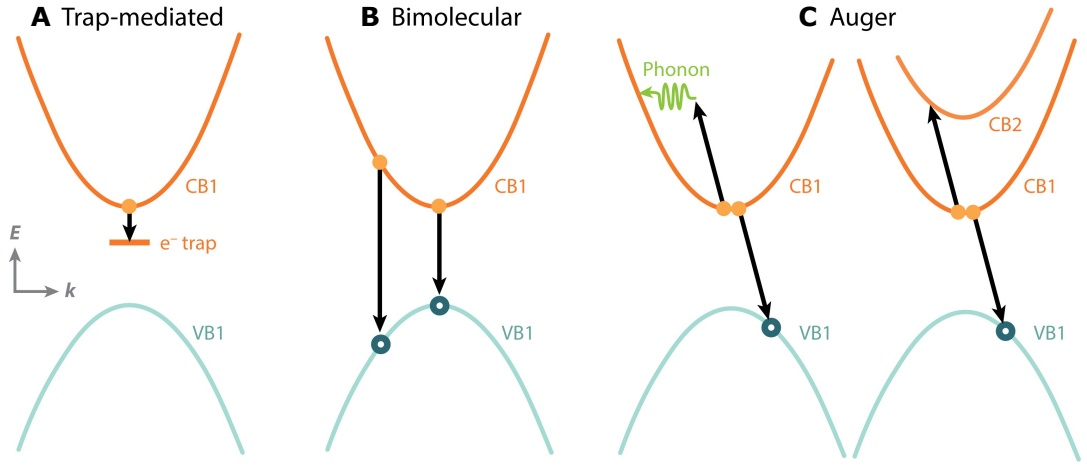


Figure 2.4: Schematic illustration of recombination mechanisms in hybrid metal halide perovskites, with the conduction band (CB) represented in orange and the valence band (VB) represented in light blue. Filled circles represent electrons, open circles represent holes. **A)** Trap-mediated, monomolecular, recombination illustrated for the case where an electron is trapped, and then recombines with a free hole. Holes may also be captured by a trap state similarly, which is not shown here. **B)** Bimolecular recombination between free electrons and holes, which may occur from states high in the band or after relaxation to the conduction band minimum/valence band maximum respectively. **C)** Auger recombination, a higher order process in which a free electron and hole recombine non-radiatively with energy transferred to another charge carrier to satisfy conservation of energy and momentum. [Reproduced from reference [87] with permission from Annual Reviews, Inc. provided by Copyright Clearance Center]

absorbing perovskite compositions, and the low values of k_2 in these materials contribute to long carrier lifetimes and diffusion lengths beneficial for photovoltaic applications.

Third-order or Auger recombination, with rate constant k_3, is a non-radiative pathway. As illustrated in Figure 2.4C, Auger recombination may involve only a third charge carrier that is excited into a suitable higher energy level, or a third charge carrier excited along with emission of a phonon, depending on the electronic structure of the material. This results in dependence of k_3 on perovskite phase, and hence band structure, that has been observed by experiment for $MAPbI_3$. [97] Since the interaction of three charge carriers is involved, Auger recombination only becomes significant at high charge-carrier densities, around $1 \times 10^{18}\,cm^{-3}$ and above, [87] that are beyond the typical operating range of a non-concentrator solar cell. [88] In fact, since trap-assisted recombination is dominant only at low fluences generating carrier densities too low to fill all traps, [67,

98] the contribution from bimolecular recombination is often the most significant in MHPs and, together with radiative pseudo-monomolecular recombination, is the pathway most directly studied in this thesis.

2.3.4 Charge transport

In a solar cell, photoexcited charge carriers must be extracted from the light-absorbing material into a charge transport layer, before passing to an electrode and thence the external circuit. This requires good transport properties in the absorber layer, so that charge carriers excited throughout this layer can reach an interface for extraction. Charge transport can be quantified by mobility, μ, or by diffusion length L_D, which is the average distance a charge carrier can move by diffusion without being lost to recombination and depends on both carrier lifetime and mobility. These parameters may be determined experimentally from photoluminescence decay data, using a diffusion model to determine the diffusion coefficient D from which to calculate L_D or μ, [99] or from photoconductivity measurements in which the photoconductivity depends on the mobility and density of excited charge carriers. [94] Long diffusion lengths, exceeding 1 μm, have been reported for a range of lead- and tin-based MHPs and contribute significantly to their suitability for use in solar cells. [66, 95, 99, 100]

While good charge transport is seen in many MHPs there is considerable variation in mobility with perovskite composition, with typically higher mobilities in tin based perovskites for example. [101] This variation reflects the influence of band structure on charge-carrier effective masses, [102–104] as well as changes in the electron-phonon coupling [101, 105] that fundamentally limits mobility. [106, 107] Alongside these intrinsic effects, charge-carrier mobility can be reduced by energetic disorder and structural instability, [66, 95] small grain size leading to scattering off grain boundaries, [108] or the presence of dopants. [109, 110]

2.3.5 Defects and trapping

Many of the processes described above, which are important to device performance, can be affected by defectiveness of the perovskite material. One common type of defect is crystallographic vacancies, which are classified as Frenkel defects when each vacancy is balanced by an interstitial of the same ion that is missing, or Schottky defects when positive vacancies are balanced by negative vacancies. [107, 111] Vacancies other than Schottky defects may give rise to sub-bandgap trap states, [111, 112] which can also originate from antisite defects where one ion occupies the position of another in the lattice, [113] or from electron-phonon coupling. [114] Additionally disorder, which may be structural in origin, has been found to introduce trap states that exist as part of a continuum of energy levels rather than as discrete states. [57, 115]

Compared to crystalline silicon, in which defect densities range from below $10^8\,\mathrm{cm}^{-3}$ to $10^{14}\,\mathrm{cm}^{-3}$ and must be kept low in devices, [116] MHPs are unusually defect tolerant. High performances have been achieved with MHP films having defect densities $10^{14}\,\mathrm{cm}^{-3}$ to $10^{17}\,\mathrm{cm}^{-3}$, [112, 117, 118] and investigation of defect chemistry in these materials has found that intrinsic vacancy defects introduce only shallow trap states in the bandgap. [111, 114] This relative insensitivity to defects has been a significant contributor to the successful use of low-temperature processed MHP films in photovoltaic devices, but there are still some detrimental effects of trapping and defectiveness. Trap states resulting from disorder contribute to sub-bandgap absorption, appearing as an exponential onset called the Urbach tail. [57, 119] Defects acting as centers for non-radiative recombination can shorten charge-carrier lifetimes [120] and diffusion lengths, [113] and limit the open circuit voltage attainable in devices. [121] Moreover, structural defects can be detrimental to the stability of the perovskite material against light or exposure to atmosphere. [122] To achieve higher performance in MHP photovoltaics it is therefore desirable to reduce disorder and defect density in these materials.

2.4 Focus: Tin-containing perovskites for next generation solar cell concepts

The development of perovskite photovoltaics to date has been largely focussed on lead-based MHPs. These lead perovskites have so far shown the highest device efficiencies [123] and there has been extensive research devoted to understanding their properties. Compositions with tin at the B site have received much less attention, but offer a number of benefits for photovoltaic applications. Tin-based MHPs are of particular interest in the context of next-generation device concepts such as hot-carrier solar cells and multi-junction devices, which aim for higher efficiencies by reducing thermalisation losses. To realise this potential, further investigation into the relevant properties of tin perovskites is needed, along with effective methods to reduce material instability due to oxidation of tin without detriment to the optoelectronic properties of the perovskite.

2.4.1 Benefits of tin and tin-lead perovskites

While much of the work devoted to the development of MHP solar cells has centered on lead-based perovskites, concerns about the toxicity of lead [124] provide motivation to develop lead-free perovskite solar cells using alternative MHP compositions. Among the alternative metal cations with suitable radii for incorporation into the ABX_3 perovskite lattice, which include Ni^{2+}, Cu^{2+}, Ge^{2+}, Sn^{2+} and Eu^{2+}, [56] tin was identified as the most promising candidate to replace lead, offering significantly higher power conversion efficiency in devices than other possibilities. [125] Early tin perovskite solar cells gave efficiencies between 4.4 – 6.4 %, [60, 61, 66, 126], lower than the first thin-film cells using lead perovskites [42] by only a few percentage points. Subsequent efforts to improve performance have resulted in numerous reports of tin perovskite solar cells with PCE values above 10 %, [127–130] and recent examples exceeding 11 %, [131] 12 %, [132] and 13 % [133] indicating that further improvements are still possible.

Although the performance of tin perovskite solar cells has so far lagged behind that of lead perovskites, tin perovskites do possess intrinsically beneficial properties beyond the reduction in toxicity. Higher charge-carrier mobilities have been observed for tin perovskites than the equivalent lead perovskite compositions [134, 135] which reflects the lower effective mass of charge carriers in tin perovskites. [136] Additionally, the bandgap of a given tin perovskite $ASnX_3$ is lower than that of the equivalent lead perovskite $APbX_3$ as a consequence of reduced spin orbit coupling. [102, 137] This is advantageous, since the bandgap of lead perovskites ranges from 1.47 – 2.3 eV, [7, 62, 138] larger than the predicted ideal bandgap of 1.3 – 1.4 eV to achieve maximum PCE in a single junction solar cell. [139, 140] By contrast the bandgaps of several tin perovskites fall within this ideal range, with $E_g = 1.35$ eV for $FASnI_3$, [141] and $E_g = 1.3$ eV for both $MASnI_3$ [61] and $CsSnI_3$. [142]

Mixed tin-lead perovskites, in which there is alloying of the two metals at the B site, offer even lower bandgaps than neat tin perovskites with the additional capacity to tune the bandgap by varying the ratio of lead to tin. This is made possible by the phenomenon of bandgap bowing, in which the bandgap varies non-linearly with composition so that some mixed compositions have lower bandgaps than the neat tin or neat lead endpoints. [60, 143–146] Bond bending in the mixed tin-lead compositions has been identified as the main factor giving rise to the bandgap bowing trend, [145] with orbital energy mismatch between tin and lead also playing a role. [146] Minimum bandgaps between 1.1 – 1.3 eV have been achieved through control of the tin:lead ratio in mixed tin-lead perovskites with a variety of A cations, [145, 147–150] making these materials particularly suitable for use in multi-junction solar cells. [14] Impressive efficiencies for single junction solar cells using tin-lead perovskite absorber layers have also been reported, at 18 – 19 % [151, 152] surpassing the performance achieved for tin perovskite cells to date. Along with tunability of the bandgap, strong performance in devices reflects the

long charge-carrier lifetimes relative to neat tin compositions, [153] and high mobilities relative to neat lead compositions, [135] that can be realised in mixed tin-lead perovskites.

2.4.2 Hot-carrier solar cells

The key concept in hot-carrier solar cells is extraction of hot charge carriers that have not cooled down to lattice temperature, reducing or wholly avoiding energy losses due to charge-carrier cooling and thereby achieving a higher cell voltage and improved efficiency. The theoretical maximum efficiency of such a device, capturing all the energy of the absorbed photons, has been predicted at 65.72 %. [154] While in practice the gains achieved with a hot-carrier cell would be lower than in this ideal case, 50 % efficiency has still been predicted allowing for non-ideal contacts and non-zero cooling rates. [10] Observations of slow carrier cooling in MHPs as discussed in Section 2.3.2 have raised interest in the possibility of developing hot-carrier cells with perovskite absorber layers. Charge-carrier cooling in MHPs is particularly slow in contrast to organic polymer solar cells, where hot excited states can be converted into other species within 50 fs. [155] The slower carrier-cooling times in the reported range for MHPs also compare favourably to inorganic semiconductor films, with cooling to equilibrium temperature over ∼3 ps reported for GaAs [79] and ∼20 ps in InN. [156] However, for a hot-carrier solar cell to function, the cooling time must be slow enough to allow hot carriers to be transported through the absorbing material to the interface with a charge transport layer, and then extracted into the transport layer. The relative rates of the transport and extraction processes are therefore also important.

Rapid charge extraction has been reported for some combinations of MHP absorber and transport layer. Sub-picosecond charge transfer has been identified between $MAPbI_3$ and metal oxide nanoparticles, [90] and hole injection to spiro-OMeTAD reported to occur in less than 80 fs, with hot holes also being injected. [157] Hole extraction within

hundreds of femtoseconds from $MA_{(1-y)}FA_yPbI_xBr_{(3-x)}$ into FDT or PTAA, [158] and $CsPbI_3$ to P3HT [159] has also been observed, and highly efficient extraction of hot electrons from $MAPbBr_3$ nanocrystals has been reported with surface-treatment and a molecular semiconductor extraction layer selected for high mobility, giving injection time of ∼0.2 ps. [81] Additionally, hot-carrier transport over hundreds of nanometers in $MAPbI_3$ has been reported, [160] which would be important for extracting long-lived hot carriers generated throughout the perovskite layer in a device.

Results such as these, together with the observed slow cooling which is particularly significant in determining attainable device efficiencies, [10, 161] motivate the ongoing interest in MHPs as materials for hot-carrier solar cells. [11] However, progress towards viable hot-carrier devices remains limited, with a recently reported device utilising a perovskite layer outside the two charge transport layers achieving only 0.45 V open circuit voltage and 5.4 mA cm^{-2} short circuit current density at best. [162] It has been suggested that hot-carrier lifetimes exceeding 1 ns are necessary to realise desirable efficiencies, [161, 163] and to date such slow cooling as this in MHPs has only been observed in one instance, for $FASnI_3$. [13] A careful assessment of the cooling times for hot carriers in MHPs, and particularly tin-based perovskites for which research on carrier cooling is relatively sparse to date, [11] is therefore needed to determine the prospects for realising predicted high efficiencies in hot-carrier solar cells.

2.4.3 All-perovskite tandem cells

In a tandem solar cell, two or more light absorbing layers with different bandgaps are incorporated into the same device stack. The largest bandgap material is used as the top layer, and lower-energy light passing through this material may then be absorbed by a lower bandgap layer beneath. This device design reduces thermalisation losses after photoexcitation in each absorbing material, and can give power conversion

efficiencies exceeding the Shockley-Queisser limit that applies to single junction cells. [8] The maximum efficiency possible for a tandem cell increases with the number of absorber layers, although the increase on moving from m to $m + 1$ layers decreases for higher m. [164] In the $m = 2$ case, which is of most relevance in this thesis, the theoretical limiting efficiency with non-concentrator light is 42.5 %. [165]

Tandem cells may be constructed either as a stack of individual subcells that each have two terminals, resulting in a 4-terminal tandem when two absorber layers are used, or with all subcells connected in series and terminals at the front and back of the whole device stack to give a 2-terminal tandem. [165] Both of these architectures have been explored for perovskite tandem cells, with the greatest amount of research attention to date being devoted to the use of perovskite top layers with silicon as the bottom absorber layer. [9, 166] The dominance of silicon cells in the existing market makes the perovskite/silicon tandem an attractive target for commercialisation, with this route being pursued by several startups. [167] Certified efficiency for 2-terminal perovskite/silicon tandem cells has now reached 29.15 %, [168] exceeding the records for either perovskite or silicon single junction cells. [21]

All-perovskite tandem cells offer additional benefits over perovskite/silicon tandems. Manufacturing costs and environmental impact can be reduced by switching from silicon to MHP absorber layers. [49, 169, 170] Additionally, the wide range of perovskite compositions available allows finer control over the bandgap of each absorber layer to optimise performance. [60, 171, 172] Over the last five years, efforts to develop all-perovskite tandems have achieved significant increases in efficiency. The first such devices to be demonstrated achieved less than 11 % PCE, [173, 174] whereas the highest reported efficiencies have now reached 24.8 % for a 2-terminal cell, [175] and 25 % for a 4-terminal cell. [176] Improvements in the low-bandgap perovskite layer have been important in

realising these efficiency gains. Since the first uses of tin-lead perovskites as the low-bandgap absorber, achieving 17 % PCE for a 2-terminal cell [150] and over 19 % for 4-terminal cells, [149, 150] these mixed-metal compositions have become the dominant choice of low-bandgap material. [14, 16] Notwithstanding the dramatic performance increases achieved so far, further improvement to all-perovskite tandems remains an important goal. Improved control over the properties of the low-bandgap absorber layer is likely to play a significant role in making such advances possible, and is addressed in this thesis.

2.4.4 Instability of tin-containing perovskites

A central challenge for the use of tin-containing perovskites in photovoltaic devices is the ready oxidation of Sn^{2+} to Sn^{4+}. This process results in tin vacancies and hole doping in the perovskite material, and is a major degradation pathway limiting the stability of tin containing perovskites. [122, 177, 178] Poor stability against exposure to oxygen is a concern for MHP solar cells, which must meet international environmental stability standards in order to be commercially viable. [179] More pressingly, the hole doping resulting from tin oxidation is detrimental to the performance of the perovskite layer, leading to rapid recombination between photoexcited electrons and background holes, and low charge-carrier mobility. [66, 141] These problems are less pronounced in mixed tin-lead perovskites with at least 50 % lead, where alloying has been found to increase stability, [178, 180] but remain a significant concern for MHPs with tin as the majority B cation. For neat tin perovskites in particular, oxidation of tin has long been identified as a key barrier to achieving higher device performances. [15, 181]

A variety of approaches to overcome the instability of tin in perovskites have been explored to date. [15] These include introducing large organic cations to form lower-dimensional perovskite structures, either 2D throughout the film [182, 183] or mixing 2D and 3D layers [184–186] as has also been done to significantly improve long-term stability

of some lead-based perovskites. [187, 188] Reduced dimensionality can increase stability by introducing hydrophobic layers and inhibiting ingress of oxygen and moisture, [189] as well as limiting defect formation, [190] but low-dimensional perovskites also have larger bandgaps and poor charge-carrier transport perpendicular to the direction of the perovskite layers. [30] The use of mixed ions has also been found to offer greater stability than a simple $ASnX_3$ composition in several cases, including for introduction of Cs [191] or hydrazinium [192] A cations mixed with FA or MA, Ge metal cations, [193] or mixed iodide-bromide anions. [194] A wide range of additives to inhibit oxidation are also used, including tin halides SnF_2, [195] $SnCl_2$ [196] or $SnBr_2$, [197] and reducing agents such as hypophosphorous acid, [198] ascorbic acid, [199] metallic tin, [200] or formic acid as a reducing solvent that leaves no residue after fabrication. [128] Tin fluoride in particular is widely used to suppress oxidation of Sn^{2+} in tin-containing perovskites, [15, 133, 141, 150, 195, 201] including in combination with other additives [129, 131, 132, 198, 200] and approaches such as ion substitution, [191, 194] surface passivation [127], or reduced dimensionality. [132, 182, 183] For neat tin perovskites, several studies have explored the impact of SnF_2 additive on optoelectronic and structural properties in detail, [202, 203] and compared the effects of different amounts of the additive. [141] A similar depth of understanding has not previously been developed for mixed tin-lead perovskites, however, and that lack is addressed in Chapter 6 of this thesis.

2.5 Key research questions addressed in this thesis

The topics covered in this chapter provide a foundation for the work presented in this thesis, which addresses the following questions relevant to the applications of tin and tin-lead perovskites and the development of next-generation solar cells to surpass the limits of single junction cells:

How slow is charge-carrier cooling in MHPs? Chapter 4 addresses the wide range of timescales observed for carrier cooling as described in Section 2.3.2, and presents a method for determining carrier temperature from measured data to better assess cooling times and identify the realistic prospects for MHP hot-carrier solar cells as discussed in Section 2.4.2.

Is $FASnI_3$ a particularly good candidate for hot-carrier extraction? In response to the particularly slow observed cooling for this tin perovskite discussed in Section 2.4.2, Chapter 5 applies the approach described in Chapter 4 to a study of $FASnI_3$ and identifies the role played by energetic disorder, related to the discussion in Section 2.3.5.

How does SnF_2 additive affect mixed tin-lead perovskites? Chapter 6 unravels the impacts of the common SnF_2 additive discussed in Section 2.4.4 on mixed tin-lead perovskites, providing a rational foundation for the careful control of material properties needed when these materials are used in all-perovskite tandem cells as described in Section 2.4.3.

Many of the results presented in this thesis to address the above questions are obtained by measurements of absorption and photoluminescence in MHPs, probing the excitation and radiative recombination processes described in Sections 2.3.1 and 2.3.3 respectively.

3 Experimental Methods

Contents

3.1 Time-integrated photoluminescence spectroscopy 27
3.1.1 Experimental setup 28
3.1.2 Spectral response calibration 30
3.2 Time-resolved photoluminescence spectroscopy 33
3.2.1 Upconversion spectroscopy 34
3.2.2 Time-correlated single photon counting 44
3.3 Absorption spectroscopy 49
3.3.1 Determining absorbance 49
3.3.2 Fourier transform infrared spectroscopy 51
3.3.3 Experimental setup 52
3.4 X-ray diffraction 53
3.4.1 Theory 53
3.4.2 Experimental setup 55

This chapter describes the main experimental techniques used for the work reported in this thesis, giving details of the underlying theory and operating principles of each technique, the specific experimental setups used, and the methods used to calibrate or correct measured data as appropriate for use in subsequent analysis. The primary techniques used were photoluminescence (PL) spectroscopy as described in Sections 3.1 and 3.2, and absorption spectroscopy described in Section 3.3. These spectroscopic techniques probe photoexcitation of charge carriers and their subsequent recombination

in competition with charge extraction and other loss pathways. As discussed in Section 2.3, these processes are central to the operation of perovskite active layers in photovoltaic devices. PL spectroscopy directly probes radiative recombination, giving information about the energy of excited charge carriers, and the population of charge carriers that recombines radiatively. Time-resolved PL measurements make it possible to track the changes in the energy and population of charge carriers over time after excitation, and give additional information about the competition between radiative recombination and other processes affecting excited charge carriers.

Results obtained using the techniques described in this chapter are reported throughout this thesis. Photoluminescence spectra from time-integrated measurements as described in Section 3.1 primarily feature in Chapter 6 as well as in Appendix A to Chapter 5. Time-resolved photoluminescence measurements using upconversion spectroscopy as described in Section 3.2.1 are employed in Chapter 5. Measurements using the complementary technique of time-correlated single photon counting as described in Section 3.2.2 feature in both Chapters 5 and 6. Absorption spectra measured using a Fourier transform infrared spectrometer as described in Section 3.3 are analysed in depth in Chapter 6. Finally, structural characterisation in Chapter 6 is achieved using X-ray diffraction, and the key principles of this technique as applied for work in this thesis are described in Section 3.4. Other experimental techniques employed by collaborators in the work reported here, such as spin-coating for sample fabrication, and terahertz spectroscopy techniques, are not discussed in this chapter. Instead, relevant specifics of these methods are given at the start of each results chapter.

3.1 Time-integrated photoluminescence spectroscopy

Time-integrated PL spectra give information about the emission profile of a material averaged over time, reflecting a population of charge carriers that has relaxed to the band

edge. In the case of direct bandgap semiconductors, the PL peak position is then typically close in energy to the absorption onset and the bandgap of the material. [112, 204, 205] The linewidth of the PL spectrum, which in perovskites often displays homogenous broadening attributable to coupling with phonons, [204] is also of interest as greater broadening reflects energetic disorder. Multiple peaks or the presence of a shoulder may be seen when there are populations of charge carriers emitting at several different energies, for example when phase-segregation occurs in a perovskite film to form regions with different bandgaps. [206]

To measure a PL spectrum, light emitted from a sample following excitation is typically focussed onto a prism or grating, which disperses the different wavelengths present in the emitted light for subsequent detection. [207] The systems used to measure spectra reported in this thesis, described below, follow this operating principle.

3.1.1 Experimental setup

Time-integrated PL spectra included in this thesis were measured on one of two setups, as shown in Figures 3.5 and 3.1. In both cases the sample is excited with a laser, then PL is focussed into a grating monochromator to be spectrally dispersed, and directed onto a detector. Long-pass or band-pass filters placed in the PL path are used to selectively block any background or scattered excitation light while allowing emission from the sample to pass through.

In the setup shown in Figure 3.5, which is also used for time-resolved measurements, the excitation beam is a pulsed laser (Mai Tai, Spectra Physics) with 80 MHz repetition rate, 80 fs pulse duration, and tunable wavelength in the range 690 – 1040 nm. For shorter wavelengths than 690 nm, a doubling crystal (β-barium borate) can be placed in the excitation beam together with a filter and polariser as shown in Figure 3.5 to selectively excite with the second harmonic of the laser instead. PL from the sample is focussed through a variable-width entrance slit into a grating monochromator (Triax,

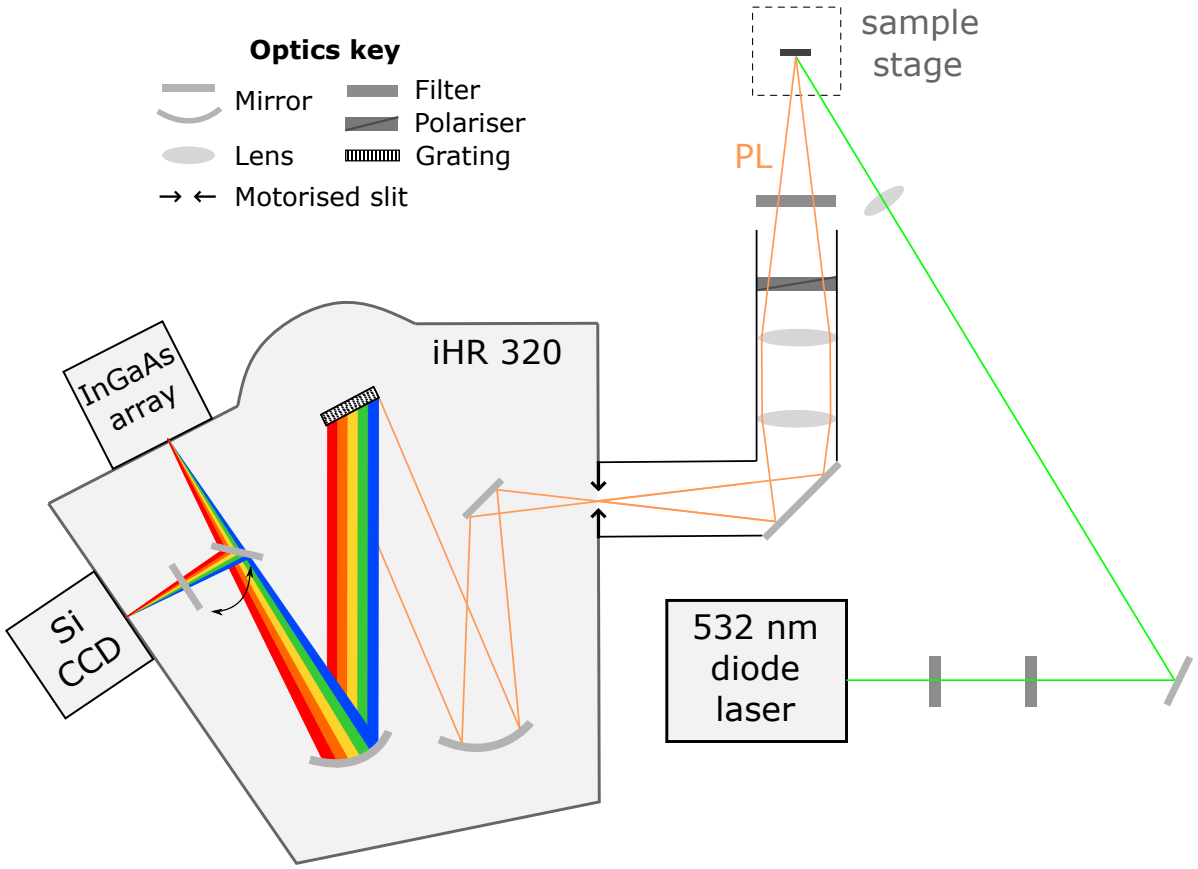


Figure 3.1: Schematic diagram of the dual-detector experimental setup used for time-integrated PL measurements on samples with emission towards the infrared.

Horiba), and then detected using a silicon charge coupled device (CCD) (Symphony, Horiba) cooled by liquid nitrogen.

For measurements on samples with emission further into the infrared where the response of the silicon CCD is low, a second time-integrated PL setup was used as shown in Figure 3.1. The excitation beam on this system is provided by a diode laser, which can be chosen interchangeably depending on the wavelength and power needed. For measurements reported in this thesis, a 532 nm continuous-wave laser (ventus, Laser Quantum) with tunable output power was used for excitation, with bandpass filters in the excitation beam to suppress other wavelengths including the second harmonic. As Figure 3.1 shows, PL from the sample is collected in a lens tube with removable long-pass filter to block scatter from the excitation beam, and variable polariser kept at fixed angle for the

work in this thesis, then focussed into a grating monochromator (iHR320, Horiba). The spectrally dispersed PL can then be directed onto either of two detectors via a movable exit mirror: a nitrogen cooled silicon CCD (Symphony, Horiba) as also used on the setup shown in Figure 3.5, or a linear InGaAs array (Symphony, Horiba) which is also nitrogen cooled and allows detection further into the infrared range, up to 1700 nm wavelength.

3.1.2 Spectral response calibration

The measured PL spectrum, in any experimental setup, depends not only on the emission profile from the sample, but also on the detector response and any filters present in the PL beam. A spectral response calibration can be performed to correct for these influences and recover as closely as possible the true PL spectrum of the sample. For the measurements included in this thesis, this was done by replacing the emissive sample in the setup with a light source of known spectrum, in this case a tungsten filament lamp (OL series 245 U). The response of the detector, allowing for any filters present in the setup, is then determined by comparison of the measured spectrum to the known spectrum of the lamp, and measured data are corrected for the measurement spectral response according to Equation 3.1.

$$I_{\text{true}} = I_{\text{measured}} \times \frac{I_{\text{lampstandard}}}{I_{\text{lampmeasured}}} \tag{3.1}$$

3.1.2.1 Combining data from two detectors

For samples which emit in the near infrared region between the spectral ranges best suited for measurement on either a silicon or an InGaAs detector, spectra may be measured on both detectors using the setup shown in Figure 3.1. Following correction for spectral response according to Equation 3.1 as described above, the data from these two detectors typically agree closely as shown in Figure 3.2 but some artefacts and increased noise in regions of low detector response remain. Spectra measured on the silicon detector, shown

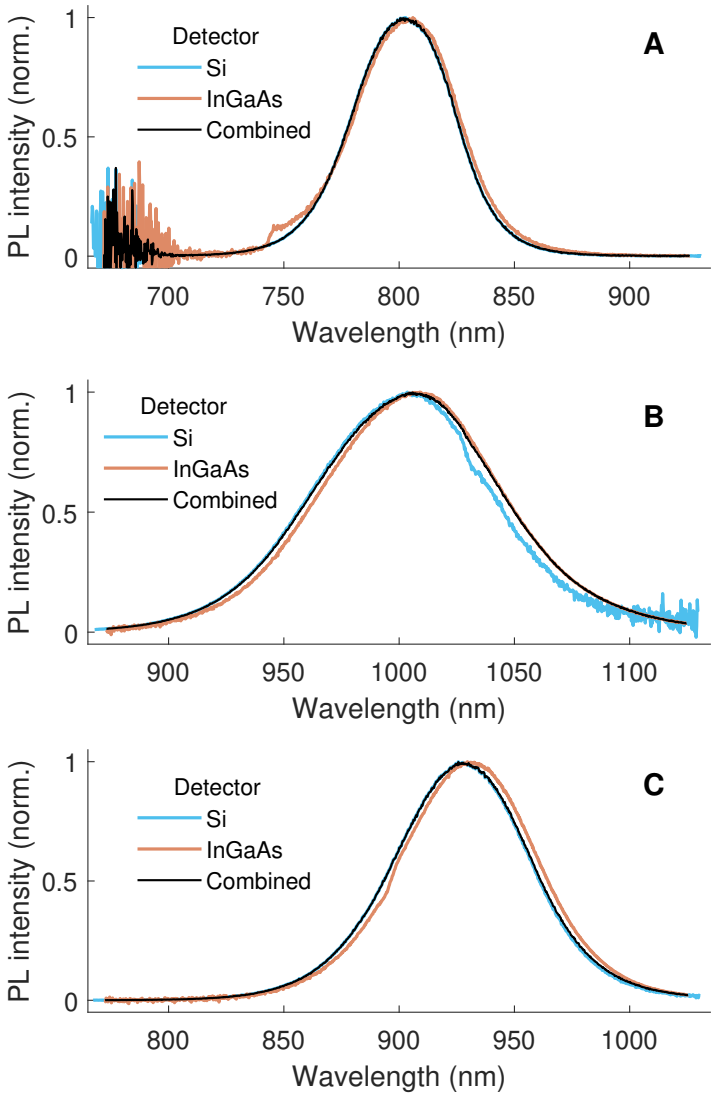


Figure 3.2: Example photoluminescence spectra measured with both Si CCD (light blue) and InGaAs array (orange) detectors, and combining data from both (black). In each panel the coloured lines show data after correcting for spectral response of the detector, and the black line shows the combined spectrum according to Equation 3.2 where at each point in the spectrum the detector with the stronger response is given greater weight to eliminate artefacts in regions of low detector response. Measurements were conducted using the setup shown in Figure 3.1 with $FA_{0.83}Cs_{0.17}Sn_xPb_{1-x}I_3$ perovskite thin films ($x = 0$ in panel A, $x = 0.6$ in panel B, $x = 1$ in panel C), which emit across the range where detector response changes significantly.

in light blue in Figure 3.2, show an artificial intensity dip near to 1030 nm and significantly increasing noise to longer wavelengths. Meanwhile spectra measured on the InGaAs detector, and shown in orange, display a similar small intensity dip around 890 nm which is identifiable as an artefact, and a larger step at 745 nm related to the onset of detection.

The data from both detectors can be combined into a single spectrum accord-

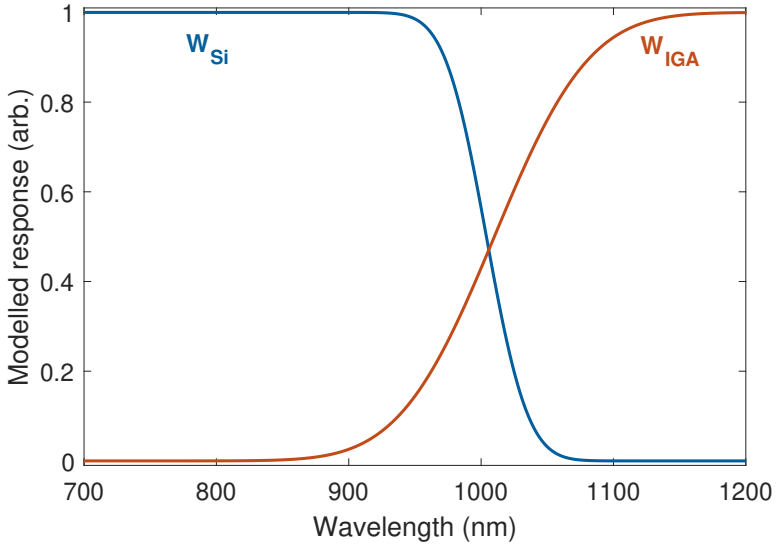


Figure 3.3: Weighting functions used in Equation 3.2 to combine data measured with Si CCD and InGaAs array detectors into a single spectrum. These functions model the drop off/rise in sensitivity for each detector using the error function, with the crossover point between the two curves occurring at the experimentally observed crossover wavelength of 1006 nm.

ing to Equation 3.2:

$$I(E) = \left(\frac{W_{\mathrm{Si}}(E)}{W_{\mathrm{Si}}(E) + W_{\mathrm{IGA}}(E)} \right) I_{\mathrm{Si}}(E) + \left(\frac{W_{\mathrm{IGA}}(E)}{W_{\mathrm{Si}}(E) + W_{\mathrm{IGA}}(E)} \right) I_{\mathrm{IGA}}(E) \tag{3.2}$$

which gives greater weight to the detector with the strongest response at each energy E across the measurement range and eliminates unwanted artefacts in the combined spectrum, shown in black in Figure 3.2. In this equation, normalised intensity data enter as I_{Si} and I_{IGA} for measurements on the Si CCD and InGaAs array respectively, and the contribution of each of these inputs in the combined spectrum is determined by the ratio of the weighting functions W_{Si} and W_{IGA}. As shown in Figure 3.3, these weighting functions model the drop off/onset of detector sensitivity using smoothly varying error functions. The specific form of each W has been chosen to preserve the experimentally observed crossover in intensity between the two detectors for the setup shown in Figure 3.1, which occurs at 1006 nm.

As can be seen in Figure 3.2, the combined spectra given by Equation 3.2 (plotted in black) closely reflect the measured data, without artefacts of low detector response.

Using this approach, there is no need to choose between detectors when the emission of a sample falls in between the ideal detection ranges. Instead, data from both detectors can be smoothly combined in a consistent manner that takes into account variations in responsivity, whatever the spectral range covered. This is particularly advantageous for MHP samples with significantly broadened PL, which would not be well captured by a single detector.

3.2 Time-resolved photoluminescence spectroscopy

The energy and density of excited charge carriers in a semiconductor both change over time as a result of competing relaxation, extraction and recombination processes as discussed in Section 2.3. These changes can be probed by time-resolved photoluminescence spectroscopy techniques, tracking the evolution of PL spectra over time or the decay transient of emission at a particular energy, from which the lifetime of charge carriers free to undergo radiative recombination can be determined.

There are a wide range of techniques for time-resolved photoluminescence measurements, with different approaches to overcoming the limit of detector response time in order to observe processes happening on timescales down to the ultrafast. One method is to spatially separate emission from different times after excitation, as is done in streak cameras where incoming photons cause emission of electrons from a photocathode, which then pass between plates with voltage varying over time so that they arrive on a detector screen at different spatial positions correlated to arrival time of the emitted light, with time resolution in the range of tens to hundreds of picoseconds. [68, 208] Another technique, time-correlated single photon counting, limits detection to single photons and registers the time after excitation at which each detection event occurs to build up a decay transient over many detection cycles. [209] To achieve even higher time resolution, optical gating techniques may be used, which allow detection of PL

only when it is coincident with a short laser gate pulse. The gate pulse may change the polarisation of the PL beam so that it can pass through a polariser to the detector, as in optical Kerr gating, [210, 211] generate a sum-frequency signal which can be selectively detected, as in upconversion, [212] or be used to generate a transient grating giving diffraction of the PL beam for detection. [213]

For the measurements reported in this thesis, upconversion spectroscopy and time-correlated single photon counting were used as complementary techniques to examine the evolution of sample PL from the sub-picosecond timescale out to tens of nanoseconds after excitation. The operating principles of each of these techniques, and the details of the experimental setups used, are described below.

3.2.1 Upconversion spectroscopy

Upconversion spectroscopy is an optically gated technique which offers time resolution limited by the pulse-width of the laser used as the gate, with strong wavelength selectivity. This technique has several key advantages for the work covered in this thesis. First, the high time resolution achieved by optical gating allows fast processes such as the cooling of charge carriers to be explored. High time resolution, with limited total range of delay times over which measurement is possible, is complementary to the other time-resolved technique of time-correlated single photon counting used in this thesis. Second, detection of background radiation in upconversion measurements can be limited by the inherent wavelength selectivity and spatial separation of beams in the sum-frequency generation process as described in Section 3.2.1.1. This is an advantage when measuring samples with relatively weaker PL, particularly in contrast to other optically gated techniques such as Kerr gating where unwanted background detection can result from scattering and emission processes in the Kerr medium. [211] Finally, upconversion spectroscopy is polarisation selective as a consequence of the phase matching

condition also described in Section 3.2.1.1, which allows measurements of polarisation anisotropy in photoluminescence to be performed with high time resolution and a single experimental setup as described in Section 3.2.1.5.

3.2.1.1 Theory of sum-frequency generation

In upconversion spectroscopy, time resolution is achieved using the phenomenon of sum frequency generation in a crystal with non-linear optical properties. This is a second-order process, occurring when the interaction of two incident beams, with different frequencies ω_1 and ω_2 and electric field amplitudes E_1 and E_2, in a medium with non-linear optical susceptibility $\chi^{(2)}$ gives second-order polarisation of the form: [214]

$$\begin{aligned} P^{(2)} =& \epsilon_0\chi^{(2)}\left[E_1^2e^{-2i\omega_1 t} + E_2^2e^{-2i\omega_2 t} + 2E_1E_2e^{-i(\omega_1+\omega_2)t} + 2E_1E_2^*e^{-i(\omega_1-\omega_2)t} + c.c.\right] \\ &+ 2\epsilon_0\chi^{(2)}\left[E_1E_1^* + E_2E_2^*\right] \end{aligned} \tag{3.3}$$

where ϵ_0 is the permittivity of free space and *c.c.* stands for the complex conjugates of the terms shown, which correspond to the response at negative frequencies. Equation 3.3 encompasses each of the possible second-order processes, including second harmonic generation (the terms with frequency $2\omega_i$), sum and difference frequency generation (the terms with frequency $\omega_1 + \omega_2$ and $\omega_1 - \omega_2$ respectively) and optical rectification, which is described by the final term depending only on electric field amplitudes. The intensity of radiation generated by each of the processes corresponding to non-zero frequency components in Equation 3.3 depends on phase matching, with the result that only one second-order process will usually be significant in generating output radiation under any given set of conditions. In the case of sum frequency generation, the output beam has frequency ω_3 and wave-vector $\mathbf{k_3}$ obeying Equations 3.4 and 3.5 which follow from conservation of energy and momentum respectively.

$$\omega_3 = \omega_1 + \omega_2 \tag{3.4}$$

$$\mathbf{k}_3 = \mathbf{k}_1 + \mathbf{k}_2 \tag{3.5}$$

Equation 3.5 expresses the phase matching condition under which the intensity of sum frequency radiation is greatest, with constructive interference occurring in the direction of propagation for sum frequency emission throughout the crystal. [214] The phase matching condition can also be expressed (in the case of collinear beams, which is represented here for simplicity) by Equation 3.6 which highlights the role of the refractive indices n_i at each frequency in determining whether phase matching is achieved.

$$\frac{n_3\omega_3}{c} = \frac{n_1\omega_1}{c} + \frac{n_2\omega_2}{c} \tag{3.6}$$

Since the frequency-dependent refractive index typically increases with increasing frequency (the normal dispersion case), the property of birefringence where refractive index depends on polarisation direction is exploited to make satisfying Equation 3.6 possible. For uniaxial crystals, there is a constant ordinary refractive index n_o and an angle-dependent extraordinary refractive index $n_\mathrm{e}(\theta)$. The ordinary refractive index applies to light polarised perpendicular to the plane containing its propagation vector and the optic axis of the crystal, while the extraordinary refractive index applies to light polarised in the plane, with the angle θ between the optic axis and the propagation vector determining the value of $n_\mathrm{e}(\theta)$. [214] Provided that one or more of the beams involved in sum frequency generation has extraordinary polarisation, it is then possible to achieve phase matching by tuning θ such that Equation 3.6 holds. For the commonly used case where the sum frequency ω_3 has extraordinary polarisation and the input beams with frequency ω_1 and ω_2 both have ordinary polarisation, the phase matching angle θ_m can be defined by Equations 3.7 and 3.8: [215]

$$\sin^2\theta_{\mathrm{m}} = \frac{[n_3(\theta_{\mathrm{m}})]^{-2} - (n_{\mathrm{o},3})^{-2}}{(n_{\mathrm{e},3})^{-2} - (n_{\mathrm{o},3})^{-2}} \tag{3.7}$$

$$n_3(\theta_{\mathrm{m}}) = n_{\mathrm{o},1}\frac{\lambda_{\mathrm{s}}}{\lambda_1} + n_{\mathrm{o},2}\frac{\lambda_{\mathrm{s}}}{\lambda_2} \tag{3.8}$$

where $n_{\mathrm{o},1}$ is the ordinary refractive index at frequency ω_1, and similarly for the other indices. By changing the angle of the crystal, phase matching can thus be achieved for different input frequencies.

3.2.1.2 Principles of upconversion spectroscopy

Applying this process of sum-frequency generation in the context of upconversion spectroscopy, photoluminescence from a sample is overlapped spatially with a pulsed gate beam in a suitable crystal so that when both beams are present simultaneously a signal beam is generated at sum-frequency $\omega_{\mathrm{s}} = \omega_{\mathrm{PL}} + \omega_{\mathrm{g}}$. A wide range of PL frequencies can be probed via upconversion with appropriate choices of gate frequency and crystal angle to allow phase matching. With a crystal of β-barium borate (BBO) for example, which is commonly used for upconversion measurements, the PL range from 250 – 2000 nm can be accessible. [212] Once phase matching is achieved the upconverted signal can be selectively detected, with the gate beam providing time resolution limited by pulse duration. As illustrated in Figure 3.4, the time window after excitation in which PL is measured is determined by the relative arrival time of the gate pulse. In addition to enabling high time resolution by optical gating, the sum frequency generation process has the advantage that the signal beam is spatially separated from the input PL and gate beams, so that background can be reduced by blocking the input beam paths after the crystal, as well as by the use of suitable filters. Further, for the PL from a given sample the energy of the upconverted signal is determined by the energy of the gate beam used, so that with a

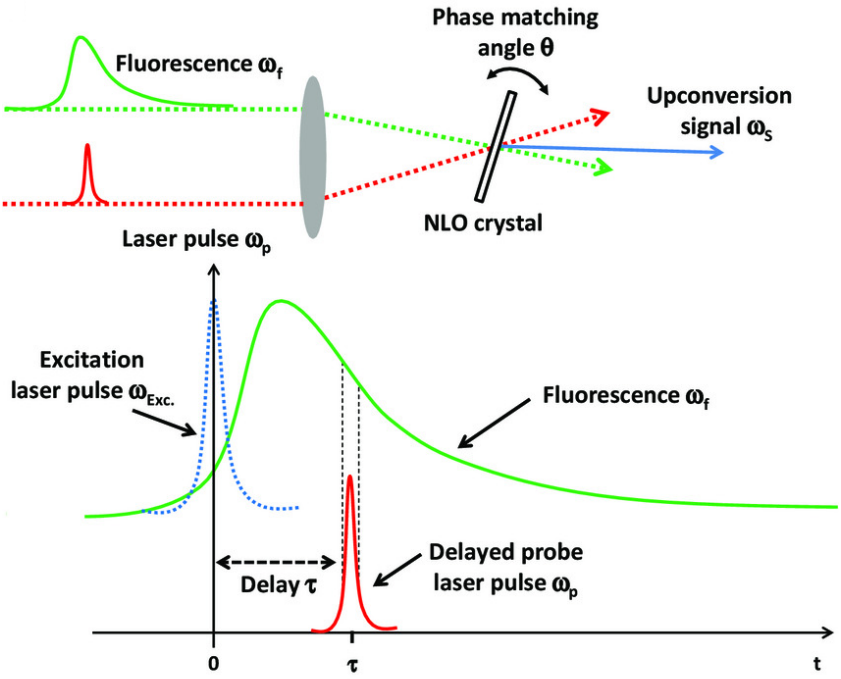


Figure 3.4: Schematic illustrating the principles of upconversion spectroscopy, reproduced with permission from reference [212]. The gate pulse is here labelled as ω_{p} rather than ω_{g}, and fluorescence ω_{f} is likewise equivalent to ω_{PL}. NLO crystal stands for non-linear optical crystal.

suitable choice of gate frequency upconversion measurements can be carried out even on samples with PL too low in energy to be measured directly by a particular detector. [216]

To measure PL decay transients using upconversion spectroscopy, the relative arrival time of the gate and PL beams can be controlled by varying path length with a delay stage, stepping through different delay times at a fixed crystal angle and detection wavelength. To measure spectra, crystal angle must be changed and detection wavelength adjusted appropriately, since the phase matching condition described by Equations 3.4 - 3.8 makes sum frequency generation a wavelength-selective process. Equivalent results for PL spectra at varying delay time after excitation have previously been obtained both by measuring a series of decay curves and reconstructing spectra after the fact, and by measuring full spectra at each time delay in a series. [217]

3.2.1.3 Experimental setup

The experimental setup used to carry out the upconversion measurements included in this thesis is shown in Figure 3.5. A mode-locked Ti:Sapphire Mai Tai laser (SpectraPhysics) with 80 MHz repetition rate and 80 fs pulse width is used, with the output from the laser being split into an excitation, or pump, beam, and a gate beam. The wavelength range over which the output beam from the laser can be tuned is 690 – 1040 nm, and to obtain shorter wavelengths the frequency of the pump beam may be doubled using a BBO crystal for second harmonic generation; this is the scenario illustrated in Figure 3.5. Before being focussed onto the sample, the pump beam is also directed through a polariser and half-waveplate, which can be used in combination to adjust excitation fluence, as well as selecting the polarisation for excitation. Photoluminescence from the sample is focussed into a BBO crystal using two off-axis parabolic mirrors, with long-pass or band-pass filters used to block any scatter from the pump beam, and the focussed PL is overlapped in this crystal with the gate beam. The relative arrival time of gate pulses is controlled by a delay stage in the gate beam path, and the time resolution as determined by the pulse width of the gate of the system is 270 fs.

Upconverted light is focussed into the grating monochromator (Triax, Horiba) with an aperture and selected filters between the BBO crystal and the entrance slit to the monochromator being used to reduce background detection. The spectrally dispersed signal is then directed from the monochromator into a nitrogen cooled silicon CCD (Symphony, Horiba) for detection. Measurements are carried out with automated control of either the delay stage, for PL decay transients, or the crystal angle and detection wavelength, for full spectra, to step across the time/wavelength range of interest. Air-sensitive MHP samples are mounted in a vacuum cell on the sample stage.

3.2.1.4 Corrections to measured spectra

Background subtraction While detection of background radiation in upconversion measurements can be suppressed to a significant extent by the use of filters and apertures some residual background may still be detected, for example from frequency doubling of the gate beam at certain crystal angles which is often close in energy to the upconverted signal and difficult to filter out entirely. Background subtraction is therefore necessary to correct the measured data. For delay scans measuring PL decay transients, the background to subtract is given by the mean intensity detected before time zero, when the PL and gate beams are both present but not arriving in the BBO crystal simultaneously. For upconversion spectra, separate measurements of the background must be taken and then subtracted from the measured signal according to Equation 3.9.

$$I_{\text{signal}} = I_{\text{both}} - I_{\text{gate}} - I_{\text{PL}} + I_{\text{none}} \tag{3.9}$$

In this way the intensity of the upconverted signal is recovered by subtracting the spectra measured with only the gate beam present (I_{gate}) and with only PL present (I_{PL}) from the initially measured spectrum of the sample with gate and PL beams overlapped (I_{both}). Since the two background spectra measured with only one beam present each also include any ambient background radiation, a fourth spectrum measured with both beams blocked (I_{none}) is added so as to avoid subtracting any ambient background twice.

Spectral response calibration Correcting for the spectral response of the detector is important when measuring full spectra, or comparing the intensity of PL decay transients measured at different wavelengths, and can be achieved using a calibration with a lamp of known spectrum as described for time-integrated PL spectra in Section 3.1.2 above. For the work included in this thesis, a tungsten filament lamp (OL series 245 U) is used as the reference. To replace sample PL with light from the reference lamp, the lamp is

placed behind the sample stage so that its light is focussed at the sample position by a lens, after which point it follows the same path as PL from a sample and is focussed into the BBO crystal to overlap with the gate beam. The measured spectrum of the lamp, with background subtraction according to Equation 3.9, can then be used for spectral response correction of measured sample spectra according to Equation 3.1.

The same configuration with a lamp of known spectrum is also used to carry out the angle calibrations needed to allow automatic selection of crystal angle and detection wavelength for a given PL wavelength. This is done by scanning over crystal angles close to the calculated value of θ_m for given gate and PL wavelengths, with detection wavelength fixed for the upconverted signal, to identify the crystal angle at which signal intensity is highest. Repeating this process for a series of PL/detection wavelengths across the full spectral window of interest provides known values of phase-matching crystal angle against PL energy for the chosen gate wavelength, and a polynomial fit to these values can then be used to calculate and set crystal angle for each point across the specified range when measuring a spectrum.

3.2.1.5 Polarisation-dependent measurements

The inherent polarisation-selectivity of sum-frequency generation, emerging from the phase matching condition as discussed in Section 3.2.1.1 above, means that only PL polarised parallel to the gate beam polarisation will be detected in upconversion measurements. Therefore, this technique is well-suited to carry out polarisation-dependent PL measurements and probe anisotropy in the emission of a sample. By varying the polarisation of the pump beam, using the polariser before the sample stage as shown in Figure 3.5, the sample can be excited with polarisation at 0° or 90° (or any angle in between) relative to the gate beam polarisation, so that detection is either parallel

or perpendicular to excitation. A half-waveplate before the polariser can be used to maintain the same excitation power between polarisations.

This technique is used to study PL polarisation memory of a tin MHP thin film in Chapter 5. The procedure followed for such measurements, and the method used to correct for small changes in alignment between polarisations, are discussed in more detail in Sections 5.1.2 and 5.1.3.

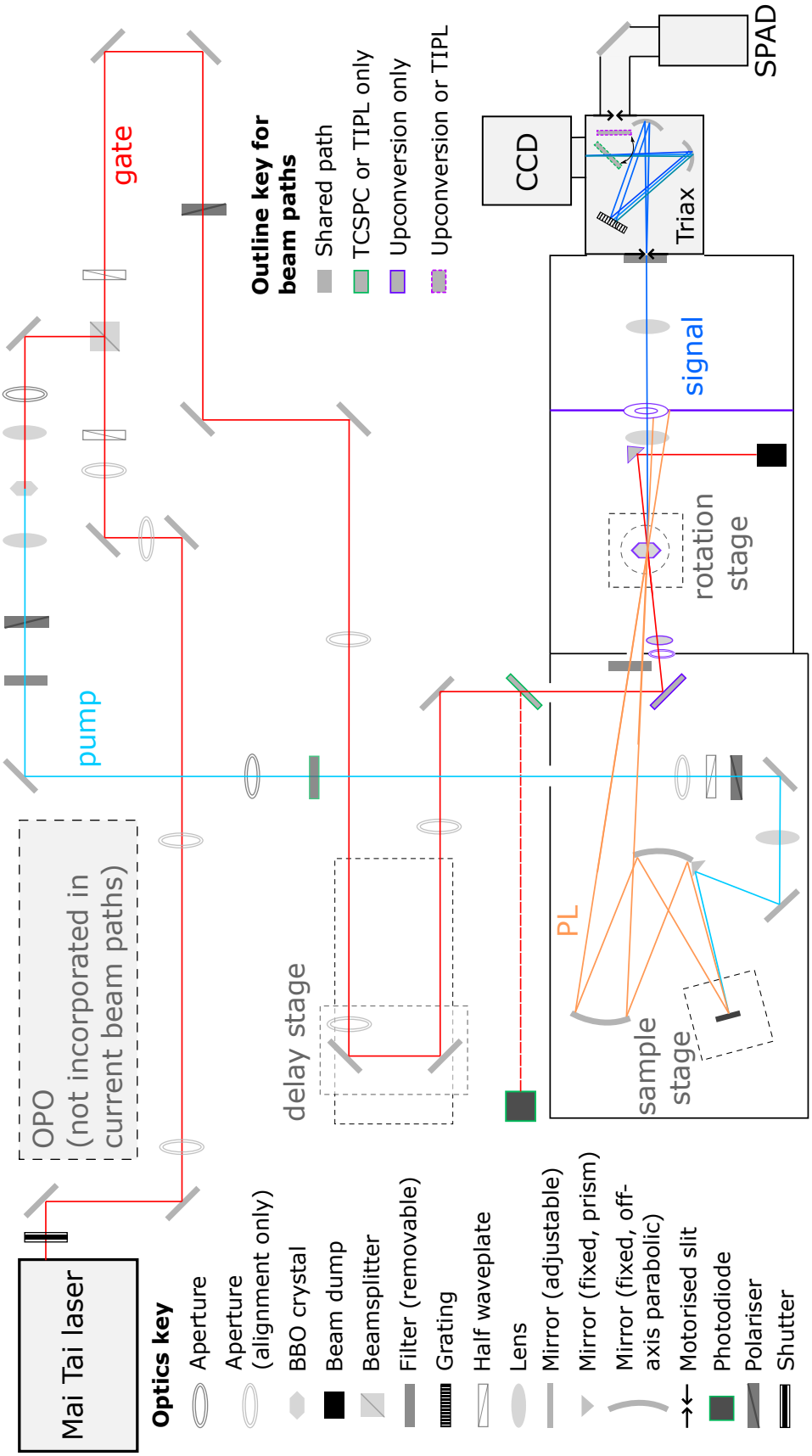


Figure 3.5: Schematic diagram of the upconversion setup used for work in thesis, also showing the beampath for TCSPC and time-integrated PL (TIPL) measurements on the same system.

3.2.2 Time-correlated single photon counting

A commonly used technique to probe PL lifetimes, time-correlated single photon counting (TCSPC) takes a statistical approach to determining the change in intensity of PL over time at the measurement wavelength. The time window after excitation covered by a single measurement can be long, as it is limited by the repetition rate of the laser used rather than the physical size of a detector or delay stage, and it is possible to detect even quite weak PL through long measurement times - in fact, it is necessary for this technique to limit the number of photons so that no more than one photon per excitation event could ever reach the detector. These features make TCSPC a complementary technique to upconversion spectroscopy, useful for probing PL decay dynamics over a longer timescale.

3.2.2.1 Principles of TCSPC

In TCSPC, the change in PL intensity over time at a wavelength of interest is determined based on probability: given that at most one photon arrives in each measurement window, the probability of a detected photon having been emitted at a given time Δt after excitation is proportional to the total number of photons emitted at that time, and so the histogram of photon counts against time built up over many cycles of excitation and detection reflects the decay of PL intensity over time. This principle is illustrated in Figure 3.6, which shows an example PL decay profile (top right) and the corresponding histogram produced by TCSPC measurement over many cycles of excitation and emission. The measured histogram can be biased to early times if multiple photons arrive in any given cycle since only the first to arrive will be recorded, so to maintain accuracy detection rates are typically limited to less than 1 photon for every 100 excitation events. [209] A suitable choice of detector is also important to ensure that the arrival of the single photon is recorded clearly and with good time resolution; options include photomultiplier

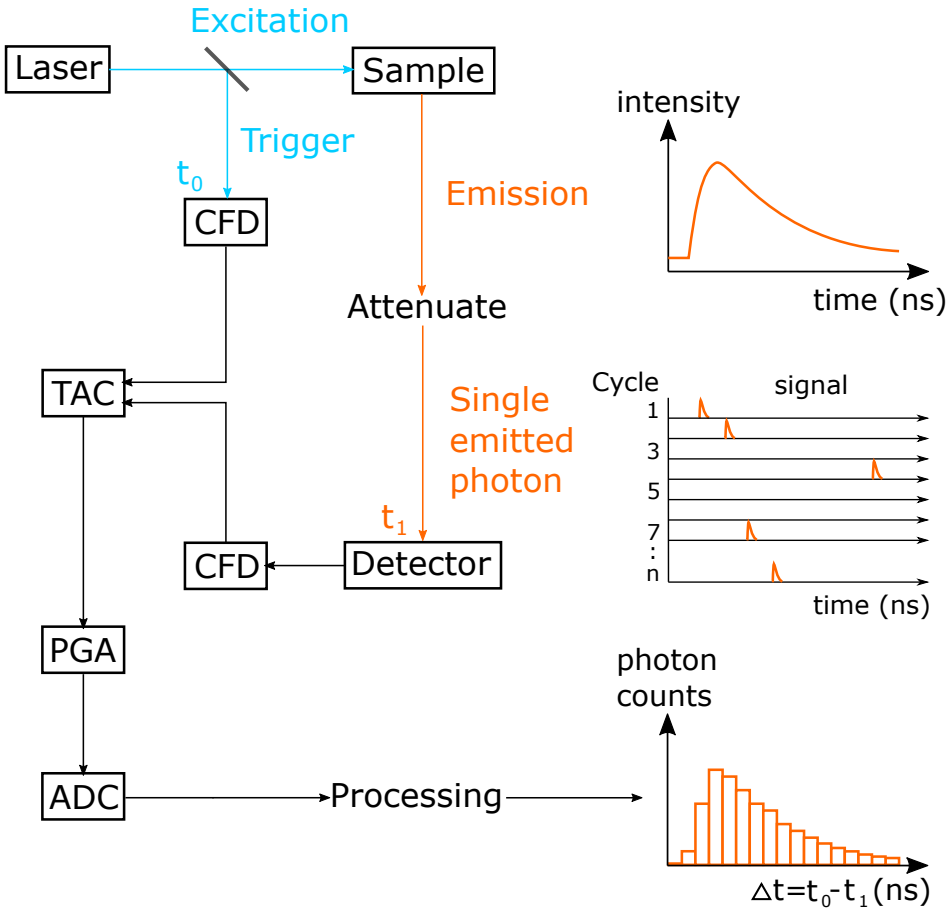


Figure 3.6: Key features of TCSPC operation. The flowchart shows a simplified schematic of the electronics used to register the arrival time t_1 of a PL photon relative to the trigger pulse for excitation at time t_0, and construct a histogram (bottom right) of photon counts against delay time Δt from such detection events over many excitation cycles (middle right) which represents the true decay profile of sample PL (top right). The decay profile and histogram shown are for illustration only, not representing the PL decay of any particular real sample.

tubes (PMTs) of various types, and single photon avalanche diodes (SPADs) as used on the setups discussed in this thesis.

In a typical TCSPC setup, as illustrated schematically in Figure 3.6, the relative arrival time Δt of a photon is determined using a time-to-amplitude converter (TAC), in which voltage in a capacitor builds linearly with time after a start signal is received, so that when a stop signal arrives the voltage built up is proportional to the time delay between the start and stop signals. [209] The start signal can be generated by splitting the beam of the laser to give a reference pulse synchronous with the excitation pulse or

by an electronic trigger which also controls timing of the laser, while the stop signal is generated by detection of a photon, and in each case a constant fraction discriminator (CFD) which avoids jitter in the timing due to variation in pulse height is used to send the signal on to the TAC. [209, 218] The voltage of the TAC once stopped may be amplified using a programmable gain amplifier (PGA) and is then converted via an analog-to-digital convertor (ADC) into a numerical value for Δt. [209] In systems with a high repetition rate laser for excitation, the start and stop signals for the TAC are reversed, so that detection of a photon starts the count, and the following excitation pulse stops the count, meaning that the time axis is reversed for the initially measured data. [218] This approach accommodates the time needed for the TAC to reset between detection events by discharging the capacitor, which is typically longer than the delay between successive excitation pulses. [209]

The time resolution achieved by TCSPC measurements is limited by the transit time spread for detector pulses across detection events, which is typically much shorter than the single photon response time of the detector for a given detection event. [218] In practice, time resolution of a TCSPC system can be determined from the instrument response function (IRF) measured by direct detection of the excitation pulse from the laser. Figure 3.8 shows such measurements for the setups used in this thesis, which are described below.

3.2.2.2 Experimental setup

TCSPC measurements included in this thesis were carried out using two different experimental setups, illustrated in Figures 3.5 and 3.7, each of which offers a different temporal resolution, and different time range over which PL decay can be measured.

For samples with short PL lifetimes, the setup used for TCSPC is shown in Figure 3.5, and shares an excitation path with the PL upconversion system. When configured for TCSPC the gate beam of the laser is directed to a photodiode alongside the delay

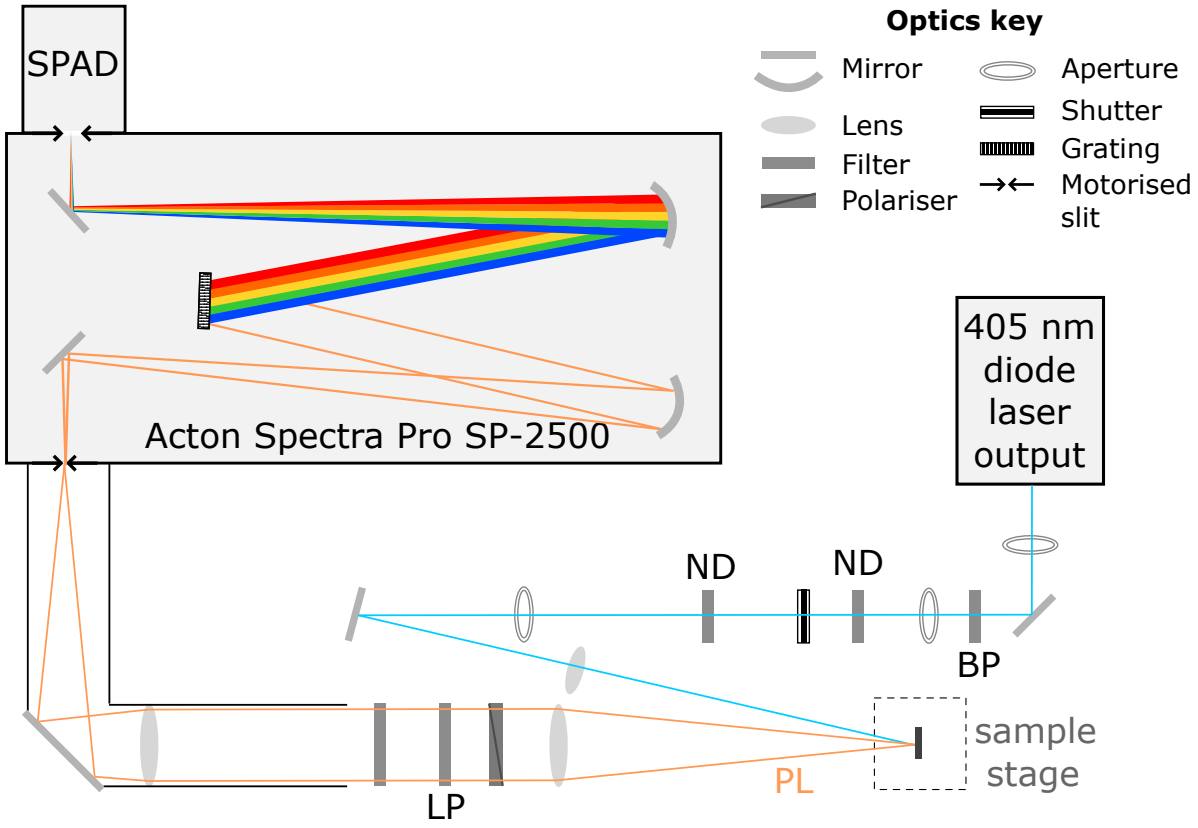


Figure 3.7: Schematic diagram of the setup used for TCSPC measurements on longer-lived samples. Filters are labelled ND for neutral density, BP for band-pass, or LP for long-pass.

stage, acting as the trigger for timing, and PL from the sample is directed from the Triax monochromator onto a SPAD detector (PDM series from MPD) with no BBO crystal in the PL path. The SPAD detector used here offers time resolution down to 50 ps, and from the measured IRF as shown in Figure 3.8 the time resolution of the system measured at 810 nm, near to the long-wavelength range where tin and tin-lead MHPs emit, is 57 ps. The excitation laser (Mai Tai, Spectra Physics) can be tuned over a wide range of excitation wavelengths, with higher energies accessible by doubling with a BBO crystal, but the repetition rate of the laser is fixed at 80 MHz. With this high repetition rate the measurement window for TCSPC is 12 ns, which is sufficient to capture the full PL decay transient for samples where emission decays back to baseline within 10 – 11 ns. For any samples with longer-lived PL, wraparound occurs as the still-decaying emission from one excitation pulse overlaps with the onset of emission for

the next excitation pulse, obscuring the true decay dynamics.

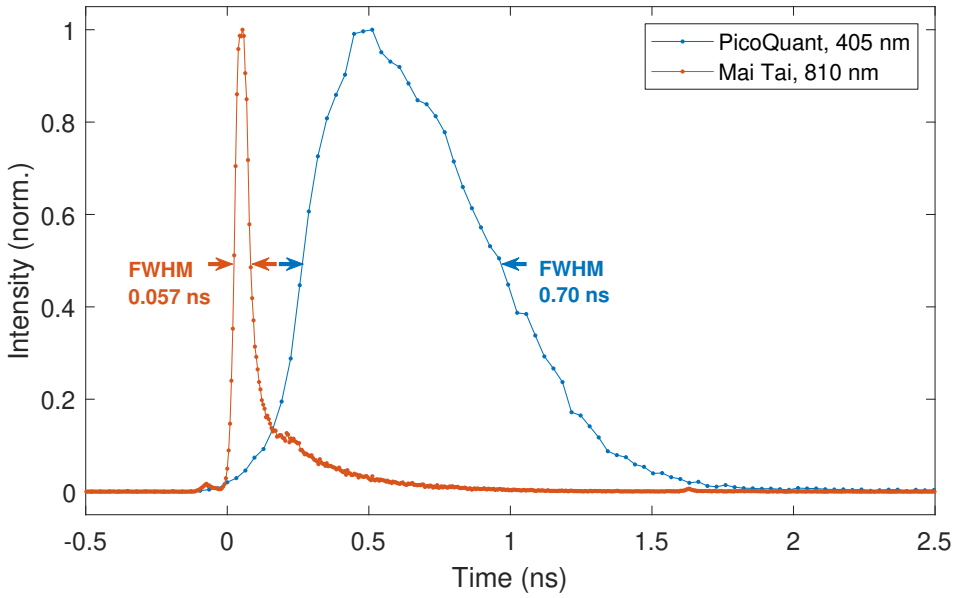


Figure 3.8: Instrument response functions for the TCSPC setups shown in Figure 3.5 (orange, measured by detecting the Mai Tai laser pulse at 810 nm) and Figure 3.7 (blue, measured by detecting the PicoQuant laser pulse at 405 nm). The full width at half maximum, marked on the figure, gives the time resolution of the system.

For samples with longer PL lifetimes, therefore, the TCSPC setup shown in Figure 3.7 is used. Excitation on this system is provided by a pulsed diode laser (Picoharp, LDH-D-C-405M) with variable repetition rate, allowing the measurement window to be extended by the use of a lower repetition rate to avoid wraparound. Timing control is achieved using a PicoHarp300 TCSPC event timer, and PL from the sample is spectrally dispersed using a grating spectrograph (Princeton Instruments, SP-2558) then directed onto a SPAD detector (PDM series from MPD). The time resolution achieved with this system as determined from the measured IRF shown in Figure 3.8 is 0.7 ns, which may underestimate the true resolution for the wavelength range of PL measured in this thesis as a result of the known increase in IRF width at blue and shorter wavelengths for SPAD detectors of this type. [219]

3.3 Absorption spectroscopy

Absorption spectroscopy is a natural complement to photoluminescence spectroscopy, probing the energy-dependent absorption characteristics of materials of interest. Many energetic transitions in different regions of the electromagnetic spectrum can be examined by absorption spectroscopy, including vibrational modes in the infrared as well as electronic transitions. The main process of interest in this thesis is excitation of electrons from the valence band into the conduction band as discussed in Section 2.3.1, which precedes the photoluminescence processes discussed above and for metal halide perovskites occurs with energies in the near-infrared or higher.

3.3.1 Determining absorbance

The absorption of any material can be quantified by the absorption coefficient α:

$$\alpha = -\frac{1}{l} \ln \frac{I(l)}{I_0} \tag{3.10}$$

where $I(l)$ is the intensity of light at a depth l, and I_0 is the initial intensity of light at the surface of the material ($l = 0$). [205] For a sample of thickness d, the directly measured quantity is a dimensionless absorbance A:

$$A = -\ln \frac{I}{I_0} \tag{3.11}$$

where I is the intensity of light measured after passing through the sample. If the value of d is known, the absorption coefficient can be calculated from the measured absorbance as $\alpha = A/d$. (It is worth noting that absorbance may also be defined using the logarithm base 10, rather than the natural logarithm, in which case the relationship between this decadic absorbance and absorption coefficient is given by $\alpha = \ln(10)A/d$. Both definitions of absorbance have been widely used, sometimes varying by research

field or application. [220] Throughout this thesis, the Napierian absorbance defined as in Equation 3.11 with the natural logarithm is used.)

In Equations 3.10 and 3.11 above, the initial intensity I_0 is most correctly considered as the intensity of light that begins propagating through the sample to be either absorbed or transmitted. This is not the same as the intensity of light that would be measured without the sample present, since such a simple measurement for I_0 neglects other processes such as scattering and reflection that can occur at the surface of the sample and reduce the intensity of light passing through the material to be absorbed or transmitted. Directly measuring the true value of I_0 is not possible, but a more accurate approach accounting for reflection from the sample surface gives absorbance in terms of the transmittance $T = I_{\text{transmitted}}/I_0$ and reflectance $R = I_{\text{reflected}}/I_0$ as:

$$A = -\ln\left(\frac{T}{1-R}\right) \tag{3.12}$$

In practice, the transmittance and reflectance values for use in Equation 3.12 are given by correcting the measured reflection and transmission of the sample against reference spectra for the source under conditions of full transmission (T_{blank}, with no sample in the path between source and detector) or full reflection (R_{mirror}, with a mirror of known reflectance ρ_{mirror} in the sample position and measured reflectance multiplied by this known value). The true sample T and R are then given by:

$$T = \frac{T_{\text{sample}} - T_{\text{mirror}}}{T_{\text{blank}} - T_{\text{mirror}}} \tag{3.13}$$

$$R = \frac{R_{\text{sample}} - R_{\text{blank}}}{R_{\text{mirror}} - R_{\text{blank}}} \tag{3.14}$$

where the backgrounds for zero transmission or reflection are given by T_{mirror} and R_{blank} respectively.

3.3.2 Fourier transform infrared spectroscopy

In contrast to dispersive spectrometers, in which a grating or prism is used and different wavelengths are measured sequentially, Fourier transform infrared (FTIR) spectroscopy uses a broadband light source together with a Michelson interferometer. The interferometer consists of a beamsplitter together with one fixed flat mirror and another movable flat mirror, as can be seen in Figure 3.9. At the beam splitter, half of the incident radiation from the source is reflected to the fixed flat mirror, half transmitted to the movable mirror, and the radiation reflected from each of these mirrors back to the beam splitter is likewise half transmitted and half reflected, giving interference where the beams from the two mirrors combine. The position of the movable mirror, together with the refractive index of the surrounding medium through which the beams propagate, defines the optical path difference. When the fixed and movable mirror are equidistant from the beamsplitter the optical path difference is zero and constructive interference occurs at all wavelengths so that the intensity of the output beam going to the detector is at a maximum, decreasing as the mirror is moved in precise increments to produce a full interferogram of measured signal against optical path difference. [221, 222]

The Fourier transform of the interferogram returns a spectrum expressed as intensity against wavenumber. A monochromatic source would give a single sinusoid as the interferogram and corresponding single peak in the spectrum after Fourier transform, whereas a broadband light source gives a more complex interferogram summing the different sinusoids for each frequency present. With a sample present, the intensity of these different frequency components in the measured interferogram is modulated by the absorption of the sample. This information is then recovered in the spectrum given by Fourier transform, allowing the absorbance of the sample to be determined from measurements taken in both transmission and reflection geometry as illustrated in Figure 3.9.

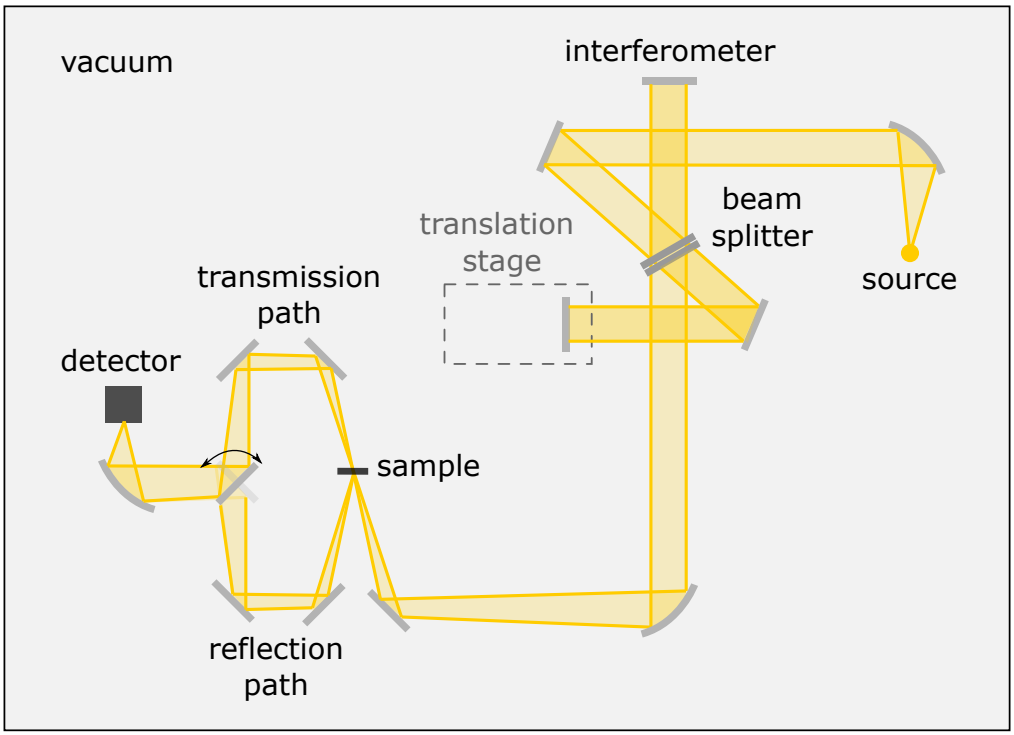


Figure 3.9: Schematic diagram of the Fourier transform infrared spectrometer configured for refection and transmission measurements.

FTIR spectroscopy has several advantages over dispersive spectroscopy, offering shorter measurement times with higher spectral resolution and signal to noise ratio. These performance improvements are due to simultaneous detection of the whole spectrum (the Fellgett or multiplex advantage, improving signal to noise); high source throughput without the need for narrow entrance slits to achieve the desired resolution (the Jacquinot advantage, further improving signal to noise); and accurate referencing of optical path difference which determines spectral resolution, achieved internally with a HeNe laser (the Connes advantage). [221, 222]

3.3.3 Experimental setup

The setup used to perform all FTIR measurements reported in this thesis uses a Bruker Vertex 80v Fourier-transform infrared spectrometer, with reflection/transmission accessory (A510/Q, Bruker) fitted. Figure 3.9 shows the key features of this setup. The light

source, beamsplitter, and detector can each be chosen depending on the spectral range of interest. Typically for the measurements shown in this thesis, a tungsten halogen lamp was used as the source, together with CaF_2 beamsplitter and a Si diode detector operating at room temperature. This configuration is suitable for measurements over the wavelength range from 476 – 1111 nm. Samples were mounted in a clip holder, with the sample compartment evacuated for all measurements.

3.4 X-ray diffraction

X-ray diffraction (XRD) is a powerful technique for examining material structure. In this thesis, XRD measurements on perovskite thin films are employed to assess crystallinity and identify crystal structure, using XRD patterns measured as intensity against the angle 2θ as described below.

3.4.1 Theory

Diffraction of X-rays incident on a crystalline material, which is more properly considered as the combined effect of elastic scattering of the X-rays by electrons in the material with interference effects, [223] occurs for wavelengths λ similar to the spacing between planes of atoms, ions, or molecules within the crystal (on the order of Angstroms). As illustrated in Figure 3.10A, constructive interference between X-rays scattering off parallel planes in a crystal with separation d occurs when the difference in path length $AO + OB$ is equal to an integer multiple of the wavelength. This condition is expressed by the Bragg Equation 3.15, and has the consequence that for any given crystal structure, constructive interference giving peaks in the intensity of diffracted X-rays will occur only for certain angles, related to the spacing between the various planes in the crystal.

$$n\lambda = 2d \sin\theta \tag{3.15}$$

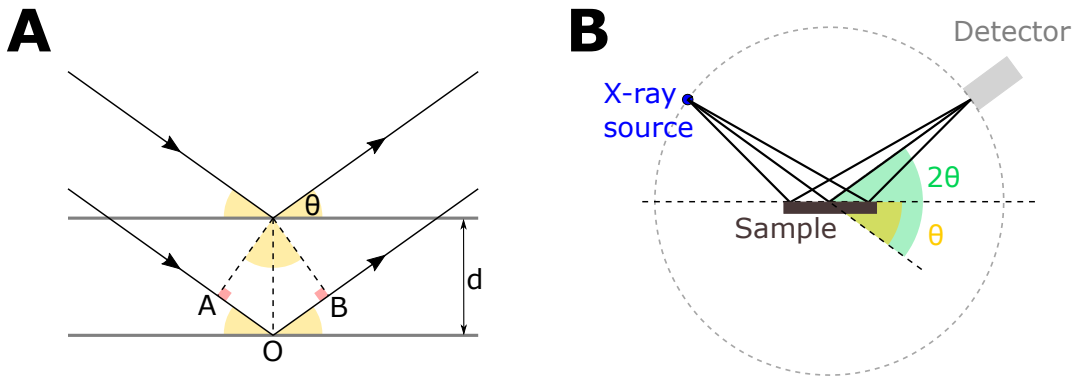


Figure 3.10: A) Geometry of X-ray scattering from which the Bragg equation is derived, where the grey horizontal lines represent planes within a crystal. **B)** Simplified schematic of the key features in an X-ray diffractometer setup for $\theta/2\theta$ measurements. The dashed circle represents the path around which the detector (and the source, if the sample is fixed in position) can be moved to change the incidence and scattering angles of the X-ray beam. Filters and slits are often used in both the incident and diffracted beam paths, but are not shown here.

Each diffraction peak originates from a set of parallel lattice planes, defined by the Miller indices (hkl) that specify the intersections of the plane with the edges of the unit cell found at a/h, a/k and a/l. The interplanar spacing d_{hkl} then determines the angle at which a diffraction peak appears as in Equation 3.15. For a given crystal structure, the set of different planes (each with unique Miller indices) and corresponding diffraction peaks is determined by the crystal system of the lattice (full descriptions of which may be found, for example, in reference [223] or [224]), while the exact angle at which those peaks appear depends on the dimensions of the unit cell and corresponding interplanar spacing.

An X-ray diffraction pattern characteristic of crystal structure can therefore be obtained by measuring the intensity of the diffracted beam over a range of angles. Figure 3.10B shows the basic principle of such measurements using a diffractometer, in which the angle θ between X-ray source and sample, and between sample and detector, is varied by a goniometer which rotates the movable components. Applying this measurement technique to a powder sample, in which the orientation of many small crystals is randomised, will in principle give a diffraction pattern in which every set of lattice planes gives a corresponding diffraction peak. By contrast the XRD pattern of a thin film sample

may be missing some peaks, because even in a polycrystalline film the orientation of crystallites may be such that only some subset of lattice planes are found lying parallel to the surface of the sample and contribute to detected diffraction peaks.

Nonetheless, XRD measurements on thin films can allow crystal structure to be identified, and the width of the measured peaks reflects the crystallinity of the sample. Smaller crystallites are known to result in broader diffraction peaks, and crystallite shapes as well as imperfections and distortions in the crystal structure also contribute to broadening. [223] Sharp, well-defined peaks in a measured XRD pattern are thus indicative of desirably high crystallinity, while broader peaks can be indicative of structural disorder and defectiveness.

3.4.2 Experimental setup

XRD patterns included in this thesis were obtained using a PANalytical X'Pert PRO Powder X-Ray Diffractometer, operating as illustrated in Figure 3.10B. In this setup thin films are secured into a sample holder with the surface of the film level and flat in the plane of the holder. The sample holder can be set to spin continuously in this plane during measurements, partially compensating for the limited number and preferential orientation of crystallites that may occur in thin films in contrast to powders with a greater number of grains in random orientations. The Cu-K_α line at 1.54 Å is used as incident radiation, and measurements are conducted under ambient conditions.

4

Determining Charge-Carrier Temperature from Measured Spectra

Contents

4.1 Motivation 57
4.2 Previous approaches to determining charge-carrier temperature 58
4.2.1 Perovskite literature 58
4.2.2 Historical context 59
4.3 An improved, full lineshape model 61
4.3.1 Choice of model 61
4.4 Impact of adopting the full lineshape model 65
4.4.1 Accounting for energy-dependent density of states 70
4.4.2 Accounting for spectral broadening 72
4.4.3 Fitting the full spectrum 74
4.5 Conclusions 77
4.6 Future outlook 78

This chapter examines the methods used to determine the temperature of photoexcited carriers in studies of charge-carrier cooling to date, and presents an improved model for use in such studies on perovskite materials. As discussed in Sections 2.3.2 and 2.4.2, understanding charge-carrier cooling and exploring the potential for hot-carrier solar cells are areas of significant interest in the pursuit of higher photovoltaic device efficiencies. However, to date there has been uncertainty about the true charge-carrier cooling times in

MHPs and the mechanisms affecting carrier cooling. Here, assumptions carried over from earlier work on inorganic quantum well systems which lead to overestimates of carrier temperature in the literature on MHPs are identified. Together with dependence on the region of measured spectra used in temperature fitting, these incorrect assumptions may contribute to the wide range of reported cooling times. In Section 4.3 a model allowing charge-carrier temperatures to be determined from the full photoluminescence lineshape is described. The impact of appropriately accounting for influences on the emission spectrum in bulk semiconductors such as MHPs that had previously been overlooked is then demonstrated in Section 4.4. Adopting this model is shown to offer a route to more accurate determination of charge-carrier temperature and cooling dynamics in future work, and more reliable comparison between studies. This could resolve the question of whether certain perovskite compositions exhibit particularly slow carrier cooling, and might be suited to hot-carrier device applications.

Work in this chapter is also published in reference [225]: Savill, K. J.; Klug, M. T.; Milot, R. L.; Snaith, H. J. and Herz, L. M., J. Phys. Chem. Lett., 2019, ***10****, 6038-6047.*

4.1 Motivation

Motivated by the prospect of achieving higher device voltages through hot-carrier extraction as discussed in Section 2.4.2, there has been growing attention given to the study of hot charge carriers and carrier cooling in MHPs. Charge-carrier cooling times, calculated to have a large impact on the efficiency of any working hot-carrier solar cell, [10, 161] are of particular interest. The reported timescales of charge-carrier cooling in MHPs to date cover a wide range of values spanning several orders of magnitude, [11] from sub-picosecond [78, 80] up to the nanosecond range [13] with intermediate reports of cooling over tens [210, 226] or hundreds of picoseconds. [85, 86] Often the long cooling times are attributed to a second, slower stage following initial energy loss, [13, 83, 227]

and explanations such as the presence of a hot-phonon bottleneck are offered. [79, 80, 159, 226–228] This alone does not explain the variation in cooling times seen, however, and a wide range of mechanisms including Auger heating, [81–84] acoustic phonons up-converting to higher energy, [85] trapping of hot carriers, [83] screening through the formation of large polarons, [86] changes to the near-bandgap density of states, [13] or local structural variations [228] have been suggested to contribute to slower cooling.

The pronounced lack of consensus over both the typical cooling time even for a single perovskite composition, and the factors affecting carrier cooling dynamics, leaves a clear need for further investigation. To enable the development of high-performance hot-carrier solar cells, materials with genuinely slow cooling must be identified, and the factors contributing to this desirable property understood. Whether or not good candidate materials for hot-carrier devices are found, clarifying the origins of slow charge-carrier cooling or the appearance thereof would improve understanding of the properties of MHPs. If errors or large variations between studies have their origins in the analysis of experimental data as opposed to the properties of the materials under investigation, these goals will remain unmet. For this reason examining the methods used to determine charge-carrier temperature, and subsequently cooling dynamics, is necessary.

4.2 Previous approaches to determining charge-carrier temperature

4.2.1 Perovskite literature

To date, studies of charge-carrier cooling in MHPs have commonly used an exponential function, of the form shown in Equation 4.1, to extract the temperature T_c of the charge-carrier population from measured emission spectra. [72, 79–82, 84, 159, 226, 228, 229] The assumption underlying this approach is that for a suitable 'tail' region at the high-energy

side of a measured PL peak, emission follows a Boltzmann distribution:

$$I(E)_{\text{Boltz}} \sim \exp\left(\frac{-E}{k_B T_c}\right) \tag{4.1}$$

Where transient absorption, rather than time resolved photoluminescence, measurements have been used, a function f_{PIA} for the contribution of photoinduced absorption (PIA) that may overlap with the emission spectrum is often added to Equation 4.1, so that the selected tail region is fitted with a model of the form $I(E) = A_1 I_{\text{Boltz}}(E) + A_2 f_{\text{PIA}}(E)$. [83, 85, 230] For either measurement type, the same assumption that high-energy emission is well approximated by a Boltzmann distribution applies, and the tail region to fit in this way must be selected. A range of approaches to identifying the tail to fit have been employed in the literature, including using fixed-energy intervals [80, 84, 226, 227] or specified ratios to the peak intensity, [83, 85] with the specific choice often made with reference to the temperature then extracted at late times, which is expected to approach the temperature of the lattice.

4.2.2 Historical context

Tracing the study of charge-carrier cooling back to previous work on inorganic semiconductors illuminates the origin of the simplified model described in Section 4.2.1. In many early studies on materials such as GaAs or CdS, [231–234] and electronically confined quantum well systems such as GaAs/AlGaAs and InGaAs/GaAs [235–244] carrier temperatures were extracted with a model as described in Equation 4.1. By disregarding other influences on the emission spectrum besides the thermalised carrier distribution, this approach greatly simplified calculations. Notably, when comparing calculated spectra for a given charge-carrier temperature against measured data, models for calculating emission spectra were employed which made fewer simplifying approximations and so would have been difficult to use in fitting to measured data to determine temperature. [245–247] At the time much of this work on inorganic semiconductors was carried out, lack of

computational power would have been a significant limitation and so approximating to a Boltzmann model, which allowed carrier temperatures to be extracted from the gradient of a straight line through data from the high-energy side of the PL spectrum plotted on a semilog scale, was adopted as a particularly accessible approach. [231–234]

Moreover, in the case of quantum well systems, the electronic density of states (DOS) is described by a step function [107] and the joint density of states for the transition between quantum levels is constant near the onset of absorption. [243] As such there is no need to consider how the Boltzmann distribution would be modified by the density of states available at a given energy when determining carrier temperature, and an exponential fit is appropriate. [235–244] Adding to the suitability of this simple approach, measured PL linewidths from quantum well systems can be below 1 meV, [248, 249] and with little influence of broadening on the shape of the spectrum the Boltzmann model is then a very good approximation.

While some problems with simplifying to a Boltzmann model were pointed out in later works on inorganic bulk semiconductors, such as deviation from the true temperature due to neglecting the density of states in InGaAs [250] or overestimation of temperature when a selected tail region was used for fitting in contrast to the full lineshape, [251, 252] this simple approach remained in common use. From a chronological viewpoint, it is therefore unsurprising that this well-established approach from the study of inorganic semiconductor materials was transferred into common use for similar studies on metal halide perovskites in recent years. However, the assumptions of constant density of states and minimal broadening, which were reasonable in the context of semiconductor quantum wells, are not at all applicable to MHPs. Neither are computational limitations an important consideration when carrying out fits to measured data today. The unsuitability of Equation 4.1 as a complete model for determination of charge-carrier temperature is immediately apparent from theory, and the wide range of reported cooling times

discussed in Section 4.1 also indicates a need to examine the methods used in studies of charge-carrier cooling in MHPs.

4.3 An improved, full lineshape model

In moving from the simplified exponential model for carrier temperature fitting to one more suitable for use in work on MHPs, there are three key factors to consider. First, as MHPs are 3D bulk semiconductors, their density of states is not energy-independent (as in a quantum well between levels) and cannot be taken as constant, instead requiring a suitable function to model the dependence on energy above the bandgap. Second, measured spectra of perovskite materials commonly display significant broadening, which will influence the emission lineshape from which carrier temperature is to be fitted. And finally, leaving open the choice of region within a measured emission peak to fit with any given model makes comparison between studies more difficult, as different choices of tail region can give different values for carrier temperature.

The remainder of this chapter describes an alternative model that addresses each of these factors, and demonstrates the influence that each of them has upon the carrier temperatures determined.

4.3.1 Choice of model

For direct-bandgap semiconductors, such as the metal halide perovskites of interest here, the energy-dependent joint density of states above the bandgap E_g can be represented by Equation 4.2: [107]

$$D_{\mathrm{J}} \propto (E - E_g)^{1/2} \tag{4.2}$$

with the assumption of parabolic, isotropic bands. From first principles calculations on lead- and tin-based perovskites it has been found that both valence and conduction bands can be well-approximated as parabolic near to the band edge. [102, 253] The range

over which such an approximation holds for $MAPbI_3$ has been quantified as extending to energies ∼250 meV from the band edge [96] which corresponds to a temperature of 2901 K. This far exceeds the carrier temperatures typically observed [11] and so a parabolic model giving the joint density of states for band-to-band transitions expressed in Equation 4.2 with E_g the bandgap of the material is appropriate for use in studies of charge-carrier cooling in MHPs.

The underlying emission intensity for MHPs can then be modelled by Equation 4.3, which incorporates the Boltzmann distribution for hot-carrier emission together with the energy-dependent joint density of states as in in Equation 4.2, with onset determined by the bandgap of the specific material in question:

$$I_{\mathrm{PL}}(E) \propto \begin{cases} (E - E_g)^{1/2} \exp\left[\frac{-(E-E_g)}{k_B T_c}\right] & E > E_g \\ 0 & \text{otherwise} \end{cases} \tag{4.3}$$

A representative emission profile calculated with this model is shown in Figure 4.1, which also includes the simple Boltzmann model subject to the same onset at the bandgap for contrast. From this figure it can be seen that the introduction of a suitable factor for the joint density of states results in a more gradual onset of emission compared to the unaltered Boltzmann distribution, with peak slightly higher in energy and a less steep decay in intensity as energy increases. Emission spectra of MHPs measured by experiment do not typically show such a defined onset as is given by Equation 4.3 and shown in Figure 4.1, but are closer to symmetrical in shape. This can be attributed to the significant degree of broadening that is seen in perovskite PL, with room temperature PL linewidths in excess of 100 meV being common. [105, 110, 204, 254, 255] Homogeneous broadening due to coupling between charge carriers and phonons has been identified as the primary contributing factor for broad PL from a variety of lead perovskites at room temperature [105, 204, 256, 257] with the same mechanism also put forward to explain broadening in $MASnI_3$. [258] Inhomogeneous broadening due to energetic disorder

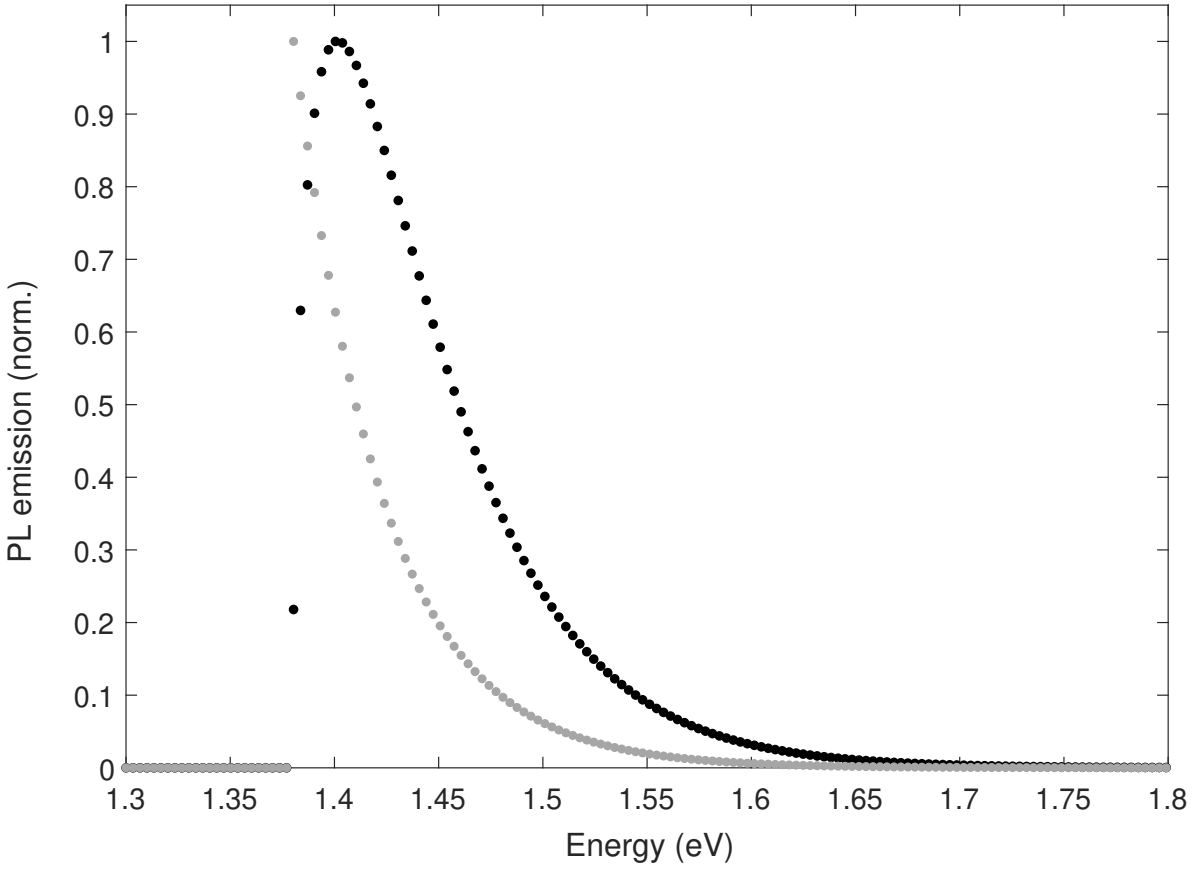


Figure 4.1: Example emission spectra calculated using Equation 4.3 with Boltzmann distribution and energy-dependent joint density of states (black square markers), and using the same equation with the density of states factor omitted to leave a Boltzmann distribution similar to Equation 4.1 (grey circle markers). The input value for carrier temperature T_c was 500 K, and for bandgap E_g was 1.38 eV, in both cases.

and charge carriers interacting with defects and trap states has also been found to dominate the measured PL line shape for a range of MHPs [97, 142, 255, 259] and may be particularly relevant for tin perovskites in which charged tin vacancies can contribute significantly to spectral broadening. [110]

To account for broadening as well as the joint density of states, a full-lineshape model can be used in which the previously identified emission profile [107, 245] is not simplified further. The general form of this model is an expression I_{PL} for spontaneous emission intensity, as given in Equation 4.3, convolved with a suitable function $f_{\mathrm{broad}}(E)$ to capture the broadening of measured spectra. The appropriate form of $f_{\mathrm{broad}}(E)$ for a given material can be identified by fitting to measured PL spectra at long delay times after

photoexcitation, or similarly to time integrated spectra, where there is little contribution from hot-carrier emission and the spectrum tends to be more symmetric with lineshape dominated by broadening. For tin-containing perovskites with significant inhomogeneous broadening, a Gaussian lineshape is often suitable. [259, 260] This is illustrated for measured $FASnI_3$ PL spectra at late time after excitation in Figure 4.2.

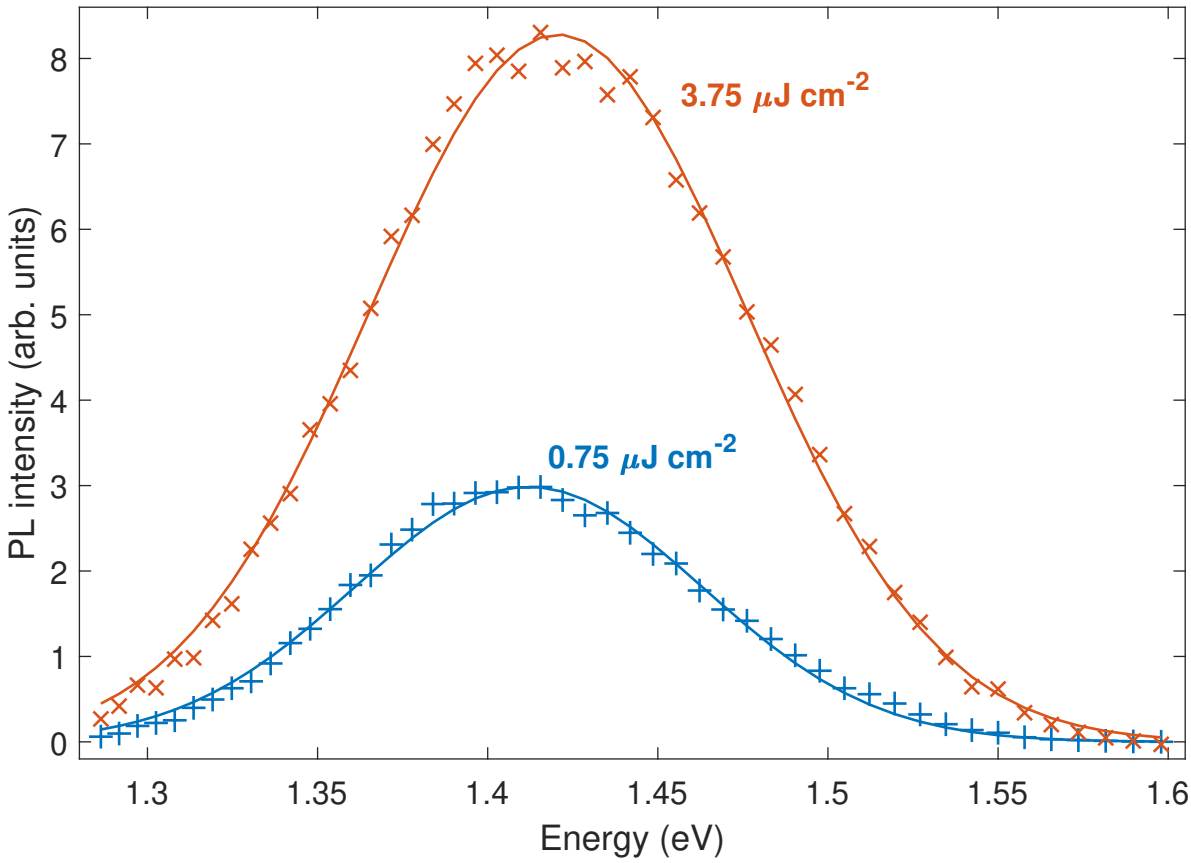


Figure 4.2: Gaussian fits (solid lines) to time resolved PL spectra of a $FASnI_3$ film on quartz substrate (+ or × markers) at 0.51 ns after photoexcitation illustrating the symmetric, broadened profile of measured spectra when there is no significant contribution from hot-carrier emission. Films were excited with fluences as indicated, at a wavelength of 730 nm.

Incorporating Gaussian broadening, the full-lineshape model for PL is as given by Equations 4.4 and 4.3, defining the emission spectrum with intensity I_{measured} at energy E.

$$I_{\text{measured}}(E) = \frac{1}{\sigma\sqrt{2\pi}} \exp\left(\frac{-(E-E_g)^2}{2\sigma^2}\right) \otimes I_{\text{PL}}(E) \tag{4.4}$$

In this model, the bandgap of the emissive material enters as a parameter E_g, while the parameter for broadening is σ defining the width of the Gaussian distribution centered at E_g. The broadening parameter relates to the full width at half maximum (FWHM) of the peak by Equation 4.5.

$$FWHM = \sqrt{8 \ln 2}\sigma \approx 2.35\sigma \tag{4.5}$$

For a given material, the values of E_g and σ can be expected to remain constant over the course of PL decay, while the charge-carrier temperature T_c, which is the parameter of interest, can vary and will be extracted from fits. A scaling parameter B, needed for the proportionality in Equation 4.3, can be free to vary also as the intensity of the measured PL peak changes with decay in the population of excited charge carriers over time. The improvements in accuracy of fitted temperatures from this model compared to the simple exponential fit are quantified in the following section.

4.4 Impact of adopting the full lineshape model

As described in Section 4.3, the full lineshape model given by Equation 4.4 improves upon the commonly used Boltzmann approximation for determining charge-carrier temperature by taking into account key influences on the emission profile of bulk semiconductor materials, and MHPs in particular. From the underlying theory, this full lineshape model is expected to yield more accurate results for charge-carrier temperatures and therefore also for cooling dynamics. To quantify the difference made by adopting this model, and illustrate the ways in which ignoring or accounting for the key influences of broadening and energy-dependent density of states impacts the results obtained, it is helpful to directly compare the two approaches. This can be done by calculating PL spectra across a range of carrier temperatures with the full lineshape model, and then fitting to a tail region of the modelled spectra using a simple exponential model such

as has been commonly used in previous work. The difference between the temperature extracted from tail fitting and the actual temperature given as input then captures the effect of changing between models, and the impact of different contributions to the emission spectrum can be isolated by changing the broadening parameter and including or excluding the energy-dependent DOS factor in the tail fit.

Results from this comparison of different models for carrier temperature are illustrated in Figure 4.3. Panel A of this figure shows spectra modelled using Equation 4.4 for progressively increasing carrier temperatures, T_c = 50, 500, and 1000 K, with a fixed value of E_g = 1.38 eV and two choices of broadening parameter σ to demonstrate realistic levels of broadening for MHPs (σ = 43 meV, FWHM = 102 meV) as well as a much lower degree of broadening (σ = 5 meV, FWHM = 11.8 meV). Across both sets of calculated spectra the signature of emission from a hot-carrier population is evident for high values of T_c, which give asymmetric spectra with a shallower slope on the high-energy side of the peak. A blueshift in the peak energy can also be seen for higher carrier temperatures. The impact of spectral broadening, explored in detail in Section 4.4.2, is also apparent in the changes to lineshape with carrier temperature, as the high-broadening case (top set of spectra in Figure 4.3A) exhibits larger peak shifts and smaller changes in gradient at the high-energy side of the peak for hot populations, as compared to the low-broadening case (bottom set of spectra).

Working with a consistently defined tail region of each calculated spectrum, as marked in grey in Figure 4.3A, fits to determine carrier temperature are shown in panel B of the same figure with the data points included in the region to fit being represented by either + or × markers. The solid lines show the curves produced by fitting each tail region with either the simple exponential model in Equation 4.1 which assumes a constant density of states, or the underlying emission profile in Equation 4.3 in which the energy-dependent density of states is accounted for while ignoring any lineshape

broadening. As energy increases, the fitted curves using either approach diverge from the modelled spectra, with this difference between data and fit being more pronounced for more broadened spectra, and at lower carrier temperatures. Differences between the two approaches to fitting, meanwhile, are more pronounced at higher carrier temperatures, where the use of Equation 4.3 gives a better fit to the data (shown in light blue) than does the simple exponential approach (shown in dark blue-black). This difference, which is quantified in panel C of the figure, illustrates the impact of correctly accounting for the density of states, discussed in Section 4.4.1.

To quantitatively assess the systematic errors in carrier-temperature determination that arise with the use of more simplified models, Figure 4.3C shows the temperatures extracted from tail fits in comparison to the actual values of T_c used in Equation 4.4 to generate the modelled spectra. By comparison to the grey solid line showing equality between the input and fitted values of T_c it is immediately apparent that carrier temperatures extracted using simplified models are artificially elevated. Overestimates at low carrier temperatures appear much more significant for realistic broadening (filled markers) than low broadening (open markers) regardless of the model used to fit, while at high carrier temperatures the difference between results for the simple exponential model (dark blue-black circle markers) and Equation 4.3 (light blue triangle markers) indicate that the treatment of the density of states is dominant for hot populations.

It is also clear from Figure 4.3C that the overestimation of carrier temperatures by tail fitting with any given method is not constant across temperatures. To better explore how the magnitude of the overestimate in fitted temperatures changes under different approximations, the relative error for each temperature series is shown in Figure 4.4, which employs the same colour scheme and markers as Figure 4.3C. This plot of relative error makes clear the scope of the variation in overestimates from tail fitting as the carrier population cools, with relative error for a simple exponential fit (dark

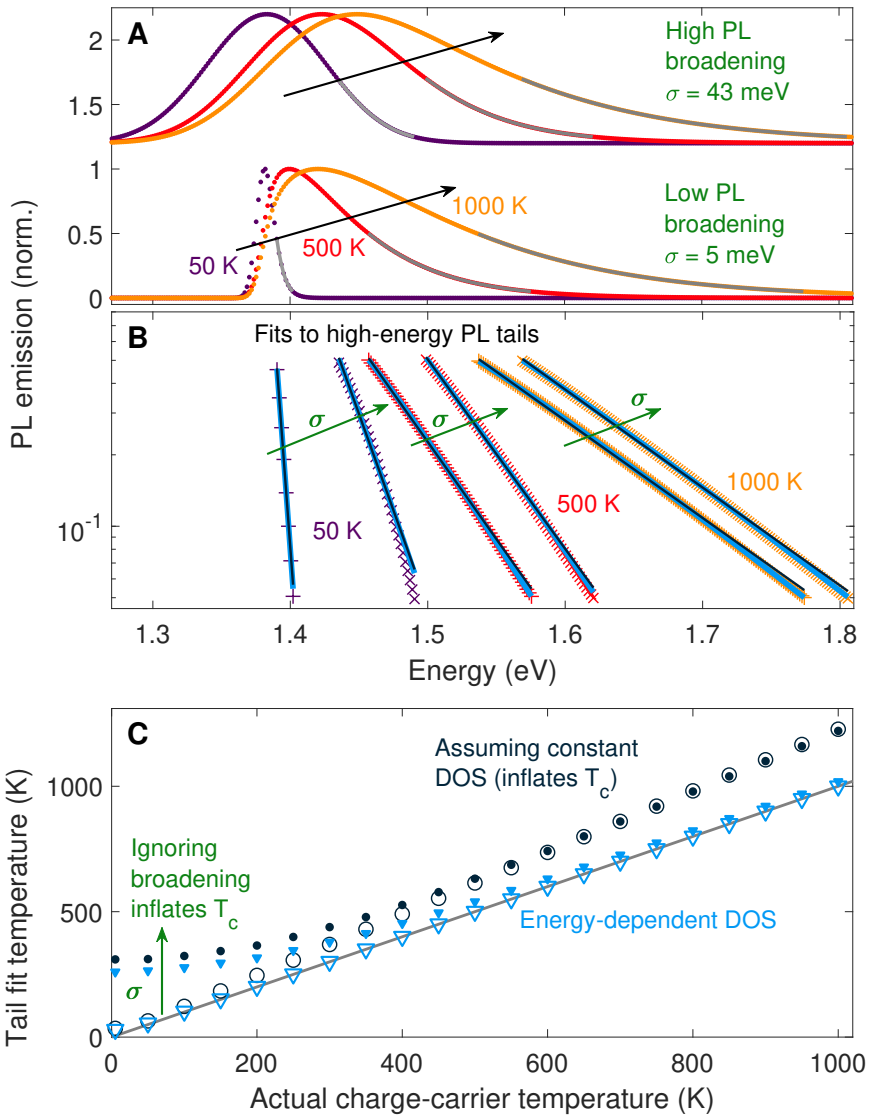


Figure 4.3: Comparison of carrier temperature fitting models. **A)** Modelled PL spectra for selected carrier temperatures as indicated, using Equation 4.4 with $E_g = 1.38\,\text{eV}$ and the broadening parameter σ set at 43.4 meV for the top set of spectra (plotted with a vertical offset) and 5 meV for the bottom set of spectra (plotted with no offset). The colour scheme denoting carrier temperature is the same for both sets of spectra. For each spectrum, the high-energy tail region selected to fit to is shown by a grey solid line and extends from 50 % to 5 % of peak PL intensity. **B)** Selected tail regions from modelled spectra as shown in panel A, and fits thereto. Data points are plotted with the same colour scheme as in panel A, using + markers for $\sigma = 5\,\text{meV}$ and × markers for $\sigma = 43.4\,\text{meV}$. Fits using the simple Boltzmann model as in Equation 4.1 are shown by thin blue-black lines. Fits using Equation 4.3, which accounts for parabolic band structure while still neglecting broadening, are shown by thicker light blue lines. **C)** Carrier temperatures extracted from fits to modelled spectra as illustrated in panel B, across the full range of input temperatures. Marker colour corresponds to the type of fit, blue-black for the simple Boltzmann model and light blue for Equation 4.3 incorporating energy-dependent density of states, as in panel B. Point and filled triangle markers show results for $\sigma = 43.4\,\text{meV}$, open circle and open triangle markers show results for $\sigma = 5\,\text{meV}$. The grey solid line is a guide to the eye showing equality between the actual temperature used to produce each spectrum, and the tail fit temperature extracted using a simpler model. [Adapted with permission from *J. Phys. Chem. Lett.* 2019, 10, 20, 6018-6047 [225] Copyright 2019 American Chemical Society.]

blue-black markers) ranging from 22 % at 1000 K up to 46 % at 300 K in the case of realistically broadened spectra, for example.

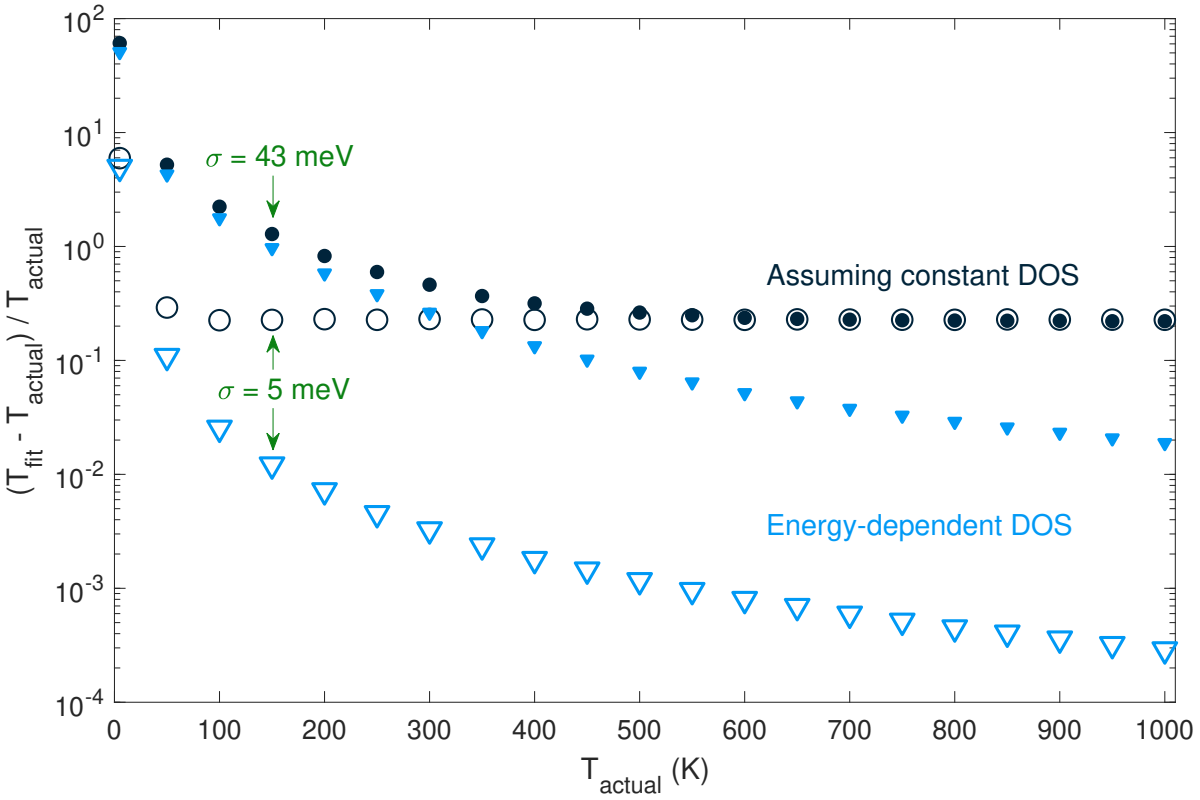


Figure 4.4: Relative error in carrier temperatures extracted from fits to a selected high-energy tail region of modelled PL spectra. Carrier temperatures T_{actual} are used as inputs to Equation 4.4 with $E_g = 1.38$ eV, and broadening parameter σ valued at either 43 meV (point and filled triangle markers) or 5 meV (open circle and open triangle markers). Fits to a selected tail region extending from 50 % to 5 % of maximum intensity at the high-energy side of the spectrum are then used to extract the carrier temperature T_{fit}, as shown in Figure 4.3. The model used for fitting is either a simple Boltzmann exponential as in Equation 4.1 which assumes a constant density of states (shown by point and open circle markers in dark blue-black) or Equation 4.3 which accounts for energy-dependent density of states with a parabolic band structure but still neglects broadening (shown by filled triangle and open triangle markers in light blue). [Adapted with permission from *J. Phys. Chem. Lett.* 2019, 10, 20, 6018-6047 [225] Copyright 2019 American Chemical Society.]

Together, Figures 4.3 and 4.4 provide a basis to identify the impact that each of the previously neglected influences on MHP emission spectra has on efforts to extract carrier temperatures and thereby study carrier cooling. This is explored in greater depth in the following sections.

4.4.1 Accounting for energy-dependent density of states

The key difference between the simple exponential model in Equation 4.1 that has been used in much of the literature to represent hot-carrier emission, and the more accurate underlying emission profile I_{PL} in Equation 4.3 is the inclusion of a term for the energy-dependent joint density of states. The impact of this change is illustrated in Figure 4.3B and C where the fits and extracted temperatures using a simple exponential model are shown in dark blue-black, and those using Equation 4.3 in light blue. For spectra modelled with low broadening, fits to a selected tail region that do account for the energy-dependent density of states, illustrated by light blue lines in Figure 4.3B and light blue open triangle markers in Figure 4.3C, give a good fit to the data and reproduce the actual charge-carrier temperatures with reasonable accuracy. In the higher broadening case, carrier temperatures from fitting with Equation 4.3 (light blue filled triangle markers) also give good accuracy for hot populations, although deviations persist at low temperature. Temperatures fitted with only the simple Boltzmann distribution (dark blue-black markers) show similar deviation at low temperatures, but substantially and increasingly overestimate carrier temperature for progressively hotter charge-carrier populations.

Overestimation of the temperature of hot carriers that have yet to cool when a simple exponential model is used can, therefore, be attributed primarily to the incorrect assumption of a constant joint density of states. The relative error quantified in Figure 4.4 further confirms this, showing that at high temperatures the error for a simple exponential model assuming constant DOS (blue-black markers) is similar for realistic or low broadening, and at least an order of magnitude greater in either case than the error using Equation 4.3. At lower temperatures, the difference in relative error with treatment of the density of states remains more significant in the low-broadening case (open markers) than with realistically large broadening (filled markers). When the joint density of states

is appropriately accounted for, relative error continuously decreases the hotter the charge-carrier population regardless of broadening, whereas fits assuming a constant density of states give a near-constant percentage error for carrier temperatures above 600 K.

The observed impact of accounting for a realistic energy-dependence of the joint density of states on extracted carrier temperatures can be understood by comparing the parabolic band structure to the simplified flat band assumed in the simple exponential model. At the bandgap, both flat and parabolic bands have zero gradient, but as energy increases above the bandgap the slope of a parabolic band becomes steeper while the density of states continually increases, and the difference between these two models becomes greater for progressively higher energies. Since the hotter populations of charge carriers, with high T_c, are those that have an energetic distribution extending further above bandgap, the choice of model used for the density of states has a greater impact on the accuracy of the extracted temperature the hotter the charge-carrier population of interest.

In practice, these comparisons show that accounting for the realistic joint density of states in MHPs is particularly important when investigating hot-carrier populations at very early times after excitation, or at high excitation densities, when the thermalised distribution extends to high energies above the bandgap with correspondingly high charge-carrier temperature. If the energy-dependence of the density of states is neglected, large overestimates in temperature under these conditions will result, along with distortion to the observed cooling dynamics. Overestimation of carrier temperatures in this way may also contribute to unrealistically high expectations for the performance of hot-carrier solar cells, suggesting a larger voltage gain from extraction of charge carriers within a given timeframe than could actually be achieved.

4.4.2 Accounting for spectral broadening

Broadening of emission spectra can be a result of several underlying mechanisms affecting excited charge carriers, including coupling with phonons, [105, 204, 257, 261] scattering with defects, [110] and the influence of trap states. [97, 259] Importantly for studies of hot carriers, these broadening mechanisms affect emission both above and below bandgap.

As illustrated in Figure 4.3B, exponential fits to a selected tail region of calculated spectra deviate more from the data in the case of realistic broadening, with $\sigma = 43.4\,\text{meV}$, than the low-broadening case with $\sigma = 5\,\text{meV}$, and worse fits are seen as carrier temperature decreases. Similarly, comparing extracted carrier temperatures against the actual input values as in Figure 4.3C shows that with realistic broadening, there is a plateau in the fitted temperatures at around 300 K as input temperatures decrease, whereas in the low-broadening case no such effect is seen. The relative error in extracted charge carrier temperatures shown in Figure 4.4 confirms this, with much larger errors at low temperature for the realistic broadening condition (filled markers) than the low-broadening condition regardless of whether the incorrect assumption of constant DOS is made. These results indicate that fits are poor and temperatures overestimated for cooler charge-carrier populations when there is significant broadening, and confirm that neglect of broadening in the model used to fit is responsible for this deviation, in contrast to the divergence at high temperature explained in Section 4.4.1. Further, comparing the open and filled triangle markers in Figure 4.4 that represent fits accounting for energy-dependent DOS but neglecting broadening, relative error is found to be larger in the case of realistic broadening than low broadening across the full temperature range.

The increasing overestimation of carrier temperature for cooler charge-carrier populations when broadening is significant can be explained by the changes in the shape of the emission spectrum over time. As T_c decreases, the high-energy emission from the hot-carrier population decays faster than emission near the band-edge and the PL

lineshape becomes more symmetrical and closer to the broadening profile. Therefore, the shape of the broadening function places a lower limit on the carrier temperatures that can be extracted by exponential fitting, with value determined by the choice of tail region to fit to. This is illustrated in Figure 4.5 where exponential fits to selected regions of a Gaussian profile are shown, with regions sufficiently close to the peak or tail of the distribution giving extreme values. The extraction of 'temperatures' approaching 300 K for a tail region extending from around 60 % of the peak down towards the edge of the distribution (shown in dark green) has no physical meaning, and is a good illustration of how exponential fits to a spectrum dominated by broadening may appear to capture cooling down to lattice temperature without being accurate to the true charge-carrier temperature. Dependence on the length of the tail region chosen as well as its position relative to the peak is also evident by comparing panels A and B in Figure 4.5. This exacerbates the problem, as discussed further in Section 4.4.3.

The artificial lower limit on carrier temperature from exponential fits that is imposed by spectral broadening becomes particularly important for analysis of residual populations of hot carriers at only slightly elevated temperature, and for any procedure where the tail region to fit to is chosen based on matching the fitted temperature at late times to the expected lattice temperature. The extent to which broadening can be safely neglected is determined by the relative magnitude of the broadened FWHM with respect to $k_B T_c$, as indicated by the absence of any overestimation for the low-broadening condition in Figure 4.3C. As room temperature FWHM values for most MHPs can be up to 100 meV, the impact of broadening is expected to be significant even for carrier temperatures up to 1000 K, encompassing most of the reported carrier temperatures in the literature.

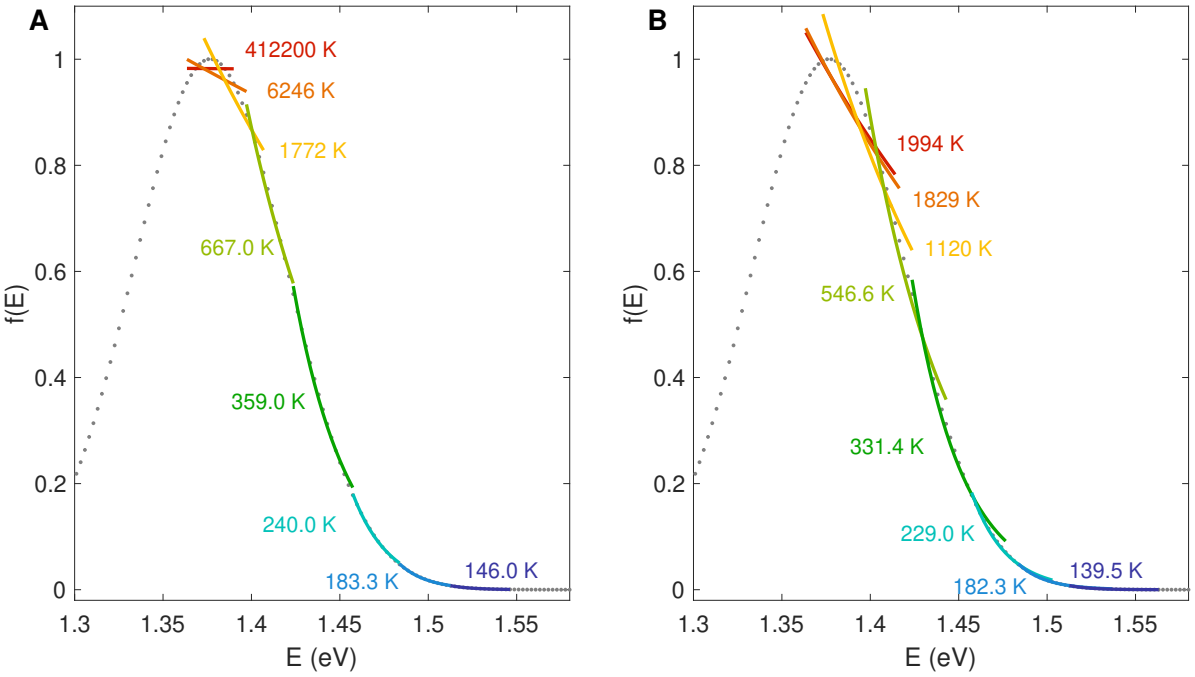


Figure 4.5: Exponential fits to various selected regions of a Gaussian distribution, showing the wide range of extracted 'temperatures' that can result from fits to the broadening profile. Point markers show the Gaussian profile of the form included in Equation 4.4 with parameter values $E_g = 1.38$ eV and $\sigma = 43.4$ meV, reflective of experimentally measured $FASnI_3$ PL spectra. Solid lines show exponential fits for each of eight selected regions, with a range of either 30 meV (A) or 50 meV (B) and common lower energy bounds used in both (A) and (B) as indicated by matching line colours. The 'temperature' extracted from the exponential fit to each region is shown adjacent to the fitted line and in the same colour. [Adapted with permission from *J. Phys. Chem. Lett.* 2019, 10, 20, 6018-6047 [225] Copyright 2019 American Chemical Society.]

4.4.3 Fitting the full spectrum

By accounting for each of the major influences on emission lineshape from photoexcited MHPs, the model expressed in Equation 4.4 can capture the full lineshape of a PL spectrum. Rather than selecting just a high-energy tail region, the full measured PL peak can then be used in fitting to extract carrier temperatures. This reduces the scope for variation in the method used between individual studies, and therefore offers a path to better comparability between results.

The impact of removing the element of choice found in an exponential fitting approach can be seen by comparing the temperatures extracted from fits with the simple exponential model to different choices of tail region for a single spectrum. This was illustrated for

a Gaussian profile in Figure 4.5, and is demonstrated for a full modelled PL spectrum in Figure 4.6 which shows six different tail regions in panel A, along with temperatures extracted for each of those choices in panel B. The different tail regions illustrated in this figure are defined by both energy interval, and position relative to the peak, starting at 70 % (red and orange markers, selections shown at the top of Figure 4.6A), 50 % (blue markers), or 30 % (green markers) of peak intensity, with two different interval widths. Comparing the extracted temperatures in panel B shows that the shorter tail regions (point markers) give higher tail fit temperatures than the longer regions (open circle markers), with the difference being greater for selections closer to the peak. Additionally, extracted temperatures are higher for choices of tail region starting closer to the peak.

These variations in the temperature extracted for different choices of tail can be explained by considering the gradient of the lineshape in different regions of the spectrum in comparison to the fitted exponential. Divergence between a fitted exponential curve and the underlying spectrum is generally larger at the higher-energy end of the range chosen to fit to, where the absolute difference between fit and data is smaller, as can be seen in Figure 4.3B. The slope where intensity is greater, at the lower-energy end of the range, then has a greater influence on the exponential fit and therefore the temperature extracted. Since spectral lineshapes tend to exhibit flattening out near to the peak, this leads to higher temperatures being extracted for fits closer to the peak where the gradient is shallower, and this effect is exaggerated for shorter ranges, as can be seen in Figure 4.6 as well as in Figure 4.5.

Dependence of fitted temperature on the choice of tail region leads to some significant problems, particularly when considered in combination with the impact of broadening at low temperature. In extracting temperatures from measured spectra, it can be assumed that at sufficiently late times after excitation the carrier temperature is equal to the temperature of the lattice, and this may be used as a criterion by which to select a region

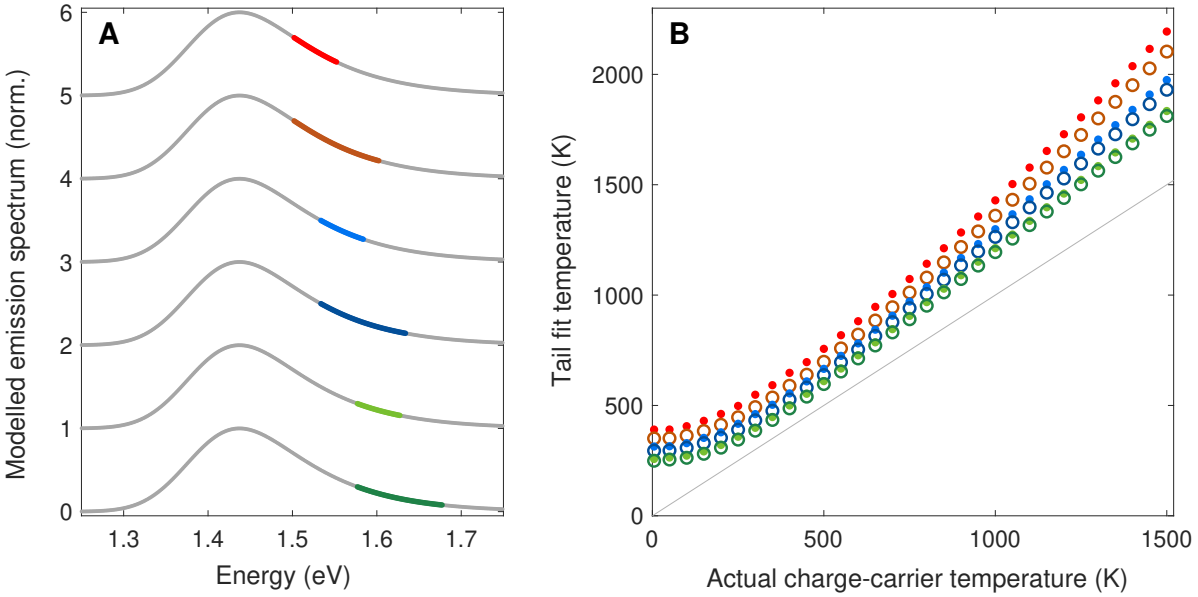


Figure 4.6: Impact of the choice of high-energy tail region to fit on carrier temperature extracted from a given PL spectrum. **A)** Different choices of tail region illustrated for a PL spectrum modelled using Equation 4.4 with $E_g = 1.38\,\text{eV}$ and $\sigma = 43.4\,\text{meV}$ with input carrier temperature 750 K. Selected tail regions beginning at 70 %, 50 % or 30 % of the peak emission amplitude and extending over a range of either 50 meV or 100 meV are plotted in colour, overlaying the modelled spectrum which is shown by grey point markers. For clarity each choice of tail is shown on a separate copy of the modelled spectrum with vertical offsets added. **B)** Charge carrier temperatures extracted from exponential fits using Equation 4.1 to the selected tail regions as illustrated in panel A. Point markers correspond to tail regions with a range of 50 meV, open circles to a range of 100 meV, and the colour scheme is the same as in panel A. The grey solid line is a guide to the eye showing equality between the tail fit temperature and the actual input temperature for modelled spectra. [Adapted with permission from *J. Phys. Chem. Lett.* 2019, 10, 20, 6018-6047 [225] Copyright 2019 American Chemical Society.]

of the spectrum to fit; suitable choices of tail region will give T_c at late times equal to the lattice temperature. However, as described in Section 4.4.2 the lower limit on temperature extracted from fitting to a tail region is heavily dependent on the broadening profile, and so choices that return physically sensible values of T_c at late time may in fact be capturing the slope due to broadening rather than the true carrier temperature. Differences in broadening between samples then undermine the intended consistency of this approach, exacerbating the difficulty of comparing cooling dynamics between studies in a meaningful way. The range of approaches used for tail selection, defined by ratios to peak intensity, [83] fixed energy intervals of varying width, [80, 84, 226, 227, 229]

or averaging of results from several different choices of tail region with systematically varying length, [85] increases the difficulty in comparing results. As shown here, each of these approaches to tail selection could return different carrier temperatures and cooling dynamics for the same set of spectra, contributing to the lack of consensus over cooling dynamics in the literature to date.

4.5 Conclusions

This chapter identified inadequacies in the widely adopted method of determining charge-carrier temperatures as a likely contributor to the lack of consensus regarding carrier cooling times in MHPs to date. As described here, the commonly used approach of fitting a simple Boltzmann model to a high-energy tail region of measured emission spectra originated in earlier studies on inorganic semiconductor quantum wells. This explains the assumptions of low broadening and constant density of states which were appropriate for quantum well systems, but are not applicable to bulk semiconductors including MHPs. Therefore, an improved full lineshape model accounting for the large spectral broadening and energy-dependent joint density of states arising from parabolic bands near the band edge in MHPs was presented. By comparing this model to simple tail fitting approaches, it was shown that assuming a constant density of states inflates the temperature of hot charge-carrier populations. Neglecting broadening also contributes to overestimates of carrier temperature, primarily affecting cooled populations. The impact of these errors in distorting cooling dynamics was highlighted, along with the dependence on the choice of tail region to fit that confounds these problems. Adopting the full lineshape model described in this chapter was thus shown to offer improved accuracy in the determination of charge-carrier temperatures and cooling dynamics, and a more consistent approach to allow meaningful comparison between the results of individual studies on different perovskite compositions.

4.6 Future outlook

The use of the full lineshape model described here in future work examining charge-carrier cooling across a range of perovskite compositions would allow the true cooling dynamics in these materials to be more accurately determined and compared. This is an important step in determining whether certain compositions do in fact show particularly slow cooling, which could be of use in hot-carrier solar cells, and allowing the mechanisms that contribute to any differences in cooling dynamics to be identified and understood.

There is also scope to customise and build upon the full lineshape model for use with a wider range of materials than the tin-based perovskites that were primarily considered here. Different forms of the broadening profile and joint density of states could be used if appropriate, for instance in any case where the band structure is not well-approximated as parabolic over the relevant energy ranges, and there is also scope to consider bandgap renormalisation explicitly.

Since the publication of work in this chapter, a study focussing specifically on transient absorption spectra has highlighted similar problems with determining charge-carrier temperature from a high-energy tail region. That work also proposed a model for the change in absorption that has carrier temperature, spectral broadening, change in bandgap due to renormalisation and Burstein-Moss shift, and Fermi energy as time-dependent parameters. [262] In future, a comparative study employing that approach with transient absorption spectra and the full lineshape model described here with time-resolved photoluminescence spectra could determine whether equivalent results are obtained for carrier temperature and cooling dynamics with each method. A truly consistent approach to the study of charge-carrier cooling in MHPs across measurement techniques could then be developed to best resolve the differences between perovskite compositions and identify candidate materials for hot-carrier solar cells.

5

Charge-Carrier Cooling Dynamics and Photoluminescence Polarisation Memory Loss in $FASnI_3$

Contents

5.1 Experimental details 80
5.1.1 Samples 80
5.1.2 Spectroscopy 82
5.1.3 Analysis 83
5.2 Charge-carrier cooling dynamics in $FASnI_3$ 89
5.2.1 Motivation 89
5.2.2 Results and discussion 89
5.2.3 Conclusions 93
5.3 Photoluminescence polarisation memory 96
5.3.1 Motivation 96
5.3.2 Results and discussion 97
5.3.3 Conclusions 101
5.4 Summary 101
5.5 Future outlook 102

This chapter examines charge-carrier dynamics in formamidinium tin triiodide, presenting the results of ultrafast time-resolved photoluminescence measurements to probe the charge-carrier cooling process and the loss of polarisation memory over time after excitation. As discussed in Section 2.4, understanding the properties of tin perovskites, and

how these differ from the more widely studied lead perovskites, is important in the search for low-toxicity lead-free solar cells and the development of devices requiring low-bandgap absorbers. $FASnI_3$ is a widely used example that forms the active layer in many of the highest efficiency tin perovskite solar cells reported to date, [127–129, 131] and is therefore a good candidate for further investigation of tin perovskites. Moreover, $FASnI_3$ has been identified as a promising choice for hot-carrier devices as discussed in Section 2.4.2.

This interest in $FASnI_3$ for hot-carrier solar cell applications provides motivation for the investigation of charge-carrier cooling presented in Section 5.2 of this chapter. Using the model developed in Chapter 4, this study reveals that the appearance of a secondary regime of unusually slow cooling in $FASnI_3$ is in fact attributable to relaxation of charge carriers amongst disordered energetic states, with true carrier cooling occurring over tens of picoseconds. In Section 5.3 of this chapter, complete loss of PL polarisation memory in $FASnI_3$ is found within 270 fs after excitation. This contrasts with previous observations of persistent polarisation memory in lead-based perovskites, [263] suggesting that further work is needed to unravel the relationship between local structure and electronic polarisation for different MHPs.

Work in this chapter is also published in reference [225]: Savill, K. J.; Klug, M. T.; Milot, R. L.; Snaith, H. J. and Herz, L. M., J. Phys. Chem. Lett., 2019, ***10****, 6038-6047.*

5.1 Experimental details

5.1.1 Samples

Thin films of $FASnI_3$ were prepared by Matthew T. Klug (Department of Physics, University of Oxford) using formamidinium iodide (FAI) purchased from Greatcell Solar, tin (II) iodide (SnI_2, 99.999 % Ultradry) purchased from Alfa Aesar, and tin (II) fluoride (SnF_2, 99 %), n,n-dimethylformamide (DMF, anhydrous, ≥99.8 %), dimethyl sulfoxide (DMSO, anhydrous, ≥99.9 %), and diethyl ether (anhydrous, ≥99.7 %) all purchased from

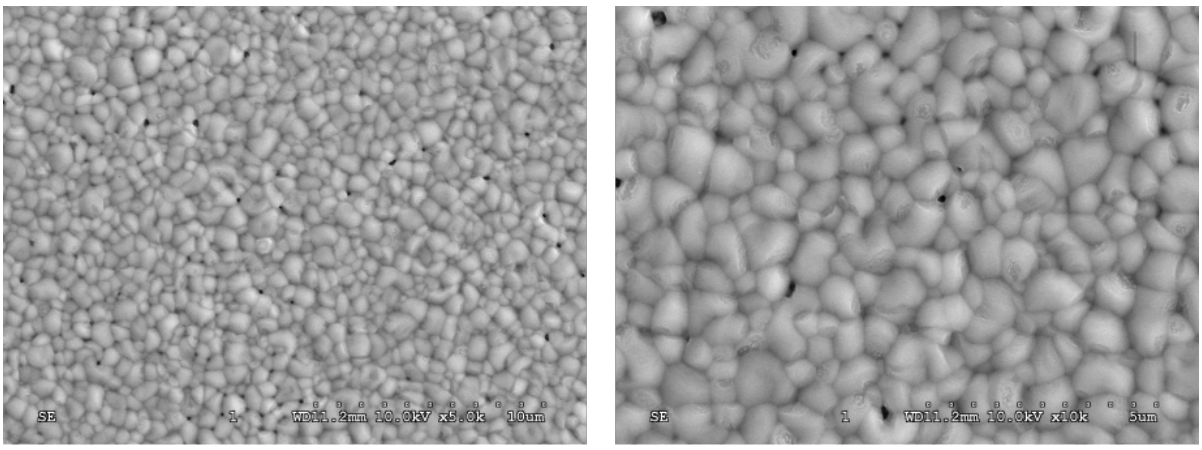


Figure 5.1: SEM micrographs of $FASnI_3$ film prepared with 5 % SnF_2 added, on FTO substrate. Measurements performed by Matthew T. Klug. [Reproduced with permission from reference [225].]

Sigma Aldrich. A stoichiometric 1.0 M solution of $FASnI_3$ was prepared in a nitrogen atmosphere by dissolving FAI and SnI_2 in a mixed solvent of 4:1 DMF:DMSO by volume. An additional amount of SnF_2 (5 % molar amount with respect to SnI_2) was dissolved in the solution. The solution was stirred overnight at room temperature and then filtered with a 0.45 µm PTFE filter prior to use. Samples for PL measurements were prepared in a nitrogen atmosphere by statically dispensing the solution on an O_2-plasma treated quartz disc and spincoating at 4 krpm for 30 s with a 6 s ramp. At 12 s from the start of the spincoating program, 200 µL of diethyl ether was dropped onto the spinning film, which caused the perovskite film to immediately darken. The films were subsequently annealed at 70 °C for 20 minutes in an N_2 atmosphere.

Samples were characterised by XRD, steady state absorption, and film thickness measurements, which are included in Appendix A. Additionally, SEM images as shown in Figure 5.1 were obtained using a Hitachi S-4300 scanning electron microscope with acceleration voltage of 10 kV and probe current of 11 μA to examine the morphology of the prepared films. These images show good film quality for these samples, which exhibit large grain sizes in the 0.5 – 1.5 μm range and consistent coverage with few pinholes.

The addition of SnF_2 in this method was intended to moderate doping resulting from oxidation of tin, with previous characterisation of samples prepared in this way having shown improvements in charge-carrier mobility and lifetimes, as well as in film quality, attributable to the use of SnF_2. [141] In that previous work, the exciton binding energy for the $FASnI_3$ films was calculated as 3.1 meV, and background hole density as $2.0\times\ 10^{19}\,cm^{-3}$. [141]

5.1.2 Spectroscopy

To minimise exposure to air, samples were loaded into a vacuum cell while still under nitrogen atmosphere, then placed under vacuum with continuous pumping to maintain pressure of $2.5\ \times 10^{-3}$ mbar or lower during measurements. For all photoluminescence measurements, samples were excited using a tunable Ti:Sapphire laser with 80 MHz repetition rate at 730 nm, and excitation power was attenuated to 12 mW or 60 mW using a half-waveplate and vertical polariser. This gave excitation fluences of 0.75 µJ cm^{-2} and 3.75 µJ cm^{-2} respectively, corresponding to charge-carrier pair densities of $6.9\times\ 10^{16}\,cm^{-3}$ and $3.4\times\ 10^{17}\,cm^{-3}$, averaging across the thickness of the film in each case.

Time-resolved photoluminescence measurements were taken using the upconversion setup described in Section 3.2.1 and shown in Figure 3.5, and the TCSPC setup also shown in that figure and described in Section 3.2.2. The excitation path was the same for upconversion, TCSPC, and for time-integrated photoluminescence measurements that used the same monochromator and detector as for upconversion, with BBO crystal removed and gate beam blocked.

PL polarisation anisotropy measurements were carried out using the upconversion setup, making use of the intrinsic polarisation selectivity of this technique as illustrated in Figure 5.2. Sum frequency generation occurs only for the component of PL with polarisation matching that of the gate beam, in this case vertical as shown by the orange

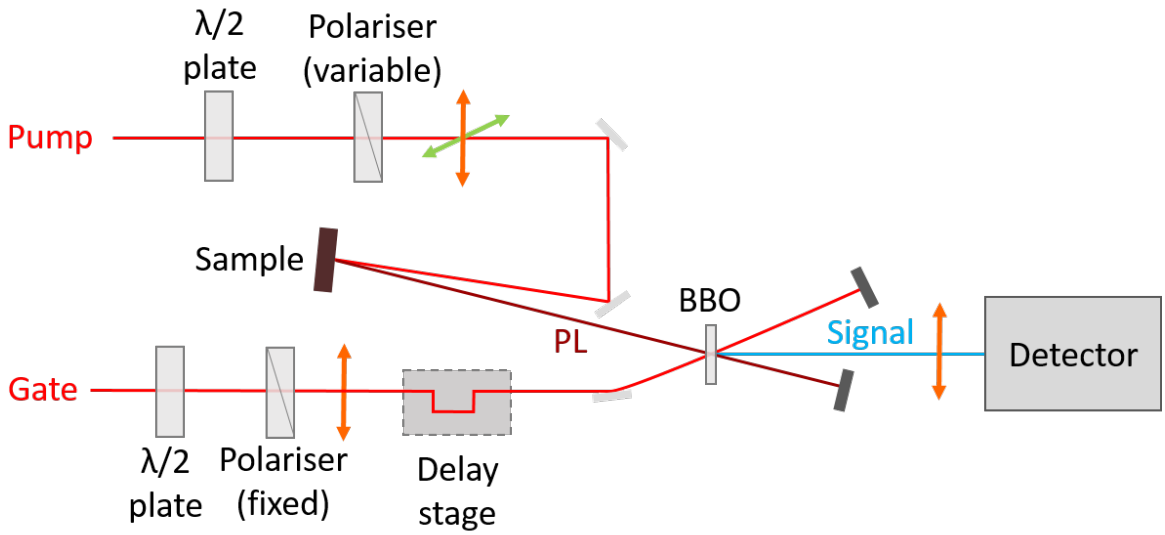


Figure 5.2: Simplified schematic of the upconversion setup used for PL polarisation anisotropy measurements. The polarisation direction of each beam at right angles to the beam path is indicated by an arrow, green for horizontal and orange for vertical. The dark grey unlabelled rectangles after the BBO crystal represent beam dumps for the transmitted gate and pump beams. [Reproduced with permission from reference [225].]

arrows. So, the excitation beam polarisation was controlled using a Glan-Thompson polariser to be either parallel (vertical, orange arrow) or perpendicular (horizontal, green arrow) to the polarisation of the upconverted signal detected. Excitation power at the sample was kept constant between polarisations by adjusting the half-waveplate. To correct for the slight change in direction of the transmitted beam with changing polariser and waveplate angles, small adjustments to alignment were made after each change between polarisations to restore optimal overlap of the PL and gate beams in the crystal for maximum upconversion signal.

5.1.3 Analysis

Charge-carrier temperatures were determined by fitting time-resolved spectra with the full lineshape model described in Chapter 4 and given in Equation 4.4. The four parameters in this model are bandgap E_g, broadening parameter σ, a scaling parameter B to account for the intensity of the PL peak as measured which will vary as the

population of charge carriers decays, and carrier temperature T_c. To determine carrier temperatures from measured data, fits for T_c were carried out with B also free to vary, and E_g and σ fixed since the bandgap and the effects leading to broadening of the emission spectrum are both expected to be properties of the sample that do not change significantly following excitation.

To determine the characteristic values of E_g and σ for use in fitting all spectra from the measured $FASnI_3$ samples, a set of spectra measured at late enough times after excitation to show no further cooling was globally fitted with T_c set to the expected temperature of 300 K for charge carriers equilibrated with the lattice. Specifically, the spectra between 0.6 to 0.7 ns after excitation were fitted globally, as illustrated for the lower excitation fluence condition in Figure 5.3, to extract the parameter values shown in Table 5.1 that completely define the broadening function for these samples. This procedure was applied separately for each of the two excitation fluences, giving the two sets of values for E_g and σ as shown in the table, because there is a small power-dependent peak shift in the photoluminescence from $FASnI_3$ (discussed in more detail in Section A.3). Since this power-dependent effect occurs independently from the observed spectral changes due to carrier cooling, and is less pronounced than the peak shift attributable to carrier cooling, using a separate fixed value of E_g for each excitation fluence to account for the power-dependent effect allows the true cooling dynamics to be better captured.

	0.75 μJ cm^{-2} excitation fluence	3.75 μJ cm^{-2} excitation fluence
E_g [eV]	1.3767	1.3850
σ [eV]	0.0434	0.0483

Table 5.1: Characteristic values of the parameters E_g and σ determined from global fits over late time $FASnI_3$ photoluminescence spectra, to be used in fitting for carrier temperature with Equation 4.4.

With the fixed parameter values in Table 5.1, measured spectra were then fitted using the full lineshape model in Equation 4.4, computed using Fourier transforms according

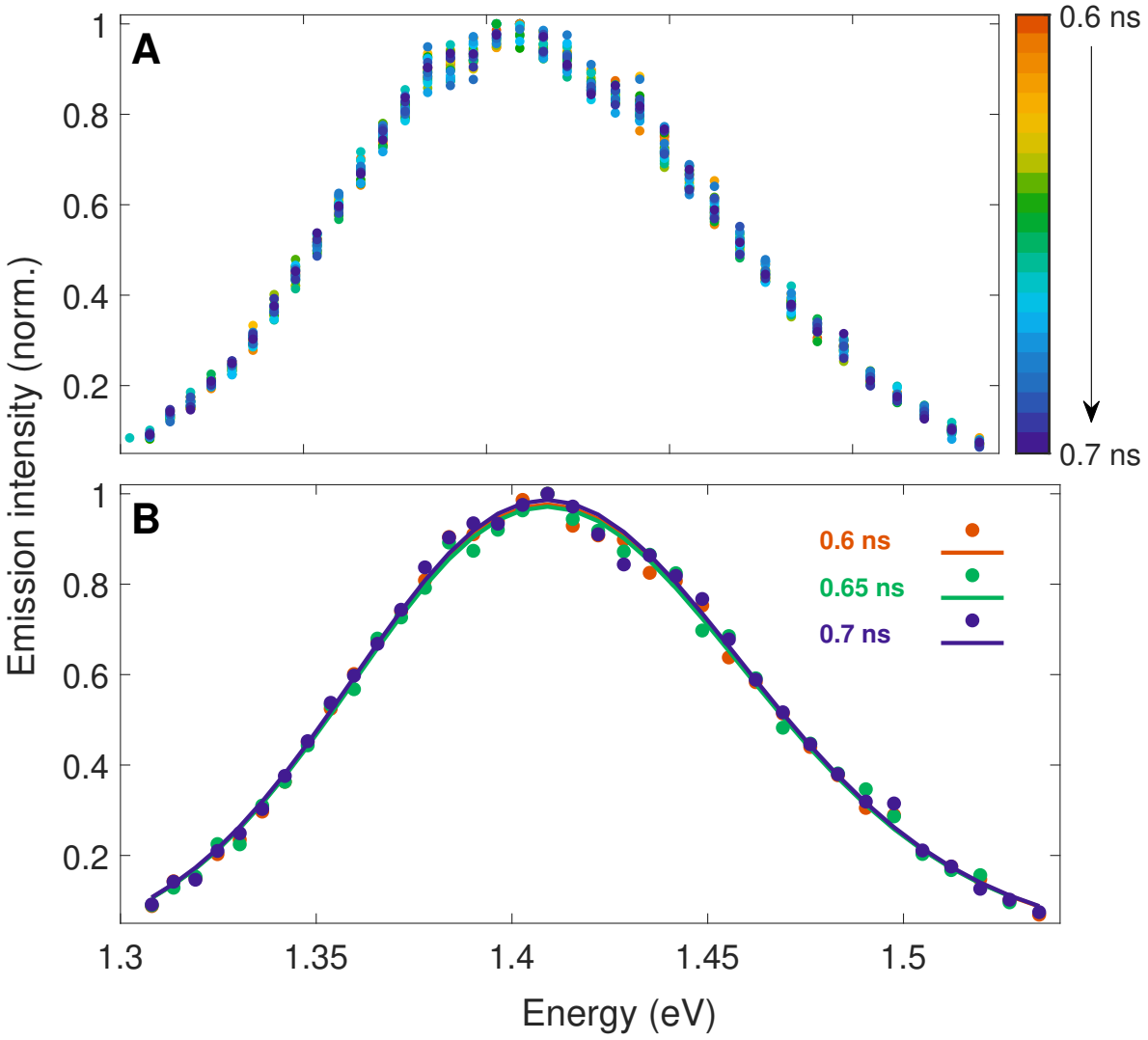


Figure 5.3: Illustration of global fits with T_c fixed at 300 K in Equation 4.4 used to determine characteristic values of E_g and σ as shown in Table 5.1 from $FASnI_3$ PL spectra at late times after 730 nm excitation with a fluence of with 0.75 μJ cm^{-2}. **A)** The full set of measured spectra between 0.6 – 0.7 ns delay time selected to use in global fitting, shown with marker colour ranging from dark orange to blue with increasing delay time as indicated by the colour bar, and illustrating the level of noise and variation between individual spectra over this interval. **B)** Fits (shown as solid lines) to the measured spectra (point markers) at 0.6, 0.65 and 0.7 ns delay time, following the same marker colour scheme as in panel A. [Adapted with permission from reference [225].]

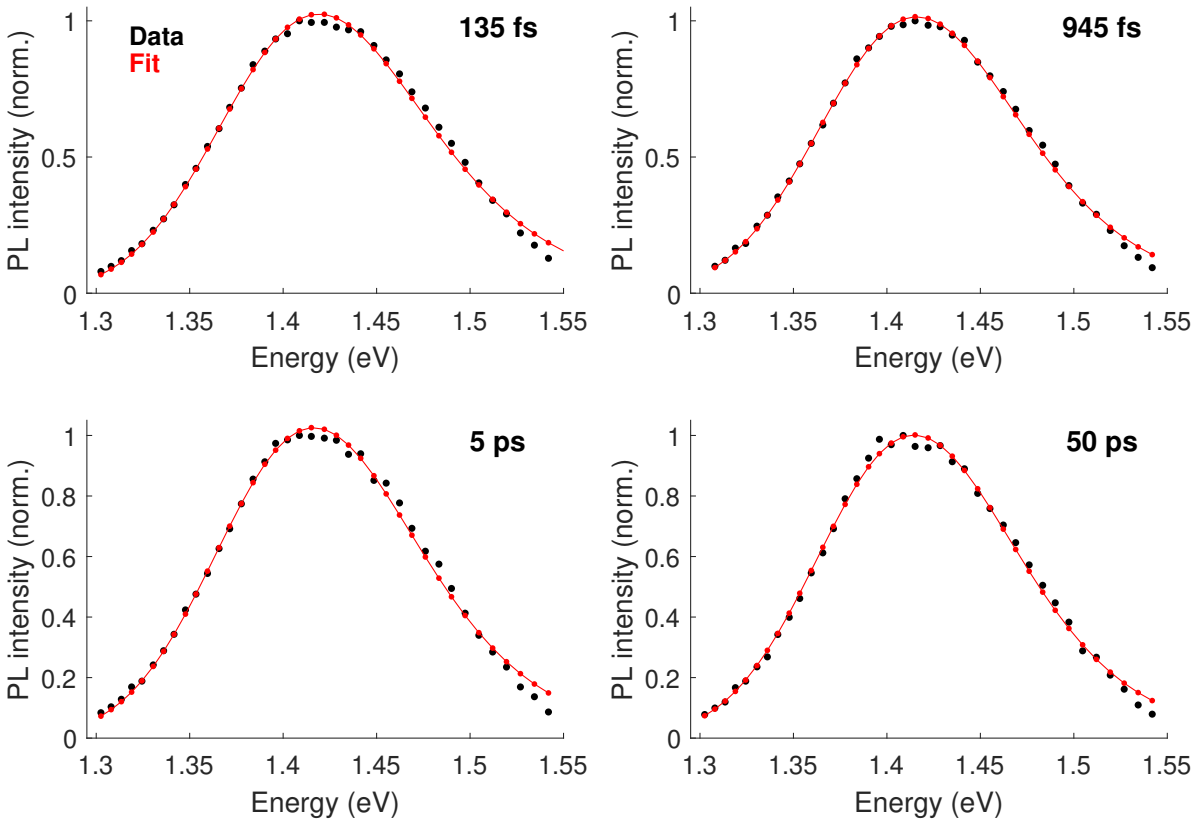


Figure 5.4: Example of fits to extract carrier temperature from measured $FASnI_3$ PL spectra, excited at 730 nm with a fluence of 0.75 μJ cm^{-2}. Measured data are shown by black point markers, fits using the full lineshape model given by Equation 4.4 with fixed parameter values $E_g = 1.3767$ eV and $\sigma = 43.4$ meV are shown as red solid lines. [Adapted with permission from reference [225].]

to Equation 5.1 which holds in general for any pair of functions G and H.

$$G \otimes H = \mathcal{F}^{-1}\left[\mathcal{F}(G) \times \mathcal{F}(H)\right] \tag{5.1}$$

In this case G is the underlying emission profile and H the Gaussian broadening function, which is its own Fourier transform. The implementation of this method is, therefore, computationally fairly simple. Representative examples of the results from this fitting process are shown in Figure 5.4 for the lower excitation fluence, with further examples also shown in Appendix A.

PL polarisation anisotropy was calculated from the measured intensities for detection parallel ($I_{||}$) and perpendicular ($I_{\perp}$) to the excitation polarisation according to Equa-

tion 5.2.

$$r = \frac{I_{||} - I_{\perp}}{I_{||} + 2I_{\perp}} \tag{5.2}$$

To account for variations in signal intensity between polarisations resulting from experimental error, in particular imperfect re-alignment to correct for the changes in beam direction when switching between parallel and perpendicular excitation polarisations, a correction was applied to the measured data as follows. A series of measurements on a single $FASnI_3$ thin film sample were taken for PL near the peak of the spectrum (1.42 eV) at a fixed delay time (3 ps) chosen to be within a range where the PL decay transient was not rapidly changing so that any small changes in path length would not have a large impact on signal intensity. Across the series, excitation polarisation was switched repeatedly between parallel and perpendicular with overlap optimisation after each change to take ten pairs of measurements across three different sample spots, as shown in Figure 5.5A. For each of these pairs of consecutive measured intensities, some of which started with parallel polarisation and some with perpendicular polarisation, the measured anisotropy was then calculated as shown in Figure 5.5B. The mean and standard deviation of the anisotropy over all ten pairs of measurements were then calculated, giving anisotropy of 0.0146 ± 0.0441 as shown by the black marker and error bar in the figure.

From this mean anisotropy, the ratio $\frac{I_{\perp}}{I_{||}} = 0.9575$ was determined by rearrangement of Equation 5.2. This ratio was then used to scale the measured data at 90 ° against the corresponding 0 ° data at 1.42 eV and (in the case of PL decay transients) at 3 ps, allowing anisotropy values to then be calculated over the full temporal and spectral ranges measured with differences in intensity due to imperfect re-alignment in any given measurement having been corrected for.

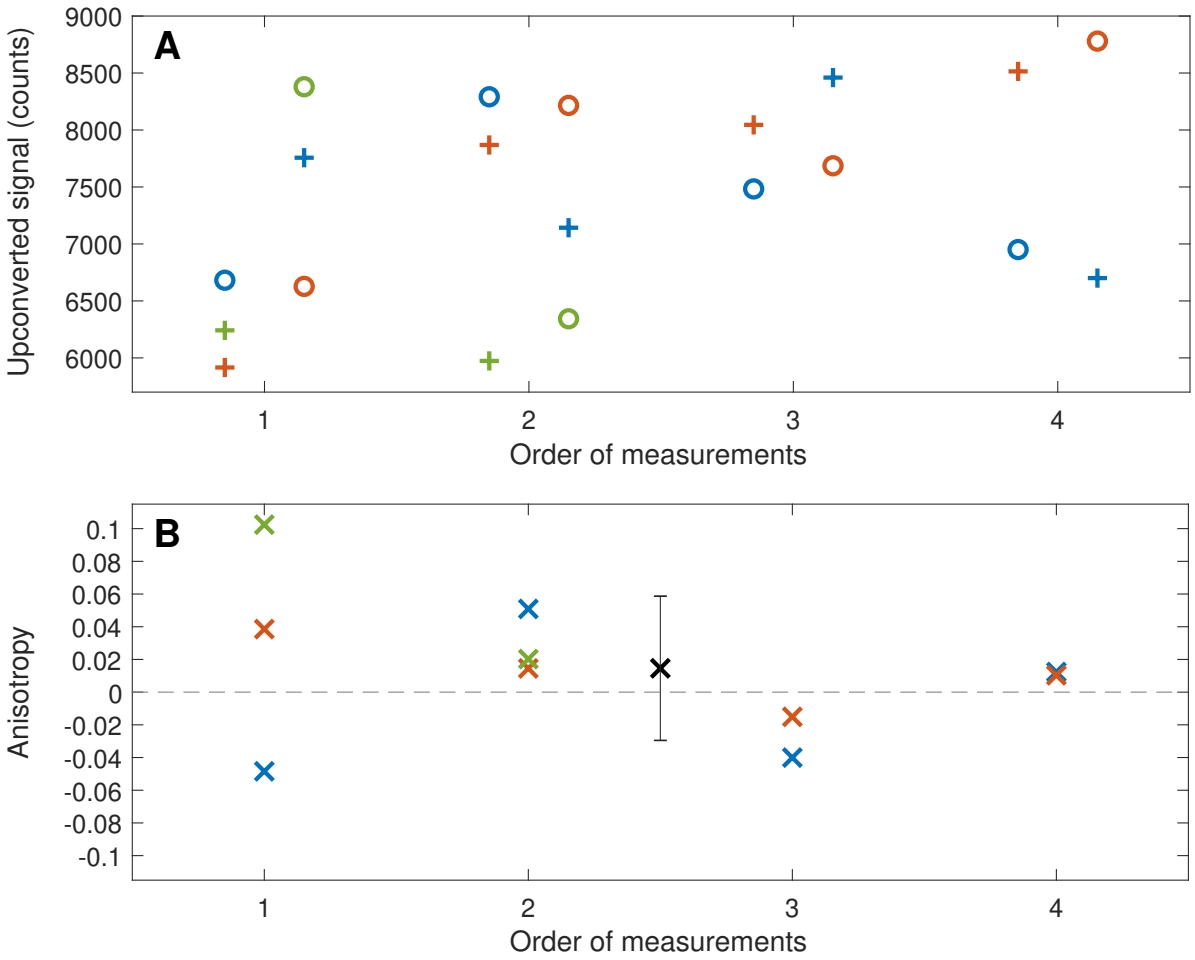


Figure 5.5: PL polarisation anisotropy measurements with repeated polarisation switching to quantify experimental error, exciting a thin film $FASnI_3$ film with fluence 0.75 μJ cm^{-2} at 730 nm and detecting at 3 ps delay time for PL at 1.42 eV, with excitation beam polarised either parallel (0 °) or perpendicular (90 °) to the detected polarisation. **A)** Measured signal intensity after optimising overlap for each polarisation, at three different sample spots indicated by the three different marker colours. For each series on a single sample spot, values are plotted in the temporal order in which they were taken, with ∘ markers for 0 ° polarisation and + markers for 90 ° polarisation. **B)** Anisotropy values calculated from the measured intensities shown in panel A according to Equation 5.2, with the same colour scheme used to distinguish measurements on different sample spots. The black marker shows the mean anisotropy across all ten pairs of measurements, with error bar calculated as the standard deviation over this set of values. [Adapted with permission from reference [225].]

5.2 Charge-carrier cooling dynamics in $FASnI_3$

This section examines the charge-carrier cooling process in $FASnI_3$, a material previously reported to show slow cooling, providing a demonstration of the full lineshape model for determining carrier temperature in use and revealing the contribution of energetic disorder to the appearance of unusually long-lived hot carriers.

5.2.1 Motivation

As discussed in Sections 2.3.2 and 2.4.2, slow cooling of hot carriers in MHPs is an interesting phenomenon to explore for potential hot-carrier-extracting photovoltaic devices with increased open circuit voltage, and to better understand the interactions between excited charge carriers and the lattice. Carrier cooling in $FASnI_3$ is of particular interest, as the previously reported hot-carrier lifetime of several nanoseconds [13] for this perovskite composition lies at the slowest extreme of the range of cooling times reported in the literature. [11] This makes $FASnI_3$ the only perovskite yet to pass the threshold of 1 ns hot-carrier lifetime thought to be necessary for high device efficiencies. [161, 163] It is therefore important to establish whether the appearance of unusually slow cooling in $FASnI_3$ is genuine, or arises from other effects in the material or the choice of method used to determine carrier temperature. The answer to this question has significance for determining the true range of cooling times accessible in MHPs and assessing the prospects for high efficiency hot-carrier solar cells.

5.2.2 Results and discussion

A representative selection of measured $FASnI_3$ PL spectra are shown in Figure 5.6A. These spectra show an emission profile changing over time after excitation in a manner typical of a hot-carrier population gradually cooling. At early times (the red end of the colour range used in this figure) the high-energy side of the PL peak is elevated in intensity, and over

time this emission at high energy drops away to give a more symmetrical profile as carriers cool, which is accompanied by a small redshift of the peak position. Carrier temperatures are extracted from these measured spectra by fitting with the full lineshape model given by Equation 4.4 as discussed in Chapter 4, with fits as shown by the solid lines in panel A of Figure 5.6. With fixed values of E_g and σ, determined from global fits to fully cooled spectra as described in Section 5.1.3, carrier temperatures T_c are then obtained for each spectrum, and plotted in dark blue in Figure 5.6 panels B and C for two different fluences.

Initial temperatures observed are around 450 K, hotter for the high fluence and cooler for the low fluence, which is on the same order of magnitude as many previous reports for similar initial carrier densities across a range of MHP compositions but somewhat colder. [80, 82, 85, 226, 230] In a few other cases, carrier temperatures exceeding 1000 K have been reported at very early times, [79, 83, 84] far exceeding the measured value here. It is to be expected that the full lineshape fit will give lower temperatures than the commonly used exponential tail fit, as explored in detail in Chapter 4, so the difference between these data and previous reports may be largely accounted for by removing systematic overestimation due to over-simplified approaches to determine carrier temperature. It is also likely that some cooling has already occurred within the 270 fs time resolution of the measurements reported here, such that the initial temperature immediately following thermalisation would be higher.

Examining the cooling dynamics shown by fitted T_c values for two different excitation fluences in panels B and C of Figure 5.6, it is apparent that charge carriers cool over tens of picoseconds initially, and then temperatures elevated above 300 K persist to later times with similar cooling curves for both excitation fluences. Until around 0.4 ns after excitation, carrier temperatures for the higher excitation fluence of 3.75 μJ cm^{-2} are higher than those for the low fluence, and in both cases equilibration to 300 K does not occur until around 0.7 ns. Comparing the two fluences, initial charge-carrier densities

averaged across the thickness of the $FASnI_3$ film (see Appendix A for details of the calculation) are $8.2 \times 10^{16}\,cm^{-3}$ and $4.1 \times 10^{17}\,cm^{-3}$ respectively, well below the threshold fluences reported elsewhere for a hot-phonon bottleneck to slow down carrier cooling. [79, 80, 83, 226] Therefore, a buildup of hot phonons preventing further cooling through hot carrier-phonon scattering is unlikely to be responsible for the observed persistence of carrier temperatures above 300 K following more rapid cooling at early times. Other mechanisms have previously been suggested to explain persistent hot carriers without a hot-phonon bottleneck, including lattice screening or Rashba-like effects that lead to unusually long-lived hot carriers, [13, 86] and such explanations might be considered to account for the dynamics seen in Figure 5.6B and C.

Before attributing residual high carrier temperatures at late time to a particular mechanism for slow cooling, it is important to rule out other effects that might give the false appearance of a long-lived population of hot charge carriers. In particular, comparing the dynamics of apparent slow cooling against decay in the overall charge-carrier population determined from the total PL intensity suggests another explanation for the elevated charge-carrier temperatures seen here at late times. In Figure 5.6B and C the total PL intensity data (calculated by integration over the whole measured spectrum at each delay time) are plotted in orange to give an overall charge-carrier population decay curve. From this it can be seen that the later time dynamics of carrier cooling closely track the decay in total PL, whereas the more rapid cooling in the first tens of picoseconds is clearly distinct.

This agreement between the cooling curve and total PL decay dynamics implies that the changes to PL spectra at late time that affect fitted carrier temperature, that is a slow reduction in intensity at the high-energy side of the peak and a slight redshift in peak position, are connected to the decay of the charge-carrier population. The faster charge-carrier cooling seen at early times, by contrast, is independent of overall carrier

population decay. The observed dependence of temperature on population decay at late times can be explained by slow charge-carrier relaxation through energetically disordered states in $FASnI_3$, a process that is limited by the occupation of charge carriers in lower-energy states extending into the band tail. Such relaxation, occurring independently from the thermalisation and subsequent cooling processes affecting free, delocalised charge carriers, is dependent on recombination of charge carriers from lower-energy states to allow higher-energy states to be depopulated, explaining the results seen here. This process is also consistent with properties of tin halide perovskites that are already well known, in particular the readiness with which Sn^{2+} will oxidise to Sn^{4+} and introduce background hole doping [66, 134] as discussed in Section 2.4.4, which leads to a locally varying electrostatic environment. To counter this, SnF_2 is often added during fabrication in order to reduce dopant density, [141] including for the samples used in this study. However, the distribution of this additive across the perovskite film is not yet known [202] and inhomogeneities are likely to contribute to local energetic variations. A further source of energetic disorder in a wide range of MHPs is the random orientation of organic cations contributing to lattice distortions and electrostatic variations [264–267] with the larger FA cation used in this study giving greater distortion than MA. [268]

Due to these various forms of disorder, the energetic landscape of $FASnI_3$ includes states with a distribution of energies both below the bandgap in a band tail [115, 269] and at higher energies, that can be occupied by carriers excited above the bandgap. Further evidence for such a distribution is given by comparing the PL decay dynamics for different regions across the PL spectrum, as shown in Figure 5.7 for four selected regions: at the high-energy edge of the spectrum (orange), either side of the PL peak (red and purple) and at the low-energy edge of the emission profile (dark blue). The lower the energy probed, the slower the decay of emission from charge carriers at that energy, indicating a slower decrease in the corresponding carrier population. This is consistent with relaxation

between energetic states limited by recombination, as relaxation down from higher-energy states replenishes the population of charge carriers in lower-energy states simultaneously with recombination, so that the slower decay is observed for low-energy PL, while the decay of higher-energy PL is limited by overall recombination rate. Importantly, this relaxation between disordered states occurs even at the low charge-carrier densities used here, for which any simple band-filling effects are expected to be minor. [65, 270, 271] The observed slow decline in fitted carrier temperatures, matching the overall dynamics of PL decay, is thus explained not by an unusual mechanism for slowing charge-carrier cooling, but by the influence of energetic disorder.

5.2.3 Conclusions

This study of charge-carrier cooling in $FASnI_3$ shows that the population of hot carriers generated by moderately above-bandgap excitation in this material cools over a timescale of tens of picoseconds. The appearance of slow cooling of a residual population of hot carriers at later times is erroneous, arising from carrier relaxation through localised energetic states resulting from disorder, which is limited by the rate of carrier recombination. Such an effect can occur in any energetically disordered semiconductor, giving artificially elevated carrier temperatures even at excitation densities too low for a hot-phonon bottleneck to slow down cooling. This false appearance of residual hot carriers can be compounded by simplifications in the approach to determining carrier temperature. In future studies of carrier cooling in MHPs, any slow cooling dynamics should therefore be compared against overall carrier population decay to rule out the disorder effects seen here. This consideration is particularly important in tin-containing perovskites where high sensitivity to oxygen can increase energetic disorder.

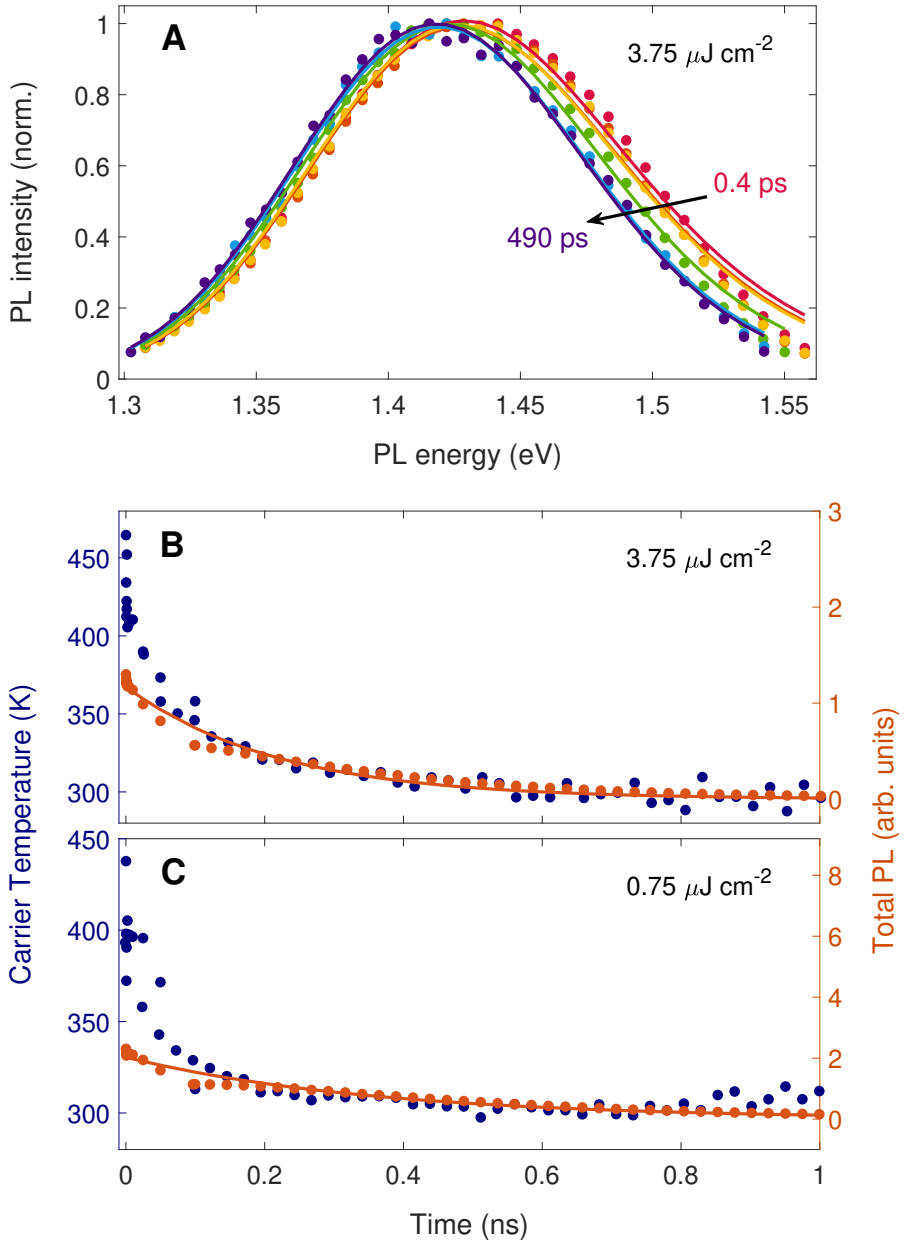


Figure 5.6: Charge-carrier cooling from PL spectra, and PL decay dynamics, of $FASnI_3$ films on quartz prepared with 5 % SnF_2 and excited at 730 nm with pulsed laser fluences as marked. **A)** Illustration of fits to representative PL spectra, as used to determine carrier temperatures plotted in panel B. Point markers show the measured data at 3.75 μJ cm^{-2} excitation fluence, and solid lines show the full lineshape fits using the model described in Equation 4.4. Each colour corresponds to a single delay time after excitation, moving to later times from red to blue as indicate by the arrow. **B, C)** Carrier cooling curves (dark blue point markers) overlaid with total PL decay curves (orange point markers) for the high- and low-fluence excitation conditions respectively. Carrier temperature data plotted in dark blue are given by fits to spectra as shown in panel A, following the process described in Section 5.1.3. Total PL data plotted in orange are given by integration over the full energy range for each measured spectrum, and orange solid lines show monoexponential fits to the total PL decay transients. [Adapted with permission from *J. Phys. Chem. Lett.* 2019, 10, 20, 6018-6047 [225] Copyright 2019 American Chemical Society.]

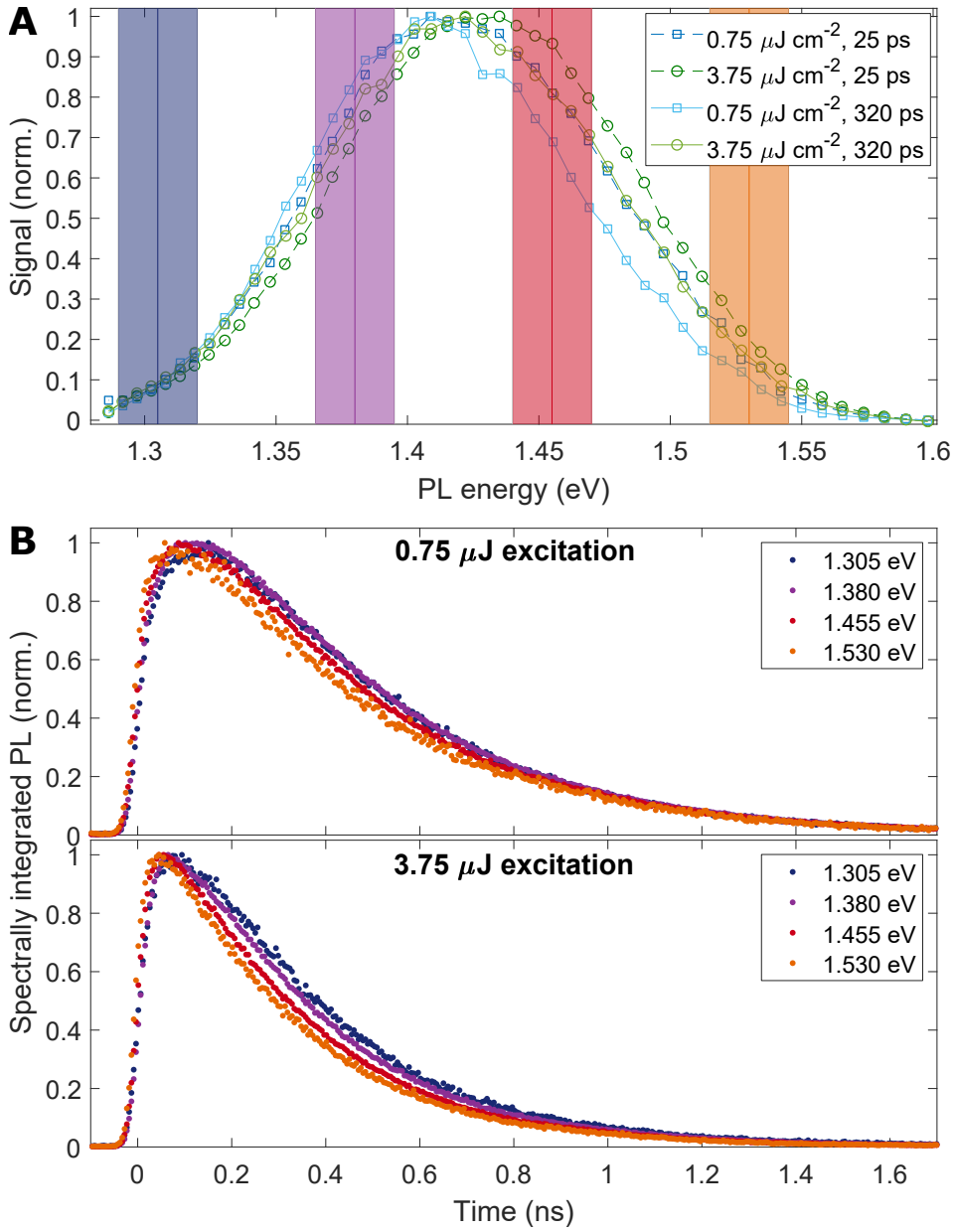


Figure 5.7: $FASnI_3$ photoluminescence decay transients, integrated over selected spectral regions. **A)** Time-resolved PL spectra of a $FASnI_3$ film on quartz at selected delay times early and late after excitation as indicated in the legend for both high and low excitation fluences. Selected 30 meV energy ranges over which to integrate are highlighted, with the darker solid line in the middle of each highlighted bar marking the energy by which the region is identified. **B)** Decay transients for the four selected energy ranges at low and high excitation fluences as indicated. Marker colour scheme for each energy interval matches that used in panel A. [Adapted with permission from reference [225].]

5.3 Photoluminescence polarisation memory

This section investigates whether polarisation memory persists in photoluminescence from $FASnI_3$ following polarised excitation, which would be indicative of structural features contributing to anisotropy in electronic states as reported for some lead-based perovskite compositions, and finds that there is no such memory retained beyond the 270 fs time resolution of measurement.

5.3.1 Motivation

In any absorbing material, illumination with linearly polarised light will only excite transitions for which there is a transition dipole matrix element in the polarisation direction, and subsequently emission from the material may retain this polarisation, or lose it over varying timescales. The timescale over which the initially anisotropic distribution of photoexcited charge carriers is lost to an isotropic distribution with no polarisation memory depends on the nature of the initial polarisation selectivity. In molecular materials that have transition dipoles aligned to the structure of the molecule, mechanisms for the loss of polarisation memory include re-orientation [272] or structural distortion [273] of excited molecules, energy transfer from the absorption site to another emissive molecule with different orientation, [274] delocalisation occurring after excitation, [273] or migration of charges between and along molecular subunits. [275] The rate of polarisation memory loss is variable, with structural distortion over around 100 ps compared to delocalisation within hundreds of femtoseconds, for example, [273] whereas molecular rotation can be observed over nanoseconds. [272] In bulk semiconductors, structural anisotropies may result in polarisation-selective absorption and subsequent memory. [276] Absent any such structural features, polarised excitation leads to initially anisotropic momenta of excited charge carriers, which is rapidly lost through carrier-

carrier scattering; this process has been observed in GaAs to give complete loss of polarisation memory in tens of femtoseconds. [277, 278]

Measurements probing polarisation memory loss therefore offer useful information about the existence of any structural features that couple to polarisation, and their evolution over time. In some lead halide perovskites transient absorption measurements have shown polarisation anisotropy persisting for several picoseconds, attributed to local lattice dynamics strongly coupled to optical properties. [263] Understanding the dynamic distortions of the lattice in MHPs is relevant not only to polarisation memory, but also to other properties affected by electron-phonon interactions, such as the mobilities and cooling rates of excited charge carriers. [80, 85, 105, 106] Local variations in the lattice of $FASnI_3$, with impacts on energetic disorder, are to be expected. The question of whether such variations have an impact on polarisation memory is interesting from both a fundamental physics perspective, and as a possible probe for the dynamics of these distortions if they are found to affect polarisation memory.

5.3.2 Results and discussion

Figure 5.8A and B show the results of time-resolved PL measurements, carried out using upconversion spectroscopy as described in Section 5.1.2 with polarisation selectivity either parallel (the 0 ° condition) or perpendicular (the 90 ° condition) to the polarisation of the excitation beam. The PL polarisation anisotropy r, calculated from these measured PL decay traces and spectra according to Equation 5.2 as described in Section 5.1.3, is shown in Figure 5.8C and D. As shown here, the calculated PL anisotropy values stay very close to zero across the full temporal and energetic range explored, from very early times after excitation out to several hundred picoseconds in panel C and for the whole emission spectrum in panel D. At late times the noise in anisotropy values across the spectrum (panel D) increases due to low signal below 1.3 eV and above 1.5 eV, but no

other change is seen. With the exception of a few stray points, calculated anisotropy values are zero to within the experimental uncertainty of 0.044 (see Figure 5.5) for all measurements. This indicates that there is no PL polarisation memory nor any evolution thereof over the timescales of PL decay or carrier cooling. It is possible that some polarisation memory persists over tens of femtoseconds after excitation, and is lost within the 270 fs time resolution of the measurement.

The apparent lack of any PL polarisation memory persisting beyond a few hundred femtoseconds in $FASnI_3$ found here forms an interesting contrast with recently reported results for some other MHP compositions. Rivett et. al. observed polarisation memory lasting several picoseconds in $MAPbI_3$, $MAPbBr_3$ and $CsPbBr_3$, attributed to coupling of electronic states with locally polarised regions of the perovskite film having defined Rashba directions, which form dynamically as the inorganic lattice distorts so that polarisation memory persists on the timescale of fluctuations in lattice structure. [263] The absence of PL polarisation memory over a similar timescale in $FASnI_3$ suggests that the same mechanism is not active in this tin-based perovskite, which raises the question of whether similar distortions are absent or simply do not have any significant effect on electronic states.

In answering this question, it is notable that the Rashba effect occurring on a local scale in several lead-based perovskites and contributing to polarisation memory arises from spin-orbit coupling, [263] which is stronger for lead than for the lighter tin cation. [102] On this basis some reduction in the polarisation anisotropy seen for tin halide perovskites relative to lead halide perovskites might be expected, even if there are similar dynamic structural anisotropies with either B cation. However, the lattice dynamics that contribute to local symmetry breaking and polarisation in lead halide perovskites involve distortions of the lead halide octahedra [263, 279, 280] which may be coupled to the orientation of the organic cation within each octahedron. [266, 281, 282] Therefore the choice of

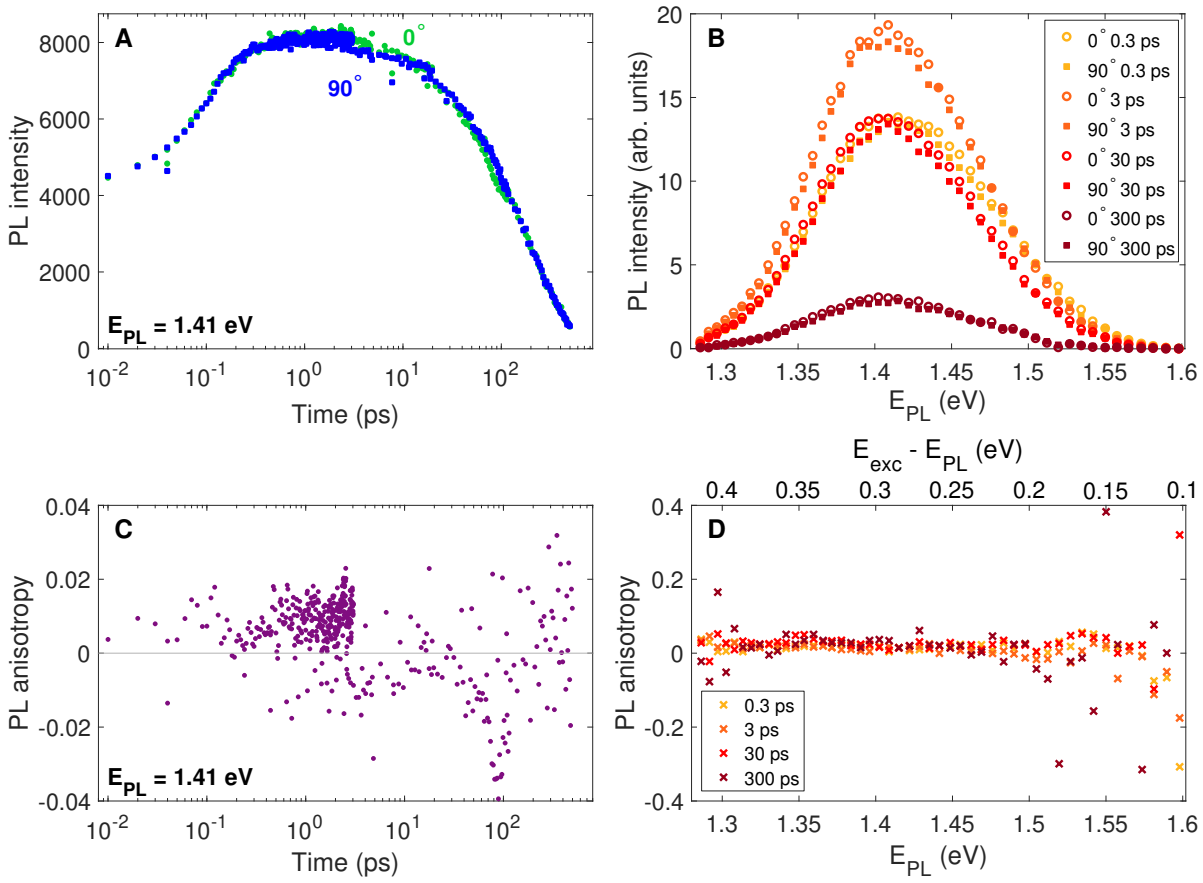


Figure 5.8: Evolution of polarisation anisotropy over time after excitation for the photoluminescence from a thin film of $FASnI_3$ excited at 730 nm with a fluence of 0.75 μJ cm^{-2}, showing both time- and energy-dependence. **A)** PL decay profiles measured at the peak of the emission spectrum, 1.41 eV, with both 0 ° polarization (green markers, detecting PL with polarisation parallel to that used for excitation) and 90 ° (blue markers, detecting perpendicular to the excitation polarisation). **B)** Time-resolved PL spectra measured at delay times between 0.3 ps and 300 ps after excitation as indicated in the legend. The 90 ° data (shown by point markers) have been scaled against the 0 ° data (shown by open circles) at the same delay time, working with the peak of the spectrum, to match the calculated ratio $I_\perp/I_\parallel$. **C)** PL polarisation anisotropy calculated from the decay profiles shown in panel A, for emission at 1.41 eV across the full range of delay times measured. Purple point markers show the calculated values, and a guide to the eye for zero anisotropy is included as a light grey solid line. **D)** PL polarisation anisotropy calculated across the full spectral range for each time delay as shown in panel B, using the same marker colour scheme. The calculated anisotropy data show the lack of dependence on emission energy, also expressed as a difference between emission and excitation energies. [Adapted with permission from *J. Phys. Chem. Lett.* 2019, 10, 20, 6018-6047 [225] Copyright 2019 American Chemical Society.]

organic cation, and its impact on lattice distortions connected to cation motion, is important to consider in explaining the observed timescale of polarisation memory for a given perovskite material. Experimental observations of cation reorientation in lead perovskites have found that reorientation of FA occurs an order of magnitude faster than MA reorientation, [283] which could then give a correspondingly more rapid fluctuation in lattice distortions leading to shorter-lived local polarisation and rapid loss of polarisation memory when FA is used rather than MA. This explanation would be consistent with the results presented here, but other reports predicting faster reorientation of MA than FA [284] and experimentally observing little difference in rate of reorientation between these two cations at room temperature [285] cast some doubt on its veracity. The true influence of the change in cation on polarisation memory in $FASnI_3$ compared to the lead halide perovskites previously studied is therefore uncertain, but the change from lead to tin likely contributes to the observed lack of persistent polarisation memory detected with 270 fs time resolution.

A further consideration previously suggested to account for differences in polarisation memory between MHP compositions is the symmetry of the perovskite lattice. For tetragonal $MAPbI_3$, polarisation memory over hundreds of picoseconds has been observed, and contrasted with the lack of apparent memory in the cubic structured mixed iodide-chloride or iodide-bromide compositions to conclude that higher lattice symmetry eliminates persistent polarisation anisotropy. [286] This hypothesis does not explain the observations of Rivett et. al., given that $MAPbBr_3$ is reported to be cubic at room temperature [171, 287] whereas $MAPbI_3$ and $CsPbI_3$ are not, but all three of these perovskites showed similar polarisation memory over picoseconds. [263] One complicating factor is that disorder in the orientation and position of organic cations can make distinguishing between cubic and pseudocubic lattice structures particularly difficult for MHPs. Considering $FASnI_3$ specifically, the structure at room temperature has been

variously assigned as either orthorhombic [126, 134, 201] or cubic [288, 289] and so there is not a clear explanation for the observed absence of persistent polarisation anisotropy from macroscale structural considerations. If it is the case that there are no structural contributions to polarisation memory either due to macroscale lattice symmetry or local distortions then the initial anisotropy following polarised excitation is expected to be lost through carrier-carrier scattering on a timescale significantly below the instrument response time of measurements reported here. This loss of anisotropy through scattering amongst the photoexcited carriers is a probable explanation for the lack of observable polarisation memory in the emission of $FASnI_3$, whatever the reason for a lack of influence from the lattice structure or its fluctuations.

5.3.3 Conclusions

This study of polarisation anisotropy in the photoluminescence of $FASnI_3$ thin films found no polarisation memory persisting beyond the system resolution of 270 fs. This result, in comparison to previous reports of polarisation memory lasting picoseconds or longer in several lead-based perovskites, indicates an absence of any slower-changing structural features coupling to the polarisation of excited charge carriers. It is possible that there are local lattice distortions in $FASnI_3$ which fluctuate too fast for corresponding polarisation memory to be observed, or that such distortions do not impact electronic structure regardless of timescale. In the latter case, a likely explanation for the difference between compositions is reduced spin-orbit coupling when tin is used as the B cation rather than lead.

5.4 Summary

This chapter explored charge-carrier cooling in $FASnI_3$, demonstrating that this process is dominated by relaxation over tens of picoseconds. The appearance of slow cooling from

a residual population of hot carriers extending over hundreds of picoseconds is explained by recombination-limited relaxation between energetically disordered states. The full lineshape model described in Chapter 4 was used to determine charge-carrier temperatures for this cooling study, demonstrating its intended application. Polarisation memory in the photoluminescence of $FASnI_3$ was also investigated, finding total loss of memory within a few hundred femtoseconds across the full emission energy range. These results demonstrate that excited charge carriers in $FASnI_3$ scatter freely with other carriers and with phonons, without screening effects to slow these processes. Local variations in the perovskite lattice are found to have effects on the energetic landscape that must be taken into consideration when interpreting cooling curves for excited carriers, but not to lead to any observable polarisation memory.

5.5 Future outlook

The study of charge-carrier cooling in $FASnI_3$ presented in this chapter illustrates the importance of careful interpretation of cooling dynamics when assessing the lifetime of hot carriers, and the prospects of perovskite materials for use in hot-carrier solar cells. The comparison of the experimentally determined cooling curve with overall recombination dynamics, which here reveals that the appearance of an unusually long-lived residual population of hot carriers arises instead from energetic disorder, should also be considered in future studies. Together with the use of the full lineshape model for temperature fitting that was demonstrated here, this would allow a more accurate assessment of the range of charge-carrier cooling times across perovskite compositions. The eventual results of such an assessment are likely to include greater consensus as to the mechanisms affecting carrier cooling and a reliable determination as to which compositions, if any, could be harnessed in hot-carrier solar cells.

The cooling time determined here for $FASnI_3$ is well below the suggested threshold of 1 ns for a high-efficiency hot-carrier solar cell, and so successful application of this perovskite composition in a hot-carrier device is unlikely. Future work comparing charge-carrier cooling between $FASnI_3$ samples with precise control over film quality and exposure to air could be of interest, however. Such a study could establish the extent to which energetic disorder exaggerates the apparent lifetime of hot carriers by comparison with the underlying cooling rate in films with varying degrees of tin oxidation and associated disorder.

Additional investigations into polarisation memory, combined with structural characterisation, would also be of interest. This study, finding rapid sub-picosecond PL polarisation memory loss in $FASnI_3$, has demonstrated significant differences in the persistence of polarisation memory between tin- and lead-based perovskite compositions that are not well explained by macroscale structure. Exploring whether differences in the dynamics of lattice distortion, or in the coupling of such distortion to electronic structure, are responsible for this difference is an avenue to deeper understanding of the properties of tin-containing perovskites important in next-generation photovoltaic applications.

6

Impact of Tin Fluoride Additive on the Properties of $FA_{0.83}Cs_{0.17}Sn_xPb_{1-x}I_3$ Perovskite Semiconductors

Contents

6.1 Motivation 105
6.2 Experimental details 106
6.2.1 Samples 106
6.2.2 X-ray diffraction measurement 108
6.2.3 Absorption and photoluminescence spectroscopy 108
6.2.4 Time-resolved photoluminescence measurement 109
6.2.5 Terahertz spectroscopy 110
6.2.6 Analysis 111
6.3 Results and discussion 114
6.3.1 Crystal structure 114
6.3.2 Background doping density 124
6.3.3 Photoluminescence lifetimes 126
6.3.4 Absorption and emission properties 128
6.3.5 Charge-carrier mobility 136
6.4 Conclusions 138
6.5 Future outlook 139

This chapter reveals the effects of the SnF_2 additive on the properties of $FA_{0.83}Cs_{0.17}Sn_xPb_{1-x}I_3$ perovskites across the full tin-lead compositional range. As discussed in Section 2.4.4, this additive is commonly used to prevent unwanted oxidation

of tin, but its impacts on mixed tin-lead perovskites of interest for tandem solar cell applications have until now been poorly understood. The study presented here identifies that addition of SnF_2 significantly reduces background hole doping density associated with the formation of tin vacancies. Consequently, photoluminescence lifetimes increase, energetic disorder decreases, Burstein-Moss shifts are reduced and charge-carrier mobilities improve, while tetragonal distortion in the perovskite structure resulting from strain caused by tin vacancies is also decreased. Beneficial effects on the optoelectronic properties of these tin-lead perovskites are found to be optimised by addition of 1 % SnF_2, with amounts of 5 % or more introducing additional, unwanted, non-radiative recombination pathways.

Work in this chapter is also published in reference [290]: Savill, K. J.; Ulatowski, A. M.; Farrar, M. D.; Johnston, M. B.; Snaith, H. J. and Herz, L. M., Adv. Funct. Mater., 2020, ***30****, 2005594*

6.1 Motivation

Mixed tin-lead perovskites are the leading choice of low-bandgap absorber for all-perovskite tandem solar cells, [14, 16] which offer high efficiencies beyond the single-junction limit with the environmental and cost benefits of using MHPs in place of a silicon absorber layer. [49, 169, 170] To realise further improvements in performance beyond the ∼25 % efficiency that has been achieved for all-perovskite tandem cells so far, [175, 176] an effective means to suppress the ready oxidation of tin [122, 177, 178] in tin-lead perovskites without compromising on other material properties is needed. While a wide range of additives, including ascorbic acid, [199] GuaSCN, [176] Cd^{2+} [100], ZnI_2 [291] and metallic tin, [175] have been used for this purpose the most common choice is SnF_2 either alone [150, 152, 180, 292–296] or in combination. [100, 175, 176, 291]

Despite this wide usage, the effects of SnF_2 have received thorough investigation only for neat tin perovskites. [141, 202, 203] Efforts to optimise the amount of SnF_2 additive in tin-lead perovskites for solar cell performance [297–299] identified different optimum amounts, and have not examined in depth the changes in material properties that contribute to performance differences. In most cases tin-lead perovskites for use as low-bandgap absorbers are prepared with 10 % SnF_2 added regardless of tin fraction, [152, 180, 292–296, 300, 301] this amount having been effective for neat tin perovskites. [141] A full understanding of the impact of SnF_2 additive on the properties of mixed tin-lead perovskites with varying tin content, and identification of the optimal amount of additive to effectively prevent tin oxidation for different mixed compositions, are clearly needed to provide a rational foundation for further improvement in devices using tin-lead perovskite absorber layers.

6.2 Experimental details

6.2.1 Samples

Thin films of $FA_{0.83}Cs_{0.17}Sn_xPb_{1-x}I_3$ were prepared by Michael D. Farrar (Department of Physics, University of Oxford) using the following method.

Solution preparation Two precursor solutions ($FA_{0.83}Cs_{0.17}PbI_3$ and $FA_{0.83}Cs_{0.17}SnI_3$ both 1.2 Molar) were prepared 12 hours before sample fabrication, in mixed DMF:DMSO solvent with volumetric ratio 4:1. A 3.5 mL $FA_{0.83}Cs_{0.17}PbI_3$ solution with tin fraction 0: 599.49 mg of formamidinium iodide (FAI, Greatcell solar), 185.50 mg of caesium iodide (CsI, Alfa Aesar) & 1936.24 mg lead (II) iodide (PbI_2, Alfa Aesar, 99.999 % mesh beads). A 3 mL $FA_{0.83}Cs_{0.17}SnI_3$ solution with tin fraction 1: 513.85 mg of FAI, 159.00 mg of CsI, 1341.07 mg of tin (II) iodide (SnI_2, Alfa Aesar, 99.999 % mesh beads) & tin (II) fluoride (SnF_2, Sigma Aldrich) corresponding to 0, 0.1, 1, 5, 10 or 20 mol % for the different

additive conditions. These two solutions were then mixed in the manner detailed in Table 6.1 to give the desired Sn fraction at each SnF_2 content.

Tin fraction, x	$FA_{0.83}Cs_{0.17}PbI_3$ (μL)	$FA_{0.83}Cs_{0.17}SnI_3$ (μL)
1	0	500
0.9	50	450
0.8	100	400
0.7	150	350
0.6	200	300
0.5	250	250
0.4	300	200
0.3	350	150
0.2	400	100
0.1	450	50
0	500	0

Table 6.1: Volumes of each of the two precursor solutions used to prepare $FA_{0.83}Cs_{0.17}Sn_xPb_{1-x}I_3$ thin films with varying tin fraction, x. Note that as SnF_2 is added to the $FA_{0.83}Cs_{0.17}SnI_3$ solution only and samples at $x = 0$ are prepared with none of this precursor solution, the actual SnF_2 content for samples at $x = 0$ is always 0 %, independent of the SnF_2 percentage added for a given set of samples.

Sample fabrication Z-cut quartz substrates were prepared by sonicating sequentially in Decon 90 detergent (1 % vol. in deionised (DI) water), DI water, acetone and ethanol for 10 minutes, followed by O_2 plasma treatment for 15 minutes. Films were prepared on these quartz substrates using a single step anti-solvent quenching method in a nitrogen filled glovebox ($H_2O \leq 0.1$ ppm, $O_2 \leq 1.0$ ppm). 20 µL of the required solution, prepared from precursors as in Table 6.1, was dispensed onto a static substrate and spun at 4000 rpm with an acceleration of 500 rpm for a total of 60 seconds. At 35 s 100 μL of anisole was dispensed into the center of the substrate at a height of roughly 5 mm from the surface in a steady stream, taking around 1 second to fully dispense. Films with tin fraction 0.7 or less turned amber when the anisole was introduced, getting progressively darker from $x = 0 - 0.7$. Films containing tin fraction 0.8 and above turned very dark brown to black instantly. Substrates were then transferred straight onto a hotplate and annealed for 10 minutes at 100 °C resulting in specular black films across the range of

tin fractions. All film preparation parameters were kept constant for each sample. After annealing, all samples were stored in a nitrogen filled glovebox.

6.2.2 X-ray diffraction measurement

XRD patterns for $FA_{0.83}Cs_{0.17}Sn_xPb_{1-x}I_3$ thin films on z-cut quartz substrates, and a blank quartz substrate for reference, were obtained using a PANalytical X'Pert PRO Powder X-Ray Diffractometer as described in Section 3.4. For each measurement a scan speed of $0.0088\,^\circ s^{-1}$ was used, covering diffraction angles 2θ from $10 - 54.5\,^\circ$. To correct for variations in sample tilt, the highest intensity z-cut quartz peak present in every measured XRD pattern was used as a reference and set to $2\theta = 50.66\,^\circ$. Each sample was transferred from the glovebox in an individual vacuum sealed bag to minimise exposure to air before starting the XRD measurement, which was the last measurement carried out for any given sample so that any degradation under ambient atmosphere in the diffractometer would not influence other results.

6.2.3 Absorption and photoluminescence spectroscopy

Absorbance spectra As described in Section 3.3, reflectance and transmittance spectra for $FA_{0.83}Cs_{0.17}Sn_xPb_{1-x}I_3$ thin films on z-cut quartz substrates were measured using a Bruker Vertex 80v Fourier-transform infrared spectrometer with a tungsten halogen lamp source, CaF_2 beamsplitter and Si diode detector. Reference spectra were measured with the sample position empty for transmittance, and with a UV-protected silver mirror (Thorlabs) in the sample position for reflectance, and Napierian absorbance was calculated from reference-corrected data as $A = -\ln(T/(1-R))$. Samples were transported under nitrogen before and after measurements, and spectra measured under low vacuum with pressure less than 3 mbar.

Photoluminescence spectra Time-integrated PL spectra were measured using the setup shown in Figure 3.1 with both Si CCD and InGaAs array detectors. $FA_{0.83}Cs_{0.17}Sn_xPb_{1-x}I_3$ thin film samples were excited using a 532 nm continuous-wave laser (ventus, Laser Quantum) at an intensity of $1.8 \pm 0.1\,\mathrm{W\,cm^{-2}}$ and PL was focussed into a grating monochromator (iHR 320, Horiba) and then directed onto each detector via a movable mirror. Long-pass filters were used to reduce background detection, and the measured spectra were corrected for spectral response of the detector as described in Section 3.1.2 before combining data from both detectors as described in Section 3.1.2.1. Samples were transported in a sealed vacuum cell, loading and unloading inside the nitrogen-filled glovebox used for storage, and were kept under vacuum during measurements with continuous pumping to maintain pressure of 10^{-2} mbar or below.

6.2.4 Time-resolved photoluminescence measurement

Time-correlated single photon counting measurements were carried out on two setups as described in Section 3.2.2.2. In each case, samples were excited at 405 nm using two different fluences, with neutral density filters used to attenuate laser power for the lower fluence condition, and long-pass filters in the PL path used to reduce background from the excitation beam. A sealed vacuum cell was used to transport samples, loading and unloading inside the nitrogen-filled glovebox used for storage, and during measurements samples were kept under vacuum with continuous pumping to maintain pressure of 10^{-2} mbar or lower.

Primary setup Using the system shown in Figure 3.7, with time resolution of 0.70 ns for TCSPC measurements, samples were excited with a pulsed diode laser (PicoQuant, LDH-D-C-405M) at fluences of $0.50 \pm 0.01\,\mu\mathrm{J\,cm^{-2}}$ (high) and $59 \pm 1\,\mathrm{nJ\,cm^{-2}}$ (low). The repetition rate of the laser was set at 10 MHz, or 5 MHz for the neat lead samples ($x = 0$) that exhibited the slowest PL decay. Sample PL was collected and coupled

into a grating spectrograph (Princeton Instruments, SP-2558), then directed onto a single photon avalanche diode detector (PDM series from MPD), with timing controlled by a PicoHarp300 TCSPC event timer.

Higher time-resolution setup For samples at high tin fraction with very short PL lifetimes, the system shown in Figure 3.5 was used for TCSPC measurements with time resolution of 57 ps. Samples were excited using a Ti:Sapphire laser (Mai Tai, Spectra Physics) with 80 MHz repetition rate, at fluences of 0.48 ± 0.1 μJ cm^{-2} (high) and 51 ± 10 nJ cm^{-2} (low). Sample PL was focussed into a grating monochromator (Triax, Horiba) and then directed onto a silicon single photon avalanche diode detector (PDM series from MPD). A gate beam split off from the excitation laser and directed onto a photodiode was used as the trigger pulse for timing.

6.2.5 Terahertz spectroscopy

Terahertz spectroscopy measurements were conducted by Aleksander M. Ulatowski (Department of Physics, University of Oxford) using the following method.

Temporal changes in photoconductivity were measured with an Optical-pump–THz-probe (OPTP) setup as described in previous publications. [92, 94, 302] $FA_{0.83}Cs_{0.17}Sn_xPb_{1-x}I_3$ thin films were photoexcited with 35 fs laser pulses originating from an 800 nm Ti-Sapphire laser system (Spectra Physics, Mai Tai - Ascend - Spitfire Ti-Sapphire regenerative amplifier, 5 kHz repetition rate), frequency doubled to 400 nm using a BBO crystal. Excitation fluence was varied between 1.33 and 22.5 μJ cm^{-2} using a variable ND filter wheel.

The photoconductivity of the films was calculated using the transmission data of the terahertz pulse probe through photoexcited samples (see Section B.2). The THz pulse was generated with a spintronic emitter (2 nm tungsten, 1.8 nm $Co_{40}Fe_{40}B_{20}$, 2 nm platinum on quartz substrate) [303] and the field strength transmitted through the

sample was measured using electro-optic sampling in a non-linear crystal (1 mm thick (110)-ZnTe). The THz pulse and gate pulse (800 nm, 35 fs, originating from the same laser system as the pump beam) were overlapped inside the ZnTe crystal and the change in polarisation of the gate beam (proportional to THz field strength) was measured using a quarter-wave plate, polarising prism and balanced photodiode detector. The time delay between the pump pulse and THz probe was controlled using optical delay stages. The pump beam was blocked using an optical chopper for every second THz pulse in order to obtain the THz transmission difference through the sample with and without photoexcited charge carriers present.

Dark conductivity spectra were acquired with the same laser setup used for OPTP measurement, without the use of the photoexcitation beam. The time-domain shape of the THz pulse transmitted through the sample was measured by changing the time-delay between the gate pulse and the THz probe using optical delay stages. A bare z-cut quartz substrate was used as a reference. [304] Dark conductivity was then calculated from the THz pulse transmission data, as described in Section B.2.

Samples were transported under nitrogen to minimise exposure to air, and both OPTP and dark conductivity measurements were conducted in a vacuum box under pressure $< 10^{-1}$ mbar.

6.2.6 Analysis

Key details of the methods used to analyse data from absorption and time-resolved photoluminescence measurements to obtain the results discussed in Section 6.3 are given here. Appendix B contains further detail on the analysis of data from terahertz measurements, which was conducted by Aleksander M. Ulatowski.

6.2.6.1 Photoluminescence lifetimes

Photoluminescence decay transients, measured as described in Section 6.2.4, were each fitted with a stretched exponential of the form given by Equation 6.1:

$$I(t) = A \exp\left(-\left(\frac{t}{k}\right)^{\beta}\right) \tag{6.1}$$

where β is a stretching parameter with value equal to 1 in the case of a monoexponential decay, taking smaller values as stretching increases. With this model, which has long been used to analyse PL decay transients for lead-based perovskites, [99, 305–307] the effective PL lifetime τ_{eff} can then be calculated according to Equation 6.2:

$$\tau_{\text{eff}} = \frac{k}{\beta}\Gamma\left(\frac{1}{\beta}\right) \tag{6.2}$$

Measured PL decay transients and stretched exponential fits for a representative set of samples across the compositional range are shown in Figure 6.1. In each case the range used in fitting extended from 0.8 ns after the intensity peak of the measured transient, an offset chosen to ensure that slight positive curvature of many decay transients near the peak would not influence the fits, to 1 % of the maximum intensity so that the very noisy data at later times would also be excluded. This figure illustrates both the large range of lifetimes between samples, and the variation in decay dynamics from close to monoexponential (appearing linear on the semilog scale in Figure 6.1) to significantly stretched that makes Equation 6.1 an appropriate choice of model to fit.

6.2.6.2 Absorption onsets

To analyse trends in the optical bandgap of $FA_{0.83}Cs_{0.17}Sn_xPb_{1-x}I_3$ samples, the absorption onset energy was determined from measured absorbance spectra, taken to be the point in the onset region of the absorbance spectrum at which the gradient is steepest. This steepest gradient method was previously identified as giving more physically sensible

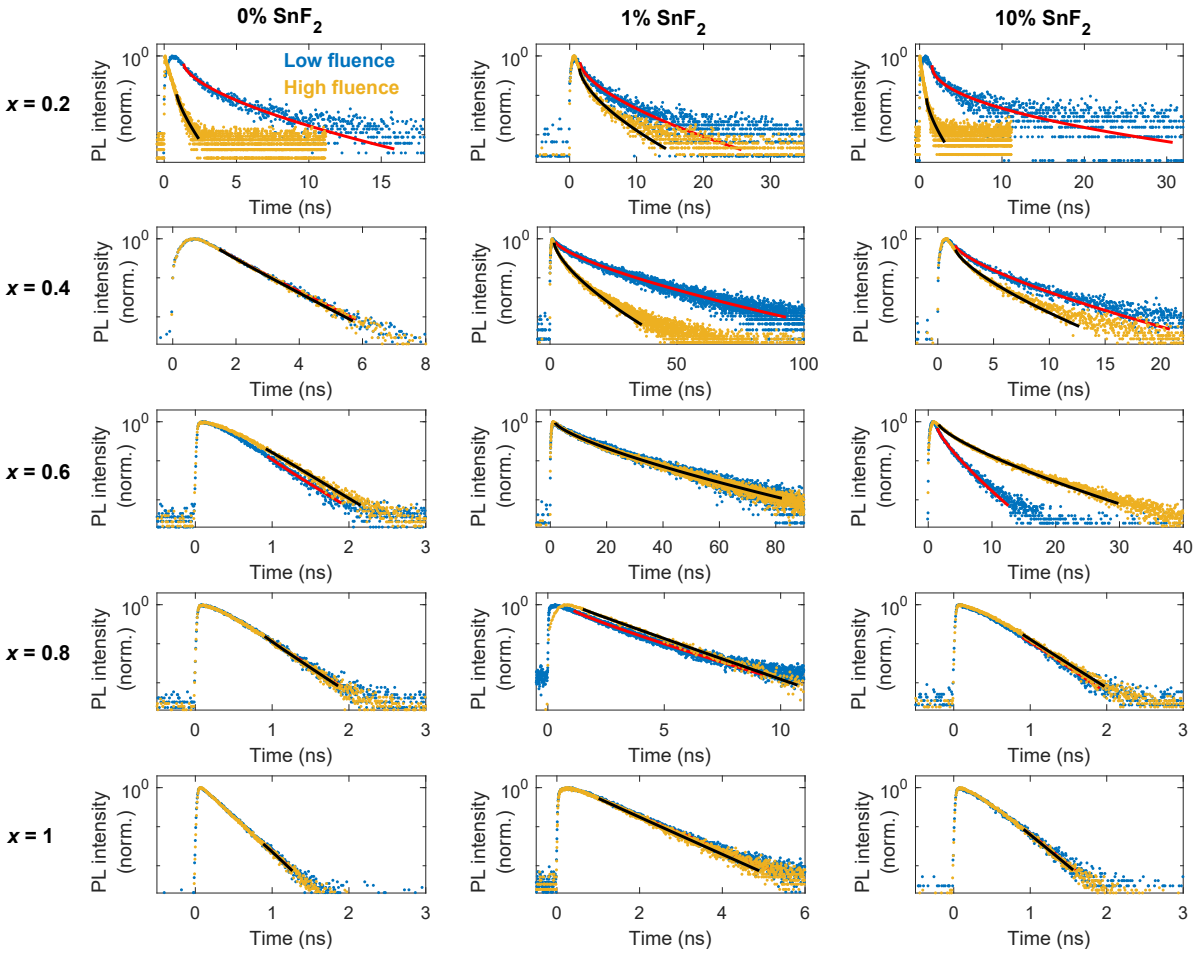


Figure 6.1: Measured PL decay transients, with stretched exponential fits, for $FA_{0.83}Cs_{0.17}Sn_xPb_{1-x}I_3$ thin films on z-cut quartz at a representative range of tin fractions x and SnF_2 percentages as indicated. Samples were excited at 405 nm, with (average) fluence of 59 nJ cm^{-2} in the low fluence case (data shown as blue point markers, fitted curves as red solid lines) and 500 nJ cm^{-2} in the high fluence case (data shown as gold point markers, fitted curves as black solid lines). For each sample, PL decay transients were measured at the PL peak energy determined from time integrated PL spectra.

results than the use of a Tauc plot [308] that ignores any influence of excitons, while still being suitable for cases where fitting with the full formula from Elliott theory [309] is impractical given scatter and reflection from the samples of interest. [145] The process applied to determine absorption onset by the steepest gradient method is illustrated in Figure 6.2 for a representative example spectrum (at $x = 0.6$), showing the existence of a clear gradient maximum (panel B) over the onset region, and illustrating the position of this steepest point on the absorbance spectrum in panel A.

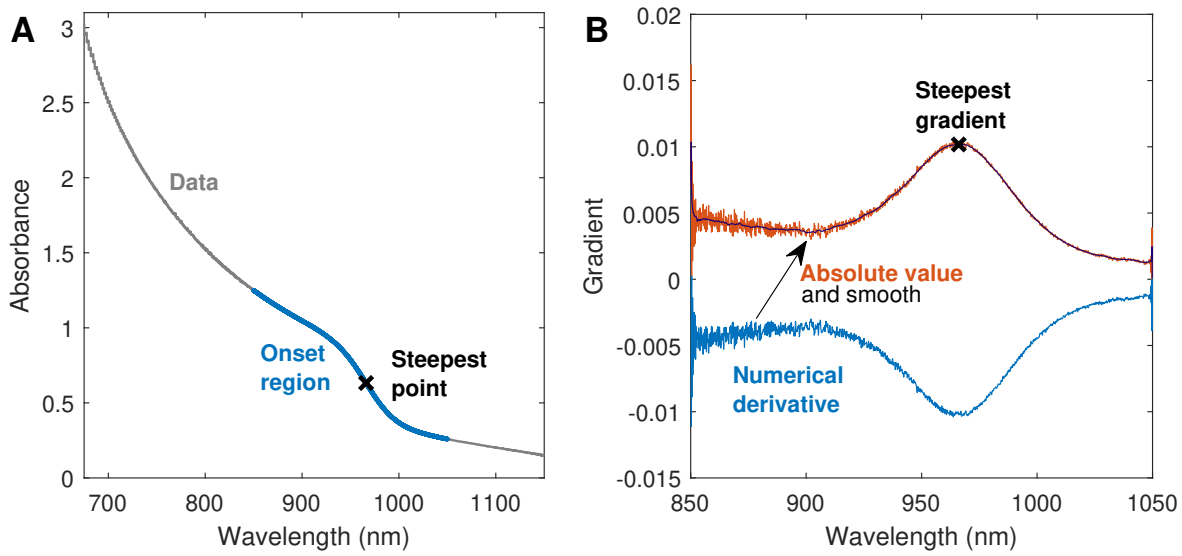


Figure 6.2: Illustration of the steepest gradient method used to determine absorption onset energy from absorbance spectra. **A)** Measured absorbance spectrum of $FA_{0.83}Cs_{0.17}Sn_{0.6}Pb_{0.4}I_3$ thin film on z-cut quartz substrate, prepared with 5 % SnF_2 added to the tin precursor solution, showing the spectral range near to the onset of absorption. The identified steepest gradient point is indicated by a black × marker, with the onset region differentiated to identify this point as in panel B shown in blue. **B)** Gradient of the absorbance onset region identified in panel A, as determined by numerical differentiation, showing the maximum point identified after smoothing as a black × marker.

6.3 Results and discussion

6.3.1 Crystal structure

6.3.1.1 XRD peak identification

To identify the crystal structure of $FA_{0.83}Cs_{0.17}Sn_xPb_{1-x}I_3$ samples with varying composition, measured XRD patterns were analysed. Figure 6.3A compares measured patterns for samples with varying tin fraction and SnF_2 addition against reference data for the precursor materials and other likely degradation products on exposure to oxygen and moisture (see Section B.1). The strongest non-perovskite peaks present in each measured XRD pattern are shown to be z-cut quartz peaks, while a weak lead iodide peak is seen for tin fraction $x = 0$ but not at higher tin fractions. Additionally, a broad peak that appears in the measured pattern for the neat tin ($x = 1$) sample with 0.1 % SnF_2

added at $2\theta \approx 26\,^\circ$ can be assigned to tin fluoride, which has the most closely matched peak of the likely impurities. These non-perovskite peaks are marked by dashed lines in Figure 6.3A. The remaining strong peaks in the measured XRD patterns are identified as originating from the perovskite material, with the solid vertical lines in the figure that mark their position not intersecting any likely impurity peaks. These perovskite peaks are well-defined, indicating that the samples are all highly crystalline in addition to containing few detectable impurities.

Further examination of the perovskite peaks identified in Figure 6.3A allows crystal structure to be identified, and individual peaks assigned with Miller indices. Tin-lead perovskites previously studied have often been identified as either (pseudo)cubic or tetragonal in structure, with tetragonal distortion observed to vary with tin fraction [60, 135, 143] or cation substitution. [144] It is therefore interesting to compare the observed peaks for $FA_{0.83}Cs_{0.17}Sn_xPb_{1-x}I_3$ thin films with the expected peak positions for a cubic or tetragonal structure with lattice constant/s determined from measured data, as shown in Figure 6.3B.

For a cubic crystal structure with lattice parameter a, Equation 6.3 predicts the position 2θ of diffraction peaks given the corresponding Miller indices hkl and the wavelength λ of the X-ray source, which in this case is $\lambda = 15.40598\,\text{nm}$:

$$\sin^2\theta = \frac{\lambda^2}{4a^2}(h^2 + k^2 + l^2) \tag{6.3}$$

Equivalently for a tetragonal structure, in which distortion away from cubic symmetry along one axis leads to a lower symmetry unit cell described by two lattice parameters a and c, peak positions are given by Equation 6.4:

$$\sin^2\theta = \frac{\lambda^2}{4}\left(\frac{h^2 + k^2}{a^2} + \frac{l^2}{c^2}\right) \tag{6.4}$$

To calculate the full set of expected peak positions for each likely crystal structure using Equations 6.3 and 6.4, lattice parameter values were first determined with reference

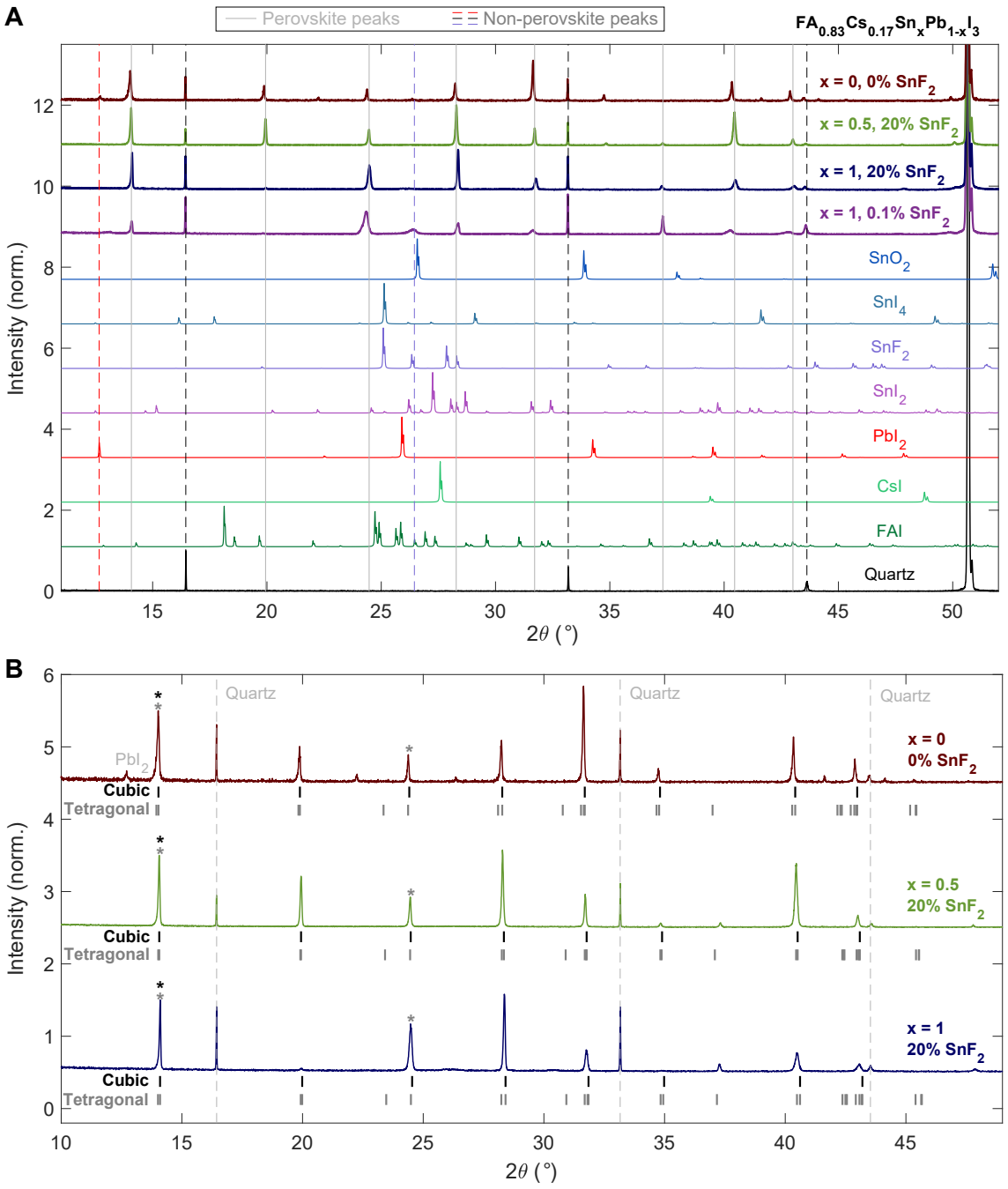


Figure 6.3: Identification of measured XRD peaks. **A)** Comparison of measured patterns against reference data for likely impurities. Measured patterns for $FA_{0.83}Cs_{0.17}Sn_xPb_{1-x}I_3$ thin films on z-cut quartz (thick solid lines) are labelled with tin fraction x and SnF_2 percentage added to the tin precursor solution. Reference XRD patterns (thin solid lines) for precursors and tin oxidation products as labelled were obtained from literature (see Table B.1). The quartz pattern was measured using a blank substrate. Notable non-perovskite peaks in the measured patterns are marked by dashed lines, colour coded by material. Grey solid lines mark perovskite peaks without counterparts in any reference pattern. **B)** Measured XRD patterns for $FA_{0.83}Cs_{0.17}Sn_xPb_{1-x}I_3$ thin films on quartz with tin fraction x and SnF_2 percentage as labelled, and calculated peak positions for cubic or tetragonal structure marked below each pattern by black and dark grey lines respectively. Measured peaks used to determine the lattice parameter/s and calculate peak positions are marked by black or dark grey asterisks.

$FA_{0.83}Cs_{0.17}Sn_xPb_{1-x}I_3$ sample	(100) peak 2θ (°)	a (nm)
$x = 0$, 0 % SnF_2	14.029	63.077
$x = 0.5$, 20 % SnF_2	14.062	62.928
$x = 1$, 20 % SnF_2	14.096	62.780

Table 6.2: Cubic lattice parameters calculated from measured XRD patterns according to Equation 6.3 for an example set of $FA_{0.83}Cs_{0.17}Sn_xPb_{1-x}I_3$ thin film samples spanning the range of tin fractions.

to the peaks marked by asterisks in Figure 6.3B. By comparison with previously reported XRD patterns for related pseudocubic MHPs, [143, 144] the peak at $2\theta \approx 14\,^\circ$ in each of the measured XRD patterns was identified as the (100) peak for a cubic structure, giving the calculated values of a shown in Table 6.2 for the compositions represented in Figure 6.3B. The black vertical markers beneath each measured pattern in this figure show the expected cubic peak positions calculated using the values of a in Table 6.2 for each (degenerate) set of Miller indices. These calculated peak positions each agree well with an experimentally observed perovskite peak, although there is one diffraction peak at $2\theta \approx 37\,^\circ$ in the measured XRD patterns for higher tin fraction samples that does not correspond to a predicted cubic peak.

Considering tetragonal crystal structure, the measured perovskite peaks near to 14 ° and 24 ° (marked with grey asterisks in Figure 6.3B) were identified as corresponding to tetragonal (110) and (022) peaks respectively by comparison to the simulated XRD patterns for cubic and tetragonal $MAPbI_3$ given by Jacobsson et al. [310] Solving Equation 6.4 simultaneously for these two peaks then gave the lattice parameter values shown in Table 6.3, following from which the full set of expected diffraction peak positions (corresponding to Miller indices that satisfy $h + k + l = 2n$ for some integer n) is as shown by dark grey vertical markers in Figure 6.3B. Each of the observed perovskite peaks corresponds to a predicted tetragonal structure diffraction peak, including the otherwise unexplained peak at $2\theta \approx 37\,^\circ$ that can be assigned as the (231) tetragonal peak. However, there are also several predicted tetragonal diffraction peaks that do not

$FA_{0.83}Cs_{0.17}Sn_xPb_{1-x}I_3$ sample	(110) peak 2θ (°)	(022) peak 2θ (°)	a (nm)	c (nm)
$x = 0$, 0 % SnF_2	14.029	24.373	89.205	126.91
$x = 0.5$, 20 % SnF_2	14.062	24.457	88.994	126.23
$x = 1$, 20 % SnF_2	14.096	24.490	88.784	126.32

Table 6.3: Tetragonal lattice parameters calculated from measured XRD patterns according to Equation 6.4 for an example set of $FA_{0.83}Cs_{0.17}Sn_xPb_{1-x}I_3$ thin film samples spanning the range of tin fractions.

have any clear counterpart in the measured XRD patterns, which may indicate that the dominant structure is very close to cubic. These include the (121) peak near 23.5 °, the (123) peak near 31 °, and the clusters of peaks around 42 ° and above 45 °. None of the absent peaks originate from the same set of crystal planes as the (231) peak, so that assignment is not contradicted by these absences and non-random orientation of crystallites in the film leading to absences for certain sets of planes could also play a role.

Overall, the comparison to calculated peak positions illustrated in Figure 6.3B supports assignment of the $FA_{0.83}Cs_{0.17}Sn_xPb_{1-x}I_3$ crystal structure as pseudocubic, but with tetragonal distortion seen for some compositions. This effect, and the relationship between structure and composition, is explored further below.

6.3.1.2 Effects of tin fraction and SnF_2 additive on crystal structure

The measured X-ray diffraction patterns of $FA_{0.83}Cs_{0.17}Sn_xPb_{1-x}I_3$ thin films show two significant trends in crystal structure as sample composition changes. First, tetragonal distortion of the pseudocubic lattice occurs at moderate to high tin fraction when no SnF_2 is added, with the addition of 20 % SnF_2 suppressing this effect. Second, lattice constants decrease as tin fraction and SnF_2 content increase, shifting diffraction peaks to higher angle.

These effects can be clearly seen in Figure 6.4 which illustrates the influence of composition on three of the highest intensity perovskite XRD peaks, identified as the (100) and (111) pseudocubic structure peaks and the tetragonal (231) peak. In panel A of

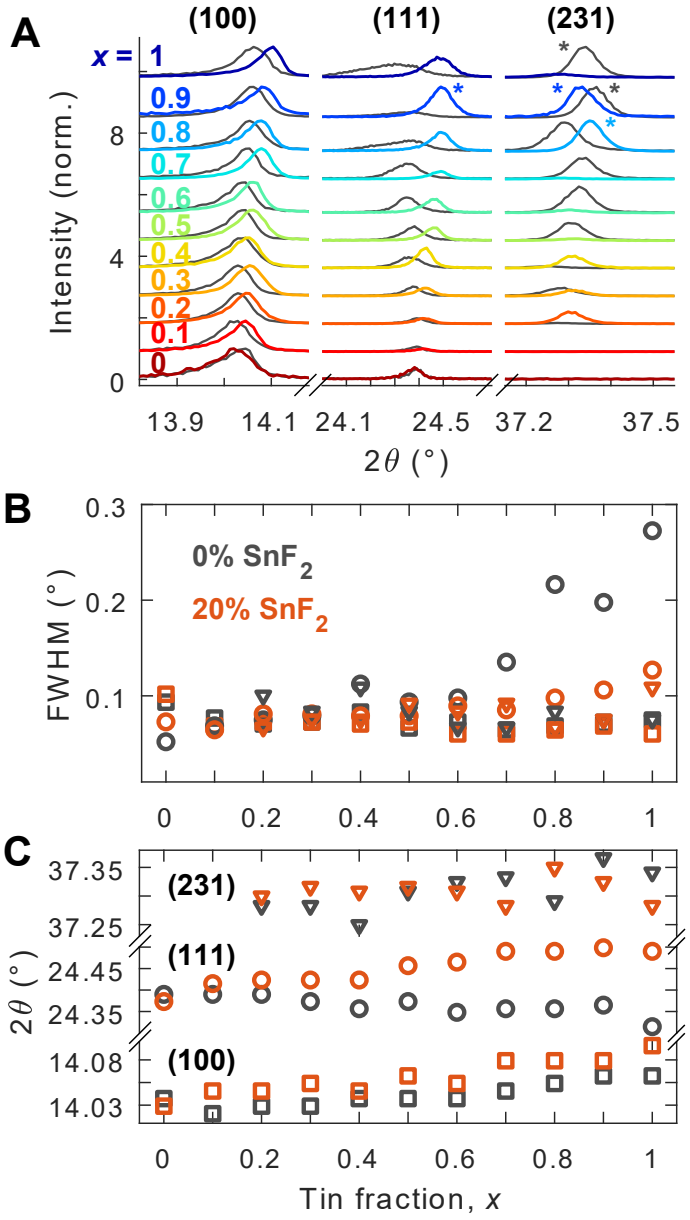


Figure 6.4: Effect of tin fraction and SnF_2 additive on the crystal structure of $FA_{0.83}Cs_{0.17}Sn_xPb_{1-x}I_3$ thin films on z-cut quartz, prepared with varying tin fraction x and either 0 % or 20 % SnF_2 added to the tin precursor solution. Data are shown for three diffraction peaks of interest: pseudocubic (100) and (111), and tetragonal (231), as marked. **A)** Normalised XRD patterns, showing three significant peaks for varying tin fractions as marked on the figure. Data for the 0 % SnF_2 condition are shown in dark grey, with data for the 20 % SnF_2 condition overlaid in colour. Vertical offsets have been added for clarity, and in all cases normalisation is to the peak near 14 ° (cubic (100)). The peak intensities near 24.4 ° and 37.3 ° are preserved relative to the (100) peak, except where marked with *, in which case the higher angle peaks are more intense and have been separately normalised in the figure. **B, C)** FWHM and position of the diffraction peaks illustrated in panel A, showing significant impact of SnF_2 addition on the (111) peak in particular. Data for the 0 % SnF_2 condition are shown in dark grey, and for 20 % SnF_2 in orange, as indicated in panel B. Square markers correspond to the (100) peak, circle markers to the (111) peak, and triangle markers to the tetragonal (231) peak, as indicated in panel C. [Reproduced with permission from *Adv. Funct. Mater.* 2020, **30**, 2005594 [290] Copyright 2020 John Wiley and Sons.]

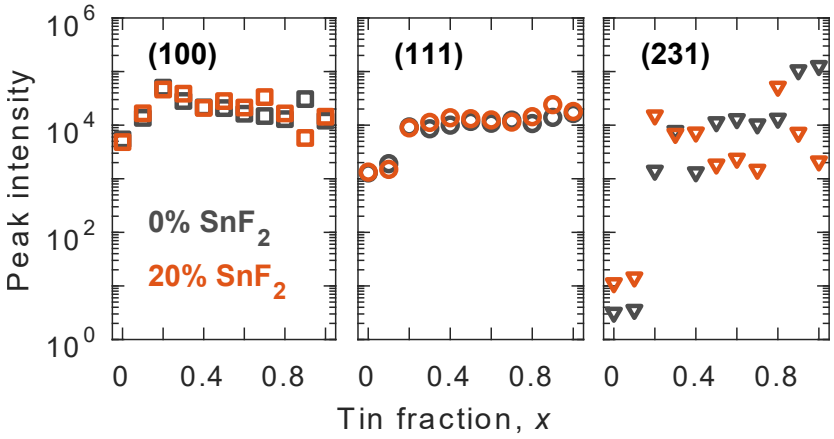


Figure 6.5: Intensity of the three XRD peaks of interest, as shown in Figure 6.4A, for $FA_{0.83}Cs_{0.17}Sn_xPb_{1-x}I_3$ thin films on z-cut quartz substrate, with either 0 % (dark grey) or 20 % (orange) SnF_2 added to the tin precursor solution during preparation. Intensity is calculated as the integral under each peak, and shows substantial variation with SnF_2 addition and tin fraction for the tetragonal (231) peak, whereas composition has little effect on intensity of the pseudocubic (100) and (111) peaks.

this figure, dark grey lines show these diffraction peaks for samples with 0 % SnF_2 added, and coloured lines are used for the 20 % SnF_2 condition. The (100) peak, to which data are normalised, is typically the strongest perovskite peak in the measured diffraction pattern, but the (231) peak increases in intensity as tin fraction increases and for many samples with tin fraction $x \geq 0.8$ this tetragonal peak dominates, and so is separately normalised in Figure 6.4A as indicated by an asterisk. The trend of increasing (231) peak intensity with tin fraction is particularly pronounced for samples without SnF_2 added and holds after accounting for broadening of diffraction peaks, as shown by the integrated intensities in Figure 6.5. For tin fraction $x \leq 0.1$, no (231) peak is present and the integral under this region of the diffraction pattern is correspondingly small.

Figure 6.4B quantifies the broadening of diffraction peaks, which can be seen in panel A of the figure to increase with tin fraction for the pseudocubic (111) peak when no SnF_2 is added, as the full width at half maximum for each peak of interest. The FWHM of the pseudocubic (100) peak (shown by open square markers) and the tetragonal 231 peak (shown by open triangle markers) show little variation across the range of tin fractions

either with 0 % SnF_2 (dark grey) or 20 % SnF_2 (orange) added. This suggests there is little variation in structural disorder with composition. By contrast, the FWHM of the (111) peak changes very little for $x = 0 - 0.6$, then dramatically increases at higher tin fractions when no SnF_2 is added. With addition of 20 % SnF_2, broadening of the (111) peak is greatly reduced with only a slight increase in FWHM seen for $x \geq 0.9$.

This apparent anomalous broadening of the (111) diffraction peak is explained by tetragonal distortion of the crystal lattice at high tin fractions, leading to peak splitting that cannot be resolved within the measurement limit and thus appears as broadening. As the calculated peak positions in Figure 6.3B illustrate, there is a particularly large separation in angle between the closest equivalent tetragonal peaks to the cubic (111) peak, so that increasing lattice distortion will significantly broaden the (111) peak towards low angles until the two tetragonal peaks can be separately resolved. The observed trends in broadening, which coincide with the increasing prominence of the tetragonal (231) peak over the same compositional range, are therefore indicative of distortion away from the pseudocubic crystal structure as tin fraction increases in the absence of SnF_2. This distortion is attributable to the formation of tin vacancies in the lattice following oxidation of Sn^{2+}. [195, 311] Lattice vacancies can induce strain and consequently distortion towards a lower symmetry structure, as previously observed when vacancies are introduced into lead-based perovskites along with intentional doping. [312, 313] When no SnF_2 is added, samples with higher tin fraction have a correspondingly higher density of Sn^{2+} vacancies that lead to greater lattice distortion, evidenced here by greater broadening of the pseudocubic (111) peak and increasing strength of the tetragonal (231) peak for these compositions. With 20 % SnF_2 added during preparation, oxidation of tin is suppressed and the formation of tin vacancies with accompanying background hole doping is reduced, so that the less-distorted pseudocubic crystal structure remains dominant even at high tin fractions. For samples with low tin fraction, most metal sites are occupied by either

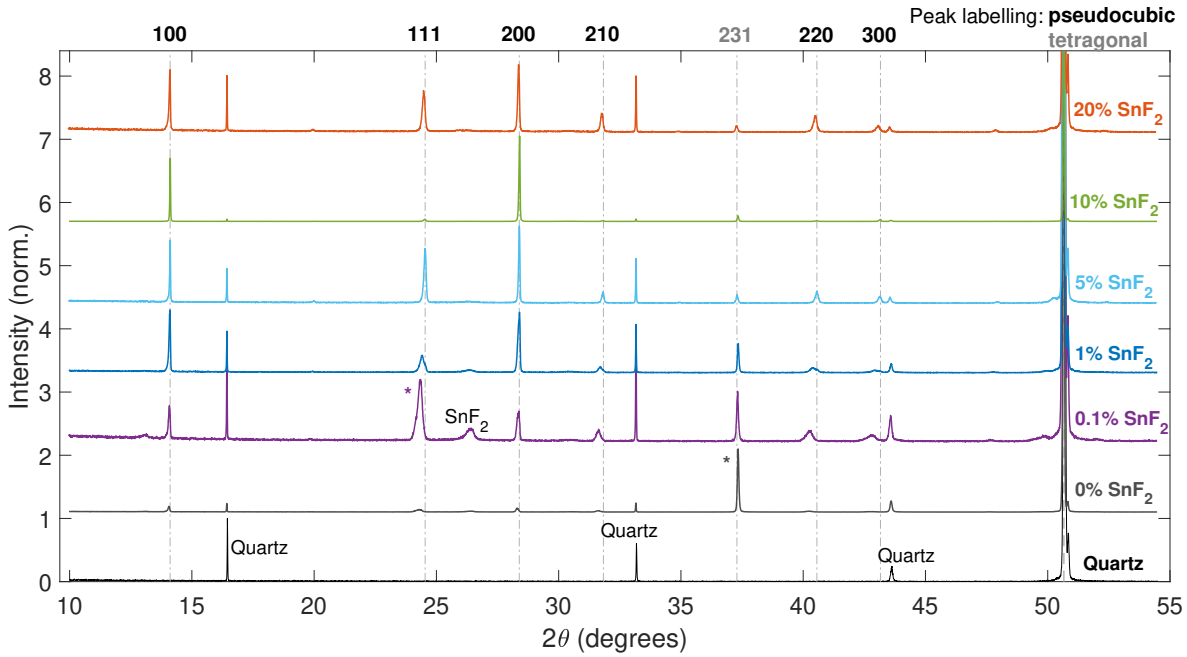


Figure 6.6: Measured XRD patterns for $FA_{0.83}Cs_{0.17}SnI_3$ (tin fraction $x = 1$) thin films on z-cut quartz substrate, with amounts of SnF_2 ranging from 0 % to 20 % added to the tin precursor solution during preparation as labelled. Sample diffraction patterns are normalised to the (100) peak, except for the 0.1 % and 0 % SnF_2 cases where the (111) peak and (231) peak respectively are much stronger and normalisation is to these peaks as marked by an asterisk for ease of display. The measured XRD pattern of a blank z-cut quartz substrate is also shown in black at the bottom of the figure. Light grey dash-dot vertical lines are included as a visual reference to mark the perovskite diffraction peaks and allow shifts in peak position to be seen more easily.

Pb^{2+} or Sn^{2+} and there are relatively few tin vacancies even when no SnF_2 has been added, evident in the lack of significant tetragonal distortion.

The trends in diffraction peak position shown in Figure 6.3C further reflect the role of SnF_2 in reducing lattice strain and distortion caused by tin vacancies. In the absence of SnF_2 the (111) peak appears to shift to slightly lower angle as tin fraction increases, whereas with 20 % SnF_2 added increasing diffraction angle with increasing tin fraction is seen, consistent with the trend for the other peaks. The anomalous behaviour seen for the 0 % SnF_2 condition is consistent with peak splitting, where the emerging lower-angle tetragonal peak appears as broadening and obscures any shift of the pseudocubic (111) peak to higher angle. The overall trend of peak position shifting to higher angle with increasing tin fraction, which is recovered for the (111) peak on addition of 20 % SnF_2,

has been reported previously for a range of tin-lead iodide perovskites. [143, 148, 314] The origin of such a shift is lattice contraction on replacing Pb^{2+} with Sn^{2+} which has a smaller ionic radius; the lattice parameters calculated from measured peak position in Table 6.2 reflect this. Further to this expected peak shift with tin fraction, addition of SnF_2 is here found to shift the observed peak position to higher angle, most clearly seen in Figure 6.3 for the (100) peak. This behaviour can be attributed to a greater propensity for Sn^{2+} ions to be incorporated into the perovskite lattice when SnF_2 is added, particularly in amounts as large as 20 mol %, that may result in higher stoichiometric tin fraction than intended and a corresponding reduction in the lattice parameter.

The effects of SnF_2 illustrated in Figure 6.4 for 20 % SnF_2 in comparison to no additive are also evident for intermediate amounts of SnF_2, as illustrated in Figure 6.6 for samples with tin fraction $x = 1$. As increasing amounts of SnF_2 are added, the intensity of the (231) peak decreases and the (111) peak becomes less broadened, along with small shifts to higher angle for each of the perovskite peaks. The extent of tetragonal distortion with 10 % SnF_2 cannot easily be assessed, as the measured pattern is instead indicative of a highly oriented film in which diffraction from the (100) crystal planes is dominant, but already for 0.1 %, 1 % and 5 % SnF_2 progressive reductions in distortion are evident.

These results demonstrate that the role of SnF_2 in preventing formation of tin vacancies has a significant impact on perovskite crystal structure by reducing lattice strain and accompanying tetragonal distortion. Broadening of the pseudocubic (111) peak, and intensity of the tetragonal (231) peak if present, are found to be strong indicators of the extent of tetragonal distortion that can be used to monitor the material quality of tin-containing perovskites.

6.3.2 Background doping density

Quantifying the background hole doping density of $FA_{0.83}Cs_{0.17}SnI_3$ thin films gives a direct indication of how thoroughly oxidation of tin is suppressed by addition of varying amounts of SnF_2. The hole doping density can be determined from terahertz dark conductivity spectra that capture the response of free charge carriers as well as that of vibrational modes of the lattice. For samples with high background doping densities, the free charge-carrier response dominates and large conductivity values are seen in the absence of photoexcitation. This is shown in Figure 6.7A for samples with $x = 1$, where the spectrally flat real dark conductivity indicates a Drude-like response from free charge carriers with short scattering time. [141] The high dark conductivity for the 0 % SnF_2 condition is significantly reduced with addition of 0.1 % SnF_2. Increasing the amount of tin fluoride additive to 1 % gives a further dramatic decrease in dark conductivity, with less significant drops on increasing SnF_2 content further. These reductions in dark conductivity reflect reductions in the hole doping density, which can be calculated as described in Section B.2 from dark conductivity (with the phonon response subtracted out) and charge-carrier mobility.

The calculated background hole doping densities, shown in Figure 6.7B, clearly illustrate the trend of reducing background doping on addition of SnF_2 that is reflected in decreasing dark conductivity. Notably, this reduction in background doping from oxidation of tin does not scale linearly with the amount of SnF_2 added, with large effects for addition of 0.1 % and 1 % SnF_2 to the tin precursor solution and only moderate further reductions on increasing the amount of additive beyond 1 %. For a given amount of SnF_2 additive, background doping density generally increases superlinearly with tin fraction, which reflects a greater tendency for tin to oxidise in higher tin fraction samples. Consequently, the effect of SnF_2 on background hole doping density is limited for $FA_{0.83}Cs_{0.17}Sn_xPb_{1-x}I_3$ samples with tin fraction $x \leq 0.6$ where substitution with lead suppresses oxidation of tin

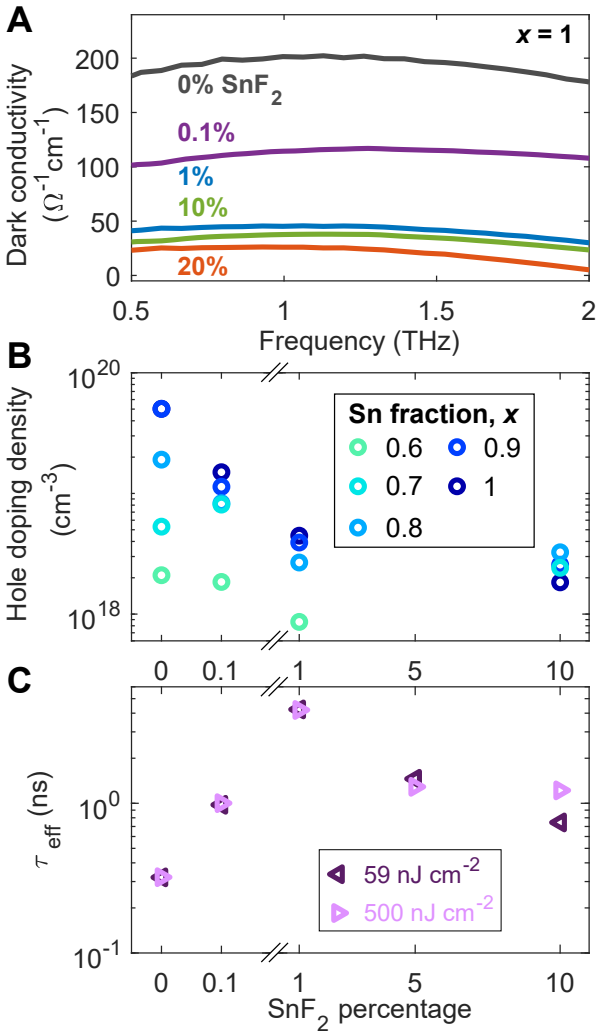


Figure 6.7: Effect of varying amounts of SnF_2 additive on the dark conductivity (panel A), background hole doping density (panel B), and effective photoluminescence lifetimes (panel C) of $FA_{0.83}Cs_{0.17}Sn_xPb_{1-x}I_3$ thin films on quartz substrates with tin fraction x between 0.6 and 1. Measurements and data analysis for panels A and B were conducted by Aleksander M. Ulatowski. **A)** Dark conductivity spectra (real part) of neat tin perovskite samples ($x = 1$) prepared with different amounts of SnF_2 added to the tin precursor solution as labelled. Conductivity drops with increasing amount of SnF_2, which is indicative of reduction in background hole doping. **B)** Change in background hole density (calculated from dark conductivity and charge-carrier mobility data) with SnF_2 additive, for samples with varying tin fraction as indicated in the legend. Samples with 5 % SnF_2 added were not included in measurements. **C)** Mean PL lifetime for samples with $x = 0.6 - 1$ at each SnF_2 percentage, determined from stretched exponential fits to measured PL decay transients for samples excited at 405 nm with fluences as in the legend. [Adapted with permission from *Adv. Funct. Mater.* 2020, **30**, 2005594 [290] Copyright 2020 John Wiley and Sons.]

significantly. Already for $x = 0.6$, dark conductivity spectra are dominated by the phonon response and differences between spectra at varying SnF_2 percentages are comparable with the uncertainty of the measurement, as shown in Figure B.3.

Background hole densities determined from terahertz dark conductivity spectra thus demonstrate that for majority tin samples, SnF_2 effectively suppresses the oxidation of tin with just 1 % additive in the tin precursor solution. Larger amounts of SnF_2 bring only modest gains, and for lower tin fractions ($x \leq 0.6$) alloying with lead appears to suppress the formation of tin vacancies and associated hole doping effectively, to make SnF_2 additive relatively obsolete.

6.3.3 Photoluminescence lifetimes

As illustrated in Figure 6.7C, the reduction in background hole doping density achieved by addition of SnF_2 results in increased photoluminescence lifetimes for $FA_{0.83}Cs_{0.17}Sn_xPb_{1-x}I_3$ samples. Specifically, the average of effective lifetimes determined as described in Section 6.2.6.1 for samples with tin fraction $x = 0.6 - 1$ shows slower PL decay when SnF_2 is added. This subset of samples is chosen for comparability with the background hole densities calculated for the same range of tin fractions as shown in panel B of the figure. Data are included in panel C for two excitation fluences spanning an order of magnitude, the low fluence condition shown by left pointing open triangle markers and the high fluence condition by right-pointing open triangles, with similar dependence on SnF_2 percentage in both cases. Moving from no additive to 0.1 % SnF_2, and then to 1 % SnF_2, PL lifetimes progressively increase while hole densities progressively decrease, in large steps. Slower PL decay when SnF_2 is added is attributable to the reduction in hole doping density and associated pseudo-monomolecular recombination of photoexcited electrons with background holes. [91, 141, 145] Increasing the amount of SnF_2 additive further results in a small decrease in lifetime relative to the 1 % SnF_2 condition, although PL

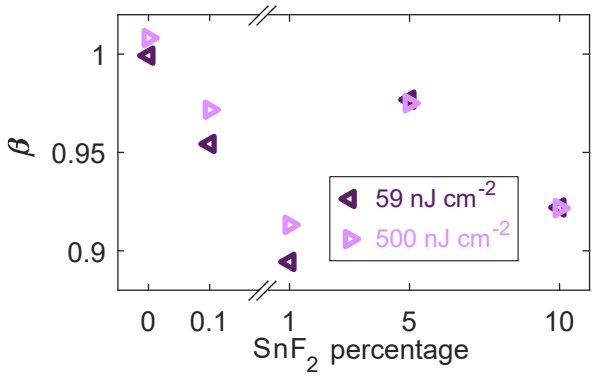


Figure 6.8: Effect of varying amounts of SnF_2 additive on the fitted stretching parameter, β, for $FA_{0.83}Cs_{0.17}Sn_xPb_{1-x}I_3$ PL decay transients. Values shown are the mean for samples with tin fraction $x = 0.6 - 1$, corresponding to the effective lifetimes shown in Figure 6.7C.

is still longer lived with 5 % or 10 % SnF_2 added than none. The change at high SnF_2 content is not explained by background hole doping, which is similar or slightly lower on addition of 10 % SnF_2 than 1 %, instead suggesting the introduction of other defects such as SnF_2 aggregates [315] or Sn^{2+} interstitials with iodide vacancies, [316] when large amounts of additive are used that create additional trap-assisted recombination pathways.

The change in stretching parameter, β, with SnF_2 percentage is consistent with the observed changes in PL lifetime being caused by reduced hole doping and subsequent introduction of defects. As shown in Figure 6.8, PL decay transients for high tin fraction samples without SnF_2 added are monoexponential with $\beta \approx 1$, and addition of SnF_2 reduces β with the largest effect for 1 % SnF_2. These changes in decay dynamics can be considered in the context of Equation 6.5 which has been previously used to describe the change in photoexcited electron population n (assumed to be equal to photoexcited hole population p) in the presence of background hole doping with density p_0: [91, 145]

$$\frac{dn}{dt} = -(k_1^{nr} + k_2^r p_0)n - k_2^r n^2 \tag{6.5}$$

When p_0 is large compared to n, the monomolecular recombination term $(k_1^{nr} + k_2^r p_0)$ (which incorporates trap-assisted, non-radiative processes and radiative recombination of photoexcited electrons with background holes) dominates and measured decay transients

appear monoexponential, with $\beta = 1$. This is the scenario seen when no SnF_2 is added. For lower doping densities, or at high fluences where n is much larger than p_0, the contribution of the bimolecular term increases and measured decay transients are non-exponential, with smaller values of β as seen here with SnF_2 addition. Additionally, non-exponential PL decay dynamics can arise at low fluence in the trap-mediated recombination regime, for example when the distribution of trap states is spatially inhomogeneous, [87, 145] as has often been observed for lead-based perovskites. [99, 305, 306] Defects contributing to trap-assisted recombination when large amounts of SnF_2 are added increase k_1^{nr} so that the monomolecular term is again more significant.

This interplay between the different monomolecular and bimolecular recombination pathways is also evident when comparing PL decay profiles of $FA_{0.83}Cs_{0.17}Sn_xPb_{1-x}I_3$ samples at different tin fractions (shown in Figure B.6). In general, effective lifetimes decrease and β approaches 1 as tin fraction increases, trends that have also been observed previously [145] and result from increases in background hole doping with tin fraction as shown in Figure 6.7B, giving increased pseudo-monomolecular recombination. On addition of SnF_2, the range of compositions for which measured decay transients are non-exponential with lower β values extends to higher tin fraction as a result of reduced background hole doping.

6.3.4 Absorption and emission properties

To further explore the effects of SnF_2 addition and the reductions in background hole doping quantified above on the optoelectronic properties of $FA_{0.83}Cs_{0.17}Sn_xPb_{1-x}I_3$, absorption and photoluminescence spectra can be examined. Figure 6.9 shows several properties of interest determined from these spectra, which are discussed in the following sections.

6.3.4.1 Absorption onset

Figure 6.9A shows the absorption onset energies E_g for $FA_{0.83}Cs_{0.17}Sn_xPb_{1-x}I_3$ thin films across the range of tin fractions, determined from measured absorbance spectra (shown in Figure B.7) as described in Section 6.2.6.2. Comparing the values of E_g for samples with varying amounts of SnF_2 added, denoted by different marker colours as indicated in the legend to Figure 6.9A, there is little variation for majority lead compositions, and for majority tin compositions E_g values remain similar for 1 – 20 % SnF_2. By contrast, samples with 0 or 0.1 % SnF_2 added (shown by dark grey and purple markers respectively) exhibit larger E_g values at high tin fraction than samples with larger amounts of SnF_2 added, the difference being most pronounced when no additive is used.

Examining the change in E_g with tin fraction, there is a non-linear variation seen as x increases, with values for the neat lead ($x = 0$) and neat tin ($x = 1$) compositions higher in energy than most of the intermediate compositions, and a minimum at $x = 0.6$ – 0.7. This trend, known as bandgap bowing, has been observed in previous studies of several tin-lead perovskites [60, 143–146] and is also known for alloys of many inorganic semiconductors. [317, 318] Explanations for this phenomenon in the case of inorganic semiconductors include contributions from variations in average crystal potential and aperiodic disorder effects. [319, 320] Structural relaxation through bond stretching was found to play a significant role, together with charge redistribution and volume deformation relative to the neat compositions. [321–323] In tin-lead perovskites, bond bending was recently identified as the main contributor to bandgap bowing, [145] while chemical effects from orbital energy mismatch between tin and lead play a smaller role. [146] For both MHPs and inorganic semiconductors the parabolic model given by Equation 6.6 can be used to describe bandgap bowing for two neat compositions with bandgap E_i mixed in a ratio x, where the bowing parameter b describes deviation from linearity. [318, 319, 324]

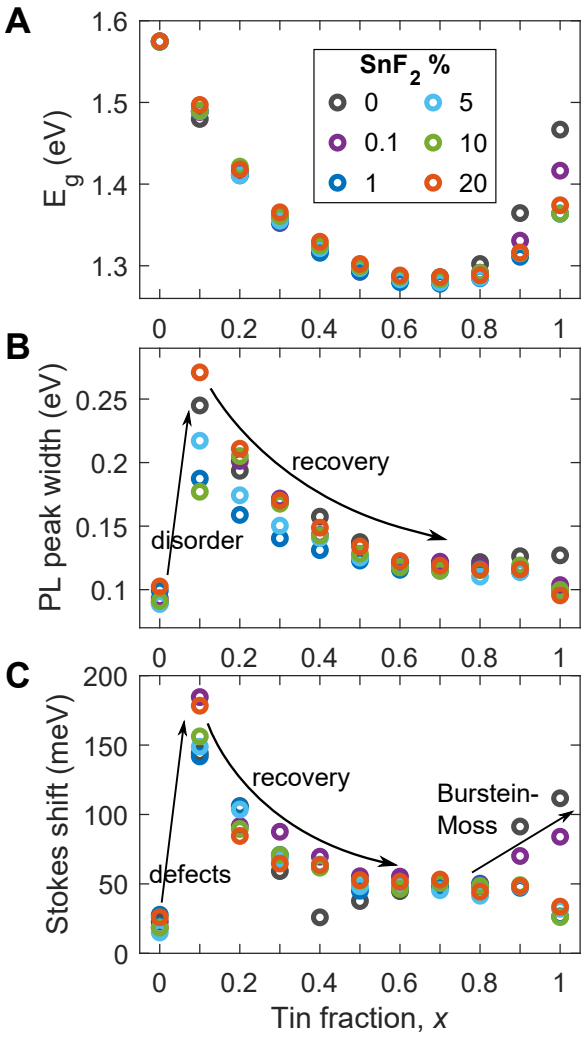


Figure 6.9: Effect of SnF_2 additive on absorption onset (panel A), photoluminescence peak broadening (panel B) and Stokes shift (panel C) for $FA_{0.83}Cs_{0.17}Sn_xPb_{1-x}I_3$ thin films with tin fraction x ranging from 0 to 1. The colour scheme for SnF_2 percentage shown in the legend in panel A is also used for panels B and C. **A)** Variation in the absorption onset energy E_g, showing deviation from the expected bandgap bowing trend at high tin fraction when little or no SnF_2 is added, with the expected trend restored on addition of 1 % SnF_2 or greater. **B)** Full width at half maximum of observed PL peaks, showing a sharp increase in disorder for samples with low tin fraction that is improved on addition of moderate amounts of SnF_2. **C)** Variation in Stokes shift, showing the impact of defects at low tin fraction, and larger Stokes shifts at high tin fraction caused by the Burstein-Moss effect, which is suppressed by addition of at least 1 % SnF_2. [Reproduced with permission from *Adv. Funct. Mater.* 2020, **30**, 2005594 [290] Copyright 2020 John Wiley and Sons.]

$$E(x) = E_1x + E_2(1-x) - bx(1-x) \tag{6.6}$$

The bandgap bowing trends seen in Figure 6.9A are similar for samples with between 1 and 20 % SnF_2 added, but for 0 and 0.1 % SnF_2 there is a steeper increase in E_g from its minimum value to the neat tin endpoint of the compositional range. Fits to the data at each SnF_2 percentage using Equation 6.6, shown in Figure 6.10 by solid lines, highlight the change in E_g at high tin fractions further. For samples with at least 1 % SnF_2 added, fitted bowing curves follow the data closely and the values of b = 0.69 – 0.73 eV obtained from these fits are similar to those previously reported for similar perovskites $FA_{0.8}Cs_{0.2}Sn_xPb_{1-x}I_3$ (b = 0.75 eV) [146] and $FASn_xPb_{1-x}I_3$ (b = 0.73 eV). [145] For samples with 0.1 % or 0 % SnF_2 added, by contrast, fits with Equation 6.6 return larger values of b and show marked deviation from the data at high tin fraction while the minimum of the bowing curve shifts to lower tin fractions, with the worst fit seen when no SnF_2 is added. These results indicate that when little or no SnF_2 is added during preparation, the observed blueshifts in the absorption onset are a deviation from the expected trend of bandgap bowing.

The increase in E_g at high tin fractions with less than 1 % SnF_2 added is explained by the high background hole doping densities present in these samples, as shown in Figure 6.7. These high doping densities lower the Fermi level of these perovskite semiconductor materials such that the valence band maximum is mostly empty of electrons (or, equivalently, mostly filled with holes). Consequently, the highest energy states from which it is possible to photoexcite an electron into the conduction band are further from the valence band maximum than would be expected in the case of an undoped semiconductor, and a blueshift in the absorption onset results. This Burstein-Moss shift [325, 326] has previously been observed in neat tin perovskites, where addition of between 5 and 20 % SnF_2 suppressed the effect. [141, 327] As shown in Figure 6.9A here,

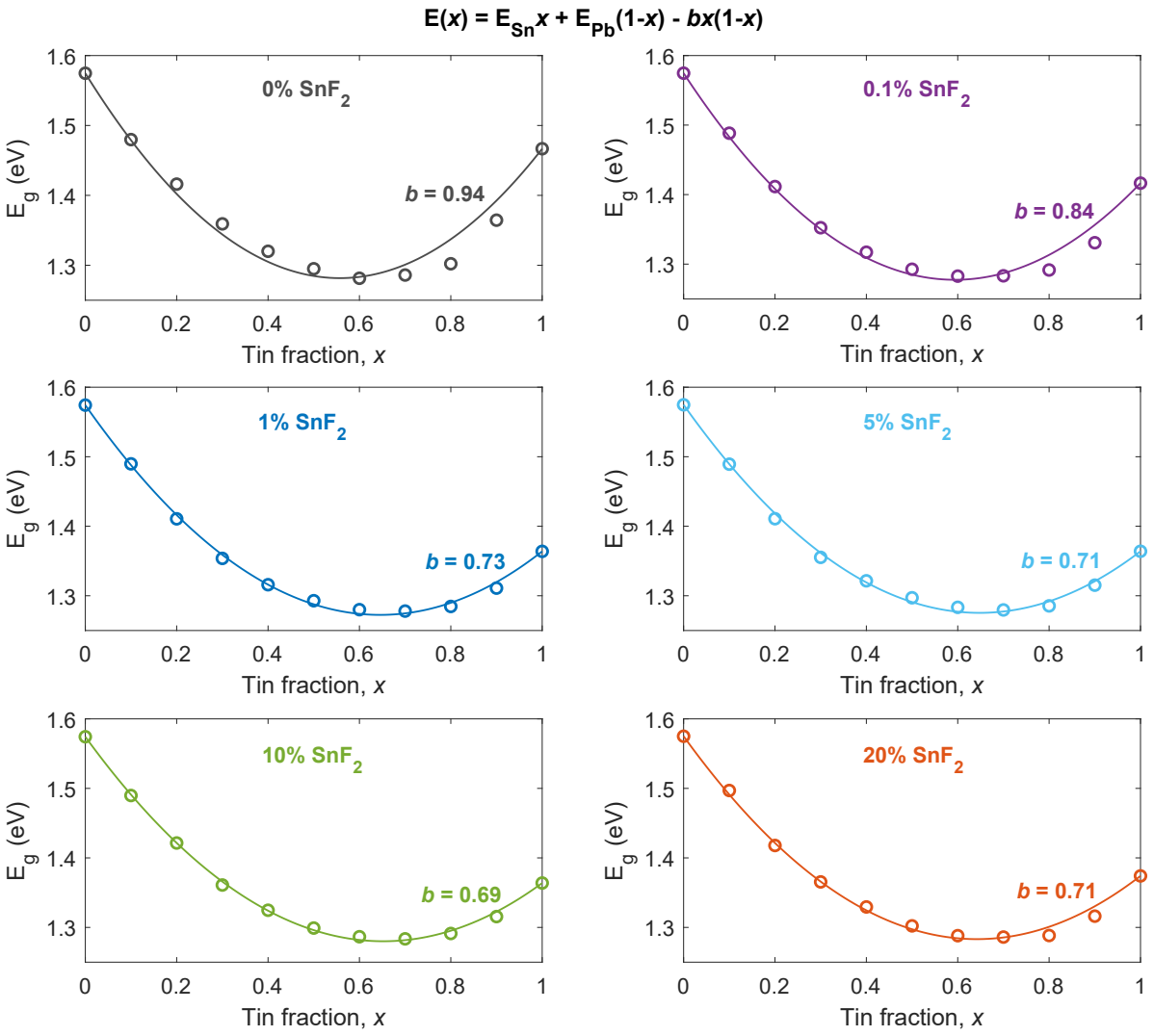


Figure 6.10: Absorption onset energy, E_g (open circles), of $FA_{0.83}Cs_{0.17}Sn_xPb_{1-x}I_3$ thin films on z-cut quartz with varying amounts of SnF_2 added to the tin precursor solution during preparation, and fits (solid lines) using the equation shown for bandgap bowing. The values of E_g are as shown in Figure 6.9A, determined from absorbance spectra as described in Section 6.2.6.2. Values of the bowing parameter b for each of the fitted bowing curves are as labelled.

such a shift is clearly discernible in tin-lead perovskites with $x > 0.8$, not only the neat tin composition. Further, any significant change in the absorption onset of these samples that arises from Burstein-Moss effects is eliminated by the addition of even 1 % SnF_2. These observations highlight the importance of taking into account background doping associated with the presence of tin vacancies when using tin-lead perovskites in two-terminal tandem cells that require careful photocurrent matching, and illustrate that a small amount of SnF_2 can compensate for the effects of such doping on the absorption onset.

6.3.4.2 Photoluminescence peak broadening

The broadening of $FA_{0.83}Cs_{0.17}Sn_xPb_{1-x}I_3$ photoluminescence peaks displays significant variation with changes in composition, as shown in Figure 6.9B where this broadening is quantified as the full width at half maximum of each PL peak. In contrast to the changes in absorption spectra with SnF_2 addition, which as discussed in Section 6.3.4.1 affect samples at high tin fraction, the features of interest in Figure 6.9B are seen for low tin fraction samples. Specifically, there is a large increase in peak width at low tin fractions $x = 0.1 - 0.4$ compared to the neat lead composition, with some dependence on SnF_2 addition and increases in tin fraction above $x = 0.1$ yielding a gradual reduction in peak width. The observed large broadening of PL spectra when small amounts of tin are introduced is attributable to disorder, consistent with the existence of an electronically defective compositional region at tin fractions $x = 0.05 - 0.2$ in tin-lead perovskites that was recently identified. [328] As no corresponding broadening of diffraction peaks was found for these low tin fraction samples (see Figure 6.4B) the crystallinity of $FA_{0.83}Cs_{0.17}Sn_xPb_{1-x}I_3$ samples is not significantly impacted by incorporation of small amounts of tin, and there is no detectable structural distortion that would broaden the XRD peaks. As such, the disorder effects evidenced by large PL peak widths in Figure 6.9B primarily arise from broadening of the energetic distribution of electronic states, discussed further in Section 6.3.4.3 below.

Considering the variation in PL peak width with different amounts of SnF_2 addition seen in Figure 6.9B, there is a clear reduction in broadening for the neat tin ($x = 1$) composition when any amount of SnF_2 is added compared to the 0 % SnF_2 condition. Additionally, at low tin fractions addition of moderate amounts of SnF_2 appears to partially compensate for the increased broadening with tin incorporation. These decreases in broadening when SnF_2 is added are attributable to a reduction in energetic disorder when formation of tin vacancies is suppressed. Where tin vacancies are present, they

will likely act as electron acceptors upon release of holes to the valence band, with the consequence that local electric field variations are introduced and the energetic landscape varies throughout the material, contributing to PL broadening. No similar reduction in broadening is seen for larger amounts of SnF_2 additive at tin fractions $x = 0.1 - 0.4$, suggesting that aggregates formed by excess SnF_2 lead to increased energetic disorder despite the accompanying suppression of tin vacancies and reduction in background hole density.

6.3.4.3 Stokes shift

The Stokes shift between absorption onset and PL peak energy, shown in Figure 6.9C, reflects significant trends in both of these properties. At low tin fractions, the Stokes shift shows a similar trend to the PL broadening, with a sudden large increase in energy on increasing tin fraction x from 0 to 0.1, followed by gradual recovery as x increases further. The absorption onsets change smoothly over the same compositional region, following the expected bandgap bowing trend as discussed in Section 6.3.4.1, and the sharp increase in Stokes shift can be traced to a large redshift in PL energy as shown in Figure 6.11. Whereas the PL peak energies for the neat lead and majority tin compositions exhibit bandgap bowing similar to that seen in the absorption onsets, although without dependence on SnF_2 percentage, emission at low tin fraction deviates from this trend with PL peaks at lower energy. This phenomenon of large PL redshift at low tin fraction has been seen previously for mixed tin-lead perovskites with a range of A cations, [145, 329, 330] and is attributable to the presence of sub-bandgap defect states, also evidenced by large Urbach energies indicative of high defect density. [135, 331] As identified in Section 6.3.4.2, the lack of diffraction peak broadening for low tin fraction samples in Figure 6.4B suggests that defectiveness at low tin fraction is due to energetic disorder rather than any phase change or extensive structural disorder. There

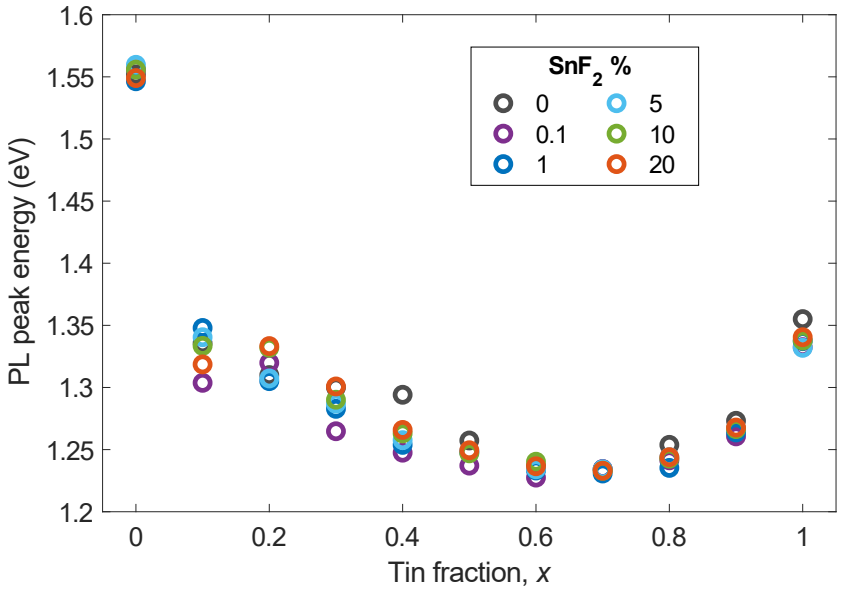


Figure 6.11: Energy of the photoluminescence peak for $FA_{0.83}Cs_{0.17}Sn_xPb_{1-x}I_3$ thin films on z-cut quartz, with different amounts of SnF_2 added to the tin precursor solution during preparation as indicated in the legend. There is a large redshift in emission energy for low tin fractions, deviating from the expected bandgap bowing trend with tin fraction, which can be attributed to the presence of defects.

is also no evidence from XRD of impurities present in the low tin fraction samples (see Figures 6.3A and B.1) that might be responsible for the introduction of defects. Rather, introduction of small amounts of tin is considered to change the nature and energy of trap states in the perovskite film, [145] enhancing sub-bandgap states and leading to the observed redshift and broadening of emission.

While observed Stokes shifts in Figure 6.9C decrease as x increases above 0.1 to a stable value over the compositional region of minimum bandgap, at high tin fractions $x > 0.8$ larger Stokes shifts return for samples with less than 1 % SnF_2 added during preparation. For high tin samples there is little variation in PL peak energy, as Figure 6.11 shows, and the increase in Stokes shifts is entirely attributable to Burstein-Moss shifts in the absorption onset when background hole doping concentration is high, as discussed in Section 6.3.4.1 and shown in Figure 6.9A. The Burstein-Moss shift only affects absorption energies, since photoexcited electrons can relax to the conduction band edge during the PL emission processes before recombining radiatively with either free

photoexcited holes or background holes occupying states near the valence band edge.

The Stokes shift as discussed here captures two key trends in the optoelectronic properties of $FA_{0.83}Cs_{0.17}Sn_xPb_{1-x}I_3$ perovskites, which must both be considered when assessing these materials for applications in low-bandgap or tandem solar cells. At low tin fractions, defectiveness and associated energetic disorder evident in large Stokes shifts are indicators of poor material quality that makes these compositions less desirable to use despite increased stability from high lead content. At high tin fractions the influence of hole doping from oxidation of tin is particularly apparent in a Burstein-Moss shift of the absorption onset giving increase Stokes shifts, which can be suppressed by addition of at least 1 mol % SnF_2

6.3.5 Charge-carrier mobility

The impact of SnF_2 addition on charge transport properties of tin-lead iodide perovskites is important to understand, as charge-carrier mobilities in a solar cell's active layer play a crucial role in determining performance. In general charge-carrier diffusion lengths in MHPs are high, [99] meeting the requirement for high photocurrent that diffusion length exceeds the thickness of the active layer. However, in tin-based perovskites reduced PL lifetime and charge-carrier mobility lead to shortened diffusion lengths and worse device performance compared to equivalent lead-based compositions. [66, 101, 141] To examine the relationship between charge-carrier mobility and background hole doping as controlled by SnF_2 addition in $FA_{0.83}Cs_{0.17}Sn_xPb_{1-x}I_3$ thin films, these two quantities are plotted in Figure 6.12 for samples with tin fraction $x \geq 0.6$. As background doping is reduced by addition of increasing amounts of SnF_2, charge-carrier mobility (determined as described in Section B.2 from OPTP measurements) increases significantly, with larger effects for samples with high tin fraction. Changes in mobility with SnF_2 addition are

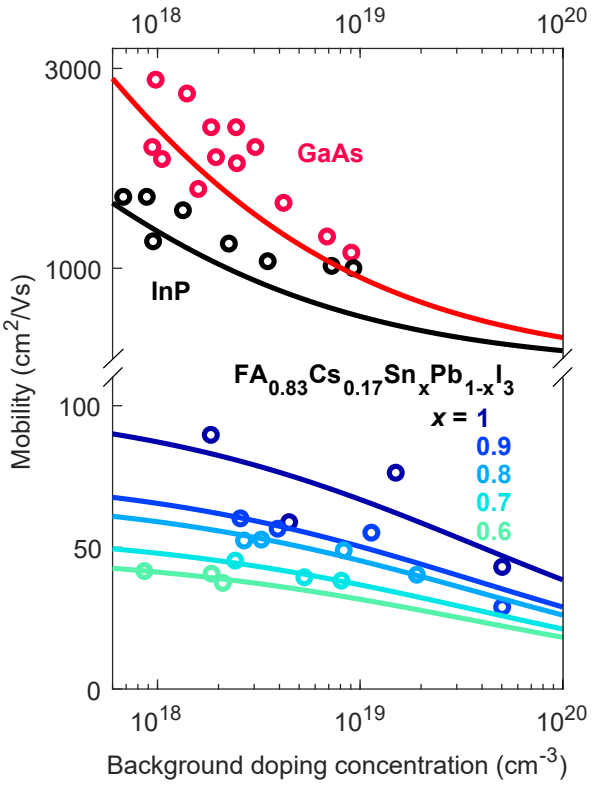


Figure 6.12: Decrease in mobility as background hole doping increases in $FA_{0.83}Cs_{0.17}Sn_xPb_{1-x}I_3$ thin films at varying tin fractions x as indicated, compared to two inorganic semiconductors. Data shown for GaAs and InP were extracted from Hilsum, C. *Simple empirical relationship between mobility and carrier concentration* Electronics Letters, 10, 13, **1974**, 259-260, and the fits shown as red and black solid lines are the same as in that study. [332] The fits shown for charge-carrier sum mobilities of the perovskite samples, as solid lines following the colour scheme indicated for tin fraction x, use the empirical formula by Hilsum, Equation 6.7 (with a normalising density optimised for all samples of $N_0 = 3.76 \times 10^{19}$ and μ_L values as shown in Table B.3), and were obtained using the least squares method. Measurements and data analysis for this figure were conducted by Aleksander M. Ulatowski. [Reproduced with permission from *Adv. Funct. Mater.* 2020, **30**, 2005594 [290] Copyright 2020 John Wiley and Sons.]

much less pronounced for samples with $x \leq 0.7$, which already have low hole doping density even when no additive is used (see Figure 6.7B).

Figure 6.12 contrasts the experimentally determined mobilities for $FA_{0.83}Cs_{0.17}Sn_xPb_{1-x}I_3$ samples with varying doping density against data for doped inorganic semiconductors previously reported to follow the relationship given in Equation 6.7: [332]

$$\mu = \frac{\mu_{\mathrm{L}}}{1 + \sqrt{N/N_0}} \tag{6.7}$$

This model assumes that charge-carrier mobility μ is limited by lattice scattering (electron-phonon coupling) μ_L and impurity scattering, with only the latter process depending on dopant concentration N whereas lattice scattering rate at room temperature is an intrinsic property of the material. [332] The normalising density of dopants in Equation 6.7, N_0, is determined empirically. Fits to the data for tin-lead perovskite samples using Equation 6.7, with parameters detailed in Table B.3, are shown in Figure 6.12 as solid lines, and indicate that the observed trends in charge-carrier mobility are consistent with the prediction that scattering off dopants limits mobility, as in inorganic semiconductors.

For samples with background hole doping significantly reduced by addition of SnF_2, there is an appreciable increase in charge-carrier mobility with increasing tin-fraction, consistent with lower calculated effective mass of charge carriers in tin-based perovskites than the lead-based equivalent. [136] This illustrates that, once oxidation of tin and consequent high background doping density is suppressed, the intrinsic material properties of tin-based perovskites that are desirable for photovoltaic applications become dominant.

6.4 Conclusions

This chapter revealed the effects of the commonly used SnF_2 additive in amounts from 0.1 to 20 mol % on the structural and optoelectronic properties of $FA_{0.83}Cs_{0.17}Sn_xPb_{1-x}I_3$ perovskites across the range of tin fractions from 0 to 1. Addition of SnF_2 was found to reduce tetragonal distortion in the perovskite crystal structure, predominantly affecting samples with high tin fractions, by alleviating the strain that results from tin vacancies formed on oxidation of Sn^{2+}. The background hole density arising from tin oxidation was quantified, and found to be significantly reduced by addition of 1 % SnF_2. Consequently, photoluminescence lifetimes increase, energetic disorder decreases, the Burstein-Moss

shift distorting the expected bandgap bowing trend in absorption onsets is reduced, and charge-carrier mobilities increase. The addition of 0.1 % SnF_2 was insufficient to realise these beneficial effects, whereas adding 5 % SnF_2 or more achieved only modest further reductions in background hole density. Additive amounts above 1% also had the undesirable effect of enhancing non-radiative recombination that leads to shorter photoluminescence lifetimes. Limited effect of SnF_2 was found for low tin fraction samples, whereas in majority tin compositions its impact in improving a wide range of properties was significant even for just 1 % additive.

6.5 Future outlook

This study provides a foundation for further improvements in the performance of low-bandgap mixed tin-lead perovskites, based on a thorough understanding of the effects of the most widely used additive to counter tin oxidation. The revelation that many of the intended benefits of SnF_2 addition can be realised with as little as 1 %, whereas for $\geq$5 % SnF_2 addition unwanted effects accompany the suppression of tin oxidation, indicates that reducing the amount of additive commonly used in preparation of tin-lead perovskites could already yield improvements in tandem cell performance. Additionally, the results in this chapter suggest that SnF_2 addition offers little benefit for majority lead compositions, so that the use of this or similar additives can be limited to samples with tin fraction above 0.5.

In future work, as well as applying the insights gained from this study to the preparation of mixed tin-lead perovskites, a more fine-grained comparison of SnF_2 percentages around 1 % could determine the optimal amount of additive. Further studies could also investigate other additives that have been used instead of, or in combination with, SnF_2 by applying the approach and techniques employed here. A comprehensive comparison of the many different additives used in mixed tin-lead perovskites, taking

this study as a starting point, would enable better control over the material quality of tin-lead perovskites. Such control is expected to enhance the performance of all-perovskite tandem cells, a promising technology that has not yet achieved efficiencies comparable with perovskite-silicon tandems.

7

Conclusions and Outlook

This thesis has focussed on understanding the properties of tin and tin-lead perovskites relevant to their applications in next-generation solar cells offering higher efficiencies than conventional single-junction devices. Approaches to determining charge-carrier temperature from photoluminescence spectra were examined, identifying several common sources of error. To address these, an improved model was presented that will allow accurate assessment of the prospects for hot-carrier extraction in perovskite solar cells and selection of the most promising MHP compositions for such work. The appearance of unusually slow charge-carrier cooling in $FASnI_3$ was investigated using time-resolved photoluminescence spectroscopy techniques. This investigation revealed the significant impact of energetic disorder on apparent cooling dynamics, and emphasised the need for careful investigation of carrier cooling in MHPs. Combining time-resolved PL with a range of complementary techniques, the impact of SnF_2 additive used to suppress oxidation of tin in $FA_{0.83}Cs_{0.17}Sn_xPb_{1-x}I_3$ was unravelled. These results laid a foundation for improved control over the material properties of low-bandgap mixed tin-lead perovskites for use in all-perovskite tandem cells.

In **Chapter 4**, methods used to determine charge-carrier temperature from time-resolved photoluminescence spectra in previous studies of carrier cooling in MHPs were examined. Incorrect assumptions carried over from earlier work on inorganic quantum well systems were identified, and the errors they introduce were analysed. Both neglecting the effect of spectral broadening, and assuming a constant joint density of states, were found to artificially inflate the carrier temperatures determined from fits to the high energy side of MHP photoluminescence spectra and distort the observed carrier cooling dynamics. An improved full lineshape model was presented that accounts for photoluminescence broadening and the energy-dependence of the density of states, and eliminates variation based on the choice of region to fit.

Adopting this full lineshape model in future work would enable more accurate determination of carrier temperature and ensure greater comparability between studies on different perovskite compositions. It would then be possible to determine how much of the variation in reported cooling times in MHPs is an artefact of different approaches to determining carrier temperature, and distinguish the real differences in carrier cooling dynamics between compositions. This is an essential step in identifying any particularly promising candidates for use in hot-carrier solar cells. There is also scope for further development of the full lineshape model through future work, for example to develop a consistent approach to carrier temperature determination from either time-resolved photoluminescence or transient absorption data.

In **Chapter 5**, charge-carrier cooling in $FASnI_3$ was examined by applying the full-lineshape model presented in Chapter 4 to time-resolved photoluminescence spectra measured using upconversion and time-correlated single photon counting techniques. By comparing the experimentally determined cooling curves to overall photoluminescence decay dynamics, the appearance of a secondary regime of slow cooling at late times was found to originate from relaxation of photoexcited charge carriers through energetic

states arising from disorder. This confirmed that the hot charge-carrier population of interest for hot-carrier solar cell applications cools over tens of picoseconds, rather than approaching the nanosecond timescale. These results highlight the importance of ruling out energetic disorder effects limited by decay of the excited charge-carrier population in MHPs with apparently slow cooling. They further indicate that $FASnI_3$ is not as promising a candidate for efficient hot-carrier solar cells as previously thought. Investigation of photoluminescence polarisation memory in $FASnI_3$, using the polarisation-dependence of the upconversion technique, showed total loss of any anisotropy in the excited charge-carrier population within 270 fs. This implies the absence of any coupling of electronic polarisation to structural features that would change on a slower timescale.

The lack of persistent polarisation memory in the photoluminescence of $FASnI_3$, when such an effect had previously been observed in some lead-based perovskites, warrants further investigation. Future work could explore whether there are local structural distortions that change over time in $FASnI_3$ without contributing to electronic polarisation, or such effects are present on a timescale that could not be captured in this work. Comparison of polarisation memory across a wider range of perovskite compositions would also be of interest to better identify its origin. The work on charge-carrier cooling in this chapter further emphasises the need for careful, thorough analysis of cooling dynamics in MHPs to determine the veracity of apparently slow cooling suggesting a population of hot charge carriers that might be extracted in a device. Comparing observed slow cooling, particularly at low fluences, against overall recombination dynamics will be an important check to apply in future studies seeking to identify candidate materials for hot-carrier solar cells.

In **Chapter 6**, the effects of different amounts of tin fluoride additive on $FA_{0.83}Cs_{0.17}Sn_xPb_{1-x}I_3$ thin films were investigated. Examining the crystal structure, hole doping density, photoluminescence lifetime, absorption and photoluminescence spectra,

and charge-carrier mobility revealed that beneficial effects were optimised for 1 mol % SnF_2 addition. Addition of SnF_2 was found to reduce the background hole doping density resulting from oxidation of tin, leading to increases in photoluminescence lifetime and charge-carrier mobility, and decreases in energetic disorder as well as in the Burstein-Moss shift affecting absorption onsets. Adding 5 % SnF_2 or more resulted in limited further reductions in hole doping density, along with the introduction of defects enhancing non-radiative recombination. Beneficial effects were found to be most pronounced for majority tin compositions, which also showed significant tetragonal distortion of the perovskite crystal structure in the absence of SnF_2. This distortion is attributable to strain in the lattice when tin vacancies form by oxidation of Sn^{2+}. Together, these results reveal the effects of the commonly used SnF_2 additive on the structural and optoelectronic properties of mixed tin-lead perovskites relevant to tandem cell applications.

Using this in-depth exploration of the effects of SnF_2 as a foundation, future work on all-perovskite tandem cells will be able to more rationally identify the optimal amount of SnF_2 additive to use for a high quality mixed tin-lead perovskite low-bandgap absorber layer. Since existing methods typically use larger amounts of SnF_2 additive, identified here to have detrimental effects that can counter the reduction in background hole doping, shifting to the use of 1 % SnF_2 could already lead to improvements in material quality and device performance. Further work to refine the optimal amount of SnF_2 with a range of values close to 1 %, and compare performance in devices could use a similar array of techniques to comprehensively assess the effects of the additive. Similarly, this approach could be applied to other additives more often used in combination with SnF_2, and mixed tin-lead perovskites with different A cations.

List of Abbreviations

A . . . . . Absorbance

α . . . . . Absorption Coefficient

E_B . . . . . Exciton Binding Energy

E_g . . . . . Bandgap Energy

k_B . . . . . Boltzmann Constant

L_D . . . . . Charge-Carrier Diffusion Length

n . . . . . Charge-Carrier Density

R . . . . . Reflectance

T . . . . . Transmittance

ADC . . . . . Analog-to-Digital Convertor

BBO . . . . . β-Barium Borate (non-linear optical crystal)

CCD . . . . . Charge Coupled Device

CFD . . . . . Constant Function Discriminator

DFT . . . . . Density Functional Theory

DMF . . . . . n,n-Dimethylformamide

DMSO . . . . . Dimethyl Sulfoxide

DOS . . . . . Density of States

DSSC . . . . . Dye-Sensitised Solar Cell

FA . . . . . Formamidinium

FDT . . . . . Fluorene-Dithiophene

FTIR . . . . . Fourier-Transform Infrared

FTO . . . . . Fluorine-doped Tin Oxide

FWHM . . . . Full Width at Half Maximum

MA . . . . . Methylammonium

MHP . . . . . Metal Halide Perovskite

MSSC . . . . . Meso-Superstructured Solar Cell

ND . . . . . Neutral Density (filter)

OPTP . . . . . Optical-Pump-Terahertz-Probe (spectroscopy)

P3HT . . . . . Poly(3-hexylthiophene-2,5-diyl)

PCE . . . . . Power Conversion Efficiency

PGA . . . . . Programmable Gain Amplifier

PIA . . . . . Photoinduced Absorption

PL . . . . . Photoluminescence

PMT . . . . . Photomultiplier Tube

PTAA . . . . . Poly(triarylamine)

PTFE . . . . . Poly(tetrafluoroethylene) (a.k.a. Teflon)

SEM . . . . . Scanning Electron Microscopy

SPAD . . . . . Single Photon Avalanche Diode

TAC . . . . . Time-to-Amplitude Converter

TCSPC . . . . Time-Correlated Single Photon Counting

THz . . . . . Terahertz

TIPL . . . . . Time-Integrated Photoluminescence (spectroscopy)

XRD . . . . . X-Ray Diffraction

Appendices

A

Supplementary figures, calculations, and sample characterisation for Chapter 5

Contents

A.1 $FASnI_3$ sample characterisation 149
A.2 Excitation density calculation 153
A.3 Power-dependent photoluminescence peak shift in $FASnI_3$. 154

This appendix collects together results from sample characterisation measurements for $FASnI_3$ samples as used in the study reported in Chapter 5 and gives detail on the calculation of excitation densities, and analysis of the power-dependent PL peak shift, which inform the discussion in that chapter.

A.1 $FASnI_3$ sample characterisation

Thin films of $FASnI_3$ prepared according to the method described in Section 5.1.1 were characterised by XRD, SEM, surface profilometry and FTIR spectroscopy to assess crystallinity, morphology, thickness, and bandgap of the samples. For XRD and SEM, O_2-plasma treated TEC15 fluorine-doped tin oxide (FTO) substrates were used in place of z-cut quartz, with no other changes to the preparation method.

Film thickness

Measurements performed by Matthew T. Klug, Department of Physics, University of Oxford. Using a Veeco Dektak 150 surface profilometer, the thickness of a single $FASnI_3$ film prepared with 5 % SnF_2 added on a z-cut quartz substrate was measured at several different positions, as shown in Table A.1. This gave an average thickness of 345 ± 15 nm for the prepared films.

Position on film	Thickness (nm)	
Left side	337.8	
Center 1	338.1	
Center 2	367.1	
Right side	337.8	
	Mean	Standard Deviation
	345.2	14.6

Table A.1: Thickness of a typical $FASnI_3$ thin film sample with 5 % SnF_2 added, as measured using a Veeco Dektak 150 surface profilometer at four different positions across the sample on z-cut quartz substrate.

Crystallinity

Measurements performed by Zhiping Wang, Department of Physics, University of Oxford. The XRD pattern shown in Figure A.1 was obtained using a Rigaku SmartLab X-ray diffractometer, with $CuK_{\alpha 1}$ (1.54060 Å) and a HyPix-3000 2D hybrid pixel array detector, and samples kept under vacuum during the measurement. The only non-perovskite peaks observed are attributable to the FTO substrate, and the perovskite peaks are labelled as for a cubic structure, giving a good match to the data but not ruling out the possibility of a lower symmetry structure since this measurement was carried out with a film rather than a powder. The FWHM values for the observed peaks are given in Table A.2, showing very similar broadening across all measured peaks. Overall these data confirm the presence of a perovskite $FASnI_3$ with good crystallinity, well-described as pseudocubic.

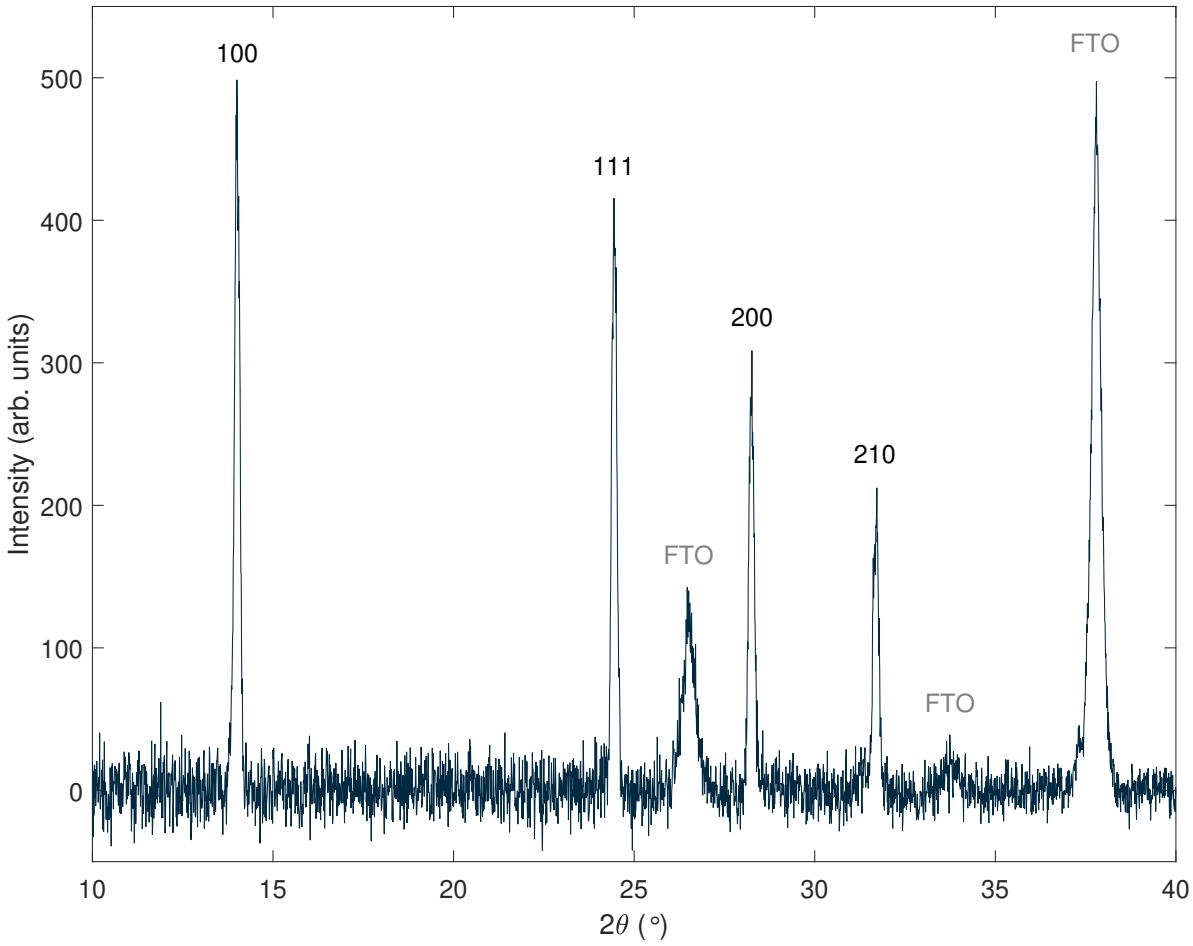


Figure A.1: X-ray diffraction pattern for a $FASnI_3$ film on FTO substrate, prepared with 5 % SnF_2 added. Measurement was performed with a Rigaku Diffractometer, keeping the sample under vacuum at room temperature, by Zhiping Wang. Substrate peaks are labelled in grey, and pseudocubic labelling for the perovskite peaks is given in black. [Adapted with permission from reference [225].]

Peak	FWHM (°)
100	0.1687
111	0.1662
200	0.1762
210	0.1687

Table A.2: Full widths at half maxima of the perovskite peaks in the measured XRD pattern of a $FASnI_3$ film as shown in Figure A.1.

Absorption onset

Measurements performed by Rebecca L. Milot, Department of Physics, University of Oxford. The optical absorbance spectrum shown in Figure A.2 was taken using a Bruker Vertex 80v Fourier-transform infrared spectrometer (as described in Section 3.3.3) with transmission/reflection accessory fitted, using a silicon diode detector. This measurement was carried out with samples mounted in a gas exchange cryostat (Oxford Instruments, OptistatCF2) and using a temperature controller (Oxford Instruments, MercuryiTC) to allow resistive heating and liquid helium cooling, although for the results in this thesis only the spectrum obtained at 295 K is of interest. The bandgap determined from the absorption onset of this spectrum by the steepest gradient method is 1.42 eV.

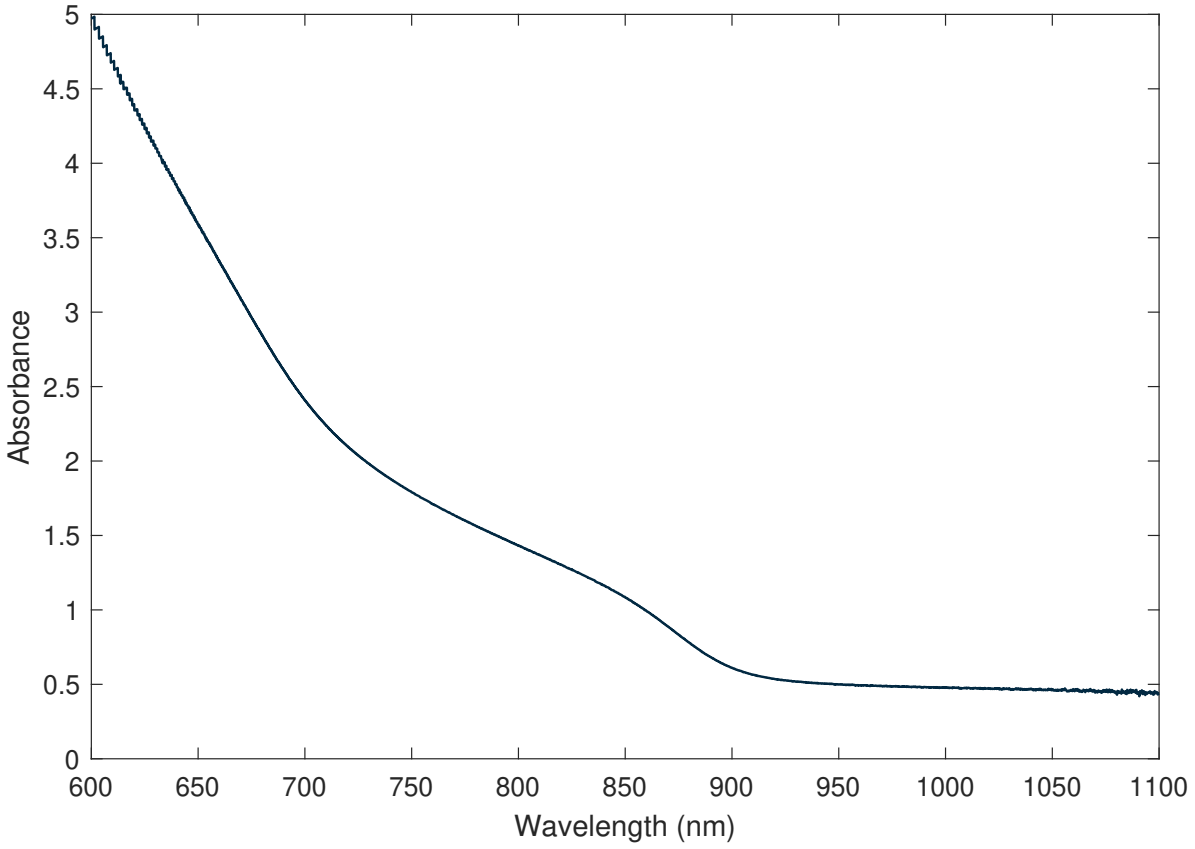


Figure A.2: Absorbance spectrum measured at 295 K of a $FASnI_3$ film on z-cut quartz, prepared with 5 % SnF_2 added. Measurement performed by Rebecca L. Milot. [Reproduced with permission from reference [225].]

A.2 Excitation density calculation

Given laser repetition rate of 80 MHz and excitation wavelength of 730 nm, the excitation fluences stated in Chapter 5 are calculated from the measured excitation spot size at the sample position of 0.02 mm^2, and measured power just in front of this position of 12 mW for low fluence and 60 mW for high fluence, as follows:

For 12 mW excitation power, pulse energy is given by

$$\frac{12 \times 10^{-3}\, W}{80 \times 10^{6}\ \text{Hz}} = 1.5 \times 10^{-10}\ \text{J}$$

from which the excitation fluence fl for each pulse is

$$\begin{aligned} fl = \frac{1.5 \times 10^{-10}\ \text{J}}{2 \times 10^{-4}\ \text{cm}^2} &= 7.5 \times 10^{-7}\ \text{J cm}^{-2} \\ &= 0.75\ \mu\ \text{J cm}^{-2} \end{aligned}$$

and similarly for 60 mW excitation power, the excitation fluence is 3.75 μJ cm^{-2}.

From these values the photoexcited charge-carrier density can be calculated, as follows:

For the low fluence condition, with excitation wavelength 730 nm, photon energy E is

$$\begin{aligned} E &= \frac{6.626 \times 10^{-34}\ \text{J s} \times 2.998 \times 10^{8}\ \text{m s}^{-1}}{730 \times 10^{-9}\ \text{m}} \\ &= 2.721 \times 10^{-19}\ \text{J} \end{aligned}$$

The film thickness d of the $FASnI_3$ samples is 345.2 nm as shown in Table A.1 and the absorbance of these samples as plotted in Figure A.2, calculated from transmittance T and reflectance R as $A = -\ln\left(\frac{T}{1-R}\right)$, is 1.98 at the excitation wavelength of 730 nm. Therefore the absorption coefficient α for these $FASnI_3$ samples is given by:

$$\begin{aligned} \alpha &= \frac{1.98}{345.2 \times 10^{-9}\ \text{m}} \\ &= 5.736 \times 10^{4}\ \text{cm}^{-1} \end{aligned}$$

Assuming that for each photon absorbed one charge-carrier pair is generated, the initial excitation density of either electrons or holes at an excitation power of 12 mW is then:

- $n_0^{\text{front}} = \frac{fl \times \alpha}{E} = 1.6 \times 10^{17}\,\text{cm}^{-3}$ at the front surface of the film
- $n_0^{\text{back}} = \frac{fl \times \alpha}{E} \times \exp(-\alpha d) = 2.2 \times 10^{16}\,\text{cm}^{-3}$ at the back surface of the film
- $n_0^{\text{average}} = \frac{fl \times (1 - \exp(-\alpha d))}{d\,E} = 6.9 \times 10^{16}\,\text{cm}^{-3}$ averaged across the film

Similarly for the high fluence condition, calculated initial excitation densities are:

- $n_0^{\text{front}} = 7.9 \times 10^{17}\,\text{cm}^{-3}$ at the front surface of the film
- $n_0^{\text{back}} = 1.1 \times 10^{17}\,\text{cm}^{-3}$ at the back surface of the film
- $n_0^{\text{average}} = 3.4 \times 10^{17}\,\text{cm}^{-3}$ averaged across the film

A.3 Power-dependent photoluminescence peak shift in $FASnI_3$

As illustrated in Figure A.3, the $FASnI_3$ photoluminescence peak shifts to higher energy as excitation power increases. This blue shift can be seen both in time-integrated measurements (panel A) where the line shape is largely unaffected by any transient hot-carrier population, and in time-resolved measurements taken at a range of different delay times (panel B). This is shown in panel A to be a general trend for excitation fluences spanning several orders of magnitude, not just the conditions under which measurements are reported in Chapter 5. Additionally, as a red-shift occurs with charge-carrier cooling at each excitation fluence, the higher fluence spectrum (gold markers in panel B) remains blue-shifted by a similar amount relative to the low fluence spectrum (green markers) at the same delay time. This indicates that this power-dependent peak shift is an independent effect from the generation and subsequent cooling of hot carriers. A possible explanation for the blueshift in peak position is state filling as the increasing fluence leads to larger excitation densities. The charge-carrier densities relevant to this work, calculated in Section A.2, lie below the previously determined onset threshold for

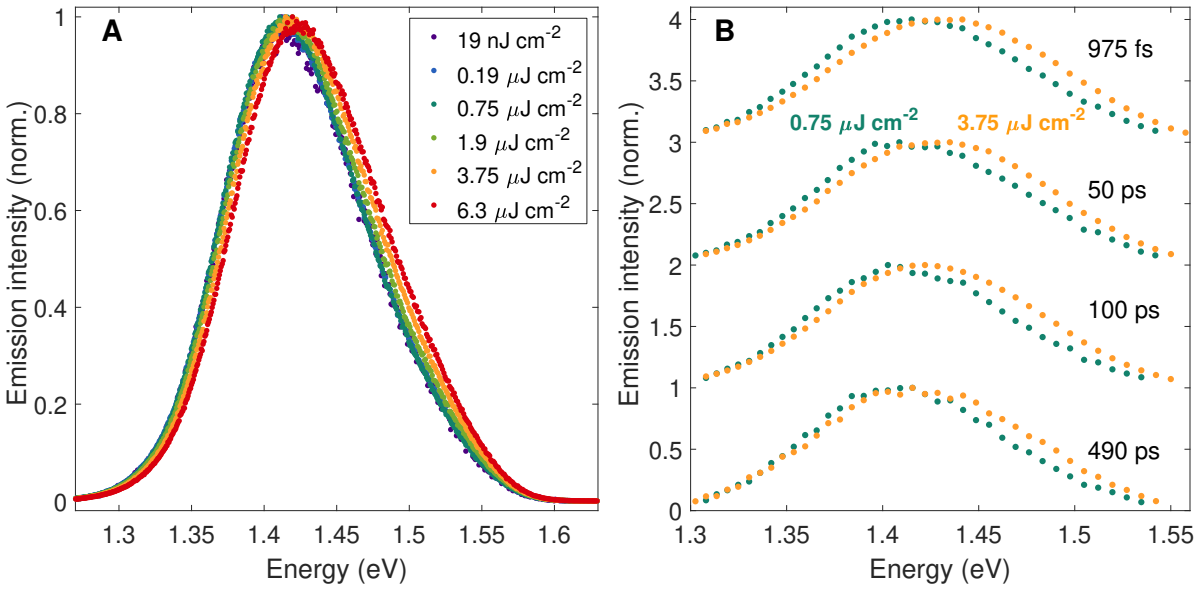


Figure A.3: Effect of excitation fluence on the photoluminescence spectrum of $FASnI_3$ thin films on quartz. **A)** Time integrated PL spectra measured with excitation fluences from 19 nJ cm^{-2} to 6.3 μJ cm^{-2} demonstrating progressively larger blue shift as fluence increases. Acquisition times were chosen independently for each excitation fluence to maximise signal to noise in the measured spectrum, and each spectrum has been normalised to its own maximum intensity for ease of comparison in this figure. **B)** Time-resolved photoluminescence spectra measured by PL upconversion spectroscopy (for the 975 fs and 50 ps delay times) or TCSPC (for the 100 ps and 490 ps delay times) with excitation fluences of 0.75 μJ cm^{-2} and 3.75 μJ cm^{-2} giving the spectra shown in green and gold respectively to match the colour scheme used in panel A. The spectral range shown in each case is the same as used in fitting carrier temperatures, comprising all points with intensity greater than or equal to 10 % of the maximum intensity for each spectrum. All spectra have been normalised to their respective maximum intensities, and vertical offsets added, for ease of comparison. [Adapted with permission from reference [225].]

Burstein-Moss shifts from simple band filling within the square root density of states [65, 270, 271, 333] and so this is not expected to be significant, but disordered energetic states may still be filled at lower excitation densities.

Ignoring this effect when carrying out fits to the measured PL spectra to determine charge-carrier temperatures and using a single fixed value of E_g for all excitation fluences would distort the results, in particular giving overestimates for carrier temperatures at higher excitation fluence. Worse fits to the measured spectra would also result, as illustrated by comparing the left and right columns in Figure A.4 in which the spectra measured at high fluence are fitted with global parameter values determined from low

fluence and high fluence spectra respectively.

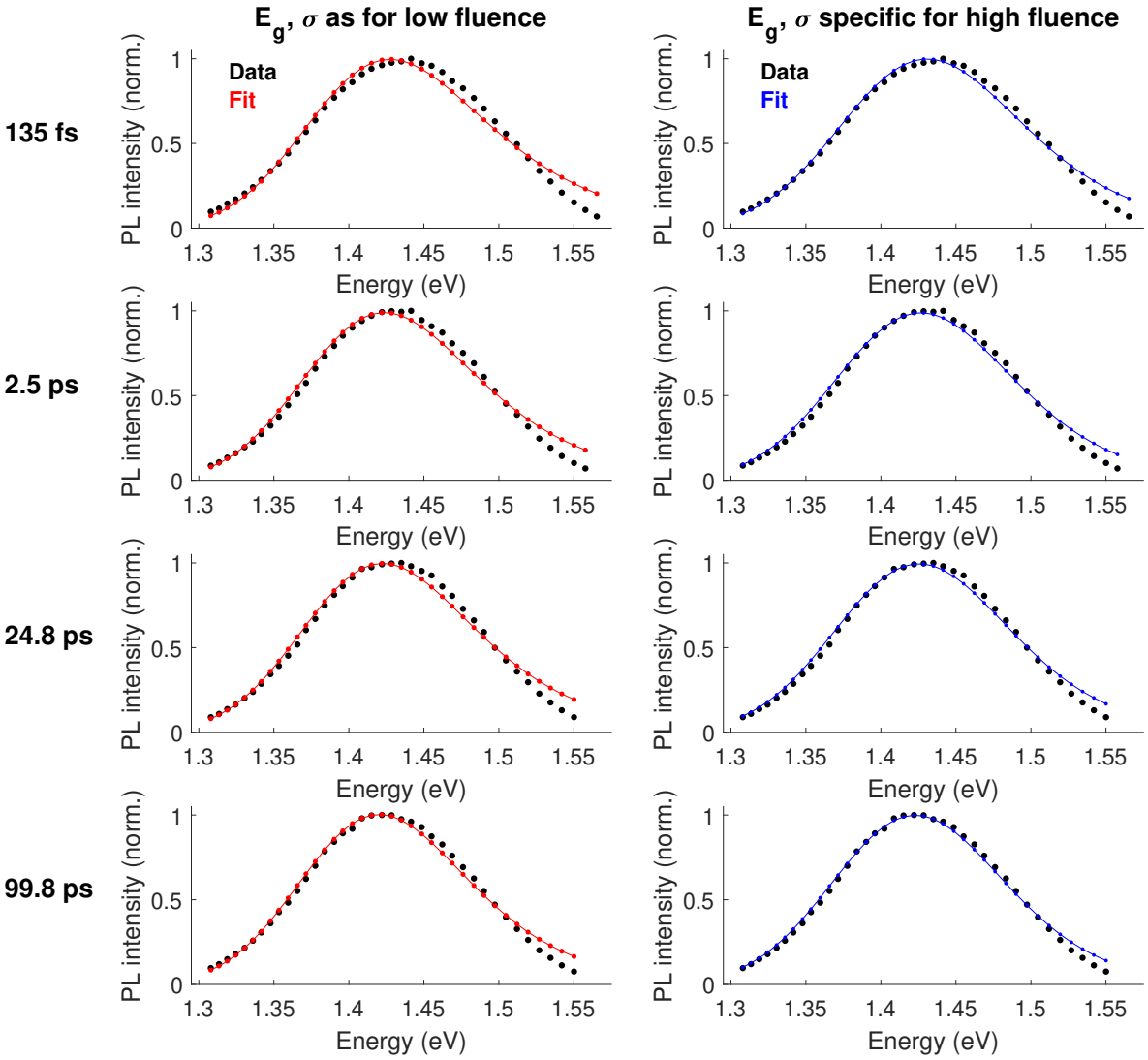


Figure A.4: Example fits to extract carrier temperature from $FASnI_3$ PL spectra excited at 730 nm with a fluence of 3.75 μJ cm^{-2}, showing the influence of assuming one set of values for E_g and σ regardless of excitation fluence (left column, red fits) versus allowing different values for each fluence (right column, blue fits). Measured data at various delay times as indicated are shown by black point markers. Fitted spectra ignoring power-dependent peak shift and using $E_g = 1.3767$ eV and $\sigma = 43.4$ meV as determined for excitation at 0.75 μJ cm^{-2} are plotted in red. Fitted spectra using the parameter values determined for 3.75 μJ cm^{-2} excitation fluence, $E_g = 1.3850$ eV and $\sigma = 48.3$ meV, which give a fitted spectrum closer to the measured data, are plotted in blue.

On the other hand, allowing the value of E_g to vary freely in each fit, including over time after excitation, would offer a route to account for state filling in the context of energetic disorder that may contribute to a red shift in peak position with decreasing carrier density over time after excitation as well as at lower excitation fluences. However, as the apparent red shift in peak position due to decreasing carrier temperature (also illustrated in Figure 4.3) is greater than the observed power-dependent shift for relevant fluences, allowing E_g to vary for each individual spectrum would risk overlooking real cooling dynamics, particularly at early times after excitation when carrier temperature is highest. The similar offset between spectra at each delay time after excitation in Figure A.3B further indicates that the small peak shift due to excitation fluence is preserved over the timescale of carrier cooling and so assuming a fixed value of E_g for carrier temperature fitting, determined separately for each excitation fluence, is an appropriate means to account for the observed power-dependent effects.

B

Supplementary figures and tables, and details of terahertz spectroscopy analysis, for Chapter 6

Contents

B.1 Structural characterisation by X-ray diffraction 158
B.2 Analysis of terahertz spectroscopy results 160
B.3 Supplementary absorption and photoluminescence figures . 169

This appendix gives additional detail on the analysis of data from X-ray diffraction and terahertz spectroscopy measurements reported in Chapter 6, and contains supplementary figures including the measured absorbance and photoluminescence spectra from which the absorption onset, PL broadening, and Stokes shift discussed in Chapter 6 were determined.

B.1 Structural characterisation by X-ray diffraction

To identify impurity peaks present in the measured XRD patterns for $FA_{0.83}Cs_{0.17}Sn_xPb_{1-x}I_3$ thin films, reference data for likely impurities were obtained from literature as detailed in Table B.1 and plotted in Figure 6.3A. The impurities considered are the known precursor materials, together with SnO_2 and SnI_4 which were identified as

the main degradation products likely to form on exposure to oxygen and moisture, aside from the precursor compounds. [178] Section 6.3.1.1 describes the full process of assigning peaks in the measured diffraction patterns, drawing on comparison to these reference data.

Material	Literature source for XRD pattern
FAI	Petrov et. al., *Acta Crystallogr., Sect. E: Crystallogr. Commun.*, **2017**, 73, 569-572 [334]
CsI	Aleksandrov, Goncharov, Makarenko and Stishov, *Phys. Rev. B*, **1991**, 43, 1990 [335]
PbI_2	Palosz, *J. Phys.: Condens. Matter*, **1990**, 2, 5285 [336]
SnI_2	Howie, Moser and Trevena, *Acta Crystallogr., Sect. B: Struct. Crystallogr. Cryst. Chem.*, **1972**, 28, 2965-2971 [337]
SnF_2	Denes, Pannetier, Lucas and Le Marouille, *J. Solid State Chem.*, **1979**, 28, 2965-2971 [338]
SnI_4	Reuter and Pawlak, *Z. Kristallogr. Cryst. Mater.*, **2001**, 216, 34-38 [339]
SnO_2	Yamanaka, Kurashima and Mimaki, *Z. Kristallogr. Cryst. Mater.*, **2000**, 215, 424-428 [340]

Table B.1: Literature sources for the XRD patterns of $FA_{0.83}Cs_{0.17}Sn_xPb_{1-x}I_3$ precursor materials and tin degradation products, as plotted in Figure 6.3A.

Figure B.1 shows the full measured diffraction patterns for $FA_{0.83}Cs_{0.17}Sn_xPx_{1-x}I_3$ samples across the tin-lead range with either 0 % or 20 % SnF_2 added during preparation. Perovskite peaks identified as described in Section 6.3.1.1 are marked in the figure, including the three peaks of interest also shown in Figure 6.4A. These are the lowest angle perovskite peak, pseudocubic (100), which is clear in each of the measured diffraction patterns; the pseudocubic (111) peak which is also common across all compositions shown and exhibits variable broadening; and the tetragonal (231) peak which appears correlated with tin fraction and anti-correlated with SnF_2 percentage. These trends are analysed in Section 6.3.1.2.

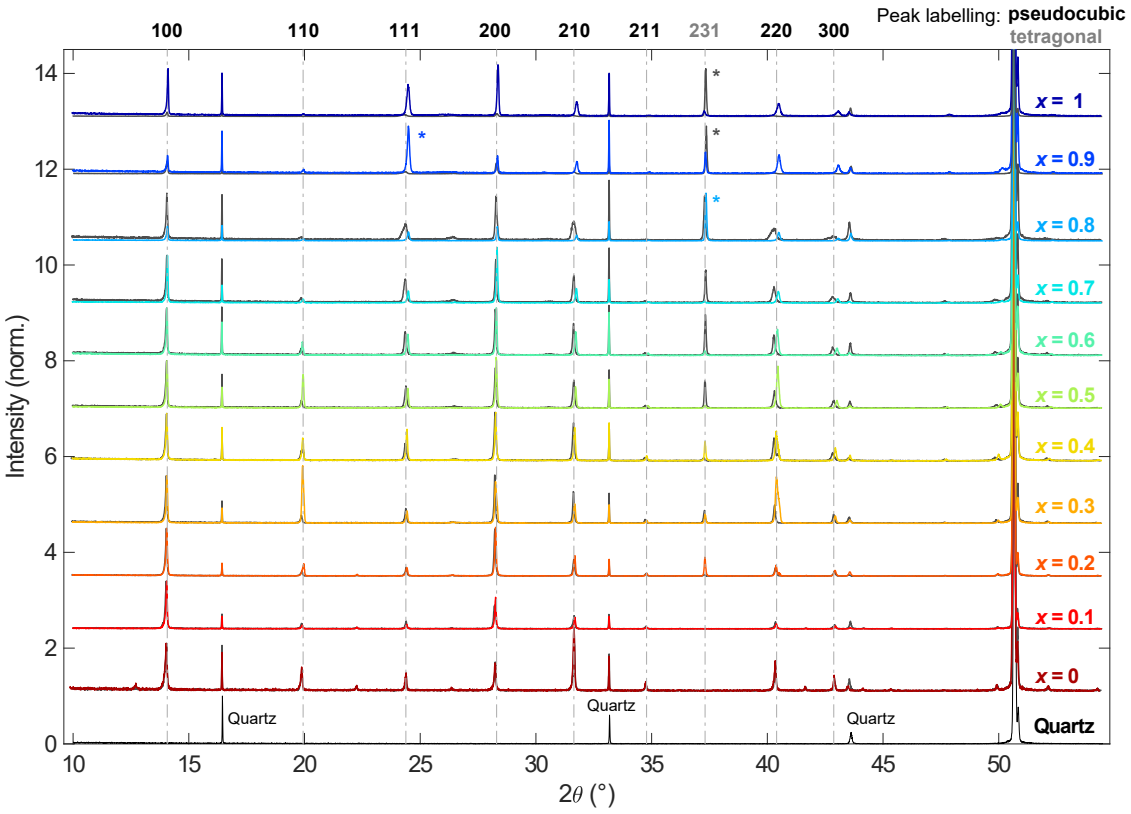


Figure B.1: Measured XRD patterns for $FA_{0.83}Cs_{0.17}Sn_xPx_{1-x}I_3$ thin films on z-cut quartz with tin fraction x ranging from 0 to 1 as indicated. Patterns for samples without SnF_2 added to the tin precursor solution during preparation are shown by dark grey lines, those for samples with 20 % SnF_2 added are overlaid using coloured lines. Peaks identified as originating from the perovskite layer are marked by light grey dash-dot lines labelled with the corresponding Miller indices, and each pattern is normalised to the (100) peak except in cases where another perovskite peak was much more intense, in which case normalisation is to the peak marked by an asterisk. The measured XRD pattern of a blank z-cut quartz substrate is included in black at the bottom of the figure for reference.

B.2 Analysis of terahertz spectroscopy results

This section provides details on the analysis of data from terahertz measurements, results of which are included in Chapter 6. *Both the original terahertz measurements and subsequent analysis as described below were conducted by Aleksander M. Ulatowski (Department of Physics, University of Oxford).*

Terahertz transmission through photoexcited films

In the literature, the relationship between photoconductivity of a thin film and the differential THz transmission signal obtained by OPTP measurements has been investigated with the assumption that the reference sample (for work in this thesis, the same thin film without photoexcitation) is not conductive. [341, 342] The photoconductivity σ_{photo} (i.e. conductivity arising from photoexcited charge carriers) is then given by Equation B.1. [92, 94, 141, 302]

$$\sigma_{\text{photo}} = \left[\frac{\epsilon_0 c(n_A + n_B)}{L}\right]\frac{\Delta T}{T} \tag{B.1}$$

Here ϵ_0 is the permittivity of free space, c the speed of light, $n_A = 1$ the vacuum refractive index, $n_B = n_{\text{quartz}} = 2.13$ [92] the refractive index of the substrate, L the thickness of the sample, and $\Delta T/T$ the ratio of the photoinduced change in THz transmission to the transmission through the sample without photoexcitation.

For tin-containing perovskites with relatively high dark conductivity, the assumption of no conductivity in the reference samples used to derive Equation B.1 [341] breaks down. Accounting for the contribution of background electric doping gives a modified equation: [343]

$$\sigma_{\text{photo}} = \left[\sigma_{\text{dark}} + \frac{\epsilon_0 c(n_A + n_B)}{L}\right]\frac{\Delta T}{T} \tag{B.2}$$

with σ_{dark} the DC Drude conductivity of the sample without photoexcitation. To evaluate the photoconductivity and hence the mobility of $FA_{0.83}Cs_{0.17}Sn_xPb_{1-x}I_3$ thin films as in Chapter 6, Equation B.2 was therefore used, with dark conductivity determined as described below.

Sample thickness used in terahertz conductivity analysis

The film thickness L used for terahertz conductivity analysis as discussed in this appendix was taken as 400 nm. This value is representative for the $FA_{0.83}Cs_{0.17}Sn_xPb_{1-x}I_3$ thin films

measured, which were determined to have mean thickness 430 ± 30 nm by calculation as $L = \frac{A}{\alpha}$ using measured values of A (see Section 6.2.3) and known values of the absorption coefficient α for samples with equivalent composition measured previously. [328]

Analysis of dark conductivity spectra

Dark conductivity spectra were measured as described in Section 6.2.5, and the measured time-dependent field strength of the THz pulse was Fourier-transformed into frequency space to calculate spectra according to Equation B.3 with transmission through a bare, non-conductive z-cut quartz substrate used as a reference.

$$\sigma_{\text{dark}}(\omega) = \left[\frac{\epsilon_0 c(n_A + n_B)}{L}\right] \frac{T_{\text{quartz}}(\omega) - T_{\text{sample}}(\omega)}{T_{\text{sample}}(\omega)} \tag{B.3}$$

Background hole densities as shown in Figures 6.7B and 6.12 were then determined from the real part of the complex dark conductivity spectra using the Drude conductivity model, with the assumption that electron and hole mobilities are balanced ($\mu_e = \mu_h = \frac{\mu}{2}$): [344]

$$\sigma_{\text{dark}}(\omega) = \frac{\sigma_{\text{DC}}}{1 - i\omega\tau} = \frac{p_0 e\mu/2}{1 - i\omega\tau} \tag{B.4}$$

In Equation B.4, σ_{DC} is the DC conductivity limit ($\omega \to 0$), τ the average charge-carrier scattering time, and p_0 the background hole density in the doped films. Since the charge-carrier scattering time in MHPs was previously shown to be short compared to THz oscillation period ($\frac{1}{\tau} >> \omega$), [141] the real dark conductivity in the 0.5 – 2 THz spectral region as shown in Figure 6.7A in Chapter 6, and Figures B.2, B.3 and B.4A here, represents the DC conductivity of samples that has a constant value as indicated in Equation B.4 and is equal to:

$$\Re\left[\sigma_{\text{dark}}(\omega < 2\,\text{THz})\right] = p_0 e\,\frac{\mu}{2} \tag{B.5}$$

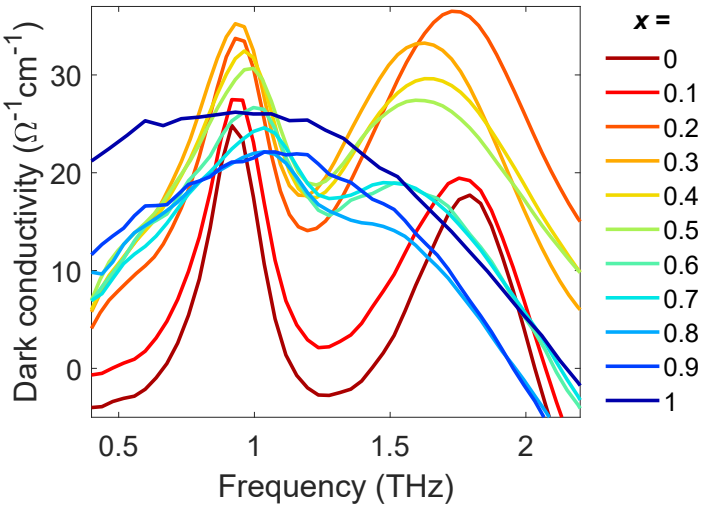


Figure B.2: Dark conductivity spectra (real part) of $FA_{0.83}Cs_{0.17}Sn_xPb_{1-x}I_3$ thin films on z-cut quartz prepared with 20 % SnF_2 added to the tin precursor solution at tin fractions x as indicated in the legend, showing the response from lattice vibrations. Spectra are shown with no vertical offsets added, to allow the phonon response strength at different tin fractions to be directly compared. Phase error due to differences in the thickness of the sample and reference substrates between measurements contributes to variations in peak intensity, with this effect being more pronounced at high frequency, as discussed by La-o-vorakiat et al. [345]

In order to extract background hole doping densities using Equation B.5 from the dark conductivity spectra calculated using Equation B.3, it was first necessary to subtract the phonon contribution from these spectra. This is because the dark conductivity spectra encapsulate the contribution of both free charge carriers and the thin film lattice response, and there are prominent optical phonon features in the spectral range of interest. [92] For samples with 20 % SnF_2 added, the contribution of free charge carriers is suppressed to the point where conductivity spectra are dominated by the optical phonon response, as shown in Figure B.2. Therefore, the dark conductivity spectra measured with 20 % SnF_2 were subtracted as the phonon response contribution.

The effect of subtracting phonon response from dark conductivity spectra is shown in Figure B.3, where the raw real dark conductivity spectra are shown on the left and the corresponding phonon-subtracted spectra on the right. Features at ∼1 THz and ∼1.5 THz originating from optical phonon modes of the tin/lead-iodide sublattice vibrations [92]

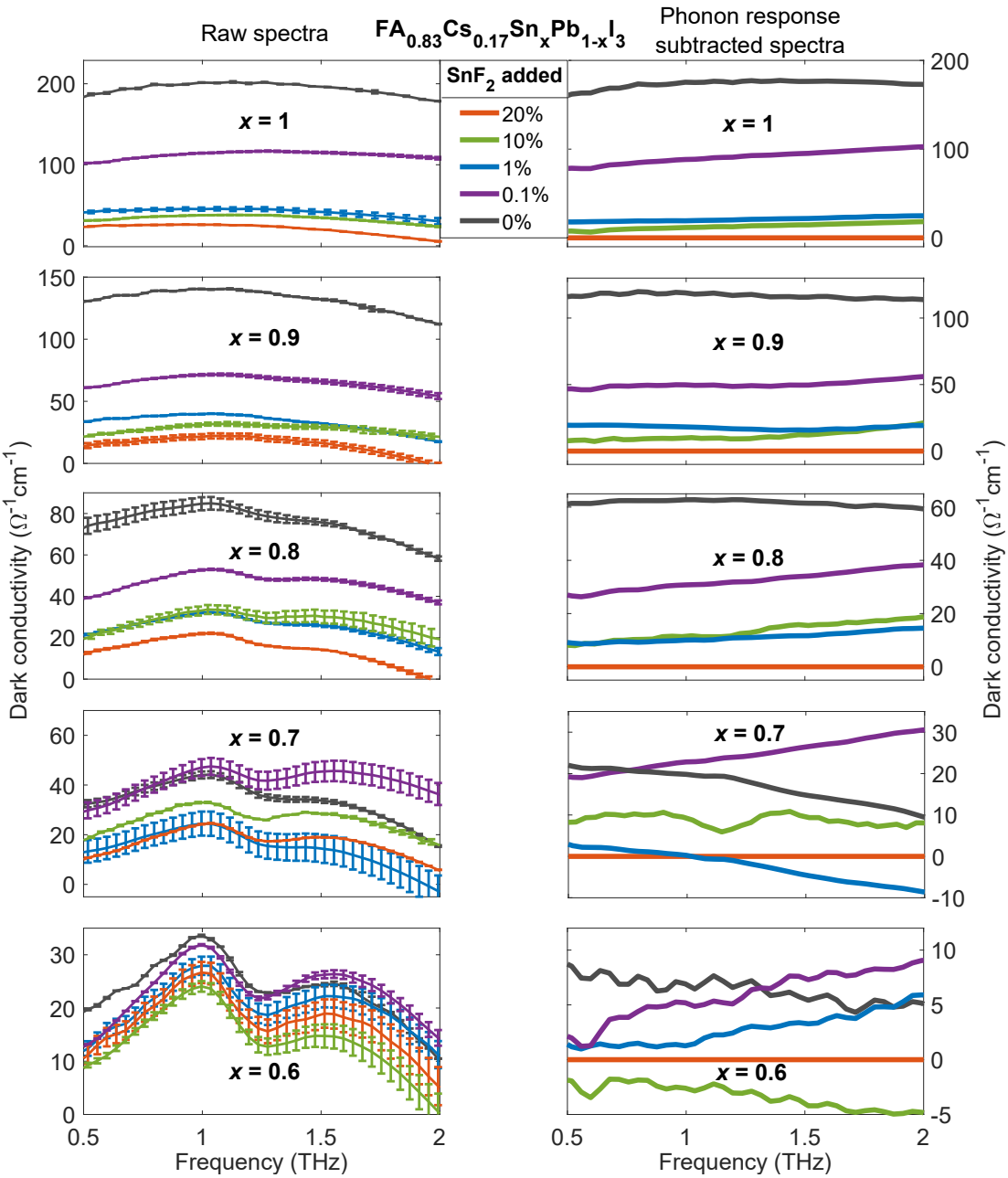


Figure B.3: Raw real dark conductivity spectra (left) including both optical phonon response and background hole conductivity from unintentional doping, and dark hole conductivity spectra with phonon contribution subtracted (right) of $FA_{0.83}Cs_{0.17}Sn_xPb_{1-x}I_3$ thin films with varying tin fraction x as labelled in each panel. The SnF_2 percentage added to the tin precursor solution for each sample is indicated in the legend.

are clearly apparent in the raw spectra only. As a consequence of taking the 20 % SnF_2 spectra at each tin fraction as the phonon response, the phonon-subtracted spectra for the 20 % SnF_2 condition (plotted in orange) are uniformly zero and cannot be used in any further analysis. Comparing the rest of the phonon-subtracted spectra it is clear that while SnF_2 addition substantially decreases dark conductivity at high tin fractions by reducing tin oxidation, at lower tin fractions there is already much lower background hole density, and no noticeable effect of SnF_2.

The phonon-subtracted real dark conductivity spectra (shown on the right in Figure B.3) were used along with mobility values obtained from OPTP measurement (as described below) to calculate background hole density according to Equation B.5.

Optical phonon response

In addition to being used to subtract phonon response before calculating background hole density as described above, the raw real dark conductivity spectra of $FA_{0.83}Cs_{0.17}Sn_xPb_{1-x}I_3$ samples with 20 % SnF_2 added can be used to examine changes in optical phonon response with tin fraction. These spectra, shown with vertical offsets for clarity in Figure B.4A, exhibit an optical phonon peak near to 1 THz that shifts to higher frequency as tin fraction increases. This peak has previously been assigned to metal-halide sublattice vibrations in lead-iodide perovskites, [92] and so the lower atomic mass of tin compared to lead can be considered to explain the frequency shift. This explanation is supported by the agreement between observed phonon frequencies and the trend predicted by a simple model of masses on a spring, as shown in Figure B.4B. The frequencies predicted by extrapolation from the phonon peak position at $x = 0$ using this simple model are plotted as a solid grey line in the figure, while the frequencies determined from measured spectra are shown by coloured markers. Within the resolution of the measurement (shown by error bars on the data points and the shaded region around the predicted trend line) there is good agreement

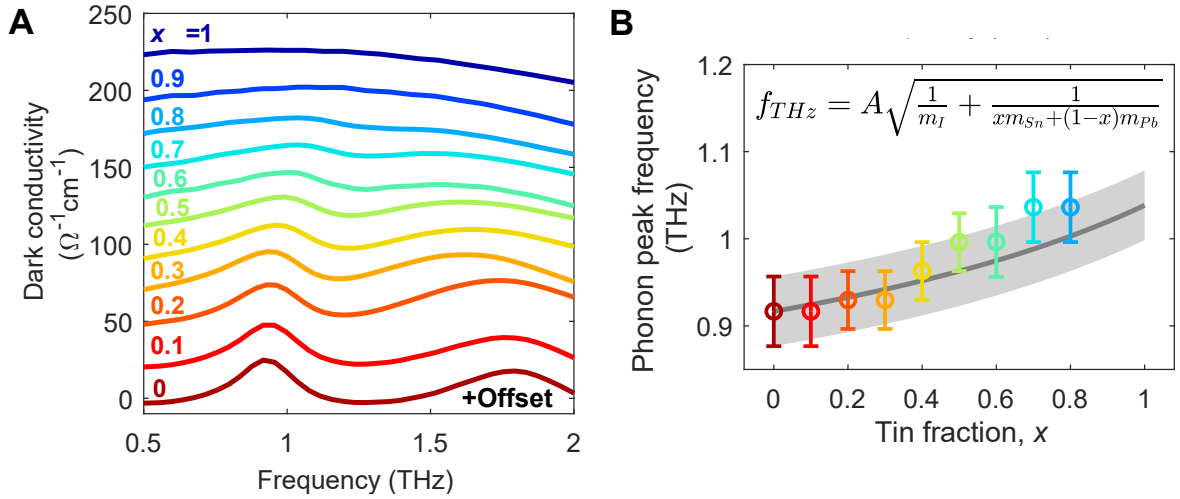


Figure B.4: Dark conductivity spectra (real part) of $FA_{0.83}Cs_{0.17}Sn_xPb_{1-x}I_3$ thin films on z-cut quartz showing phonon response (panel A), and trend in frequency of the optical phonon peak near 0.8 – 1 THz across the lead to tin range (panel B). Perovskite samples were prepared with 20 % SnF_2 added to the tin precursor solution in each case. **A)** Dark conductivity spectra (real part) of perovskite samples at tin fractions x as labelled, showing the broadening and shift in frequency of the optical phonon peak with increasing tin fraction. Vertical offsets of $+20\,\Omega^{-1}$ cm^{-1} per sample have been added for clarity. **B)** Relationship between tin fraction and frequency of the optical phonon peak near 1 THz associated with vibration of the tin/lead-iodide sublattice. Error bars representing the spectral resolution of the measurement are shown for each peak position. The grey solid line shows frequencies predicted from the $x = 0$ phonon peak using the equation shown for a simple relationship between frequency and reduced mass of the inorganic elements. The shaded grey region shows the error on these predicted values. Frequency data are not shown for $x = 0.9$ or 1, as for these samples spectra are too broadened to clearly identify phonon peak position. [Adapted with permission from *Adv. Funct. Mater.* 2020, **30**, 2005594 [290] Copyright 2020 John Wiley and Sons.]

between observed frequencies and the prediction based on changes in average atomic mass of the metal cation with tin fraction. This explanation is therefore sufficient, and any structural changes that might influence phonon peak position can play only a minor role.

Observation of this shift in phonon peak frequency has not previously been possible for tin-based perovskites because of the dual limitations of spectral broadening and large contribution of background hole doping to measured dark conductivity spectra, which was reduced here by addition of 20 % SnF_2. Significant broadening is still seen as tin fraction increases, and is associated with reduced optical phonon lifetime, [346] which based on calculations for inorganic semiconductors can be partially attributed to decreasing mass of the metal cation. [347, 348]

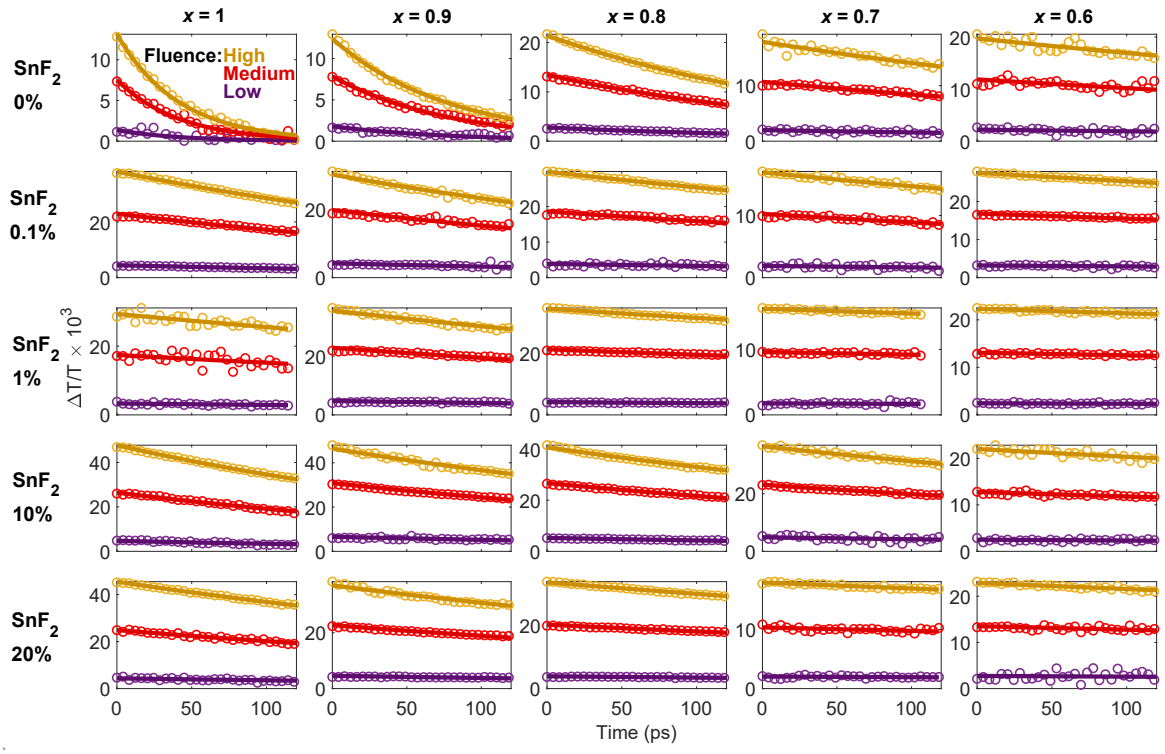


Figure B.5: Photoconductivity dynamics of $FA_{0.83}Cs_{0.17}Sn_xPb_{1-x}I_3$ thin films at varying tin fraction x and with different added SnF_2 percentages as labelled. Photoconductivity measurements were conducted at three different excitation fluences for each sample, which are colour coded in the figure as indicated with values listed in Table B.2.

Calculating charge-carrier mobility from OPTP measurements

The sum mobility of photoexcited charge carriers, μ, was estimated from the onset of measured terahertz photoconductivity (shown in Figure B.5) at time = 0 using the Drude model of low-frequency (DC) conductivity: [349]

$$\sigma_{\text{photo}}(t) = \Big[\mu_{\text{e}} n(t) + \mu_{\text{h}} p(t)\Big] e \overset{\text{t=0}}{=} \mu n_0 e \tag{B.6}$$

In this equation μ_{e} and μ_{h} are the individual electron and hole mobilities, μ is the sum mobility of the charge carriers ($\mu_{\text{e}} + \mu_{\text{h}} = \mu$), n and p are the number densities of photoexcited electrons and holes respectively, n_0 is the initial number density of photoexcited electron-hole pairs, and e is the elementary charge.

The value of n_0 used in Equation B.6 was calculated using steady-state absorption data at the pump wavelength (400 nm) and the excitation fluence as shown in Table B.2,

Fluence set (μJ cm^{-2})			Samples measured
Low	Medium	High	
1.33	7.53	12.74	$x = 0.7$: 0, 0.1, 1, and 20 % SnF_2
1.47	8.13	13.97	$x = 0.6$: 0, 1, 10 and 20 % SnF_2. $x = 1$: 0, 1, 10 and 20 % SnF_2
1.97	10.77	18.1	$x = 0.6$: 0.1 % SnF_2 $x = 0.8$: 0, 0.1, 1, and 20 % SnF_2 $x = 0.9$: 0, 0.1, 1, and 20 % SnF_2 $x = 1$: 0.1 % SnF_2
2.36	13.26	22.5	$x = 0.7$: 10 % SnF_2. $x = 0.8$: 10 % SnF_2 $x = 0.9$: 10 % SnF_2.

Table B.2: Photoexcitation beam fluences used for terahertz photoconductivity decay measurements as shown in Figure B.5.

with the assumption that each absorbed photon generates one photoexcited electron-hole pair (this is realistic given the low exciton binding energy reported for MHPs). [58, 63, 64, 92]. The mobilities shown in Figure 6.12 are averages of the values calculated for each sample included in Figure B.5 at all three excitation fluences. The calculated charge-carrier mobility does not depend on the thickness of the thin film samples, as the thickness dependence of the photoconductivity (calculated according to Equation B.2) and of the initial density of photoexcited charge-carrier pairs cancel out. [92]

Fitting empirical relationship between charge-carrier mobility and doping density

Fits to the calculated charge-carrier mobilities, as shown in Figure 6.12, were carried out using the empirical relationship between mobility and doping density as given by Hilsum in Equation B.7: [332]

$$\mu = \frac{\mu_{\mathrm{L}}}{1 + \sqrt{N/N_0}} \tag{B.7}$$

The values of the lattice-scattering-limited charge-carrier mobility μ_L, and the normalising density of dopants N_0, from these fits are recorded in Table B.3.

Tin fraction, x	μ_L (cm^2/Vs)	N_0 (cm^{-3})
0.6	48.00	3.76×10^{19}
0.7	55.75	3.76×10^{19}
0.8	68.68	3.76×10^{19}
0.9	76.26	3.76×10^{19}
1	101.43	3.76×10^{19}

Table B.3: Values of the parameters in Equation B.7 from the fits as shown in Figure 6.12 in Chapter 6. The normalising density N_0 was globally optimised for all tin fractions included here.

B.3 Supplementary absorption and photoluminescence figures

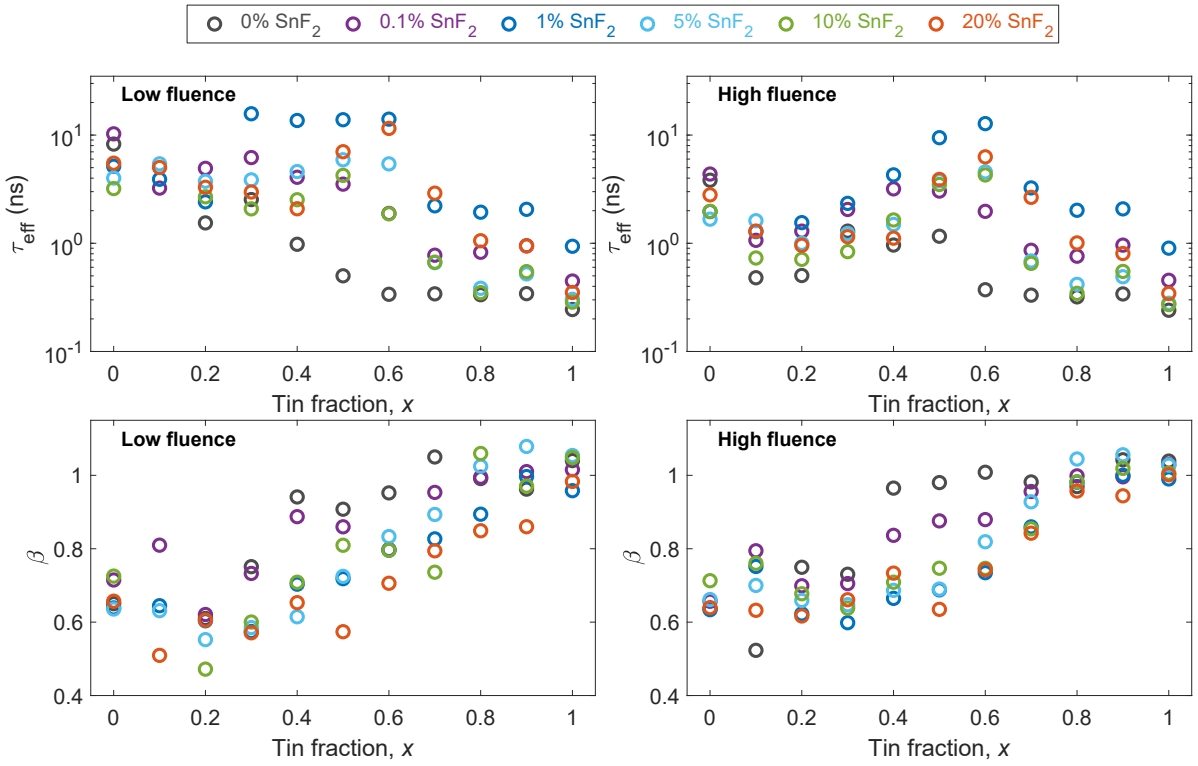


Figure B.6: Effect of SnF_2 additive, at different percentages as indicated in the legend, on PL decay dynamics of $FA_{0.83}Cs_{0.17}Sn_xPb_{1-x}I_3$ thin films with varying tin fraction x, as quantified by effective lifetime (top) and stretching parameter (bottom) from stretched exponential fits. The spread of values for samples at $x = 0$ reflects experimental error and variation between sets of samples without intended changes in composition, since these $x = 0$ samples are prepared with none of the tin precursor solution to which the specified amounts of SnF_2 are added.

Photoluminescence decay transients

Figure B.6 shows the values of τ_{eff} and β obtained from stretched exponential fits as described in Section 6.2.6.1 for the full set of tin fractions and SnF_2 percentages covered. Experimental error on these values, indicated by the spread for samples at $x = 0$ which are all equivalent in composition, is relatively large. Taking this into account, it is still possible to identify overall trends of decreasing PL lifetime with increasing tin fraction, longer lifetimes on addition of SnF_2 with particularly large effect at tin fractions 0.5 and 0.6 and with 1 % SnF_2, and increasing β as tin fraction increases which is partially counteracted by addition of SnF_2. These trends are discussed in Section 6.3.3 with reference to majority tin samples; for low tin fractions, as can be seen here, there is no meaningful trend in either lifetime or stretching parameter with SnF_2 addition.

Absorbance spectra

Figure B.7 shows the full set of absorbance spectra measured for $FA_{0.83}Cs_{0.17}Sn_xPb_{1-x}I_3$ samples across the range of tin fractions x from 0 to 1 and SnF_2 percentages from 0 to 20 %. These spectra show bandgap bowing across the range of tin fractions giving a redshift in the absorption edge as x increases from 0 and smaller blueshift from intermediate compositions up to $x = 1$, and a shift to lower energy with SnF_2 addition for high tin fraction samples. Both trends are quantified by the absorption onset energies in Figures 6.9A and 6.10.

Photoluminescence spectra

Figure B.8 shows representative sets of $FA_{0.83}Cs_{0.17}Sn_xPb_{1-x}I_3$ photoluminescence spectra measured for samples across the full range of tin fractions, with varying amounts of SnF_2 added. For each spectrum, data measured on two detectors are combined as described in Section 3.1.2.1 in order to best capture the broad emission of these samples over a spectral range where the response of both Si and InGaAs detectors is changing significantly.

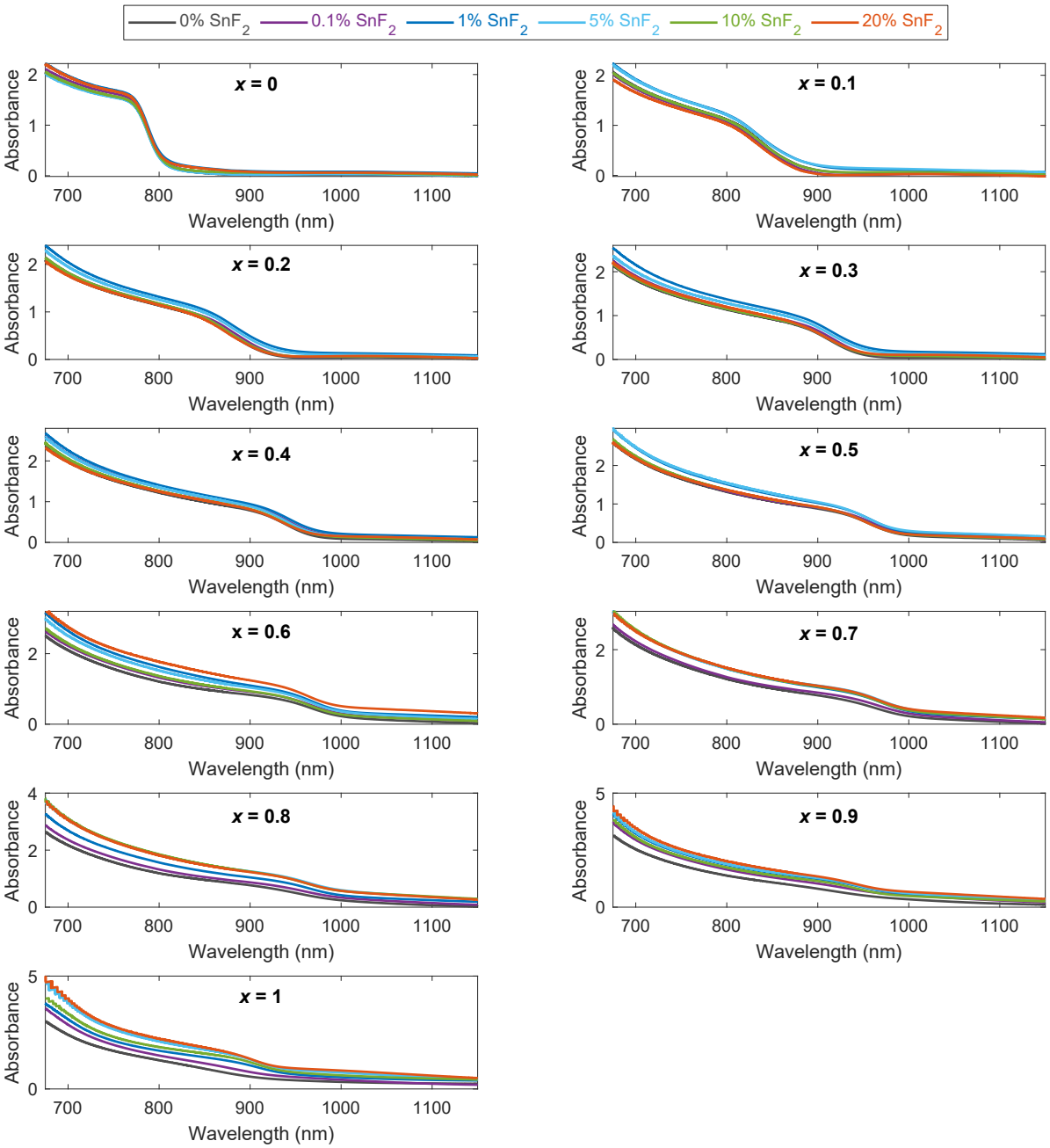


Figure B.7: Absorbance spectra of $FA_{0.83}Cs_{0.17}Sn_xPb_{1-x}I_3$ thin films on z-cut quartz substrates with tin fractions as labelled, and different amounts of SnF_2 added to the tin precursor solution during preparation as indicated in the legend. Absorbance is calculated as $A = -\ln(T/(1-R))$ from measured reflectance and transmittance spectra. Note that the six spectra plotted for $x = 0$ were measured on individual samples prepared as part of the set with SnF_2 added to the tin precursor solution in the percentage indicated by line colour, but the actual SnF_2 content at $x = 0$ is 0 % in all cases.

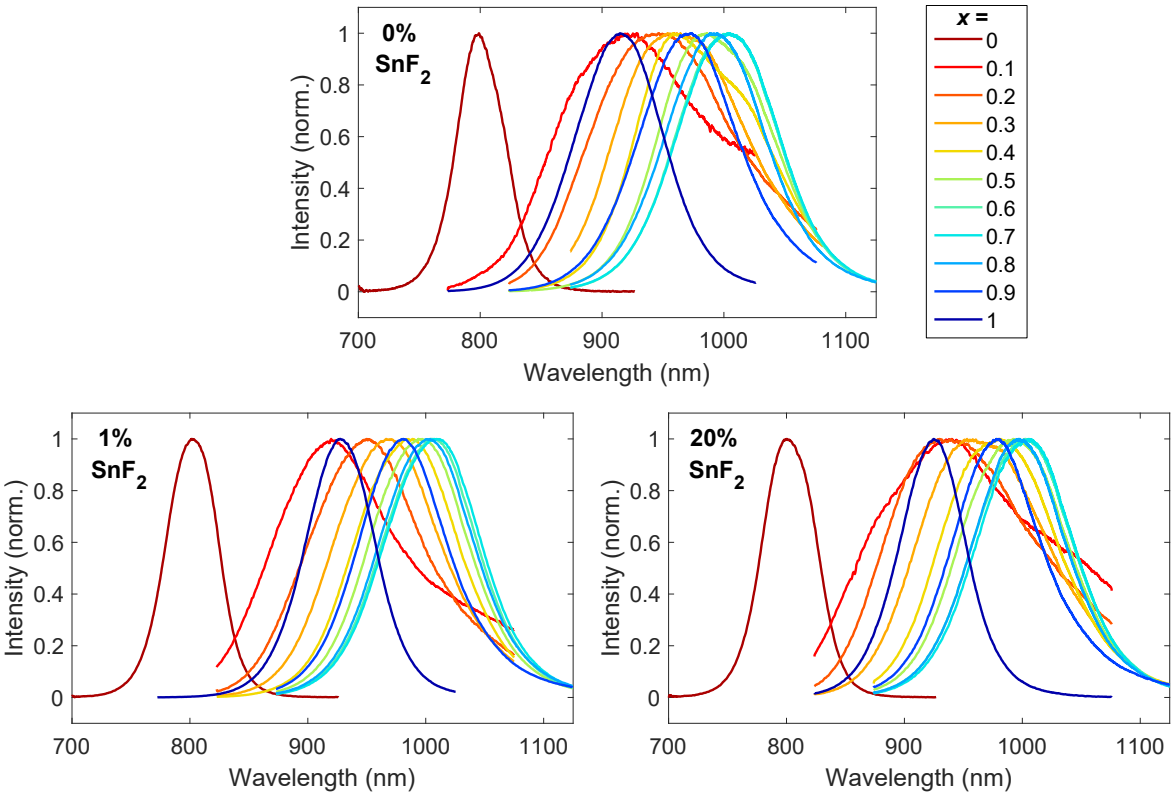


Figure B.8: Photoluminescence spectra of $FA_{0.83}Cs_{0.17}Sn_xPb_{1-x}I_3$ thin films on z-cut quartz, with 0, 1 or 20 % SnF_2 added to the tin precursor solution during preparation as indicated. Spectra shown combine data measured on both Si and InGaAs detectors as described in Section 6.2.3, using the procedure detailed in Section 3.1.2.1. The same colour scheme for tin fraction x indicated in the legend is used in all three panels.

The FWHM values shown in Figure 6.9B are determined from these combined PL spectra (and the equivalent sets for 0.1 %, 5 % and 10 % SnF_2), as are the peak energies shown in Figure 6.11 which are used to calculate Stokes shifts as shown in Figure 6.9C.

C

Permissions for reuse of material previously published

C.1 Reuse of content from self-authored articles

Where research work reported in this thesis has also been published, as indicated in the publications list and in the captions to figures reproduced or adapted from published articles, permission for reuse of content was obtained as below:

Permission to reuse material from *J. Phys. Chem. Lett.*, 2019, 10, 20, 6018-6047, [225] including figures as noted in Chapters 4 and 5 and Appendix A was granted by the American Chemical Society. The direct link to the original article is https://pubs.acs.org/doi/10.1021/acs.jpclett.9b02353. Any further permissions related to this material in the future should be directed to the ACS.

Permission to reuse material from *Adv. Funct. Mater.*, 2020, 30, 2005594, [290] including figures as noted in Chapter 6 and Appendix B was granted by John Wiley and Sons, and conveyed through Copyright Clearance Center, Inc. The original article can be viewed at https://doi.org/10.1002/adfm.202005594.

C.2 Reuse of content from articles authored by others

Where figures in this thesis have been reproduced from others' published work, permission for reuse was obtained as below:

Figure 2.3 is reprinted from Materials Today, 17, P. P. Boix, K. Nonomura, N. Mathews and S. G. Mhaisalkar, Current progress and future perspectives for organic/inorganic perovskite solar cells, 16-23, Copyright (2014), with permission from Elsevier.

Figure 2.4 is reprinted with permission of Annual Reviews, Inc. from Charge-Carrier Dynamics in Organic-Inorganic Metal Halide Perovskites, L. M. Herz, Annual Review of Physical Chemistry, 67, 2016; permission conveyed through Copyright Clearance Center, Inc.

Figure 3.4 is reprinted with permission of John Wiley and Sons from Ultrafast fluorescence upconversion technique and its applications to proteins, Chosrowjan, H., Taniguchi, S. and Tanaka, F., FEBS Journal, 282, 2015; permission conveyed through Copyright Clearance Center, Inc.

References

[1] UNFCCC. 'Adoption of the Paris Agreement'. *United Nations Framework Convention on Climate Change*. 2015.

[2] *United Nations Treaty Collection*. https://treaties.un.org/Pages/ViewDetails.aspx?src=TREATY&mtdsg_no=XXVII-7-d&chapter=27&clang=_en#EndDec (visited on 13/07/2020).

[3] IEA. *World Energy Outlook 2019*. Tech. rep. Paris, 2019. https://www.iea.org/reports/world-energy-outlook-2019.

[4] International Renewable Energy Agency (IRENA). *Renewable Capacity Statistics 2020*. Tech. rep. Abu Dhabi, 2020.

[5] National Renewable Energy Laboratory (NREL). *Best Research-Cell Efficiency Chart*. 2020. https://www.nrel.gov/pv/cell-efficiency.html (visited on 26/06/2020).

[6] Baikie, T.; Fang, Y.; Kadro, J. M.; Schreyer, M.; Wei, F.; Mhaisalkar, S. G.; Graetzel, M. and White, T. J. 'Synthesis and Crystal Chemistry of the Hybrid Perovskite $(CH_3NH_3)PbI_3$ for Solid-State Sensitised Solar Cell Applications'. *J. Mater. Chem. A*, 2013, **1**, 5628–5641.

[7] Borchert, J.; Milot, R. L.; Patel, J. B.; Davies, C. L.; Wright, A. D.; Martínez Maestro, L.; Snaith, H. J.; Herz, L. M. and Johnston, M. B. 'Large-Area, Highly Uniform Evaporated Formamidinium Lead Triiodide Thin Films for Solar Cells'. *ACS Energy Lett.*, 2017, **2**, 2799–2804.

[8] Eperon, G. E.; Hörantner, M. T. and Snaith, H. J. 'Metal Halide Perovskite Tandem and Multiple-Junction Photovoltaics'. *Nat. Rev. Chem.*, 2017, **1**, 1–18.

[9] Song, Z; Chen, C; Li, C; Awni, R. A.; Zhao, D and Yan, Y. 'Wide-Bandgap, Low-Bandgap, and Tandem Perovskite Solar Cells'. *Semicond. Sci. Technol.*, 2019, **34**.

[10] Le Bris, A and Guillemoles, J.-F. 'Hot Carrier Solar Cells: Achievable Efficiency Accounting for Heat Losses in the Absorber and Through Contacts'. *Appl. Phys. Lett.*, 2010, **97**, 113506.

[11] Li, M.; Fu, J.; Xu, Q. and Sum, T. C. 'Slow Hot-Carrier Cooling in Halide Perovskites: Prospects for Hot-Carrier Solar Cells'. *Adv. Mater.*, 2019, **31**, 1802486.

[12] Hirst, L. C. and Ekins-Daukes, N. J. 'Fundamental Losses in Solar Cells'. *Prog. Photovolt. Res. Appl.*, 2011, **19**, 286–293.

[13] Fang, H.-H.; Adjokatse, S.; Shao, S.; Even, J. and Loi, M. A. 'Long-Lived Hot-Carrier Light Emission and Large Blue Shift in Formamidinium Tin Triiodide Perovskites'. *Nat. Commun.*, 2018, **9**, 243.

[14] Wang, C.; Song, Z.; Li, C.; Zhao, D. and Yan, Y. 'Low-Bandgap Mixed Tin-Lead Perovskites and Their Applications in All-Perovskite Tandem Solar Cells'. *Adv. Funct. Mater.*, 2019, **29**, 1808801.

[15] Yao, H; Zhou, F; Li, Z; Ci, Z; Ding, L and Jin, Z. 'Strategies for Improving the Stability of Tin-Based Perovskite ($ASnX_3$) Solar Cells'. *Adv. Sci.*, 2020, **7**, 1903540.

[16] Gu, S; Lin, R; Han, Q; Gao, Y; Tan, H and Zhu, J. 'Tin and Mixed Lead–Tin Halide Perovskite Solar Cells: Progress and their Application in Tandem Solar Cells'. *Adv. Mater.*, 2020, **32**, 1907392.

[17] IPCC. *Summary for Policymakers. In: Global Warming of 1.5°C. An IPCC special report on the impacts of global warming of 1.5°C above pre-industrial levels and related global greenhouse gas emission pathways, in the context of strengthening the global response to the threat of climate change, sustainable development, and efforts to eradicate poverty.* Tech. rep. 2018.

[18] Kannan, N. and Vakeesan, D. 'Solar Energy for Future World: - A Review'. *Renewable Sustainable Energy Rev.*, 2016, **62**, 1092–1105.

[19] Prăvălie, R.; Patriche, C. and Bandoc, G. 'Spatial Assessment of Solar Energy Potential at Global Scale. A Geographical Approach'. *J. Cleaner Prod.*, 2019, **209**, 692–721.

[20] Fischer, M.; Woodhouse, M.; Herritsch, S. and Trube, J. *International Technology Roadmap for Photovoltaic 2020.* Frankfurt, 2020. https://itrpv.vdma.org/en/ueber-uns.

[21] Green, M. A.; Dunlop, E. D.; Hohl-Ebinger, J.; Yoshita, M.; Kopidakis, N. and Ho-Baillie, A. W. Y. 'Solar Cell Efficiency Tables (Version 56)'. *Prog. Photovolt. Res. Appl.*, 2020, **28**, 629–638.

[22] Gerbinet, S.; Belboom, S. and Léonard, A. 'Life Cycle Analysis (LCA) of Photovoltaic Panels: A Review'. *Renewable Sustainable Energy Rev.*, 2014, **38**, 747–753.

[23] Hou, G.; Sun, H.; Jiang, Z.; Pan, Z.; Wang, Y.; Zhang, X.; Zhao, Y. and Yao, Q. 'Life Cycle Assessment of Grid-Connected Photovoltaic Power Generation from Crystalline Silicon Solar Modules in China'. *Appl. Energy*, 2016, **164**, 882–890.

[24] Wagner, P.; Wackers, G.; Cardinaletti, I.; Manca, J. and Vanacken, J. 'From Colossal Magnetoresistance to Solar Cells: An Overview on 66 Years of Research into Perovskites'. *Phys. Status Solidi A*, 2017, **214**, 1700394.

[25] Weber, D. '$CH_3NH_3PbX_3$, ein Pb (II)-System mit Kubischer Perowskitstruktur/$CH_3NH_3PbX_3$, a Pb (II)-System with Cubic Perovskite Structure'. *Z. Naturforsch. B*, 1978, **33**, 1443–1445.

[26] Wasylishen, R. E.; Knop, O. and Macdonald, J. B. 'Cation Rotation in Methylammonium Lead Halides'. *Solid State Commun.*, 1985, **56**, 581–582.

[27] Poglitsch, A. and Weber, D. 'Dynamic Disorder in Methylammoniumtrihalogenoplumbates (II) Observed by Millimeter-Wave Spectroscopy'. *J. Chem. Phys.*, 1987, **87**, 6373–6378.

[28] Goldschmidt, V. M. 'Die Gesetze der Krystallochemie'. *Naturwissenschaften*, 1926, **14**, 477–485.

[29] Papavassiliou, G. C. 'Synthetic Three-and Lower-Dimensional Semiconductors Based on Inorganic Units'. *Mol. Cryst. Liq. Cryst.*, 1996, **286**, 231–238.

[30] Saidaminov, M. I.; Mohammed, O. F. and Bakr, O. M. 'Low-Dimensional-Networked Metal Halide Perovskites: The Next Big Thing'. *ACS Energy Lett.*, 2017, **2**, 889–896.

[31] Mitzi, D. B.; Feild, C.; Harrison, W. and Guloy, A. 'Conducting Tin Halides with a Layered Organic-Based Perovskite Structure'. *Nature*, 1994, **369**, 467–469.

[32] Kagan, C.; Mitzi, D. and Dimitrakopoulos, C. 'Organic-Inorganic Hybrid Materials as Semiconducting Channels in Thin-Film Field-Effect Transistors'. *Science*, 1999, **286**, 945–947.

[33] Chondroudis, K. and Mitzi, D. B. 'Electroluminescence from an Organic-Inorganic Perovskite Incorporating a Quaterthiophene Dye Within Lead Halide Perovskite Layers'. *Chem. Mater.*, 1999, **11**, 3028–3030.

[34] Mitzi, D. B.; Dimitrakopoulos, C. D. and Kosbar, L. L. 'Structurally Tailored Organic–Inorganic Perovskites: Optical Properties and Solution-Processed Channel Materials for Thin-Film Transistors'. *Chem. Mater.*, 2001, **13**, 3728–3740.

[35] Hamann, T. W.; Jensen, R. A.; Martinson, A. B. F.; Van Ryswyk, H and Hupp, J. T. 'Advancing Beyond Current Generation Dye-Sensitized Solar Cells'. *Energy Environ. Sci.*, 2008, **1**, 66–78.

[36] Kojima, A.; Teshima, K.; Shirai, Y. and Miyasaka, T. 'Organometal Halide Perovskites as Visible-Light Sensitizers for Photovoltaic Cells'. *J. Am. Chem. Soc.*, 2009, **131**, 6050–6051.

[37] Burschka, J.; Dualeh, A.; Kessler, F.; Baranoff, E.; Cevey-Ha, N.-L.; Yi, C.; Nazeeruddin, M. K. and Grätzel, M. 'Tris(2-(1H-pyrazol-1-yl)pyridine)cobalt(III) as p-Type Dopant for Organic Semiconductors and Its Application in Highly Efficient Solid-State Dye-Sensitized Solar Cells'. *J. Am. Chem. Soc.*, 2011, **133**, 18042–18045.

[38] Im, J.-H.; Lee, C.-R.; Lee, J.-W.; Park, S.-W. and Park, N.-G. '6.5% Efficient Perovskite Quantum-Dot-Sensitized Solar Cell'. *Nanoscale*, 2011, **3**, 4088–4093.

[39] Snaith, H. J. 'Perovskites: the Emergence of a New Era for Low-Cost, High-Efficiency Solar Cells'. *J. Phys. Chem. Lett.*, 2013, **4**, 3623–3630.

[40] Burschka, J.; Pellet, N.; Moon, S.-J.; Humphry-Baker, R.; Gao, P.; Nazeeruddin, M. K. and Grätzel, M. 'Sequential Deposition as a Route to High-Performance Perovskite-Sensitized Solar Cells'. *Nature*, 2013, **499**, 316–319.

[41] Lee, M. M.; Teuscher, J.; Miyasaka, T.; Murakami, T. N. and Snaith, H. J. 'Efficient Hybrid Solar Cells Based on Meso-Superstructured Organometal Halide Perovskites'. *Science*, 2012, **338**, 643–647.

[42] Ball, J. M.; Lee, M. M.; Hey, A. and Snaith, H. J. 'Low-Temperature Processed Meso-Superstructured to Thin-Film Perovskite Solar Cells'. *Energy Environ. Sci.*, 2013, **6**, 1739–1743.

[43] Boix, P. P.; Nonomura, K.; Mathews, N. and Mhaisalkar, S. G. 'Current Progress and Future Perspectives for Organic/Inorganic Perovskite Solar Cells'. *Mater. Today*, 2014, **17**, 16–23.

[44] Liu, M.; Johnston, M. B. and Snaith, H. J. 'Efficient Planar Heterojunction Perovskite Solar Cells by Vapour Deposition'. *Nature*, 2013, **501**, 395–398.

[45] Liu, D. and Kelly, T. L. 'Perovskite Solar Cells with a Planar Heterojunction Structure Prepared Using Room-Temperature Solution Processing Techniques'. *Nat. Photonics*, 2014, **8**, 133–138.

[46] Yang, W. S.; Noh, J. H.; Jeon, N. J.; Kim, Y. C.; Ryu, S.; Seo, J. and Seok, S. I. 'High-Performance Photovoltaic Perovskite Layers Fabricated Through Intramolecular Exchange'. *Science*, 2015, **348**, 1234–1237.

[47] Li, Z.; Klein, T. R.; Kim, D. H.; Yang, M.; Berry, J. J.; van Hest, M. F. A. M. and Zhu, K. 'Scalable Fabrication of Perovskite Solar Cells'. *Nat. Rev. Mater.*, 2018, **3**, 1–20.

[48] Mailoa, J. P.; Bailie, C. D.; Johlin, E. C.; Hoke, E. T.; Akey, A. J.; Nguyen, W. H.; McGehee, M. D. and Buonassisi, T. 'A 2-Terminal Perovskite/Silicon Multijunction Solar Cell Enabled by a Silicon Tunnel Junction'. *Appl. Phys. Lett.*, 2015, **106**, 121105.

[49] Leijtens, T.; Bush, K. A.; Prasanna, R. and McGehee, M. D. 'Opportunities and Challenges for Tandem Solar Cells Using Metal Halide Perovskite Semiconductors'. *Nat. Energy*, 2018, **3**, 828–838.

[50] Xu, Q.; Zhao, Y. and Zhang, X. 'Light Management in Monolithic Perovskite/Silicon Tandem Solar Cells'. *Solar RRL*, 2020, **4**, 1900206.

[51] Jeon, N. J.; Noh, J. H.; Yang, W. S.; Kim, Y. C.; Ryu, S.; Seo, J. and Seok, S. I. 'Compositional Engineering of Perovskite Materials for High-Performance Solar Cells'. *Nature*, 2015, **517**, 476–480.

[52] Zhao, Z.; Gu, F.; Rao, H.; Ye, S.; Liu, Z.; Bian, Z. and Huang, C. 'Metal Halide Perovskite Materials for Solar Cells with Long-Term Stability'. *Adv. Energy Mater.*, 2019, **9**, 1802671.

[53] Zhao, Y. and Zhu, K. 'Organic–Inorganic Hybrid Lead Halide Perovskites for Optoelectronic and Electronic Applications'. *Chem. Soc. Rev.*, 2016, **45**, 655–689.

[54] Haque, M. A.; Sheikh, A. D.; Guan, X. and Wu, T. 'Metal Oxides as Efficient Charge Transporters in Perovskite Solar Cells'. *Adv. Energy Mater.*, 2017, **7**, 1602803.

[55] Zhang, F. and Zhu, K. 'Additive Engineering for Efficient and Stable Perovskite Solar Cells'. *Adv. Energy Mater.*, 2020, **10**, 1902579.

[56] Manser, J. S.; Christians, J. A. and Kamat, P. V. 'Intriguing Optoelectronic Properties of Metal Halide Perovskites'. *Chem. Rev.*, 2016, **116**, 12956–13008.

[57] De Wolf, S.; Holovsky, J.; Moon, S.-J.; Löper, P.; Niesen, B.; Ledinsky, M.; Haug, F.-J.; Yum, J.-H. and Ballif, C. 'Organometallic Halide Perovskites: Sharp Optical Absorption Edge and its Relation to Photovoltaic Performance'. *J. Phys. Chem. Lett.*, 2014, **5**, 1035–1039.

[58] Saba, M.; Quochi, F.; Mura, A. and Bongiovanni, G. 'Excited State Properties of Hybrid Perovskites'. *Acc. Chem. Res.*, 2015, **49**, 166–173.

[59] Filip, M. R.; Eperon, G. E.; Snaith, H. J. and Giustino, F. 'Steric Engineering of Metal-Halide Perovskites with Tunable Optical Band Gaps'. *Nat. Commun.*, 2014, **5**.

[60] Hao, F.; Stoumpos, C. C.; Chang, R. P. H. and Kanatzidis, M. G. 'Anomalous Band Gap Behavior in Mixed Sn and Pb Perovskites Enables Broadening of Absorption Spectrum in Solar Cells'. *J. Am. Chem. Soc.*, 2014, **136**, 8094–8099.

[61] Hao, F.; Stoumpos, C. C.; Cao, D. H.; Chang, R. P. H. and Kanatzidis, M. G. 'Lead-Free Solid-State Organic-Inorganic Halide Perovskite Solar Cells'. *Nat. Photonics*, 2014, **8**, 489–494.

[62] Sutter-Fella, C. M.; Li, Y.; Amani, M.; Ager III, J. W.; Toma, F. M.; Yablonovitch, E.; Sharp, I. D. and Javey, A. 'High Photoluminescence Quantum Yield in Band Gap Tunable Bromide Containing Mixed Halide Perovskites'. *Nano Lett.*, 2015, **16**, 800–806.

[63] D'Innocenzo, V.; Grancini, G.; Alcocer, M. J. P.; Kandada, A. R. S.; Stranks, S. D.; Lee, M. M.; Lanzani, G.; Snaith, H. J. and Petrozza, A. 'Excitons Versus Free Charges in Organo-Lead tri-Halide Perovskites'. *Nat. Commun.*, 2014, **5**, 3586.

[64] Galkowski, K.; Mitioglu, A.; Miyata, A.; Plochocka, P.; Portugall, O.; Eperon, G. E.; Wang, J. T.-W.; Stergiopoulos, T.; Stranks, S. D.; Snaith, H. J. *et al.* 'Determination of the Exciton Binding Energy and Effective Masses for Methylammonium and Formamidinium Lead tri-Halide Perovskite Semiconductors'. *Energy Environ. Sci.*, 2016, **9**, 962–970.

[65] Manser, J. S. and Kamat, P. V. 'Band Filling with Free Charge Carriers in Organometal Halide Perovskites'. *Nat. Photonics*, 2014, **8**, 737–743.

[66] Noel, N. K.; Stranks, S. D.; Abate, A.; Wehrenfennig, C.; Guarnera, S.; Haghighirad, A.-A.; Sadhanala, A.; Eperon, G. E.; Pathak, S. K.; Johnston, M. B. *et al.* 'Lead-Free Organic–Inorganic Tin Halide Perovskites for Photovoltaic Applications'. *Energy Environ. Sci.*, 2014, **7**, 3061–3068.

[67] Deschler, F.; Price, M.; Pathak, S.; Klintberg, L. E.; Jarausch, D.-D.; Higler, R.; Hüttner, S.; Leijtens, T.; Stranks, S. D.; Snaith, H. J. *et al.* 'High Photoluminescence Efficiency and Optically Pumped Lasing in Solution-Processed Mixed Halide Perovskite Semiconductors'. *J. Phys. Chem. Lett.*, 2014, **5**, 1421–1426.

[68] Saba, M.; Cadelano, M.; Marongiu, D.; Chen, F.; Sarritzu, V.; Sestu, N.; Figus, C.; Aresti, M.; Piras, R.; Lehmann, A. G. *et al.* 'Correlated Electron–Hole Plasma in Organometal Perovskites'. *Nat. Commun.*, 2014, **5**, 5049.

[69] Draguta, S.; Thakur, S.; Morozov, Y. V.; Wang, Y.; Manser, J. S.; Kamat, P. V. and Kuno, M. 'Spatially Non-Uniform Trap State Densities in Solution-Processed Hybrid Perovskite Thin Films'. *J. Phys. Chem. Lett.*, 2016, **7**, 715–721.

[70] Schoenlein, R. W.; Lin, W. Z.; Ippen, E. P. and Fujimoto, J. G. 'Femtosecond Hot-Carrier Energy Relaxation in GaAs'. *Appl. Phys. Lett.*, 1987, **51**, 1442–1444.

[71] Rota, L.; Lugli, P.; Elsaesser, T. and Shah, J. 'Ultrafast Thermalization of Photoexcited Carriers in Polar Semiconductors'. *Phys. Rev. B*, 1993, **47**, 4226.

[72] Richter, J. M.; Branchi, F.; Valduga de Almeida Camargo, F.; Zhao, B.; Friend, R. H.; Cerullo, G. and Deschler, F. 'Ultrafast Carrier Thermalization in Lead Iodide Perovskite Probed with Two-Dimensional Electronic Spectroscopy'. *Nat. Commun.*, 2017, **8**, 376.

[73] Shah, J. *Ultrafast Spectroscopy of Semiconductors and Semiconductor Nanostructures.* Springer, 1999.

[74] Ponseca Jr., C. S. and Sundström, V. 'Revealing the Ultrafast Charge Carrier Dynamics in Organo Metal Halide Perovskite Solar Cell Materials Using Time Resolved THz Spectroscopy'. *Nanoscale*, 2016, **8**, 6249–6257.

[75] Shi, J.; Li, Y.; Li, Y.; Li, D.; Luo, Y.; Wu, H. and Meng, Q. 'From Ultrafast to Ultraslow: Charge-Carrier Dynamics of Perovskite Solar Cells'. *Joule*, 2018, **2**, 879–901.

[76] König, D; Yao, Y; Puthen-Veettil, B and Smith, S. C. 'Non-Equilibrium Dynamics, Materials and Structures for Hot Carrier Solar Cells: a Detailed Review'. *Semicond. Sci. Technol.*, 2020, **35**, 73002.

[77] Xing, G.; Mathews, N.; Sun, S.; Lim, S. S.; Lam, Y. M.; Grätzel, M.; Mhaisalkar, S. and Sum, T. C. 'Long-Range Balanced Electron-And Hole-Transport Lengths in Organic-Inorganic $CH_3NH_3PbI_3$'. *Science*, 2013, **342**, 344–347.

[78] Hsu, H.-Y.; Wang, C.-Y.; Fathi, A.; Shiu, J.-W.; Chung, C.-C.; Shen, P.-S.; Guo, T.-F.; Chen, P.; Lee, Y.-P. and Diau, E. W.-G. 'Femtosecond Excitonic Relaxation Dynamics of Perovskite on Mesoporous Films of Al_2O_3 and NiO Nanoparticles'. *Angew. Chem.*, 2014, **126**, 9493–9496.

[79] Yang, Y.; Ostrowski, D. P.; France, R. M.; Zhu, K.; van de Lagemaat, J.; Luther, J. M. and Beard, M. C. 'Observation of a Hot-Phonon Bottleneck in Lead-Iodide Perovskites'. *Nat. Photonics*, 2016, **10**, 53–59.

[80] Price, M. B.; Butkus, J.; Jellicoe, T. C.; Sadhanala, A.; Briane, A.; Halpert, J. E.; Broch, K.; Hodgkiss, J. M.; Friend, R. H. and Deschler, F. 'Hot-Carrier Cooling and Photoinduced Refractive Index Changes in Organic-Inorganic Lead Halide Perovskites'. *Nat. Commun.*, 2015, **6**, 8420.

[81] Li, M.; Bhaumik, S.; Goh, T. W.; Kumar, M. S.; Yantara, N.; Grätzel, M.; Mhaisalkar, S.; Mathews, N. and Sum, T. C. 'Slow Cooling and Highly Efficient Extraction of Hot Carriers in Colloidal Perovskite Nanocrystals'. *Nat. Commun.*, 2017, **8**, 14350.

[82] Fu, J.; Xu, Q.; Han, G.; Wu, B.; Huan, C. H. A.; Leek, M. L. and Sum, T. C. 'Hot Carrier Cooling Mechanisms in Halide Perovskites'. *Nat. Commun.*, 2017, **8**, 1300.

[83] Papagiorgis, P.; Protesescu, L.; Kovalenko, M. V.; Othonos, A. and Itskos, G. 'Long-Lived Hot Carriers in Formamidinium Lead Iodide Nanocrystals'. *J. Phys. Chem. C*, 2017, **121**, 12434–12440.

[84] Chen, J.; Messing, M. E.; Zheng, K.; Pullerits, T.; Messing, M. E.; Zheng, K. and Pullerits, T. 'Cation-Dependent Hot Carrier Cooling in Halide Perovskite Nanocrystals'. *J. Am. Chem. Soc.*, 2019, **141**, 3532–3540.

[85] Yang, J.; Wen, X.; Xia, H.; Sheng, R.; Ma, Q.; Kim, J.; Tapping, P.; Harada, T.; Kee, T. T. W.; Huang, F. *et al.* 'Acoustic-Optical Phonon Up-Conversion and Hot-Phonon Bottleneck in Lead-Halide Perovskites'. *Nat. Commun.*, 2017, **8**, 14120.

[86] Zhu, H.; Miyata, K.; Fu, Y.; Wang, J.; Joshi, P. P.; Niesner, D.; Williams, K. W.; Jin, S. and Zhu, X.-Y. 'Screening in Crystalline Liquids Protects Energetic Carriers in Hybrid Perovskites'. *Science*, 2016, **353**, 1409–1413.

[87] Herz, L. M. 'Charge-Carrier Dynamics in Organic-Inorganic Metal Halide Perovskites'. *Ann. Rev. Phys. Chem.*, 2016, **67**, 65–89.

[88] Johnston, M. B. and Herz, L. M. 'Hybrid Perovskites for Photovoltaics: Charge-Carrier Recombination, Diffusion, and Radiative Efficiencies'. *Acc. Chem. Res.*, 2015, **49**, 146–154.

[89] Wetzelaer, G.-J. A.; Scheepers, M.; Sempere, A. M.; Momblona, C.; Ávila, J. and Bolink, H. J. 'Trap-Assisted Non-Radiative Recombination in Organic–Inorganic Perovskite Solar Cells'. *Adv. Mater.*, 2015, **27**, 1837–1841.

[90] Corani, A.; Li, M.-H.; Shen, P.-S.; Chen, P.; Guo, T.-F.; El Nahhas, A.; Zheng, K.; Yartsev, A.; Sundström, V. and Ponseca Jr, C. S. 'Ultrafast Dynamics of Hole Injection and Recombination in Organometal Halide Perovskite Using Nickel Oxide as p-Type Contact Electrode'. *J. Phys. Chem. Lett.*, 2016, **7**, 1096–1101.

[91] Milot, R. L.; Eperon, G. E.; Green, T.; Snaith, H. J.; Johnston, M. B. and Herz, L. M. 'Radiative Monomolecular Recombination Boosts Amplified Spontaneous Emission in $HC(NH_2)_2SnI_3$ Perovskite Films'. *J. Phys. Chem. Lett.*, 2016, **7**, 4178–4184.

[92] Wehrenfennig, C.; Liu, M.; Snaith, H. J.; Johnston, M. B. and Herz, L. M. 'Charge-Carrier Dynamics in Vapour-Deposited Films of the Organolead Halide Perovskite $CH_3NH_3PbI_{3-x}Cl_x$'. *Energy Environ. Sci.*, 2014, **7**, 2269–2275.

[93] Ma, L.; Hao, F.; Stoumpos, C. C.; Phelan, B. T.; Wasielewski, M. R. and Kanatzidis, M. G. 'Carrier Diffusion Lengths of over 500 nm in Lead-Free Perovskite $CH_3NH_3SnI_3$ Films'. *J. Am. Chem. Soc.*, 2016, **138**, 14750–14755.

[94] Wehrenfennig, C.; Eperon, G. E.; Johnston, M. B.; Snaith, H. J. and Herz, L. M. 'High Charge Carrier Mobilities and Lifetimes in Organolead Trihalide Perovskites'. *Adv. Mater.*, 2014, **26**, 1584–1589.

[95] Rehman, W.; Milot, R. L.; Eperon, G. E.; Wehrenfennig, C.; Boland, J. L.; Snaith, H. J.; Johnston, M. B. and Herz, L. M. 'Charge-Carrier Dynamics and Mobilities in Formamidinium Lead Mixed-Halide Perovskites'. *Adv. Mater.*, 2015, **27**, 7938–7944.

[96] Davies, C. L.; Filip, M. R.; Patel, J. B.; Crothers, T. W.; Verdi, C.; Wright, A. D.; Milot, R. L.; Giustino, F.; Johnston, M. B. and Herz, L. M. 'Bimolecular Recombination in Methylammonium Lead Triiodide Perovskite is an Inverse Absorption Process'. *Nat. Commun.*, 2018, **9**, 293.

[97] Milot, R. L.; Eperon, G. E.; Snaith, H. J.; Johnston, M. B. and Herz, L. M. 'Temperature-Dependent Charge-Carrier Dynamics in $CH_3NH_3PbI_3$ Perovskite Thin Films'. *Adv. Funct. Mater.*, 2015, **25**, 6218–6227.

[98] Ponseca Jr, C. S.; Hutter, E. M.; Piatkowski, P.; Cohen, B.; Pascher, T.; Douhal, A.; Yartsev, A.; Sundström, V. and Savenije, T. J. 'Mechanism of Charge Transfer and Recombination Dynamics in Organo Metal Halide Perovskites and Organic Electrodes, PCBM, and Spiro-OMeTAD: Role of Dark Carriers'. *J. Am. Chem. Soc.*, 2015, **137**, 16043–16048.

[99] Stranks, S. D.; Eperon, G. E.; Grancini, G.; Menelaou, C.; Alcocer, M. J. P.; Leijtens, T.; Herz, L. M.; Petrozza, A. and Snaith, H. J. 'Electron-Hole Diffusion Lengths Exceeding 1 Micrometer in an Organometal Trihalide Perovskite Absorber'. *Science*, 2013, **342**, 341–344.

[100] Yang, Z; Yu, Z; Wei, H; Xiao, X; Ni, Z; Chen, B; Deng, Y; Habisreutinger, S. N.; Chen, X; Wang, K *et al.* 'Enhancing Electron Diffusion Length in Narrow-Bandgap Perovskites for Efficient Monolithic Perovskite Tandem Solar Cells'. *Nat. Commun.*, 2019, **10**, 4498.

[101] Herz, L. M. 'Charge-Carrier Mobilities in Metal Halide Perovskites: Fundamental Mechanisms and Limits'. *ACS Energy Lett.*, 2017, **2**, 1539–1548.

[102] Umari, P.; Mosconi, E. and De Angelis, F. 'Relativistic GW Calculations on $CH_3NH_3PbI_3$ and $CH_3NH_3SnI_3$ Perovskites for Solar Cell Applications'. *Sci. Rep.*, 2014, **4**, 4467.

[103] Amat, A.; Mosconi, E.; Ronca, E.; Quarti, C.; Umari, P.; Nazeeruddin, M. K.; Grätzel, M. and De Angelis, F. 'Cation-Induced Band-Gap Tuning in Organohalide Perovskites: Interplay of Spin–Orbit Coupling and Octahedra Tilting'. *Nano Lett.*, 2014, **14**, 3608–3616.

[104] Berdiyorov, G. R.; El-Mellouhi, F; Madjet, M. E.; Alharbi, F. H.; Peeters, F. M. and Kais, S. 'Effect of Halide-Mixing on the Electronic Transport Properties of Organometallic Perovskites'. *Sol. Energy Mater. Sol. Cells*, 2016, **148**, 2–10.

[105] Wright, A. D.; Verdi, C.; Milot, R. L.; Eperon, G. E.; Pérez-Osorio, M. A.; Snaith, H. J.; Giustino, F.; Johnston, M. B. and Herz, L. M. 'Electron–Phonon Coupling in Hybrid Lead Halide Perovskites'. *Nat. Commun.*, 2016, **7**, 11755.

[106] Filippetti, A.; Mattoni, A; Caddeo, C.; Saba, M. and Delugas, P. 'Low Electron-Polar Optical Phonon Scattering as a Fundamental Aspect of Carrier Mobility in Methylammonium Lead Halide $CH_3NH_3PbI_3$ Perovskites'. *Phys. Chem. Chem. Phys.*, 2016, **18**, 15352–15362.

[107] Yu, P. Y. and Cardona, M. *Fundamentals of Semiconductors: Physics and Materials Properties*. Springer, 2010.

[108] Reid, O. G.; Yang, M.; Kopidakis, N.; Zhu, K. and Rumbles, G. 'Grain-Size-Limited Mobility in Methylammonium Lead Iodide Perovskite Thin Films'. *ACS Energy Lett.*, 2016, **1**, 561–565.

[109] Wang, Q.; Shao, Y.; Xie, H.; Lyu, L.; Liu, X.; Gao, Y. and Huang, J. 'Qualifying Composition Dependent p and n Self-Doping in $CH_3NH_3PbI_3$'. *Appl. Phys. Lett.*, 2014, **105**, 163508.

[110] Parrott, E. S.; Milot, R. L.; Stergiopoulos, T.; Snaith, H. J.; Johnston, M. B. and Herz, L. M. 'Effect of Structural Phase Transition on Charge-Carrier Lifetimes and Defects in $CH_3NH_3SnI_3$ Perovskite'. *J. Phys. Chem. Lett.*, 2016, **7**, 1321–1326.

[111] Kim, J.; Lee, S.-H.; Lee, J. H. and Hong, K.-H. 'The Role of Intrinsic Defects in Methylammonium Lead Iodide Perovskite'. *J. Phys. Chem. Lett.*, 2014, **5**, 1312–1317.

[112] Stranks, S. D.; Burlakov, V. M.; Leijtens, T.; Ball, J. M.; Goriely, A. and Snaith, H. J. 'Recombination Kinetics in Organic-Inorganic Perovskites: Excitons, Free Charge, and Subgap States'. *Phys. Rev. Appl.*, 2014, **2**, 34007.

[113] Buin, A.; Pietsch, P.; Xu, J.; Voznyy, O.; Ip, A. H.; Comin, R. and Sargent, E. H. 'Materials Processing Routes to Trap-Free Halide Perovskites'. *Nano Lett.*, 2014, **14**, 6281–6286.

[114] Wu, X.; Trinh, M. T.; Niesner, D.; Zhu, H.; Norman, Z.; Owen, J. S.; Yaffe, O.; Kudisch, B. J. and Zhu, X.-Y. 'Trap States in Lead Iodide Perovskites'. *J. Am. Chem. Soc.*, 2015, **137**, 2089–2096.

[115] Wright, A. D.; Milot, R. L.; Eperon, G. E.; Snaith, H. J.; Johnston, M. B. and Herz, L. M. 'Band-Tail Recombination in Hybrid Lead Iodide Perovskite'. *Adv. Funct. Mater.*, 2017, **27**, 1700860.

[116] Haynes, J. and Hornbeck, J. 'Trapping of Minority Carriers in Silicon. II. n-Type Silicon'. *Phys. Rev.*, 1955, **100**, 606.

[117] Hutter, E. M.; Eperon, G. E.; Stranks, S. D. and Savenije, T. J. 'Charge Carriers in Planar and Meso-Structured Organic–Inorganic Perovskites: Mobilities, Lifetimes, and Concentrations of Trap States'. *J. Phys. Chem. Lett.*, 2015, **6**, 3082–3090.

[118] Xing, G.; Mathews, N.; Lim, S. S.; Yantara, N.; Liu, X.; Sabba, D.; Grätzel, M.; Mhaisalkar, S. and Sum, T. C. 'Low-Temperature Solution-Processed Wavelength-Tunable Perovskites for Lasing'. *Nat. Mater.*, 2014, **13**, 476–480.

[119] Urbach, F. 'The Long-Wavelength Edge of Photographic Sensitivity and of the Electronic Absorption of Solids'. *Phys. Rev.*, 1953, **92**, 1324.

[120] Baumann, A.; Vaäth, S.; Rieder, P.; Heiber, M. C.; Tvingstedt, K. and Dyakonov, V. 'Identification of Trap States in Perovskite Solar Cells'. *J. Phys. Chem. Lett.*, 2015, **6**, 2350–2354.

[121] Leijtens, T.; Eperon, G. E.; Barker, A. J.; Grancini, G.; Zhang, W.; Ball, J. M.; Kandada, A. R. S.; Snaith, H. J. and Petrozza, A. 'Carrier Trapping and Recombination: the Role of Defect Physics in Enhancing the Open Circuit Voltage of Metal Halide Perovskite Solar Cells'. *Energy Environ. Sci.*, 2016, **9**, 3472–3481.

[122] Lanzetta, L; Aristidou, N and Haque, S. A. 'Stability of Lead and Tin Halide Perovskites: The Link between Defects and Degradation'. *J. Phys. Chem. Lett.*, 2020, **11**, 574–585.

[123] Roy, P.; Sinha, N. K.; Tiwari, S. and Khare, A. 'A Review on Perovskite Solar Cells: Evolution of Architecture, Fabrication Techniques, Commercialization Issues and Status'. *Sol. Energy*, 2020, **198**, 665–688.

[124] Shi, Z.; Guo, J.; Chen, Y.; Li, Q.; Pan, Y.; Zhang, H.; Xia, Y. and Huang, W. 'Lead-Free Organic–Inorganic Hybrid Perovskites for Photovoltaic Applications: Recent Advances and Perspectives'. *Adv. Mater.*, 2017, **29**, 1605005.

[125] Zhang, M.; Lyu, M.; Chen, P.; Hao, M.; Yun, J.-H. and Wang, L. 'Recent Advances in Low-Toxic Lead-Free Metal Halide Perovskite Materials for Solar Cell Application'. *Asia-Pac. J. Chem. Eng.*, 2016, **11**, 392–398.

[126] Lee, S. J.; Shin, S. S.; Kim, Y. C.; Kim, D.; Ahn, T. K.; Noh, J. H.; Seo, J. and Seok, S. I. 'Fabrication of Efficient Formamidinium Tin Iodide Perovskite Solar Cells through SnF_2–Pyrazine Complex'. *J. Am. Chem. Soc.*, 2016, **138**, 3974–3977.

[127] Kamarudin, M. A.; Hirotani, D.; Wang, Z.; Hamada, K.; Nishimura, K.; Shen, Q.; Toyoda, T.; Iikubo, S.; Minemoto, T.; Yoshino, K. *et al.* 'Suppression of Charge Carrier Recombination in Lead-Free Tin Halide Perovskite via Lewis Base Post-Treatment'. *J. Phys. Chem. Lett.*, 2019, **10**, 5277–5283.

[128] Meng, X.; Wu, T.; Liu, X.; He, X.; Noda, T.; Wang, Y.; Segawa, H. and Han, L. 'Highly Reproducible and Efficient $FASnI_3$ Perovskite Solar Cells Fabricated with Volatilizable Reducing Solvent'. *J. Phys. Chem. Lett.*, 2020, **11**, 2965–2971.

[129] Meng, X.; Wang, Y.; Lin, J.; Liu, X.; He, X.; Barbaud, J.; Wu, T.; Noda, T.; Yang, X. and Han, L. 'Surface-Controlled Oriented Growth of $FASnI_3$ Crystals for Efficient Lead-free Perovskite Solar Cells'. *Joule*, 2020, **4**, 902–912.

[130] Liu, X.; Wang, Y.; Wu, T.; He, X.; Meng, X.; Barbaud, J.; Chen, H.; Segawa, H.; Yang, X. and Han, L. 'Efficient and Stable Tin Perovskite Solar Cells Enabled by Amorphous-Polycrystalline Structure'. *Nat. Commun.*, 2020, **11**, 2678.

[131] Wang, C.; Gu, F.; Zhao, Z.; Rao, H.; Qiu, Y.; Cai, Z.; Zhan, G.; Li, X.; Sun, B.; Yu, X. *et al.* 'Self-Repairing Tin-Based Perovskite Solar Cells with a Breakthrough Efficiency Over 11%'. *Adv. Mater.*, 2020, **32**, 1907623.

[132] Jiang, X.; Wang, F.; Wei, Q.; Li, H.; Shang, Y.; Zhou, W.; Wang, C.; Cheng, P.; Chen, Q.; Chen, L. *et al.* 'Ultra-High Open-Circuit Voltage of Tin Perovskite Solar Cells via an Electron Transporting Layer Design'. *Nat. Commun.*, 2020, **11**, 1–7.

[133] Nishimura, K.; Kamarudin, M. A.; Hirotani, D.; Hamada, K.; Shen, Q.; Iikubo, S.; Minemoto, T.; Yoshino, K. and Hayase, S. 'Lead-Free Tin-Halide Perovskite Solar Cells with 13% Efficiency'. *Nano Energy*, 2020, **74**, 104858.

[134] Stoumpos, C. C.; Malliakas, C. D. and Kanatzidis, M. G. 'Semiconducting Tin and Lead Iodide Perovskites with Organic Cations: Phase Transitions, High Mobilities, and Near-Infrared Photoluminescent Properties'. *Inorg. Chem.*, 2013, **52**, 9019–9038.

[135] Zhao, B.; Abdi-Jalebi, M.; Tabachnyk, M.; Glass, H.; Kamboj, V. S.; Nie, W.; Pearson, A. J.; Puttisong, Y.; Gödel, K. C.; Beere, H. E. *et al.* 'High Open-Circuit Voltages in Tin-Rich Low-Bandgap Perovskite-Based Planar Heterojunction Photovoltaics'. *Adv. Mater.*, 2017, **29**, 1604744.

[136] Even, J.; Pedesseau, L.; Jancu, J.-M. and Katan, C. 'DFT and k · p Modelling of the Phase Transitions of Lead and Tin Halide Perovskites for Photovoltaic Cells'. *Phys. Status Solidi RRL*, 2014, **8**, 31–35.

[137] Tao, S. X.; Cao, X. and Bobbert, P. A. 'Accurate and Efficient Band Gap Predictions of Metal Halide Perovskites Using the DFT-1/2 method: GW Accuracy with DFT Expense'. *Sci. Rep.*, 2017, **7**, 1–9.

[138] Li, Z.; Yang, M.; Park, J.-S.; Wei, S.-H.; Berry, J. J. and Zhu, K. 'Stabilizing Perovskite Structures by Tuning Tolerance Factor: Formation of Formamidinium and Cesium Lead Iodide Solid-State Alloys'. *Chem. Mater.*, 2016, **28**, 284–292.

[139] Henry, C. H. 'Limiting Efficiencies of Ideal Single and Multiple Energy Gap Terrestrial Solar Cells'. *J. Appl. Phys.*, 1980, **51**, 4494–4500.

[140] Meillaud, F; Shah, A.; Droz, C; Vallat-Sauvain, E. and Miazza, C. 'Efficiency Limits for Single-Junction and Tandem Solar Cells'. *Sol. Energy Mater. Sol. Cells*, 2006, **90**, 2952–2959.

[141] Milot, R. L.; Klug, M. T.; Davies, C. L.; Wang, Z.; Kraus, H.; Snaith, H. J.; Johnston, M. B. and Herz, L. M. 'The Effects of Doping Density and Temperature on the Optoelectronic Properties of Formamidinium Tin Triiodide Thin Films'. *Adv. Mater.*, 2018, **30**, 1804506.

[142] Shum, K.; Chen, Z.; Qureshi, J.; Yu, C.; Wang, J. J.; Pfenninger, W.; Vockic, N.; Midgley, J. and Kenney, J. T. 'Synthesis and Characterization of $CsSnI_3$ Thin Films'. *Appl. Phys. Lett.*, 2010, **96**, 3–5.

[143] Liu, C.; Fan, J.; Li, H.; Zhang, C. and Mai, Y. 'Highly Efficient Perovskite Solar Cells with Substantial Reduction of Lead Content'. *Sci. Rep.*, 2016, **6**, 35705.

[144] Prasanna, R.; Gold-Parker, A.; Leijtens, T.; Conings, B.; Babayigit, A.; Boyen, H.-G.; Toney, M. F. and McGehee, M. D. 'Band Gap Tuning Via Lattice Contraction and Octahedral Tilting in Perovskite Materials for Photovoltaics'. *J. Am. Chem. Soc.*, 2017, **139**, 11117–11124.

[145] Parrott, E. S.; Green, T.; Milot, R. L.; Johnston, M. B.; Snaith, H. J. and Herz, L. M. 'Interplay of Structural and Optoelectronic Properties in Formamidinium Mixed Tin–Lead Triiodide Perovskites'. *Adv. Funct. Mater.*, 2018, **28**, 1802803.

[146] Rajagopal, A.; Stoddard, R. J.; Hillhouse, H. and Jen, A. K. Y. 'On Understanding Bandgap Bowing and Optoelectronic Quality in Pb-Sn Alloy Hybrid Perovskites'. *J. Mater. Chem. A*, 2019, **7**, 16285–16293.

[147] Im, J.; Stoumpos, C. C.; Jin, H.; Freeman, A. J. and Kanatzidis, M. G. 'Antagonism between Spin–Orbit Coupling and Steric Effects Causes Anomalous Band Gap Evolution in the Perovskite Photovoltaic Materials $CH_3NH_3Sn_{1-x}Pb_xI_3$'. *J. Phys. Chem. Lett.*, 2015, **6**, 3503–3509.

[148] Anaya, M.; Correa-Baena, J. P.; Lozano, G.; Saliba, M.; Anguita, P.; Roose, B.; Abate, A.; Steiner, U.; Grätzel, M.; Calvo, M. E. *et al.* 'Optical Analysis of $CH_3NH_3Sn_xPb_{1-x}I_3$ Absorbers: a Roadmap for Perovskite-on-Perovskite Tandem Solar Cells'. *J. Mater. Chem. A*, 2016, **4**, 11214–11221.

[149] Yang, Z.; Rajagopal, A.; Chueh, C.-C.; Jo, S. B.; Liu, B.; Zhao, T. and Jen, A. K.-Y. 'Stable Low-Bandgap Pb–Sn Binary Perovskites for Tandem Solar Cells'. *Adv. Mater.*, 2016, **28**, 8990–8997.

[150] Eperon, G. E.; Leijtens, T.; Bush, K. A.; Prasanna, R.; Green, T.; Wang, J. T.-W.; McMeekin, D. P.; Volonakis, G.; Milot, R. L.; May, R. *et al.* 'Perovskite-Perovskite Tandem Photovoltaics with Optimized Band Gaps'. *Science*, 2016, **354**, 861–865.

[151] Zhao, D.; Chen, C.; Wang, C.; Junda, M. M.; Song, Z.; Grice, C. R.; Yu, Y.; Li, C.; Subedi, B.; Podraza, N. J. *et al.* 'Efficient Two-Terminal All-Perovskite Tandem Solar Cells Enabled by High-Quality Low-Bandgap Absorber Layers'. *Nat. Energy*, 2018, **3**, 1093.

[152] Li, C.; Song, Z.; Zhao, D.; Xiao, C.; Subedi, B.; Shrestha, N.; Junda, M. M.; Wang, C.; Jiang, C.-S.; Al-Jassim, M. *et al.* 'Reducing Saturation-Current Density to Realize High-Efficiency Low-Bandgap Mixed Tin–Lead Halide Perovskite Solar Cells'. *Adv. Energy Mater.*, 2019, **9**, 1803135.

[153] Zhao, D.; Yu, Y.; Wang, C.; Liao, W.; Shrestha, N.; Grice, C. R.; Cimaroli, A. J.; Guan, L.; Ellingson, R. J.; Zhu, K. *et al.* 'Low-Bandgap Mixed Tin–Lead Iodide Perovskite Absorbers with Long Carrier Lifetimes for All-Perovskite Tandem Solar Cells'. *Nat. Energy*, 2017, **2**, 17018.

[154] Ross, R. T. and Nozik, A. J. 'Efficiency of Hot-Carrier Solar Energy Converters'. *J. Appl. Phys.*, 1982, **53**, 3813–3818.

[155] Grancini, G; Maiuri, M; Fazzi, D; Petrozza, A; Egelhaaf, H. J.; Brida, D; Cerullo, G and Lanzani, G. 'Hot Exciton Dissociation in Polymer Solar Cells'. *Nat. Mater.*, 2013, **12**, 29–33.

[156] Chen, F.; Cartwright, A.; Lu, H. and Schaff, W. J. 'Time-Resolved Spectroscopy of Recombination and Relaxation Dynamics in InN'. *Appl. Phys. Lett.*, 2003, **83**, 4984–4986.

[157] Brauer, J. C.; Lee, Y. H.; Nazeeruddin, M. K. and Banerji, N. 'Ultrafast Charge Carrier Dynamics in $CH_3NH_3PbI_3$: Evidence for Hot Hole Injection Into Spiro-OMeTAD'. *J. Mater. Chem. C*, 2016, **4**, 5922.

[158] Grancini, G.; Viola, D.; Lee, Y.; Saliba, M.; Paek, S.; Cho, K. T.; Orlandi, S.; Cavazzini, M.; Fungo, F.; Hossain, M. I. *et al.* 'Femtosecond Charge-Injection Dynamics at Hybrid Perovskite Interfaces'. *ChemPhysChem*, 2017, **18**, 2381–2389.

[159] Shen, Q.; Ripolles, T. S.; Even, J.; Zhang, Y.; Ding, C.; Liu, F.; Izuishi, T.; Nakazawa, N.; Toyoda, T.; Ogomi, Y. *et al.* 'Ultrafast Selective Extraction of Hot Holes from Cesium Lead Iodide Perovskite Films'. *J. Energy Chem.*, 2018, **27**, 1170–1174.

[160] Guo, Z.; Wan, Y.; Yang, M.; Snaider, J.; Zhu, K. and Huang, L. 'Long-Range Hot-Carrier Transport in Hybrid Perovskites Visualized by Ultrafast Microscopy'. *Science*, 2017, **356**, 59–62.

[161] Takeda, Y.; Ito, T.; Motohiro, T.; König, D.; Shrestha, S. and Conibeer, G. 'Hot Carrier Solar Cells Operating Under Practical Conditions'. *J. Appl. Phys.*, 2009, **105**, 074905.

[162] Wang, G.; Liao, L. P.; Elseman, A. M.; Yao, Y. Q.; Lin, C. Y.; Hu, W.; Liu, D. B.; Xu, C. Y.; Zhou, G. D.; Li, P. *et al.* 'An Internally Photoemitted Hot Carrier Solar Cell Based on Organic-Inorganic Perovskite'. *Nano Energy*, 2020, **68**, 104383.

[163] Kahmann, S. and Loi, M. A. 'Hot Carrier Solar Cells and the Potential of Perovskites for Breaking the Shockley–Queisser Limit'. *J. Mater. Chem. C*, 2019, **7**, 2471–2486.

[164] Brown, A. S. and Green, M. A. 'Limiting Efficiency for Current-Constrained Two-Terminal Tandem Cell Stacks'. *Prog. Photovolt. Res. Appl.*, 2002, **10**, 299–307.

[165] Conibeer, G. 'Third-Generation Photovoltaics'. *Mater. Today*, 2007, **10**, 42–50.

[166] Jošt, M.; Kegelmann, L.; Korte, L. and Albrecht, S. 'Monolithic Perovskite Tandem Solar Cells : A Review of the Present Status and Advanced Characterization Methods Toward 30% Efficiency'. *Adv. Energy Mater.*, 2020, **10**, 1904102.

[167] Extance, A. 'The Reality Behind Solar Power's Next Star Material'. *Nature*, 2019, **570**, 429–432.

[168] Helmholtz Zentrum Berlin. *World Record: Efficiency of perovskite silicon tandem solar cell jumps to 29.15 per cent*. 2020. https://www.helmholtz-berlin.de/pubbin/news_seite?nid=21020;sprache=en;seitenid= (visited on 30/06/2020).

[169] Song, Z.; Phillips, A. B.; Celik, I.; Liyanage, G. K.; Zhao, D.; Apul, D.; Yan, Y. and Heben, M. J. 'Manufacturing Cost Analysis of Perovskite Solar Modules in Single-Junction and All-Perovskite Tandem Configurations'. *2018 IEEE 7th World Conference on Photovoltaic Energy Conversion (WCPEC)(A Joint Conference of 45th IEEE PVSC, 28th PVSEC & 34th EU PVSEC)*. IEEE. 2018, 1134–1138.

[170] Celik, I.; Phillips, A. B.; Song, Z.; Yan, Y.; Ellingson, R. J.; Heben, M. J. and Apul, D. 'Environmental Analysis of Perovskites and Other Relevant Solar Cell Technologies in a Tandem Configuration'. *Energy Environ. Sci.*, 2017, **10**, 1874–1884.

[171] Noh, J. H.; Im, S. H.; Heo, J. H.; Mandal, T. N. and Seok, S. I. 'Chemical Management for Colorful, Efficient, and Stable Inorganic–Organic Hybrid Nanostructured Solar Cells'. *Nano Lett.*, 2013, **13**, 1764–1769.

[172] Unger, E. L.; Kegelmann, L.; Suchan, K; Sörell, D; Korte, L. and Albrecht, S. 'Roadmap and Roadblocks for the Band Gap Tunability of Metal Halide Perovskites'. *J. Mater. Chem. A*, 2017, **5**, 11401–11409.

[173] Li, Z.; Boix, P. P.; Xing, G.; Fu, K.; Kulkarni, S. A.; Batabyal, S. K.; Xu, W.; Cao, A.; Sum, T. C.; Mathews, N. *et al.* 'Carbon Nanotubes as an Efficient Hole Collector for High Voltage Methylammonium Lead Bromide Perovskite Solar Cells'. *Nanoscale*, 2016, **8**, 6352–6360.

[174] Heo, J. H. and Im, S. H. '$CH_3NH_3PbBr_3$–$CH_3NH_3PbI_3$ Perovskite–Perovskite Tandem Solar Cells with Exceeding 2.2 V Open Circuit Voltage'. *Adv. Mater.*, 2016, **28**, 5121–5125.

[175] Lin, R; Xiao, K; Qin, Z; Han, Q; Zhang, C; Wei, M; Saidaminov, M. I.; Gao, Y; Xu, J; Xiao, M *et al.* 'Monolithic All-Perovskite Tandem Solar Cells with 24.8% Efficiency Exploiting Comproportionation to Suppress Sn(II) Oxidation in Precursor Ink'. *Nat. Energy*, 2019, **4**, 864–873.

[176] Tong, J.; Song, Z.; Kim, D. H.; Chen, X.; Chen, C.; Palmstrom, A. F.; Ndione, P. F.; Reese, M. O.; Dunfield, S. P.; Reid, O. G. *et al.* 'Carrier Lifetimes of >1 μs in Sn-Pb Perovskites Enable Efficient All-Perovskite Tandem Solar Cells'. *Science*, 2019, **364**, 475–479.

[177] Takahashi, Y.; Hasegawa, H.; Takahashi, Y. and Inabe, T. 'Hall Mobility in Tin Iodide Perovskite $CH_3NH_3SnI_3$: Evidence for a Doped Semiconductor'. *J. Solid State Chem.*, 2013, **205**, 39–43.

[178] Leijtens, T.; Prasanna, R.; Gold-Parker, A.; Toney, M. F. and McGehee, M. D. 'Mechanism of Tin Oxidation and Stabilization by Lead Substitution in Tin Halide Perovskites'. *ACS Energy Lett.*, 2017, **2**, 2159–2165.

[179] Wang, D.; Wright, M.; Elumalai, N. K. and Uddin, A. 'Stability of Perovskite Solar Cells'. *Sol. Energy Mater. Sol. Cells*, 2016, **147**, 255–275.

[180] Leijtens, T.; Prasanna, R.; Bush, K. A.; Eperon, G. E.; Raiford, J. A.; Gold-Parker, A.; Wolf, E. J.; Swifter, S. A.; Boyd, C. C.; Wang, H.-P. *et al.* 'Tin–Lead Halide Perovskites with Improved Thermal and Air Stability for Efficient All-Perovskite Tandem Solar Cells'. *Sustainable Energy Fuels*, 2018, **2**, 2450–2459.

[181] Konstantakou, M. and Stergiopoulos, T. 'A Critical Review on Tin Halide Perovskite Solar Cells'. *J. Mater. Chem. A*, 2017, **5**, 11518–11549.

[182] Qiu, J.; Xia, Y.; Zheng, Y.; Hui, W.; Gu, H.; Yuan, W.; Yu, H.; Chao, L.; Niu, T.; Yang, Y. *et al.* '2D Intermediate Suppression for Efficient Ruddlesden–Popper (RP) Phase Lead-Free Perovskite Solar Cells'. *ACS Energy Lett.*, 2019, **4**, 1513–1520.

[183] Xu, H.; Jiang, Y.; He, T.; Li, S.; Wang, H.; Chen, Y.; Yuan, M. and Chen, J. 'Orientation Regulation of Tin-Based Reduced-Dimensional Perovskites for Highly Efficient and Stable Photovoltaics'. *Adv. Funct. Mater.*, 2019, **29**, 1807696.

[184] Wang, F.; Jiang, X.; Chen, H.; Shang, Y.; Liu, H.; Wei, J.; Zhou, W.; He, H.; Liu, W. and Ning, Z. '2D-Quasi-2D-3D Hierarchy Structure for Tin Perovskite Solar Cells with Enhanced Efficiency and Stability'. *Joule*, 2018, **2**, 2732–2743.

[185] Yuan, J.; Jiang, Y.; He, T.; Shi, G.; Fan, Z. and Yuan, M. 'Two-Dimensional Perovskite Capping Layer for Stable and Efficient Tin-Lead Perovskite Solar Cells'. *Sci. China: Chem.*, 2019, **107**.

[186] Li, C.; Pan, Y.; Hu, J.; Qiu, S.; Zhang, C.; Yang, Y.; Chen, S.; Liu, X.; Brabec, C. J.; Nazeeruddin, M. K. *et al.* 'Vertically Aligned 2D/3D Pb–Sn Perovskites with Enhanced Charge Extraction and Suppressed Phase Segregation for Efficient Printable Solar Cells'. *ACS Energy Lett.*, 2020, **5**, 1386–1395.

[187] Grancini, G.; Roldán-Carmona, C.; Zimmermann, I.; Mosconi, E.; Lee, X.; Martineau, D.; Narbey, S.; Oswald, F.; De Angelis, F.; Graetzel, M. *et al.* 'One-Year Stable Perovskite Solar Cells by 2D/3D Interface Engineering'. *Nat. Commun.*, 2017, **8**, 1–8.

[188] Grancini, G. and Nazeeruddin, M. K. 'Dimensional Tailoring of Hybrid Perovskites for Photovoltaics'. *Nat. Rev. Mater.*, 2019, **4**, 4–22.

[189] Lin, Y.; Bai, Y.; Fang, Y.; Wang, Q.; Deng, Y. and Huang, J. 'Suppressed Ion Migration in Low-Dimensional Perovskites'. *ACS Energy Lett.*, 2017, **2**, 1571–1572.

[190] Peng, W.; Yin, J.; Ho, K.-T.; Ouellette, O.; De Bastiani, M.; Murali, B.; El Tall, O.; Shen, C.; Miao, X.; Pan, J. *et al.* 'Ultralow Self-Doping in Two-Dimensional Hybrid Perovskite Single Crystals'. *Nano Lett.*, 2017, **17**, 4759–4767.

[191] Gao, W; Ran, C; Li, J; Dong, H; Jiao, B; Zhang, L; Lan, X; Hou, X and Wu, Z. 'Robust Stability of Efficient Lead-Free Formamidinium Tin Iodide Perovskite Solar Cells Realized by Structural Regulation'. *J. Phys. Chem. Lett.*, 2018, **9**, 6999–7006.

[192] Tsarev, S.; Boldyreva, A. G.; Luchkin, S. Y.; Elshobaki, M.; Afanasov, M. I.; Stevenson, K. J. and Troshin, P. A. 'Hydrazinium-Assisted Stabilisation of Methylammonium Tin Iodide for Lead-Free Perovskite Solar Cells'. *J. Mater. Chem. A*, 2018, **6**, 21389–21395.

[193] Chen, M.; Ju, M.-G.; Garces, H. F.; Carl, A. D.; Ono, L. K.; Hawash, Z.; Zhang, Y.; Shen, T.; Qi, Y.; Grimm, R. L. *et al.* 'Highly Stable and Efficient All-Inorganic Lead-Free Perovskite Solar Cells with Native-Oxide Passivation'. *Nat. Commun.*, 2019, **10**, 16.

[194] Lee, S. J.; Shin, S. S.; Im, J; Ahn, T. K.; Noh, J. H.; Jeon, N. J.; Seok, S. I. and Seo, J. 'Reducing Carrier Density in Formamidinium Tin Perovskites and Its Beneficial Effects on Stability and Efficiency of Perovskite Solar Cells'. *ACS Energy Lett.*, 2018, **3**, 46–53.

[195] Kumar, M. H.; Dharani, S.; Leong, W. L.; Boix, P. P.; Prabhakar, R. R.; Baikie, T.; Shi, C.; Ding, H.; Ramesh, R.; Asta, M. *et al.* 'Lead-Free Halide Perovskite Solar Cells with High Photocurrents Realized Through Vacancy Modulation'. *Adv. Mater.*, 2014, **26**, 7122–7127.

[196] Marshall, K.; Walker, M; Walton, R. and Hatton, R. 'Enhanced Stability and Efficiency in Hole-Transport-Layer-Free $CsSnI_3$ Perovskite Photovoltaics'. *Nat. Energy*, 2016, **1**, 1–9.

[197] Heo, J. H.; Kim, J.; Kim, H.; Moon, S. H.; Im, S. H. and Hong, K.-H. 'Roles of SnX_2 (X= F, Cl, Br) Additives in Tin-Based Halide Perovskites Toward Highly Efficient and Stable Lead-Free Perovskite Solar Cells'. *J. Phys. Chem. Lett.*, 2018, **9**, 6024–6031.

[198] Li, W.; Li, J.; Li, J.; Fan, J.; Mai, Y. and Wang, L. 'Addictive-Assisted Construction of All-Inorganic $CsSnIBr_2$ Mesoscopic Perovskite Solar Cells with Superior Thermal Stability up to 473 K'. *J. Mater. Chem. A*, 2016, **4**, 17104–17110.

[199] Xu, X.; Chueh, C.-C.; Yang, Z.; Rajagopal, A.; Xu, J.; Jo, S. B. and Jen, A. K.-Y. 'Ascorbic Acid as an Effective Antioxidant Additive to Enhance the Efficiency and Stability of Pb/Sn-Based Binary Perovskite Solar Cells'. *Nano Energy*, 2017, **34**, 392–398.

[200] Gu, F.; Ye, S.; Zhao, Z.; Rao, H.; Liu, Z.; Bian, Z. and Huang, C. 'Improving Performance of Lead-Free Formamidinium Tin Triiodide Perovskite Solar Cells by Tin Source Purification'. *Solar RRL*, 2018, **2**, 1800136.

[201] Koh, T. M.; Krishnamoorthy, T.; Yantara, N.; Shi, C.; Leong, W. L.; Boix, P. P.; Grimsdale, A. C.; Mhaisalkar, S. G. and Mathews, N. 'Formamidinium Tin-Based Perovskite with Low E_g for Photovoltaic Applications'. *J. Mater. Chem. A*, 2015, **3**, 14996–15000.

[202] Gupta, S.; Cahen, D. and Hodes, G. 'How SnF_2 Impacts the Material Properties of Lead-Free Tin Perovskites'. *J. Phys. Chem. C*, 2018, **122**, 13926–13936.

[203] Hartmann, C.; Gupta, S.; Bendikov, T.; Kozina, X.; Kunze, T.; Félix, R.; Hodes, G.; Wilks, R. G.; Cahen, D. and Bär, M. 'Impact of SnF_2 Addition on the Chemical and Electronic Surface Structure of $CsSnBr_3$'. *ACS Appl. Mater. Interfaces*, 2020, **12**, 12353–12361.

[204] Wehrenfennig, C.; Liu, M.; Snaith, H. J.; Johnston, M. B. and Herz, L. M. 'Homogeneous Emission Line Broadening in the Organo Lead Halide Perovskite $CH_3NH_3PbI_{3-x}Cl_x$'. *J. Phys. Chem. Lett.*, 2014, **5**, 1300–1306.

[205] Fox, M. *Optical Properties of Solids : Optical Properties of Solids*. Oxford University Press, Incorporated, 2010.

[206] Knight, A. J.; Wright, A. D.; Patel, J. B.; McMeekin, D. P.; Snaith, H. J.; Johnston, M. B. and Herz, L. M. 'Electronic Traps and Phase Segregation in Lead Mixed-Halide Perovskite'. *ACS Energy Lett.*, 2018, **4**, 75–84.

[207] Pelant, I. and Valenta, J. *Luminescence Spectroscopy of Semiconductors*. Oxford University Press, 2012.

[208] Wirth, M. J. 'Ultrafast Spectroscopy'. *Anal. Chem.*, 1990, **62**, 270A–277A.

[209] Lakowicz, J. R. *Principles of Fluorescence Spectroscopy*. Springer US, 2006.

[210] Chen, K.; Barker, A. J.; Morgan, F. L. C.; Halpert, J. E. and Hodgkiss, J. M. 'Effect of Carrier Thermalization Dynamics on Light Emission and Amplification in Organometal Halide Perovskites'. *J. Phys. Chem. Lett.*, 2014, **6**, 153–158.

[211] Schmidt, B; Laimgruber, S; Zinth, W and Gilch, P. 'A Broadband Kerr Shutter for Femtosecond Fluorescence Spectroscopy'. *Appl. Phys. B*, 2003, **76**, 809–814.

[212] Chosrowjan, H.; Taniguchi, S. and Tanaka, F. 'Ultrafast Fluorescence Upconversion Technique and its Applications to Proteins'. *FEBS J.*, 2015, **282**, 3003–3015.

[213] Chen, K.; Gallaher, J. K.; Barker, A. J. and Hodgkiss, J. M. 'Transient Grating Photoluminescence Spectroscopy: an Ultrafast Method of Gating Broadband Spectra'. *J. Phys. Chem. Lett.*, 2014, **5**, 1732–1737.

[214] Boyd, R. W. *Nonlinear Optics. [electronic resource]*. Ebook central. Elsevier Science & Technology, 2008.

[215] Shah, J. 'Ultrafast Luminescence Spectroscopy using Sum Frequency Generation'. *IEEE J. Quantum Electron.*, 1988, **24**, 276–288.

[216] Bright, F. V. and Munson, C. A. 'Time-Resolved Fluorescence Spectroscopy for Illuminating Complex Systems'. *Anal. Chim. Acta*, 2003, **500**, 71–104.

[217] Murakami, H. 'Femtosecond Time-Resolved Fluorescence Up-Conversion Spectrometer Corrected for Wavelength-Dependent Conversion Efficiency Using Continuous White Light'. *Rev. Sci. Instrum.*, 2006, **77**, 113105.

[218] Becker, W. *The bh TCSPC Handbook*. Berlin, 2019. http://www.becker-hickl.de/handbook.htm.

[219] PicoQuant GmbH. *PDM Series: Single Photon Avalanche Diodes*. Berlin, 2018. https://www.picoquant.com/images/uploads/downloads/pdm_series.pdf.

[220] Paterson, M. 'The Determination of Hydroxyl by Infrared Absorption in Quartz, Silicate Glasses and Similar Materials'. *Bull. Mineral.*, 1982, **105**, 20–29.

[221] Christy, A. A.; Ozaki, Y and Gregoriou, V. G. *Modern Fourier Transform Infrared Spectroscopy [electronic resource]*. Comprehensive Analytical Chemistry ; v. 35. Elsevier, 2001.

[222] Newport. *Technical Note: Introduction to FTIR Spectroscopy*. https://www.newport.com/n/introduction-to-ftir-spectroscopy (visited on 21/04/2020).

[223] Birkholz, M.; Genzel, C. and Fewster, P. F. *Thin Film Analysis by X-Ray Scattering*. John Wiley & Sons, 2006.

[224] Ladd, M. and Palmer, R. *Structure Determination by X-ray Crystallography*. Springer US, 2013.

[225] Savill, K. J.; Klug, M. T.; Milot, R. L.; Snaith, H. J. and Herz, L. M. 'Charge-Carrier Cooling and Polarization Memory Loss in Formamidinium Tin Triiodide'. *J. Phys. Chem. Lett.*, 2019, **10**. PMID: 31545045, 6038–6047. eprint: https://doi.org/10.1021/acs.jpclett.9b02353.

[226] Shen, Q.; Ripolles, T. S.; Even, J.; Ogomi, Y.; Nishinaka, K.; Izuishi, T.; Nakazawa, N.; Zhang, Y.; Ding, C.; Liu, F. *et al.* 'Slow Hot Carrier Cooling in Cesium Lead Iodide Perovskites'. *Appl. Phys. Lett.*, 2017, **111**, 153903.

[227] Jia, X.; Jiang, J.; Zhang, Y.; Qiu, J.; Wang, S.; Chen, Z.; Yuan, N. and Ding, J. 'Observation of Enhanced Hot Phonon Bottleneck Effect in 2D Perovskites'. *Appl. Phys. Lett.*, 2018, **112**, 143903.

[228] Nah, S.; Spokoyny, B. M.; Soe, C. M. M.; Stoumpos, C. C.; Kanatzidis, M. G. and Harel, E. 'Ultrafast Imaging of Carrier Cooling in Metal Halide Perovskite Thin Films'. *Nano Lett.*, 2018, **18**, 1044–1048.

[229] Chauhan, K. K.; Prodhan, S; Ghosh, D; Waghale, P; Bhattacharyya, S; Dutta, P. K. and Datta, P. K. 'Long Carrier Diffusion Length and Slow Hot Carrier Cooling in Thin Film Mixed Halide Perovskite'. *IEEE J. Photovoltaics*, 2020, **10**, 803–810.

[230] Verma, S. D.; Gu, Q.; Sadhanala, A.; Venugopalan, V. and Rao, A. 'Slow Carrier Cooling in Hybrid Pb–Sn Halide Perovskites'. *ACS Energy Lett.*, 2019, **4**, 736–740.

[231] Shah, J. and Leite, R. C. C. 'Radiative Recombination from Photoexcited Hot Carriers in GaAs'. *Phys. Rev. Lett.*, 1969, **22**, 22–25.

[232] Motisuke, P; Argüello, C. A. and Leite, R. C. C. 'Hot Electron and Hot Phonon Contributions to Radiative Emission Spectra in CdS at High Excitation Intensities'. *Solid State Commun.*, 1975, **16**, 763–765.

[233] Shah, J.; Lin, C.; Leheny, R. F. and DiGiovanni, A. E. 'Pump Wavelength Dependence of Hot Electron Temperature in GaAs'. *Solid State Commun.*, 1976, **18**, 487–489.

[234] Leo, K. and Rühle, W. W. 'Influence of Carrier Lifetime on the Cooling of a Hot Electron-Hole Plasma in GaAs'. *Solid State Commun.*, 1987, **62**, 659–662.

[235] Ryan, J. F.; Taylor, R. A.; Turberfield, A. J.; Maciel, A.; Worlock, J. M.; Gossard, A. C. and Wiegmann, W. 'Time-Resolved Photoluminescence of Two-Dimensional Hot Carriers in GaAs-AlGaAs Heterostructures'. *Phys. Rev. Lett.*, 1984, **53**, 1841–1844.

[236] Xu, Z. Y. and Tang, C. L. 'Picosecond Relaxation of Hot Carriers in Highly Photoexcited Bulk GaAs and GaAs-AlGaAs Multiple Quantum Wells'. *Appl. Phys. Lett.*, 1984, **44**, 692–694.

[237] Ryan, J. F. 'Time-Resolved Photoluminescence for Quantum Well Semiconductor Heterostructures'. *Physica B+C*, 1985, **134**, 403–411.

[238] Shum, K; Ho, P; Alfano, R; Welch, D; Wicks, G and Eastman, L. 'Dependence of Electron Temperature on Well Width in the $Al_{0.48}In_{0.52}As/Ga_{0.47}In_{0.53}As$ Single-Quantum Well'. *IEEE J. Quantum Electron.*, 1986, **QE-22**, 1811–1815.

[239] Leo, K; Rühle, W. W. and Ploog, K. 'Hot-Carrier Energy-Loss Rates in $GaAs/Al_xGa_{1-x}As$ Quantum Wells'. *Phys. Rev. B*, 1988, **38**, 1947–1957.

[240] Leo, K; Rühle, W. W.; Queisser, H. J. and Ploog, K. 'Reduced Dimensionality of Hot-Carrier Relaxation in GaAs Quantum Wells'. *Phys. Rev. B*, 1988, **37**, 7121–7124.

[241] Leo, K; Rühle, W. W. and Ploog, K. 'Hot Carrier Thermalization in GaAs/AlAs Superlattices'. *Solid-State Electron.*, 1989, **32**, 1863–1867.

[242] Andersson, T. G.; Chen, Z.-G.; Xu, Z.-Y.; Xu, J.-Z. and Ge, W.-K. 'Hot Carrier Photoluminescence from Strained $In_xGa_{1-x}As/GaAs$ Single Quantum Wells'. *J. Cryst. Growth*, 1989, **95**, 215–219.

[243] Nozik, A. J.; Parsons, C. A.; Dunlavy, D. J.; Keyes, B. M. and Ahrenkiel, R. K. 'Dependence of Hot Carrier Luminescence on Barrier Thickness in GaAs/AlGaAs Superlattices and Multiple Quantum Wells'. *Solid State Commun.*, 1990, **75**, 297–301.

[244] Ge, W.; Xu, Z.; Li, Y.; Xu, Z.; Xu, J.; Zheng, B. and Zhuang, W. 'Hot Carrier Relaxation Processes and Nonequilibrium Phonon Effect in Multiple Quantum Well Structures'. *J. Lumin.*, 1990, **46**, 137–145.

[245] Mooradian, A. and Fan, H. Y. 'Recombination Emission in InSb'. *Phys. Rev.*, 1966, **148**, 873–885.

[246] Ulbrich, R. 'Energy Relaxation of Photoexcited Hot Electrons in GaAs'. *Phys. Rev. B*, 1973, **8**, 5719–5727.

[247] Meneses, E. A.; Jannuzzi, N; Ramos, J. G. P.; Luzzi, R and Leite, R. C. C. 'Many-Body and Hot-Phonon Effects in the Radiative Emission Spectrum of CdS Under High Excitation Intensities'. *Phys. Rev. B*, 1975, **11**, 2213.

[248] Ploog, K; Fischer, A; Tapfer, L and Feuerbacher, B. F. 'Narrow Luminescence Linewidth in GaAs Single Quantum Wells by Insertion of Thin AlAs Smoothing Layers'. *J. Cryst. Growth*, 1991, **111**, 344–347.

[249] Gotoh, H; Akasaka, T; Tawara, T; Kobayashi, Y; Makimoto, T and Nakano, H. 'Efficient Observation of Narrow Isolated Photoluminescence Spectra from Spatially Localized Excitons in InGaN Quantum Wells'. *Jpn. J. Appl. Phys., Part 2*, 2005, **44**, L1381–L1384.

[250] Kash, K. and Shah, J. 'Carrier Energy Relaxation in $In_{0.53}Ga_{0.47}As$ Determined from Picosecond Luminescence Studies'. *Appl. Phys. Lett.*, 1984, **45**, 401–403.

[251] Collet, J. H.; Rühle, W. W.; Pugnet, M; Leo, K and Million, A. 'Electron-Hole Plasma Dynamics in CdTe in the Picosecond Regime'. *Phys. Rev. B*, 1989, **40**, 12296.

[252] Collet, J. H.; Rühle, W. W.; Pugnet, M.; Leo, K. and Million, A. 'Electron-Hole Plasma Relaxation in CdTe'. *J. Cryst. Growth*, 1990, **101**, 773–777.

[253] He, Y. and Galli, G. 'Perovskites for Solar Thermoelectric Applications: A First Principle Study of $CH_3NH_3AI_3$ (A= Pb and Sn)'. *Chem. Mater.*, 2014, **26**, 5394–5400.

[254] Dar, M. I.; Jacopin, G.; Meloni, S.; Mattoni, A.; Arora, N.; Boziki, A.; Zakeeruddin, S. M.; Rothlisberger, U. and Grätzel, M. 'Origin of Unusual Bandgap Shift and Dual Emission in Organic-Inorganic Lead Halide Perovskites'. *Sci. Adv.*, 2016, **2**, e1601156.

[255] Arend, T. R.; Tönnies, M.; Reisbeck, P.; Rieckmann, C. J. P. and Kersting, R. 'Physical Vapor Deposition of Methylammonium Tin Iodide Thin Films'. *Phys. Status Solidi A*, 2017, **214**, 1600796.

[256] Wu, K.; Bera, A.; Ma, C.; Du, Y.; Yang, Y.; Li, L. and Wu, T. 'Temperature-Dependent Excitonic Photoluminescence of Hybrid Organometal Halide Perovskite Films'. *Phys. Chem. Chem. Phys.*, 2014, **16**, 22476–22481.

[257] Phuong, L. Q.; Braly, I. L.; Katahara, J. K.; Hillhouse, H. W. and Kanemitsu, Y. 'Nonlinear Photocarrier Recombination Dynamics in Mixed-Halide $CH_3NH_3Pb(I_{1-x}Br_x)_3$ Perovskite Thin Films'. *Appl. Phys. Express*, 2017, **10**, 102401.

[258] Handa, T.; Aharen, T.; Wakamiya, A. and Kanemitsu, Y. 'Radiative Recombination and Electron-Phonon Coupling in Lead-Free $CH_3NH_3SnI_3$ Perovskite Thin Films'. *Phys. Rev. Mater.*, 2018, **2**, 75402.

[259] Straus, D. B.; Hurtado Parra, S.; Iotov, N.; Gebhardt, J.; Rappe, A. M.; Subotnik, J. E.; Kikkawa, J. M. and Kagan, C. R. 'Direct Observation of Electron–Phonon Coupling and Slow Vibrational Relaxation in Organic–Inorganic Hybrid Perovskites'. *J. Am. Chem. Soc.*, 2016, **138**, 13798–13801.

[260] Klingshirn, C. F. *Semiconductor Optics*. Springer, 2012.

[261] Handa, T.; Aharen, T.; Wakamiya, A. and Kanemitsu, Y. 'Photoelectronic Properties of Lead-Free $CH_3NH_3SnI_3$ Perovskite Solar Cell Materials and Devices'. *Organic, Hybrid, and Perovskite Photovoltaics XIX*. Vol. 10737. International Society for Optics and Photonics. 2018, 107371X.

[262] Lim, J. W. M.; Giovanni, D.; Righetto, M.; Feng, M.; Mhaisalkar, S. G.; Mathews, N. and Sum, T. C. 'Hot Carriers in Halide Perovskites: How Hot Truly?' *J. Phys. Chem. Lett.*, 2020, **11**, 2743–2750.

[263] Rivett, J. P. H.; Tan, L. Z.; Price, M. B.; Bourelle, S. A.; Davis, N. J. L. K.; Xiao, J.; Zou, Y.; Middleton, R.; Sun, B.; Rappe, A. M. *et al.* 'Long-Lived Polarization Memory in the Electronic States of Lead-Halide Perovskites from Local Structural Dynamics'. *Nat. Commun.*, 2018, **9**, 3531.

[264] Ma, J. and Wang, L.-W. 'Nanoscale Charge Localization Induced by Random Orientations of Organic Molecules in Hybrid Perovskite $CH_3NH_3PbI_3$'. *Nano Lett.*, 2014, **15**, 248–253.

[265] Juarez-Perez, E. J.; Sanchez, R. S.; Badia, L.; Garcia-Belmonte, G.; Kang, Y. S.; Mora-Sero, I. and Bisquert, J. 'Photoinduced Giant Dielectric Constant in Lead Halide Perovskite Solar Cells'. *J. Phys. Chem. Lett.*, 2014, **5**, 2390–2394.

[266] Motta, C.; El-Mellouhi, F.; Kais, S.; Tabet, N.; Alharbi, F. and Sanvito, S. 'Revealing the Role of Organic Cations in Hybrid Halide Perovskite $CH_3NH_3PbI_3$'. *Nat. Commun.*, 2015, **6**, 7026.

[267] March, S. A.; Riley, D. B.; Clegg, C.; Webber, D.; Liu, X.; Dobrowolska, M.; Furdyna, J. K.; Hill, I. G. and Hall, K. C. 'Four-Wave Mixing in Perovskite Photovoltaic Materials Reveals Long Dephasing Times and Weaker Many-Body Interactions than GaAs'. *ACS Photonics*, 2017, **4**, 1515–1521.

[268] Frost, J. M.; Butler, K. T.; Brivio, F.; Hendon, C. H.; Van Schilfgaarde, M. and Walsh, A. 'Atomistic Origins of High-Performance in Hybrid Halide Perovskite Solar Cells'. *Nano Lett.*, 2014, **14**, 2584–2590.

[269] He, H.; Yu, Q.; Li, H.; Li, J.; Si, J.; Jin, Y.; Wang, N.; Wang, J.; He, J.; Wang, X. *et al.* 'Exciton Localization in Solution-Processed Organolead Trihalide Perovskites'. *Nat. Commun.*, 2016, **7**, 10896.

[270] Yang, Y.; Yan, Y.; Yang, M.; Choi, S.; Zhu, K.; Luther, J. M. and Beard, M. C. 'Low Surface Recombination Velocity in Solution-Grown $CH_3NH_3PbBr_3$ Perovskite Single Crystal'. *Nat. Commun.*, 2015, **6**, 7961.

[271] Whalley, L. D.; Frost, J. M.; Morgan, B. J. and Walsh, A. 'Impact of Nonparabolic Electronic Band Structure on the Optical and Transport Properties of Photovoltaic Materials'. *Phys. Rev. B*, 2019, **99**, 085207.

[272] Siegel, J.; Suhling, K.; Lévêque-Fort, S.; Webb, S. E.; Davis, D. M.; Phillips, D.; Sabharwal, Y and French, P. M. 'Wide-Field Time-Resolved Fluorescence Anisotropy Imaging (TR-FAIM): Imaging the Rotational Mobility of a Fluorophore'. *Rev. Sci. Instrum.*, 2003, **74**, 182–192.

[273] Gong, J. Q.; Parkinson, P.; Kondratuk, D. V.; Gil-Ramírez, G.; Anderson, H. L. and Herz, L. M. 'Structure-Directed Exciton Dynamics in Templated Molecular Nanorings'. *J. Phys. Chem. C*, 2015, **119**, 6414–6420.

[274] Chan, F. T. S.; Kaminski, C. F. and Kaminski Schierle, G. S. 'HomoFRET Fluorescence Anisotropy Imaging as a Tool to Study Molecular Self-Assembly in Live Cells'. *ChemPhysChem*, 2011, **12**, 500–509.

[275] Herz, L. M. and Phillips, R. T. 'Effects of Interchain Interactions, Polarization Anisotropy, and Photo-Oxidation on the Ultrafast Photoluminescence Decay from a Polyfluorene'. *Phys. Rev. B*, 2000, **61**, 13691–13697.

[276] Lavallard, P and Suris, R. A. 'Polarized Photoluminescence of an Assembly of Non Cubic Microcrystals in a Dielectric Matrix'. *Solid State Commun.*, 1995, **95**, 267–269.

[277] Zemskii, V. I.; Zakharchenya, B. P. and Mirlin, D. N. 'Polarization of Hot Photoluminescence in Semiconductors of the GaAs Type'. *JETP Lett.*, 1976, **24**, 82–85.

[278] Portella, M. T.; Bigot, J.-Y.; Schoenlein, R. W.; Cunningham, J. E. and Shank, C. V. 'k-Space Carrier Dynamics in GaAs'. *Appl. Phys. Lett.*, 1992, **60**, 2123–2125.

[279] Yaffe, O.; Guo, Y.; Tan, L. Z.; Egger, D. A.; Hull, T.; Stoumpos, C. C.; Zheng, F.; Heinz, T. F.; Kronik, L.; Kanatzidis, M. G. *et al.* 'Local Polar Fluctuations in Lead Halide Perovskite Crystals'. *Phys. Rev. Lett.*, 2017, **118**, 136001.

[280] Wu, X.; Tan, L. Z.; Shen, X.; Hu, T.; Miyata, K.; Trinh, M. T.; Li, R.; Coffee, R.; Liu, S.; Egger, D. A. *et al.* 'Light-Induced Picosecond Rotational Disordering of the Inorganic Sublattice in Hybrid Perovskites'. *Sci. Adv.*, 2017, **3**, e1602388.

[281] Beecher, A. N.; Semonin, O. E.; Skelton, J. M.; Frost, J. M.; Terban, M. W.; Zhai, H.; Alatas, A.; Owen, J. S.; Walsh, A. and Billinge, S. J. L. 'Direct Observation of Dynamic Symmetry Breaking Above Room Temperature in Methylammonium Lead Iodide Perovskite'. *ACS Energy Lett.*, 2016, **1**, 880–887.

[282] Etienne, T.; Mosconi, E. and De Angelis, F. 'Dynamical Origin of the Rashba Effect in Organohalide Lead Perovskites: A Key to Suppressed Carrier Recombination in Perovskite Solar Cells?' *J. Phys. Chem. Lett.*, 2016, **7**, 1638–1645.

[283] Kubicki, D. J.; Prochowicz, D.; Hofstetter, A.; Péchy, P.; Zakeeruddin, S. M.; Grätzel, M. and Emsley, L. 'Cation Dynamics in Mixed-Cation $(MA)_x(FA)_{1-x}PbI_3$ Hybrid Perovskites from Solid-State NMR'. *J. Am. Chem. Soc.*, 2017, **139**, 10055–10061.

[284] Motta, C.; El-Mellouhi, F. and Sanvito, S. 'Exploring the Cation Dynamics in Lead-Bromide Hybrid Perovskites'. *Phys. Rev. B*, 2016, **93**, 235412.

[285] Fabini, D. H.; Siaw, T. A.; Stoumpos, C. C.; Laurita, G.; Olds, D.; Page, K.; Hu, J. G.; Kanatzidis, M. G.; Han, S. and Seshadri, R. 'Universal Dynamics of Molecular Reorientation in Hybrid Lead Iodide Perovskites'. *J. Am. Chem. Soc.*, 2017, **139**, 16875–16884.

[286] Zhai, Y.; Sheng, C. X.; Zhang, C. and Vardeny, Z. V. 'Ultrafast Spectroscopy of Photoexcitations in Organometal Trihalide Perovskites'. *Adv. Funct. Mater.*, 2016, **26**, 1617–1627.

[287] Wang, K.-H.; Li, L.-C.; Shellaiah, M. and Sun, K. W. 'Structural and Photophysical Properties of Methylammonium Lead Tribromide ($MAPbBr_3$) Single Crystals'. *Sci. Rep.*, 2017, **7**, 13643.

[288] Schueller, E. C.; Laurita, G.; Fabini, D. H.; Stoumpos, C. C.; Kanatzidis, M. G. and Seshadri, R. 'Crystal Structure Evolution and Notable Thermal Expansion in Hybrid Perovskites Formamidinium Tin Iodide and Formamidinium Lead Bromide'. *Inorg. Chem.*, 2018, **57**, 695–701.

[289] Mitzi, D. B. and Liang, K. 'Synthesis, Resistivity, and Thermal Properties of the Cubic Perovskite $NH_2CH{=}NH_2SnI_3$ and Related Systems'. *J. Solid State Chem.*, 1997, **134**, 376–381.

[290] Savill, K. J.; Ulatowski, A. M.; Farrar, M. D.; Johnston, M. B.; Snaith, H. J. and Herz, L. M. 'Impact of Tin Fluoride Additive on the Properties of Mixed Tin-Lead Iodide Perovskite Semiconductors'. *Adv. Funct. Mater.*, 2020, **30**, 2005594. eprint: https://onlinelibrary.wiley.com/doi/pdf/10.1002/adfm.202005594.

[291] Bowman, A. R.; Klug, M. T.; Doherty, T. A. S.; Farrar, M. D.; Senanayak, S. P.; Wenger, B; Divitini, G; Booker, E. P.; Andaji-Garmaroudi, Z; Macpherson, S *et al.* 'Microsecond Carrier Lifetimes, Controlled p-Doping, and Enhanced Air Stability in Low-Bandgap Metal Halide Perovskites'. *ACS Energy Lett.*, 2019, **4**, 2301–2307.

[292] Rajagopal, A.; Yang, Z.; Jo, S. B.; Braly, I. L.; Liang, P.-W.; Hillhouse, H. W. and Jen, A. K.-Y. 'Highly Efficient Perovskite–Perovskite Tandem Solar Cells Reaching 80% of the Theoretical Limit in Photovoltage'. *Adv. Mater.*, 2017, **29**, 1702140.

[293] Zhao, D.; Wang, C.; Song, Z.; Yu, Y.; Chen, C.; Zhao, X.; Zhu, K. and Yan, Y. 'Four-Terminal All-Perovskite Tandem Solar Cells Achieving Power Conversion Efficiencies Exceeding 23%'. *ACS Energy Lett.*, 2018, **3**, 305–306.

[294] Palmstrom, A. F.; Eperon, G. E.; Leijtens, T.; Prasanna, R.; Habisreutinger, S. N.; Nemeth, W.; Gaulding, E. A.; Dunfield, S. P.; Reese, M.; Nanayakkara, S. *et al.* 'Enabling Flexible All-Perovskite Tandem Solar Cells'. *Joule*, 2019, **3**, 2193–2204.

[295] Wang, J; Datta, K; Li, J; Verheijen, M. A.; Zhang, D; Wienk, M. M. and Janssen, R. A. J. 'Understanding the Film Formation Kinetics of Sequential Deposited Narrow-Bandgap Pb–Sn Hybrid Perovskite Films'. *Adv. Energy Mater.*, 2020, **10**, 2000566.

[296] Wei, M; Xiao, K; Walters, G; Lin, R; Zhao, Y; Saidaminov, M. I.; Todorović, P; Johnston, A; Huang, Z; Chen, H *et al.* 'Combining Efficiency and Stability in Mixed Tin–Lead Perovskite Solar Cells by Capping Grains with an Ultrathin 2D Layer'. *Adv. Mater.*, 2020, **32**, 1907058.

[297] Tsai, C.-M.; Wu, H.-P.; Chang, S.-T.; Huang, C.-F.; Wang, C.-H.; Narra, S.; Yang, Y.-W.; Wang, C.-L.; Hung, C.-H. and Diau, E. W.-G. 'Role of Tin Chloride in Tin-Rich Mixed-Halide Perovskites Applied as Mesoscopic Solar Cells with a Carbon Counter Electrode'. *ACS Energy Lett.*, 2016, **1**, 1086–1093.

[298] Rajagopal, A.; Liang, P.-W.; Chueh, C.-C.; Yang, Z. and Jen, A. K.-Y. 'Defect Passivation via a Graded Fullerene Heterojunction in Low-Bandgap Pb–Sn Binary Perovskite Photovoltaics'. *ACS Energy Lett.*, 2017, **2**, 2531–2539.

[299] Igual-Muñoz, A. M.; Ávila, J; Boix, P. P. and Bolink, H. J. '$FAPb_{0.5}Sn_{0.5}I_3$: A Narrow Bandgap Perovskite Synthesized through Evaporation Methods for Solar Cell Applications'. *Solar RRL*, 2020, **4**.

[300] Li, C.; Wang, Z. S.; Zhu, H. L.; Zhang, D.; Cheng, J.; Lin, H.; Ouyang, D. and Choy, W. C. H. 'Thermionic Emission–Based Interconnecting Layer Featuring Solvent Resistance for Monolithic Tandem Solar Cells with Solution-Processed Perovskites'. *Adv. Energy Mater.*, 2018, **8**, 1801954.

[301] Yao, Y; Lv, F; Luo, L; Liao, L; Wang, G; Liu, D; Xu, C; Zhou, G; Zhao, X and Song, Q. 'Highly Efficient Sn–Pb Perovskite Solar Cell and High-Performance All-Perovskite Four-Terminal Tandem Solar Cell'. *Solar RRL*, 2020, **4**, 1900396.

[302] Tiwana, P.; Parkinson, P.; Johnston, M. B.; Snaith, H. J. and Herz, L. M. 'Ultrafast Terahertz Conductivity Dynamics in Mesoporous TiO_2: Influence of Dye Sensitization and Surface Treatment in Solid-State Dye-Sensitized Solar Cells'. *J. Phys. Chem. C*, 2010, **114**, 1365–1371.

[303] Seifert, T.; Jaiswal, S; Martens, U; Hannegan, J; Braun, L.; Maldonado, P.; Freimuth, F; Kronenberg, A; Henrizi, J; Radu, I *et al.* 'Efficient Metallic Spintronic Emitters of Ultrabroadband Terahertz Radiation'. *Nat. Photonics*, 2016, **10**, 483–488.

[304] Davies, C. L.; Patel, J. B.; Xia, C. Q.; Herz, L. M. and Johnston, M. B. 'Temperature-Dependent Refractive Index of Quartz at Terahertz Frequencies'. *J. Infrared, Millimeter, Terahertz Waves*, 2018, **39**, 1236–1248.

[305] Eperon, G. E.; Stranks, S. D.; Menelaou, C.; Johnston, M. B.; Herz, L. M. and Snaith, H. J. 'Formamidinium Lead trihalide: a Broadly Tunable Perovskite for Efficient Planar Heterojunction Solar Cells'. *Energy & Environmental Science*, 2014, **7**, 982–988.

[306] de Quilettes, D. W.; Vorpahl, S. M.; Stranks, S. D.; Nagaoka, H.; Eperon, G. E.; Ziffer, M. E.; Snaith, H. J. and Ginger, D. S. 'Impact of Microstructure on Local Carrier Lifetime in Perovskite Solar Cells'. *Science*, 2015, **348**, 683–686.

[307] Pydzińska-Białek, K.; Szeremeta, J.; Wojciechowski, K. and Ziółek, M. 'Insights into the Femtosecond to Nanosecond Charge Carrier Kinetics in Perovskite Materials for Solar Cells'. *J. Phys. Chem. C*, 2019, **123**, 110–119.

[308] Tauc, J; Grigorovici, R. and Vancu, A. 'Optical Properties and Electronic Structure of Amorphous Germanium'. *Phys. Status Solidi B*, 1966, **15**, 627–637.

[309] Elliott, R. 'Intensity of Optical Absorption by Excitons'. *Phys. Rev.*, 1957, **108**, 1384.

[310] Jacobsson, T. J.; Schwan, L. J.; Ottosson, M.; Hagfeldt, A. and Edvinsson, T. 'Determination of Thermal Expansion Coefficients and Locating the Temperature-Induced Phase Transition in Methylammonium Lead Perovskites Using X-ray Diffraction'. *Inorg. Chem.*, 2015, **54**, 10678–10685.

[311] Shi, T.; Zhang, H.-S.; Meng, W.; Teng, Q.; Liu, M.; Yang, X.; Yan, Y.; Yip, H.-L. and Zhao, Y.-J. 'Effects of Organic Cations on the Defect Physics of Tin Halide Perovskites'. *J. Mater. Chem. A*, 2017, **5**, 15124–15129.

[312] Jena, A. K.; Kulkarni, A.; Sanehira, Y.; Ikegami, M. and Miyasaka, T. 'Stabilization of α-$CsPbI_3$ in Ambient Room Temperature Conditions by Incorporating Eu into $CsPbI_3$'. *Chem. Mater.*, 2018, **30**, 6668–6674.

[313] Zhou, Y. and Zhao, Y. 'Chemical Stability and Instability of Inorganic Halide Perovskites'. *Energy Environ. Sci.*, 2019, **12**, 1495–1511.

[314] Zong, Y; Wang, N; Zhang, L; Ju, M.-G.; Zeng, X. C.; Sun, X. W.; Zhou, Y and Padture, N. P. 'Homogenous Alloys of Formamidinium Lead Triiodide and Cesium Tin Triiodide for Efficient Ideal-Bandgap Perovskite Solar Cells'. *Angew. Chem., Int. Ed.*, 2017, **56**, 12658–12662.

[315] Liao, W.; Zhao, D.; Yu, Y.; Grice, C. R.; Wang, C.; Cimaroli, A. J.; Schulz, P.; Meng, W.; Zhu, K.; Xiong, R.-G. *et al.* 'Lead-Free Inverted Planar Formamidinium Tin Triiodide Perovskite Solar Cells Achieving Power Conversion Efficiencies up to 6.22%'. *Adv. Mater.*, 2016, **28**, 9333–9340.

[316] Meggiolaro, D.; Ricciarelli, D.; Alasmari, A. A.; Alasmary, F. A. S. and De Angelis, F. 'Tin versus Lead Redox Chemistry Modulates Charge Trapping and Self-Doping in Tin/Lead Iodide Perovskites'. *J. Phys. Chem. Lett.*, 2020, **11**, 3546–3556.

[317] Hill, R and Richardson, D. 'A Comparison of the EPM and DM Methods for Calculations in Mixed Zincblende Alloys'. *J. Phys C: Solid State Phys.*, 1971, **4**, L339.

[318] Vurgaftman, I; Meyer, J. R. and Ram-Mohan, L. R. 'Band Parameters for III–V Compound Semiconductors and their Alloys'. *J. Appl. Phys.*, 2001, **89**, 5815–5875.

[319] Cardona, M. 'Optical Properties of the Silver and Cuprous Halides'. *Phys. Rev.*, 1963, **129**, 69.

[320] Van Vechten, J. A. and Bergstresser, T. K. 'Electronic Structures of Semiconductor Alloys'. *Phys. Rev. B*, 1970, **1**, 3351.

[321] Zunger, A. and Jaffe, J. 'Structural Origin of Optical Bowing in Semiconductor Alloys'. *Phys. Rev. Lett.*, 1983, **51**, 662.

[322] Bernard, J. E. and Zunger, A. 'Electronic Structure of ZnS, ZnSe, ZnTe, and their Pseudobinary Alloys'. *Phys. Rev. B*, 1987, **36**, 3199.

[323] Schnohr, C. 'Compound Semiconductor Alloys: From Atomic-Scale Structure to Bandgap Bowing'. *Appl. Phys. Rev.*, 2015, **2**, 031304.

[324] Thompson, A. and Woolley, J. 'Energy-Gap Variation in Mixed III–V Alloys'. *Can. J. Phys.*, 1967, **45**, 255–261.

[325] Burstein, E. 'Anomalous Optical Absorption Limit in InSb'. *Phys. Rev.*, 1954, **93**, 632.

[326] Moss, T. S. 'The Interpretation of the Properties of Indium Antimonide'. *Proc. Phys. Soc., Sect. B*, 1954, **67**, 775–782.

[327] Handa, T.; Yamada, T.; Kubota, H.; Ise, S.; Miyamoto, Y. and Kanemitsu, Y. 'Photocarrier Recombination and Injection Dynamics in Long-Term Stable Lead-Free $CH_3NH_3SnI_3$ Perovskite Thin Films and Solar Cells'. *J. Phys. Chem. C*, 2017, **121**, 16158–16165.

[328] Klug, M. T.; Milot, R. L.; Patel, J. B.; Green, T.; Sansom, H. C.; Farrar, M. D.; Ramadan, A. J.; Martani, S.; Wang, Z.; Wenger, B. *et al.* 'Metal Composition Influences Optoelectronic Quality in Mixed-Metal Lead–Tin Triiodide Perovskite Solar Absorbers'. *Energy Environ. Sci.*, 2020, **13**, 1776–1787.

[329] Zhu, Z.; Li, N.; Zhao, D.; Wang, L. and Jen, A. K.-Y. 'Improved Efficiency and Stability of Pb/Sn Binary Perovskite Solar Cells Fabricated by Galvanic Displacement Reaction'. *Adv. Energy Mater.*, 2019, **9**, 1802774.

[330] Yang, Z.; Zhang, X.; Yang, W.; Eperon, G. E. and Ginger, D. S. 'Tin-Lead Alloying for Efficient and Stable All-Inorganic Perovskite Solar Cells'. *Chem. Mater.*, 7 2020, **32**, 2782–2794.

[331] Subedi, B; Li, C; Junda, M. M.; Song, Z; Yan, Y and Podraza, N. J. 'Effects of Intrinsic and Atmospherically Induced Defects in Narrow Bandgap $(FASnI_3)_x(MAPbI_3)_{1-x}$ Perovskite Films and Solar Cells'. *J. Chem. Phys.*, 2020, **152**, 064705.

[332] Hilsum, C. 'Simple Empirical Relationship Between Mobility and Carrier Concentration'. *Electron. Lett.*, 1974, **10**, 259–260.

[333] Ghosh, T.; Aharon, S.; Etgar, L. and Ruhman, S. 'Free Carrier Emergence and Onset of Electron–Phonon Coupling in Methylammonium Lead Halide Perovskite Films'. *J. Am. Chem. Soc.*, 2017, **139**, 18262–18270.

[334] Petrov, A. A.; Goodilin, E. A.; Tarasov, A. B.; Lazarenko, V. A.; Dorovatovskii, P. V. and Khrustalev, V. N. 'Formamidinium Iodide: Crystal Structure and Phase Transitions'. *Acta Crystallogr., Sect. E: Crystallogr. Commun.*, 2017, **73**, 569–572.

[335] Aleksandrov, I.; Goncharov, A.; Makarenko, I. and Stishov, S. 'X-ray-Diffraction Study of the Equation of State and the Phase Transition in Cesium Iodide at Nearly Hydrostatic Pressure'. *Phys. Rev. B*, 1991, **43**, 6194.

[336] Palosz, B. 'The Structure of PbI_2 Polytypes 2H and 4H: a Study of the 2H-4H Transition'. *J. Phys.: Condens. Matter*, 1990, **2**, 5285.

[337] Howie, R.; Moser, W and Trevena, I. 'The Crystal Structure of Tin (II) Iodide'. *Acta Crystallogr., Sect. B: Struct. Crystallogr. Cryst. Chem.*, 1972, **28**, 2965–2971.

[338] Denes, G; Pannetier, J; Lucas, J and Le Marouille, J. 'About SnF_2 Stannous Fluoride. I. Crystallochemistry of α-SnF_2'. *J. Solid State Chem.*, 1979, **30**, 335–343.

[339] Reuter, H and Pawlak, R. 'Zinnhalogenverbindungen. II. Die Molekül und Kristallstrukturen von Zinn (IV)-Bromid und Iodid'. *Z. Kristallogr. Cryst. Mater.*, 2001, **216**, 34–38.

[340] Yamanaka, T; Kurashima, R and Mimaki, J. 'X-ray Diffraction Study of Bond Character of Rutile-Type SiO_2, GeO_2 and SnO_2'. *Z. Kristallogr. Cryst. Mater.*, 2000, **215**, 424–428.

[341] Nienhuys, H.-K. and Sundström, V. 'Intrinsic Complications in the Analysis of Optical-Pump, Terahertz Probe Experiments'. *Phys. Rev. B*, 2005, **71**, 235110.

[342] Lloyd-Hughes, J. and Jeon, T.-I. 'A Review of the Terahertz Conductivity of Bulk and Nano-Materials'. *J. Infrared, Millimeter, Terahertz Waves*, 2012, **33**, 871–925.

[343] Ulatowski, A. M.; Herz, L. M. and Johnston, M. B. 'Terahertz Conductivity Analysis for Highly Doped Thin-Film Semiconductors'. *Submitted*, 2020.

[344] Ulatowski, A. M.; Wright, A. D.; Wenger, B.; Buizza, L. R.; Motti, S. G.; Eggimann, H. J.; Savill, K. J.; Borchert, J.; Snaith, H. J.; Johnston, M. B. *et al.* 'Charge-Carrier Trapping Dynamics in Bismuth-Doped Thin Films of $MAPbBr_3$ Perovskite'. *J. Phys. Chem. Lett.*, 2020, **11**, 3681–3688.

[345] La-O-Vorakiat, C.; Cheng, L.; Salim, T.; Marcus, R. A.; Michel-Beyerle, M. E.; Lam, Y. M. and Chia, E. E. 'Phonon Features in Terahertz Photoconductivity Spectra due to Data Analysis Artifact: A Case Study on Organometallic Halide Perovskites'. *Appl. Phys. Lett.*, 2017, **110**.

[346] Beechem, T. and Graham, S. 'Temperature and Doping Dependence of Phonon Lifetimes and Decay Pathways in GaN'. *J. Appl. Phys.*, 2008, **103**, 093507.

[347] Klemens, P. 'Anharmonic Decay of Optical Phonons'. *Phys. Rev.*, 1966, **148**, 845.

[348] Bhatt, A.; Kim, K. and Stroscio, M. 'Theoretical Calculation of Longitudinal-Optical-Phonon Lifetime in GaAs'. *J. Appl. Phys.*, 1994, **76**, 3905–3907.

[349] Grundmann, M. *Physics of Semiconductors*. Vol. 11. Springer, 2010.